REGGE PHENOMENOLOGY OF INCLUSIVE REACTIONS

S.N. GANGULI and D.P. ROY

Tata Institute of Fundamental Research, Bombay 400005, India

REGGE PHENOMENOLOGY OF INCLUSIVE REACTIONS

S.N. GANGULI and D.P. ROY

Tata Institute of Fundamental Research, Bombay 400005, India

Contents*

* Sections 3, 4 and subsections 2.3, 2.4 are by SNG, and the rest by DPR.

Abstract:

This project is devoted to updating the Regge phenomenology of inclusive reaction and correlation, with the help of the low p_T data acquired over the last 5 years or so. The analyses over the fragmentation region are largely based on the Mueller–Regge formalism. For the central cross-section and correlation data, however, the Mueller–Regge formalism is seen to be inadequate; and the analyses are largely based on the multiperipheral cluster model and the Gribov calculus. The effort has been to make the individual sections self-contained, at the cost of some duplication. The important gaps remaining in the data, as also in the theoretical interpretation of the available data, are brought out at the end of the relevant sections.

1. Introduction

The Regge phenomenology of inclusive reactions, like the Regge phenomenology in general, has virtually come to a halt since last five years or so. However, there has been a slow but steady accumulation of inclusive reaction and correlation data at low p_T, over these years. Indeed, many of these experiments were designed with the purpose of Regge analysis and are qualitatively superior to the older experiments of their kind. The time lag is simply the typical gestation time of a present day electronics experiment, further stretched in some cases no doubt by the declining interest in the field. This project aims to update the status of the Regge phenomenology of inclusive reaction and correlation, using these new data.

At the outset, of course, such a project has to face the two questions which underlie the current decline of interest in the S-matrix approach. Firstly, is there a useful role any more for an admittedly phenomenological approach like the S-matrix, in view of the progress made in a more fundamental theory of hadron interaction in terms of quarks and gluons – i.e. QCD? Secondly, is there anything worth knowing in the S-matrix approach, which is not already known? To a good extent, we believe, the answers to both the questions are in the affirmative. (i) What one presumably has so far is a perturbative QCD theory, which is only applicable in the deep inelastic region – i.e. large p_T ($\gg 1$ GeV, say) region. It is evident from fig. 1 that this region accounts for an extremely small fraction of hadron interaction. The bulk of the events are concentrated in the low p_T (<1 GeV) region, where unfortunately the perturbative QCD breaks down†. Efforts at developing a nonperturbative QCD theory are nowhere near a stage, where a meaningful phenomenology is feasible. In other words we may not have a viable alternative to the S-matrix approach for the low p_T physics for a long time to come. Moreover, a majority of the QCD experts seem to share the hope that when a successful non-perturbative theory is finally developed, it will generate the S-matrix objects like dual Regge poles from the underlying quark and gluon fields. In this case, of course, the S-matrix approach will continue to play a meaningful phenomenological role for low p_T physics. (ii) As regards the second point, we shall see in the subsequent sections that these new data provide, for the first time, precise quantitative answers to some of the long standing questions. Moreover, there are still a number of significant gaps in the data as also in our theoretical understanding of the available data, which we shall try to articulate at the end of the relevant sections.

The following sections discuss in detail the inclusive kinematics, the Mueller–Regge formalism, the duality predictions and the predictions related to the Pomeron (i.e. Pomeron factorisation, f–P proportionality and the decoupling theorems). Much of this is available in the existing reviews on the subject [2–9], in particular that of Roberts [8]. The subsequent sections will be devoted to the

---

† Although some models for the low p_T phenomenology, based on perturbative QCD, have been proposed [1], they are essentially empirical in nature and limited in scope.
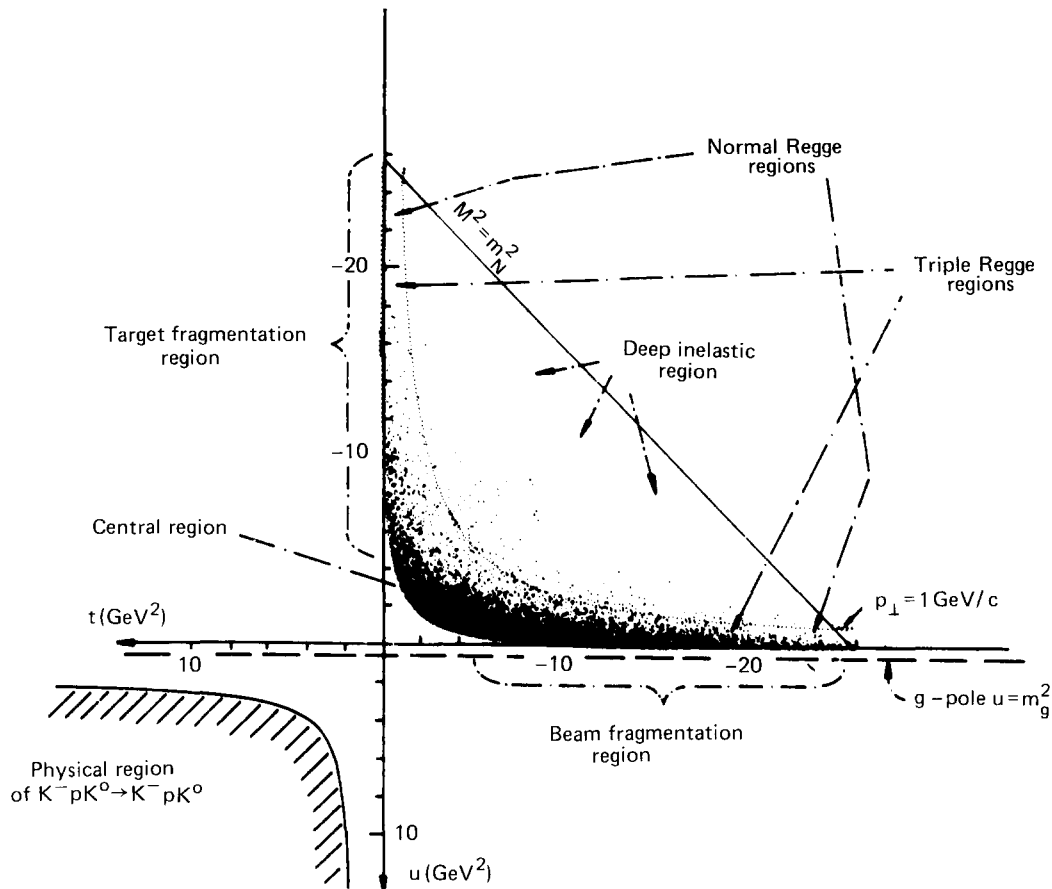
Fig. 1.1. The phase space event distribution for the inclusive reaction $K^-p \to \bar{K}^0 X$ at 14.3 GeV/c [66]. The figure is taken from ref. [8].

phenomenology of the various aspects of inclusive reaction and correlation. As indicated earlier, the emphasis will be on the data, accumulated over the last 5–6 years, much of which have remained unused so far. For the sake of perspective, and completeness, however, we shall also cover the essential features of the existing analyses, based on the older data.

Let us add a few words about the layout. The formalism developed in this introductory section is primarily for the single particle inclusive cross-section and the Mueller–Regge model. However, the phenomenological analysis of the subsequent sections will also involve two particle inclusive cross-section, i.e. in correlation; and more importantly some alternative Regge models like the multi-peripheral cluster model and Gribov calculus model, as in the cases of the central cross-section and correlation. The additional formalism necessary for these will be included in the respective sections. We find this more convenient, as it minimises cross reference between different sections. For the same reason, the parts of the Mueller–Regge formalism, relevant for the subsequent sections will also be summarised in the respective sections. This helps to make each section self-contained at the cost of some duplication. The equations and the figures for each section will be numbered separately. In referring to the equations and figures the section index would be dropped, except for the rare occasions when a cross reference is made between different sections. We feel that a reader, with some familiarity with the field, can proceed straight to the section of his choice.

1.1. Kinematics

Consider the inclusive reaction
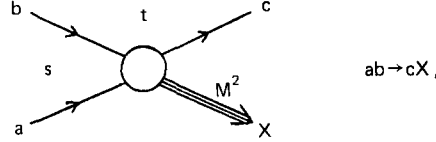
where a, b and c refer respectively to the beam, target and the detected particles. We have here 4 invariants – the energy square of ab(s), the momentum transfer squares between bc(t) and ac(u), and the missing mass square (M^2). Of course, only 3 of these 4 are independent, since

$$s + t + u = m_a^2 + m_b^2 + m_c^2 + M^2. \tag{1.1}$$

At large s, the phase space of the final particle c can be naturally divided into 3 parts – the two fragmentation regions and the central region. The fragmentation regions correspond to the regions of finite t (b-fragmentation region) and finite u (a-fragmentation region). Intuitively, of course, c can be looked upon as a fragment of b(a) when the momentum transfer between the two remains finite at large s. Over the b(a) fragmentation region the reaction ab→cX is often written in the form b —^{a}→ c(a —^{b}→ c). The central region corresponds to the remainder, i.e. where t and u are both large†. Since identical considerations apply to the 2 fragmentation regions we shall discuss only one (b-fragmentation region) explicitly.

For Regge analyses, the most convenient variables for the b-fragmentation region are s, t, M^2 and those for the central region s, t, u. However, the experimental data is mostly available in terms of the directly measurable quantities s and p_L, p_T – the longitudinal and transverse momenta of c. The longitudinal momentum is measured either in the lab. (p_L) or the CM(p_L^*) systems. In the latter case it is usually given in terms of the Feynman variable,

$$x = p_L^*/p_{in}. \tag{1.2}$$

The purpose of scaling the variable with the incident CMS momentum p_{in} is connected, of course, with the scaling hypothesis as we shall see later‡. Let us simply note here that at large s the entire phase space of c is spanned by the range $x = 1$ to -1, independent of s. It can therefore, be used for describing the central and both the fragmentation regions. In contrast p_L is only suitable for the description of the target fragmentation region. For a range of finite p_L only spans the b-fragmentation region as $s \to \infty$ – the central and the a-fragmentation regions correspond to ranges of p_L increasing indefinitely with s. The 2 sets of variables (x, p_T) and (p_L, p_T) are related through

$$x = -\frac{1}{p_{in}} \left[\frac{1}{s} ((m_b + E_a)(p_L^2 + \kappa^2)^{1/2} - p_a p_L)^2 - \kappa^2 \right]^{1/2} \tag{1.3}$$

$$= \frac{p_L - (p_L^2 + \kappa^2)^{1/2}}{m_b} + O(1/s), \text{ at finite } p_L \tag{1.3a}$$

† See fig. 1 and remember that we are only interested in the low p_T (≤ 1 GeV) region.

‡ Sometimes the quantities $\sqrt{s/2}$ or p^{*Max} have been used instead of p_{in} in the definition of x. Asymptotically they are all the same, and at moderate energies none is more sacred than the others.

where E_a, p_a are the incident lab. energy, momentum and

$$\kappa = [m_c^2 + p_T^2]^{1/2} = [E^2 - p_L^2]^{1/2} \tag{1.4}$$

is referred to by some as the longitudinal mass and by others as the transverse mass. The 2 sets of variables are related to the relevant invariant quantities as follows. For the lab. system (p_L, p_T)

$$\frac{M^2}{s} = \frac{1}{s}(m_a^2 + m_b^2 + m_c^2) + \frac{2}{s}[m_b E_a - (m_b + E_a)(p_L^2 + \kappa^2)^{1/2} + p_a p_L] \tag{1.4a}$$

$$= 1 - \frac{(p_L^2 + \kappa^2)^{1/2} - p_L}{m_b} + O(1/s), \text{ at finite } p_L \tag{1.4b}$$

$$t = m_b^2 + m_c^2 - 2m_b[p_L^2 + \kappa^2]^{1/2}. \tag{1.5}$$

For the CM system (x, p_T)

$$\frac{M^2}{s} = 1 - \frac{2E^*}{\sqrt{s}} + m_c^2/s$$

$$= 1 - \frac{2}{\sqrt{s}}[x^2 p_{in}^2 + \kappa^2]^{1/2} + \frac{m_c^2}{s} \tag{1.6}$$

$$= 1 - |x| + O(1/s), \text{ at finite } x \tag{1.6a}$$

$$t, u = m_{b,a}^2 + m_c^2 - 2E_{b,a}^* E^* + 2p_{b,a}^* p_L^*$$

i.e.

$$t = m_b^2 + m_c^2 - 2[(x^2 p_{in}^2 + \kappa^2)(p_{in}^2 + m_b^2)]^{1/2} - 2x p_{in}^2 \tag{1.7}$$

$$= m_b^2 + m_c^2 - |x| m_b^2 - \kappa^2/|x| + O(1/s), \text{ at finite negative } x, \tag{1.7a}$$

$$u = m_a^2 + m_c^2 - 2[(x^2 p_{in}^2 + \kappa^2)(p_{in}^2 + m_a^2)]^{1/2} + 2x p_{in}^2 \tag{1.8}$$

$$= m_a^2 + m_c^2 - x m_a^2 - \kappa^2/x + O(1/s), \text{ at finite positive } x, \tag{1.8a}$$

and at very small $|x|(<2\kappa/s^{1/2})$

$$t, u = m_{b,a}^2 + m_c^2 - s^{1/2}\kappa \left(1 \pm \frac{xs^{1/2}}{2\kappa} + \frac{x^2 s}{8\kappa^2} \cdots\right) + O(s^{-1/2}). \tag{1.9}$$

One sees from eqs. (7, 8 and 9) that the negative (positive) finite x region corresponds to b(a) fragmentation, i.e. $t(u)$ finite; whereas the central region corresponds to a small neighbourhood around

$x = 0$. Strictly speaking, both t and $u \to \infty$ only over an infinitesimal segment

$$-2\kappa/s^{1/2} < x < 2\kappa/s^{1/2}.$$

For a practical phenomenology, of course, one treats $t, u > 5\,\text{GeV}^2$, as the central region. For $\kappa^2 \geq 0.5\,\text{GeV}^2$, and ISR energy range, this would correspond to the strip $-0.1 < x < 0.1$. Lastly, one may note from eq. (6) that the low missing mass (M^2) region corresponds to the ends $x \simeq \pm 1$.

1.1.1. Rapidity

Another longitudinal variable, which has been extensively used is the rapidity. In general the rapidity of a particle is related to its 4-momentum via

$$y = \sinh^{-1}\left(\frac{p_L}{\kappa}\right) = \ln\left(\frac{E + p_L}{\kappa}\right) = \tfrac{1}{2}\ln\left(\frac{E + p_L}{E - p_L}\right) \tag{1.10}$$

and the 4-momentum

$$p = (\kappa \cosh y, p_T, \kappa \sinh y). \tag{1.11}$$

Naturally y depends on the frame in which p_L is measured; but one attractive feature of this variable is its simple additive nature under boosts along the longitudinal direction. One can simply see this by taking another particle, with 4-momentum

$$p' = (\kappa' \cosh y', p_T', \kappa' \sinh y'). \tag{1.11a}$$

It then follows from the Lorentz invariance of the scalar product $p \cdot p'$, that for any longitudinal boost the rapidity difference $y - y'$ remains invariant. In other words the rapidities of all the particle are boosted by the same amount, in going from one longitudinal frame to another.

Let us look at the kinematics for our inclusive reaction $ab \to cX$. In the lab. frame, we have

$$p_a = (m_a \cosh Y, 0, m_a \sinh Y)$$
$$p_b = (m_b, 0, 0) \tag{1.12}$$
$$p_c = (\kappa \cosh y, p_T, \kappa \sinh y)$$

where Y and y denote the rapidities of the beam a and the detected particle c. Now,

$$s = (p_a + p_b^2) \simeq m_a m_b\, e^Y, \quad \text{i.e.}$$
$$Y \simeq \ln(s/m_a m_b), \quad \text{at large } s, \tag{1.13}$$

and

$$-\ln(m_b/\kappa) < y < Y + \ln(m_a/\kappa), \tag{1.14}$$

which simply follows from eq. (18) below. Thus the rapidity range of c grows like $\ln s$. The b-fragmentation region, of course, corresponds to a finite region as one simply sees from the definition (10) above.

In the CMS frame, we have

$$p_a^* = (m_a \cosh Y_a^*, 0, m_a \sinh Y_a^*)$$

$$p_b^* = (m_b \cosh Y_b^*, 0, m_b \sinh Y_b^*) \tag{1.15}$$

$$p_c^* = (\kappa \cosh y^*, p_T, \kappa \sinh y^*)$$

$$Y_{a,b}^* = \pm \sinh^{-1}(p_{in}/m_{a,b}) \simeq \pm \ln(s^{1/2}/m_{a,b}) \quad \text{at large } s \tag{1.16}$$

$$y^* = \sinh^{-1}\frac{xp_{in}}{\kappa} \simeq \frac{x}{|x|}\ln\frac{|x|s^{1/2}}{\kappa} \quad \text{at large } s \text{ and finite } x(|x|s^{1/2} \gg \kappa) \tag{1.17}$$

i.e.

$$-\ln(s^{1/2}/\kappa) < y^* < \ln(s^{1/2}/\kappa),$$

or

$$Y_b^* - \ln(m_b/\kappa) < y^* < Y_a^* + \ln(m_a/\kappa). \tag{1.18}$$

One may note in particular that for $m_c < m_{a,b}$ (e.g. $pp \to \pi X$) the rapidity range of the produced particle exceeds those of the incident ones. Thus, for the pp collision at the highest ISR energy ($\ln s \simeq 8$) one has $Y_{a,b}^* \simeq \pm 4$, and the rapidity range for the produced pions ($\langle \kappa \rangle \approx 0.4$) is $-5 \lesssim y^* \lesssim 5$. One may also see from eqs. (17, 18) that unlike x the rapidity range increases indefinitely with $s(\sim \ln s)$. But more importantly the increase comes entirely from the central ($x \simeq 0$) region. The finite x regions ($x = \pm(0.1$ to 1)) correspond to finite ranges of rapidity ($\simeq 2$ units each) – just pushed farther and farther apart with increasing s. Thus for $pp \to \pi X$ at the highest ISR energy the central region ($x = -0.1$ to 0.1) covering only 10% of the x plot, gets stretched in the y^* plot to cover over 50% as illustrated in fig. 2. It means
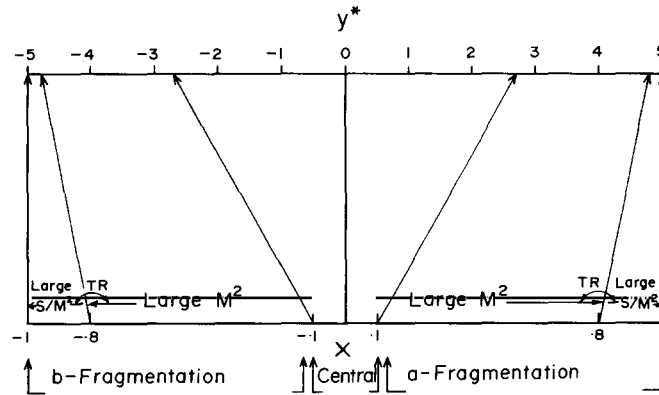

Fig. 1.2. The correspondence between the x and y plots for $pp \to \pi X$ at the top ISR energy.

that the variable y^* has a far greater advantage over x for the central region analysis, particularly its dependence on the longitudinal variable. Of course, it also means that unlike x, the y^* is unsuitable for the fragmentation region, as it corresponds to different ranges of y^* at different energies. For the fragmentation region one has to use the lab. rapidity y. This is only a minor inconvenience, however, since the two are simply related by

$$y^* = y + Y_b^* = y - \sinh^{-1}(p_{in}/m_b) \simeq y - \tfrac{1}{2}\ln(s/m_b^2). \tag{1.19}$$

The set (y, p_T) or (y^*, p_T) can be related to the invariant quantities by using eqs. (4–10). The most useful ones are

$$y^* \simeq \tfrac{1}{2}\ln(t/u) \tag{1.20}$$

$$\kappa^2 \simeq ut/s \tag{1.21}$$

both valid over the central region (large t and u); and

$$y \simeq -\ln(m_b/\kappa) - \ln(1 - M^2/s) \tag{1.22}$$

valid over the b-fragmentation region.

Finally a variable often used in place of rapidity is the so-called pseudo rapidity

$$\eta = -\ln \cdot \tan(\theta/2) \tag{1.23}$$

θ being simply the polar angle of the detected particle c. It is evident from comparing eqs. (10) and (23) that

$$\eta \simeq y, \quad \text{for } m_c \ll p_T \tag{1.24}$$

which is a reasonable approximation for pions. Obviously η is a useful variable to measure in experiments, that do not have momentum measurement facility.

1.1.2. Invariant cross-section

The Lorentz invariant cross-section for this inclusive reaction is defined as[†]

$$F(s, p_c) = E_c \, d\sigma/d^3p_c \tag{1.25}$$

where the factor E_c comes because the Lorentz invariant phase space is d^3p_c/E_c.

From the relation between the different sets of variables, as given above, one can construct the corresponding Jacobians. Thus one can relate the differential cross-section, expressed in different sets of variables, with one another. The relations are, in fact, extremely simple, i.e.

[†] Similarly the invariant two-particle inclusive cross-section is $F(s, p_c, p_d) = E_c E_d \, d\sigma/d^3p_c \, d^3p_d$.

$$
\begin{aligned}
F(s, p_c) &= E_c \frac{d\sigma}{d^3 p_c} = \frac{E}{2\pi} \frac{d\sigma}{p^2 \sin\theta \, d\theta \, dp} \\
&= \frac{E}{\pi} \frac{d\sigma}{dp_L \, dp_T^2} = \frac{E^*}{\pi p_{in}^*} \frac{d\sigma}{dx \, dp_T^2} \\
&= \frac{1}{\pi} \frac{d\sigma}{dy \, dp_T^2} = \frac{1}{\pi} \frac{d\sigma}{dy^* \, dp_T^2} \\
&= \frac{(2p_{in}^*/\sqrt{s})}{\pi} \frac{d\sigma}{dt \, dM^2/s} = \frac{(2p_{in}^*\sqrt{s})}{\pi} \frac{d\sigma}{dt \, du}
\end{aligned}
\tag{1.26}
$$

where the subscripts c from E_c, p_c have been dropped following the convention developed above.

Let us close this subsection with two observations, which are important for practical phenomenology. (i) The relation between the 3 longitudinal variables p_L, x and y_L involve p_T. Thus when only the p_T integrated distribution is given it is not possible to transform one longitudinal variable to the others (e.g. from $d\sigma/dp_L$ to $d\sigma/dy$ or $d\sigma/dx$). The practice in the past has been to assume that one can go ahead simply by substituting p_T with its average value. We have explicitly checked in the case of pp→πX, where both y_L and x distributions are available from the same experiment, that the error involved in this procedure is much too large, and it should therefore be avoided. Of course, when the double distribution is available, one can freely transform from one set of variables to another using the relation between them, as given above, along the eq. (26). (ii) The different choices of scaling variables in the fragmentation region (p_L, p_T); (x, p_T); (y, p_T); $(M^2/s, t)$ are of course, related to one another independent of s as $s \to \infty$. Thus the scaling of the cross-section in one implies scaling in all the others at asymptotic energies. There are important sub-asymptotic effects, however, represented by the $O(1/s)$ terms in these relations. As a result a precocious scaling in one variable, over the PS range ($s = 20$–$60\,\text{GeV}^2$, say) would imply a significant scale breaking in another, over the same range of s. In particular for pp→π$^-$X, as we shall see in the next section, exact scaling for a fixed $(M^2/s, t)$ bite implies typically a 25–35% scale breaking for a fixed (x, p_T^2) bite over the above range of s. Thus a quantitative study of scaling with the PS data, is rather sensitive to the choice of scaling variables. It is a phenomenon to which sufficient attention has not been paid in the past. This is of course analogous to the case of Bjorken scaling for the deep inelastic scattering where precocious scaling has been observed for some specific choice of the scaling variable.

1.2. Mueller–Regge formalism

To a large extent the interest in the inclusive reactions was sparked off by the scaling prediction of Feynman [10] and Yang et al. [11]–i.e. the hadronic inclusive cross-sections are asymptotically independent of energy s, when certain variables (p_L, p_T), (x, p_T) or $(s/M^2, t)$ are held fixed. Of course, the arguments of Feynman and Yang were based on physical intuition, e.g. by analogy with e.m. radiation from a classical current, in Feynman's case. However, it was soon pointed out by Mueller [12] that the same results follow in the standard S-matrix approach as a generalisation of the constancy (approx.) of the total cross-sections at high energy.

1.2.1. Mueller's optical theorem

Let us recall the standard optical theorem connecting the total cross-section to the discontinuity of the forward elastic amplitude, i.e.
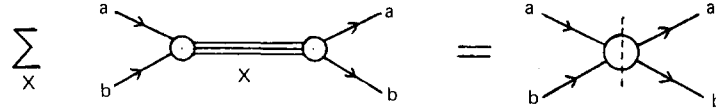
$$\sigma_{ab}^{T} = \frac{1}{2i}\,\text{Disc.}\,f_{ab}(s) = \text{Im}\,f_{ab}(s) \tag{1.27}$$

which follows from unitarity. The phenomenological advantage of this relation, is, of course, that a seemingly complicated situation (i.e. sum of exclusive processes with varying energy dependences) gets converted into a manageable one – a single 2 body amplitude. Mueller suggested an extension of this theorem, which connects the inclusive cross-section to the corresponding discontinuity of a 3-body forward elastic amplitude, i.e.
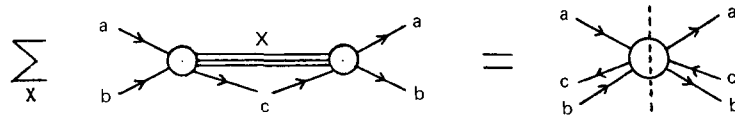
$$E_c\,d\sigma/dp_c^3 = \frac{1}{2i}\,\text{Disc.}\,f_{ab\bar{c}}(M^2) = F. \tag{1.28}$$

There are, of course, some additional complications for the 3-body case. On the formal side, the physical region of the inclusive reaction corresponds to an unphysical region of the 3-body elastic amplitude (fig. 1), which is evident from the fact that the subenergies of bc(t) and ac(u) are negative. Thus the relation assumes an analytic continuation of the 3-body amplitude into this unphysical region. Moreover, two independent variables (notably M^2 and s) have overlapping cuts which complicates the definition of the appropriate discontinuity. However, it has been explicitly checked that such an analytic continuation is possible in certain field theoretic models and that the overlapping singularities can be properly taken into account [13–15]. A detailed account of these is given in ref. [9]. Let us simply state here that the theorem, while lacking a rigorous proof, has been generally accepted as a very plausible hypothesis. The appropriate discontinuity, corresponds to
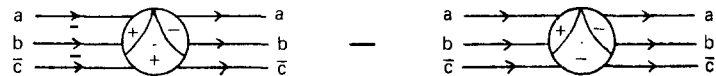
$$\text{Disc.}\,f_{ab\bar{c}}(M^2) = f_{ab\bar{c}}(s + i\,\varepsilon, M^2 + i\,\varepsilon, s' - i\,\varepsilon) - f_{ab\bar{c}}(s + i\,\varepsilon, M^2 - i\,\varepsilon, s' - i\,\varepsilon). \tag{1.29}$$

On the practical side the 3-body amplitude is not a measurable quantity (even in its physical region), unlike the 2-body case. Hence, the Mueller's optical theorem cannot be subjected to direct experimental test. However, one can predict many features of the 3-body amplitude from the Regge theory and duality, which can be tested with the inclusive data. This is similar, of course, to testing things like exchange degeneracy and Regge behaviour of a 2-body elastic amplitude with the total cross-section data. Let us write down the Regge expansion of the 3-body amplitude in both the fragmentation and the central regions [12]. A general criterion for Regge expansion of a multiparticle amplitude is that all the invariants spanning across the Regge exchange be large compared to all the invariants lying on its either

side. And since different invariant quantities become large over different parts of the phase space (see figs. 1, 2), the corresponding Regge expansions are different.

1.2.2. Fragmentation region

(a) Large M^2 (single Regge expansion): Let us consider the b-fragmentation region only. Here the 3-body amplitude can be approximated by the leading Regge exchanges in aā, i.e.
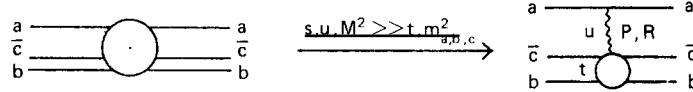
$$F = \beta_P(s/M^2, t)s^{\alpha_P(0)-1} + \sum_{R=\rho,\omega,f,A_2} \beta_R(s/M^2, t)s^{\alpha_R(0)-1}$$

$$= \beta_P(s/M^2, t) + \sum_R \beta_R s^{-1/2} \qquad (1.30)$$

where P and R are the Pomeron ($\alpha_P(0) = 1$) and the leading meson trajectories ($\alpha_R(0) = \frac{1}{2}$), which we shall often refer to simply as the Reggons. Thus like the total cross-sections, the inclusive cross-section asymptotically goes to a constant, with the Reggeon contribution going down as $s^{-1/2}$. In other words the Mueller–Regge model automatically leads to the Feynman–Yang scaling, and in addition predicts how the scaling limit is reached.

(b) Large s/M^2 (standard Regge expansion): Here the standard Regge expansion in the $t(b\bar{c})$-channel applies to the amplitude $ab \to cX$, i.e.
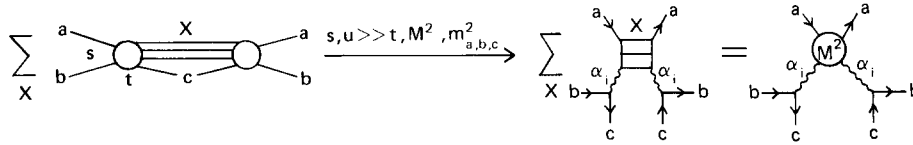
$$F = s \frac{d\sigma}{dt\, dM^2} = (\beta_{bc}^i)^2 \cdot s^{2\alpha_i-1} \cdot \text{Im}\, f_{ia}(M^2) \qquad (1.31)$$

where α_i is the leading Regge pole in the $b\bar{c}$ channel, and the last factor represents the forward discontinuity of the elastic Reggeon-particle amplitude (i.e. the Reggeon-particle total cross-section). Of course, when more than one Regge exchange in $b\bar{c}$ are considered, the expression gets a little more involved because of the interference terms. One gets

$$F = \sum_{ij} \beta_{bc}^i \beta_{bc}^j \xi_i \xi_j^* s^{\alpha_i+\alpha_j-1} \text{Im}\, f_{ia,ja}(M^2), \qquad (1.32)$$

where ξ stands for the signature factor.

(c) Large s/M^2 and M^2 (triple Regge expansion): Evidently this corresponds to the overlap of regions a and b above (figs. 1, 2). Here one can further expand the Reggeon-particle amplitude in terms of the leading Regge exchanges in aā, which leads to the triple-Regge graph below:
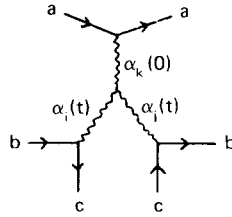
$$F = \sum_{ijk} \beta^i_{bc}\beta^j_{bc}\beta^k_{aa} g_{ijk}\xi_i\xi_j^* \, s^{\alpha_i+\alpha_j-1}(M^2)^{\alpha_k(0)-\alpha_i-\alpha_j}$$

$$= \sum_{ijk} G_{ijk} s^{\alpha_i+\alpha_j-1}(M^2)^{\alpha_k(0)-\alpha_i-\alpha_j} \tag{1.33}$$

where g_{ijk} stands for the triple-Regge coupling. The first derivation of the triple-Regge formula in the Mueller–Regge model, was due to De Tar et al. [16]. The term $-\alpha_i - \alpha_j$ in the exponent of M^2 arises because the relevant Reggeon-particle amplitude corresponds to maximal helicity flip of the Reggeon legs. A detailed account of the helicity pole formalism can be found in refs. [16, 9]. Let us simply note here that this term is, indeed, necessary for the consistency of eq. (33) with eq. (30), of which it is a special case.

Finally let us note that for M^2 and s/M^2 both large (>5, say) it is necessary to go beyond the PS energies for a reasonable range of s and/or M^2. Whereas, almost all the old triple-Regge fits are based on the PS data, it is only in the last 5–6 years that one has a reasonable amount of FNAL and ISR data over the triple Regge region.

(d) Finite mass sum rule: One sees from eqs. (32, 33) above that the forward Reggeon-particle amplitude has an asymptotic behaviour, very similar to that of a 2-body amplitude. Further it has been checked in the perturbation theory [17] and the dual resonance models [18] that the forward Reggeon-particle amplitude has the same analyticity and crossing properties as the ordinary 2-body amplitude. On the basis of these analytically crossing and asymptotic behaviours, a set of dispersion sum rules have been constructed for the forward Reggeon-particle amplitude [19–22] which are analogous to the finite energy sum rule (FESR) [23] for the 2-body amplitude. These are called the finite mass sum rule (FMSR), since the missing mass M^2 plays the role of dispersion variable here analogous to the energy variable in the 2-body case. It is convenient to define a variable

$$\nu = 2p_a \cdot (p_b - p_c) = (M^2 - t - m_a^2) \tag{1.34}$$

antisymmetric under crossing ($b \leftrightarrow c$). In terms of this antisymmetric variable, the FMSR read

$$\int_{\nu_0}^{N} [\mathrm{Im}\, A_{ia,ja}(\nu, t) - (-1)^n\, \mathrm{Im}\, A_{\bar{j}a,\bar{i}a}(\nu, t)]\nu^n \, d\nu = \sum_k \beta^k_{aa} g_{ijk}[1 - (-1)^n \tau_i \tau_j \tau_k]\frac{N^{\alpha_k(0)-\alpha_i-\alpha_j+n+1}}{\alpha_k(0) - \alpha_i - \alpha_j + n + 1} \tag{1.35}$$

where $\tau_{i,j,k}$ are the signatures (± 1) of the respective trajectories. The integrand has been constructed to be anti-symmetric under crossing ($\nu \rightarrow -\nu$), in order to eliminate the fixed pole contribution as in the

2-body case. The corresponding FMSR for the inclusive cross-section are

$$
\int_{\nu_0}^{N} \left[s \frac{d\sigma(ab \to cX)}{dt\, d\nu} - (-1)^n \frac{d\sigma(ac \to bX)}{dt\, d\nu} \right] \nu^n \, d\nu
$$

$$
= \sum_{ijk} G_{ijk} s^{\alpha_i + \alpha_j - 1} [1 - (-1)^n \tau_i \tau_j \tau_k] \frac{N^{\alpha_k(0) - \alpha_i - \alpha_j + n + 1}}{\alpha_k(0) - \alpha_i - \alpha_j + n + 1} \,. \tag{1.36}
$$

Thus the triple-Regge couplings can be estimated from the low M^2 data, through FMSR. This is particularly useful at PS energies, where the condition $s/M^2 \gg 1$, only holds over the low M^2 region.

Finally, in analogy with the Dolen–Horn–Schmid duality in 2-body scattering [23, 24], one may expect the FMSR to hold semilocally [25]. Thus for a $b\bar{c}$ system, which filters out a single Reggeon i, one expects

$$
\left\langle \frac{d\sigma(ab \to cX)}{dt\, d\nu} \pm \frac{d\sigma(ac \to bX)}{dt\, d\nu} \right\rangle \simeq s^{2\alpha_i - 2} \sum_{k = P, R} G_{iik} (1 \pm \tau_k)(\nu)^{\alpha_k(0) - 2\alpha_i}. \tag{1.37}
$$

Further, one may supplement this by the Harari–Freund hypothesis [26, 27] (see next subsection), which suggests that the Pomeron (P) and Reggeons (R) are separately dual, to the resonance and background contributions in the missing mass channel X, i.e.

$$
\left\langle \frac{d\sigma(ab \to cX)}{dt\, d\nu} \pm \frac{d\sigma(ac \to bX)}{dt\, d\nu} \right\rangle^{\text{Res,BG}} \simeq s^{2\alpha_i - 2} G_{iiR,P} \cdot (1 \pm \tau_{R,P})(\nu)^{\alpha_{R,P}(0) - 2\alpha_i}. \tag{1.38}
$$

These are evidently very powerful duality predictions, both for inclusive and quasi 2-body phenomenology. In particular they provide a correlation between the resonance mass and its production cross-section, which string together a host of quasi 2-body reactions, as we shall see in section 3.

1.2.3. Central region (double Regge expansion)

Here s, t and u all become large with a fixed ratio $ut/s = \kappa^2$ (eq. (21)). The 3-body amplitude can be approximated by the double Regge graph shown below:
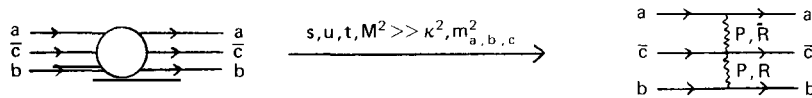
$$
F = \gamma_{PP}(\kappa) + \sum_{R} [\gamma_{PR}(\kappa) t^{-1/2} + \gamma_{RP}(\kappa) u^{-1/2}] + \sum_{RR'} \gamma_{RR'}(\kappa)(tu)^{-1/2}
$$

$$
= \gamma_{PP}(\kappa) + \kappa^{-1/2} s^{-1/4} \sum_{R} [\gamma_{PR}(\kappa) e^{-y^*/2} + \gamma_{RP}(\kappa) e^{y^*/2}] + \kappa^{-1} s^{-1/2} \sum_{RR'} \gamma_{RR'}(\kappa) \tag{1.39}
$$

with

$$
\gamma_{ij}(\kappa) = \beta^i_{aa} \beta^j_{bb} \gamma^c_{ij}(\kappa). \tag{1.40}
$$

At asymptotic energies the inclusive cross-section in the central region goes to a constant, independent of both energy and rapidity, as predicted by Feynman [10]. Thus the Mueller–Regge model again leads to Feynman scaling, and in addition predicts how the scaling limit is reached. One may note that for all practical purposes the central region phenomenology is restricted to the ISR data, i.e. to $pp \to cX$. For this system the leading non-scaling term (PR) simplifies to

$$2\kappa^{-1/2}s^{-1/4}\cosh(y^*/2)\sum_R \gamma_{PR}(\kappa).$$

In closing this subsection let us note that the scaling predictions of eqs. (30) and (39) above are not crucially dependent on the Pomeron being a factorising pole singularity with intercept exactly at 1. If it were a branch point singularity or its intercept slightly away from 1, one would have a $\log s$ or s^ε deviation from scaling, which would be phenomenologically hard to distinguish from the exact scaling results. However, if we have a factorising pole Pomeron and/or a Pomeron intercept of exactly 1, then we have further phenomenological predictions. Similarly, there will be additional phenomenological predictions arising from the duality hypothesis for the Reggeons. These predictions are discussed in the following subsections.

1.3. Duality

In 2-body scattering the duality predictions generally refer to two types of phenomena: (i) the semilocal averaging of the low energy scattering amplitude by the leading Regge exchanges $(P + R)$ as observed by Dolen, Horn and Schmid [24]; and (ii) the separate identification of the resonance and background components with the Reggeon (R) and Pomeron (P) exchanges as proposed by Harari and Freund [26, 27]. We have already described the extension of the first to the 3-body amplitude, in the last subsection. Let us discuss here the extension of the second type of prediction – the 2-component duality of Harari and Freund to the 3-body case.

1.3.1. 2-component duality (2-body amplitude)

Let us recall the essential features of the 2-component duality. The production amplitude can be split into 2-components, which correspond to the planar quark diagrams shown in fig. 3a. The 1st corresponds to a resonant $(q\bar{q})$ state, and the 2nd to a nonresonant $(q\bar{q}q\bar{q})$ state which can be expressed, however, as a two resonance state. The last diagram for each is simply a short hand notation where the $q\bar{q}$ pairs of the external legs are shown as a single line (wavy for a resonance).

Squaring each and summing over the final states $(r_i$ and $r_i, r_j)$ gives the total cross-section, i.e. $\mathrm{Im}\, f_{ab}^{el}$ (fig. 3b); where the components 1 and 2 have the particles ab lying on the same and separate quark loops. The 1st component, corresponding to resonant $(q\bar{q})$ channel, also corresponds to $q\bar{q}$ exchange in t, i.e. the standard Reggeons R. The 2nd component, corresponding to nonresonant $(q\bar{q}q\bar{q})$ s-channel, corresponds to vacuum exchange in t – i.e. the so-called topological Pomeron. Evidently, for exotic amplitudes like K^+p and pp only the 2nd component is present. Now, the most crucial part of the hypothesis (sometimes called the strong Harai–Freund hypothesis) is that this topological Pomeron contains only the leading vacuum singularity at $\alpha \simeq 1$ (the standard Pomeron) – i.e. it does not have a component at $\alpha \simeq \frac{1}{2}$, corresponding to the f, ω contributions. With this hypothesis, of course, the exotic cross-sections like K^+p and pp are predicted to be roughly constant, which is the famous exchange degeneracy result.

Fig. 1.3. The 2-component duality configurations for (a) the production amplitude; and (b) the total cross-section (2-body elastic amplitude).

In recent times the strong Harari–Freund hypothesis has been under some fire. (1) It has been suggested from the phenomenology of rising cross-sections (fig. 4), that a monotonically rising Pomeron contribution would require a significant positive contribution to $\sigma^T_{Kp,pp}$ from f–ω exchange – i.e. a significant breaking of exchange degeneracy $(\beta^f \gtrsim 2\beta^\omega)$ [28, 29, 30]. (2) However, equally good fits have been obtained with f, ω exchange degeneracy, but with a nonmonotonic Pomeron contribution [31]. (3) Finally, the simplest dual unitarisation models for Pomeron seem to eliminate the f contribution $(\beta^f = 0)$ i.e. it implies a strong breaking of the f, ω exchange degeneracy but in the opposite direction [32]. This model has also been reconciled with the total cross-section data, but at the cost of an even more nonmonotonic Pomeron contribution [33]. In fact a dynamical model for the nonmonotonic Pomeron contribution has been suggested in ref. [33], in terms of the successive thresholds for new quantum number excitation. It seems a reasonable model, although too qualitative to be able to distinguish between fits 2 and 3.

In summary, the topological Pomeron contribution, as represented by the Kp and pp total cross-sections, is flat over a wide energy range, but its interpretation in terms of the strong Harari–Freund hypothesis (exchange degenerate f, ω and constant Pomeron contribution) is not unambiguous. In extending the duality prediction to the 3-body case, all we shall need to assume is this constancy of the
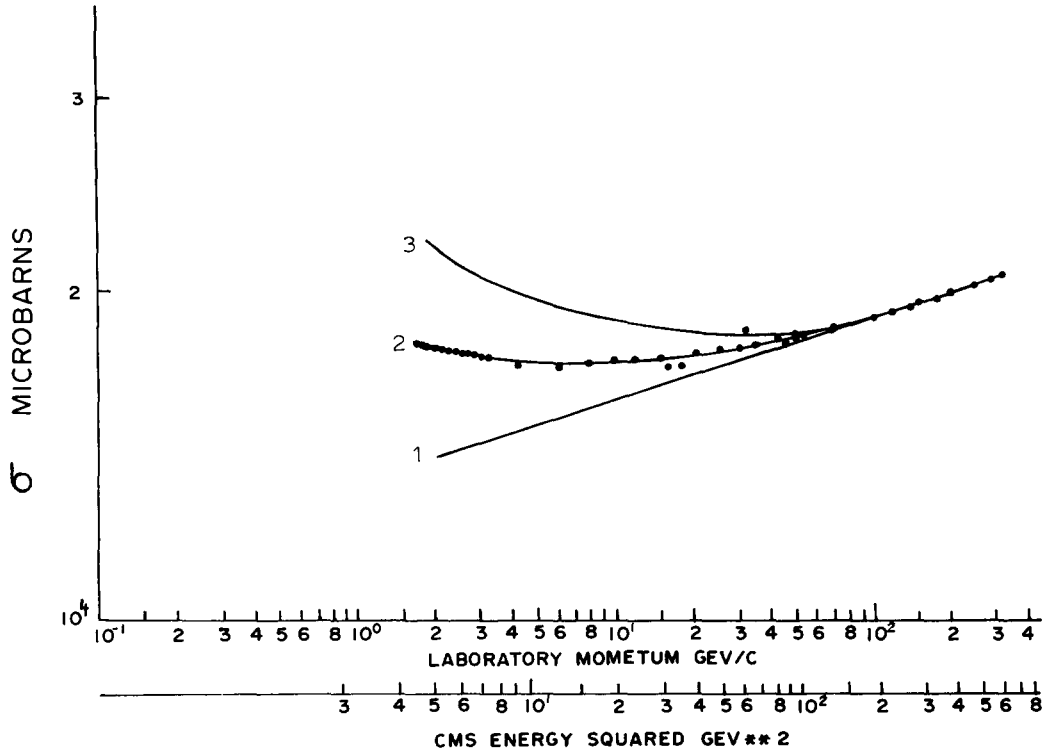
Fig. 1.4. The K^+p total cross-section data [67]. The solid lines roughly sketch the Pomeron contributions for the 3 models described in the text.

topological Pomeron contribution; although we shall continue to use $\beta^f = \beta^\omega$ and $\alpha_P = 1$ as its simplest parametrisation. It should be borne in mind, nevertheless, that in the absence of the strong Harari–Freund hypothesis, one may regard the constancy of the topological Pomeron contribution in $\sigma^T_{Kp,pp}$ as accidental phenomena, which need not repeat for other situations [34, 35].

1.3.2. 7-component duality (3-body amplitude)

The 2-component duality scheme for the 2-body amplitude, extends quite naturally to a 7-component scheme for the 3-body amplitude [34–36]. There are 3 independent configurations for single resonance production, 3 independent ones for two-resonance production and 1 for three-resonance production, as shown in fig. 5a. Squaring each and summing over the resonance states, we get the corresponding 7 components for the 3-body elastic amplitude, as shown in fig. 5b.

Here again particles lying on the same quark loop are connected by the Reggeon exchange, and those lying on different quark loops are connected by the topological Pomeron exchange. Thus we have for large s, t, u (which hopefully holds for moderate t, u also)

$$1, 2, 3, 4 \propto t^{\alpha_R(0)-1} \cdot u^{\alpha_R(0)-1}$$

$$5 \propto t^{\alpha_P(0)-1} \cdot u^{\alpha_R(0)-1}$$

$$6 \propto t^{\alpha_R(0)-1} \cdot u^{\alpha_P(0)-1}$$

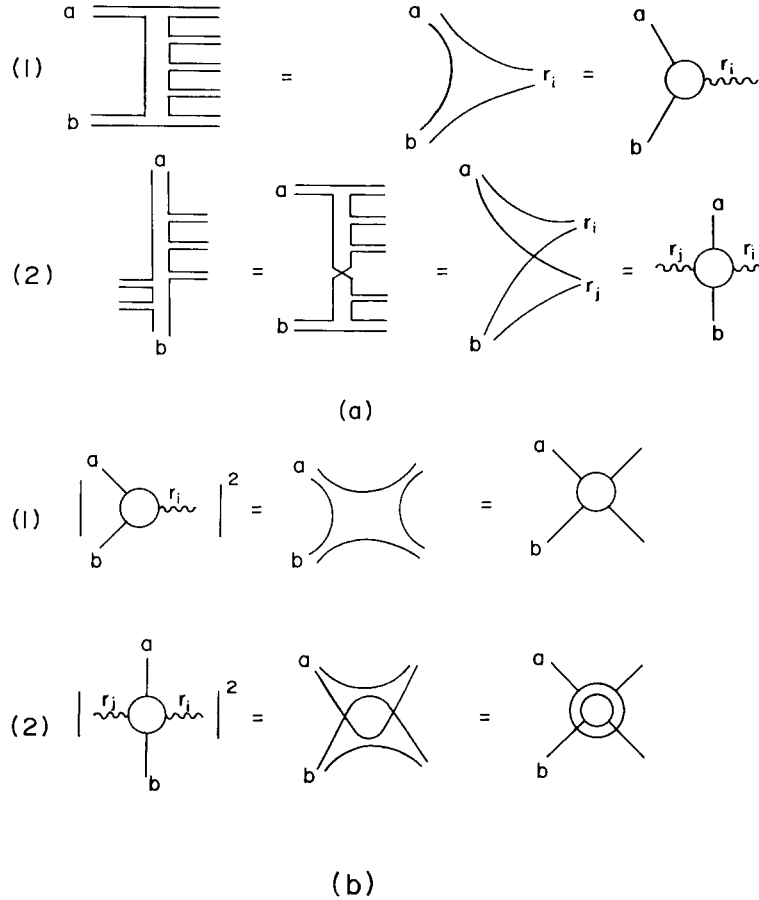$$7 \propto t^{\alpha_P(0)-1} \cdot u^{\alpha_P(0)-1}.$$

(1.41)
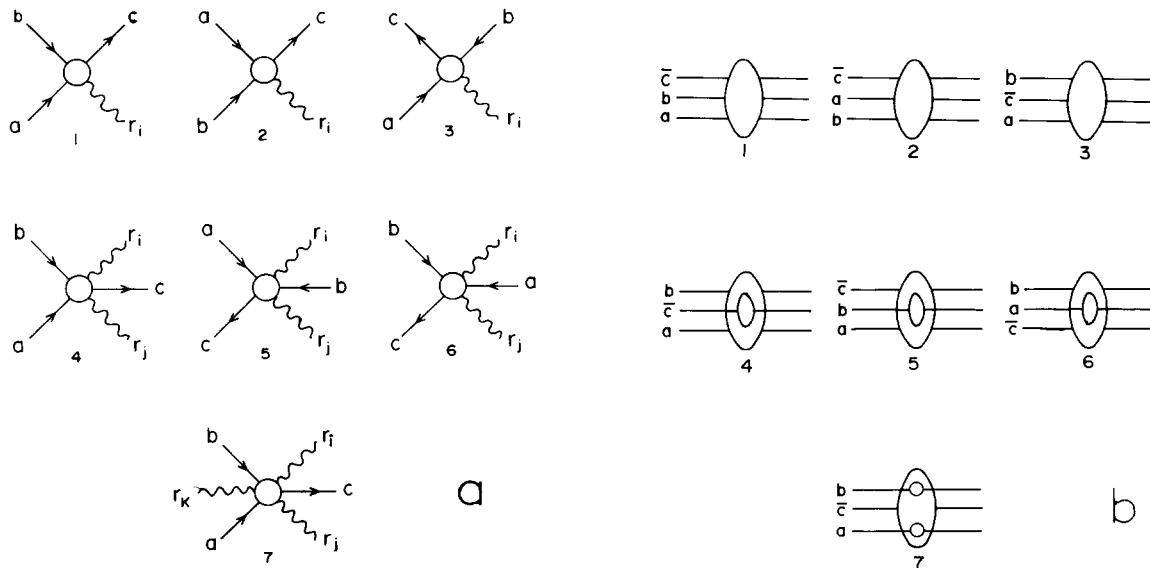
Fig. 1.5. The 7-component duality configurations for (a) the production amplitude; and (b) the inclusive cross-section (3-body elastic amplitude).

One may note that in the central region (eq. (39)) the scaling term comes from component 7, the leading nonscaling terms from 5, 6 and the tertiary terms from 1–4. Similarly in the b-fragmentation region (eq. (30)) the scaling terms come from components 6, 7 and the nonscaling terms from 1–5.

Note that each of the 7 components is the square of a production amplitude and hence positive. The interference terms are neglected. For instance, the interference term between 1–2 corresponds to
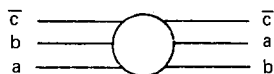
which vanishes for high energy forward amplitude, analogous to the vanishing of the $s-u$ planar amplitude

in the 2-body case. Similarly the 1–6 interference term is absent unless either a or $b\bar{c}$ have vacuum quantum numbers. Thus many of the interference terms can be explicitly seen to go away. The rest are assumed away.

1.3.3. Early scaling predictions (exoticity criteria)

Of course, the components 1–3 are absent if the system $ab\bar{c}$ is exotic, and 4, 5, 6 are absent if the systems ab, $a\bar{c}$, $b\bar{c}$ are respectively exotic. Thus if certain channels are exotic, duality would predict the non-scaling (Reggeon) contributions in eq. (41) to vanish and the inclusive cross-section to show precocious scaling, analogous to the K^+p or pp total cross-section. Thus the sufficient condition for early scaling in the b-fragmentation region is for the components 1–5 to vanish, i.e. the systems $ab\bar{c}$, ab and $a\bar{c}$ to be exotic, and that for the central region is, for 1–6 to vanish, i.e. the systems $ab\bar{c}$, ab, $a\bar{c}$ and $b\bar{c}$ to be exotic [36].

However, one expects some of the components to be kinematically suppressed relative to the others over a significant part of the fragmentation region (i.e. small t) and hence a less stringent exoticity criterion for early scaling, as suggested by Chan et al. [37, 38]. At small $t(\ll 1)$, the components with $b\bar{c}$ next to each other on the same quark loop are expected to be dominant, provided $b\bar{c}$ is nonexotic†. One can see this either by naively extrapolating the Pomeron and Reggeon exchange formulae (fig. 5b) to $t \ll 1$, or from the planar production amplitudes of fig. 5a. Thus the dominant scaling component is 6 and the dominant nonscaling components are 1 and 3. The corresponding early scaling criterion is

exotic $ab\bar{c}$ and nonexotic $b\bar{c}$.   (I)

On the other hand two more severe exoticity criteria have been suggested. They are

exotic $ab\bar{c}$ and ab (II)

by Ellis et al. [36a], to ensure vanishing of the 4th component, and

exotic $ab\bar{c}$, ab and $a\bar{c}$ (III)

by Einhorn et al. [36] to ensure vanishing of the 4th and 5th components – i.e. all the nonscaling components. Evidently there is no conflict in principle amongst the three exoticity criteria mentioned above – each being an approximation over the subsequent one. Of course, how small the smaller nonscaling components 4 and 5 are, over the phenomenologically significant range of t, is something which can only be decided by data. The older data sets have all been in agreement with the simplest exoticity criterion (I) above. With the much higher precision data available now, one can probe into the smaller components 4 and 5. And we shall see in the next section that, while confirming the criterion I to be a good first approximation, they seem to show a small but systematic deviation, characteristic of the component 4. Finally, there is general agreement that at large x (the standard Regge and triple Regge regions) the relevant components are 1, 3 and 6 corresponding the criterion I. This is evidently equivalent to the Harari–Freund criterion for the Reggeon ($b\bar{c}$)-particle (a) amplitude, assumed in the last subsection (eq. (38)).

In the central region the conditions $a\bar{c}$ and $b\bar{c}$ exotic ensure the vanishing of the secondary terms (5, 6), and $ab\bar{c}$ and ab exotic ensure the vanishing of the tertiary terms (1–4). Hence they constitute the early scaling criterion in the central region.

Let us emphasise that all these works [36–38] assume the leading components, corresponding to the topological Pomeron exchange, to be constant a la the Harari–Freund hypothesis. Since all the components are positive, they predict the inclusive cross-section either to be constant or to fall to this constant limit from above; but they cannot account for a rising inclusive cross-section. In contrast Tye and Veneziano [35] have suggested, as indicated earlier, a departure from the Harari–Freund hypothesis – i.e. the topological Pomeron contains in addition to the constant term represented by the standard Pomeron exchange ($\alpha(0) = 1$), a significant non-scaling term arising out of f, ω exchange degeneracy breaking ($\alpha(0) = \frac{1}{2}$). Moreover, they have presented plausibility arguments to suggest that this non-scaling term is negative. They have proposed this to account for the observed rise in the inclusive cross-sections over the central region. They also expect the cross-section rise to show up in the

---

† For exotic $b\bar{c}$ the dominant components vanish, and the scheme becomes more complicated. However, such processes are of little significance in terms of practical phenomenology, since these fragmentation cross-sections are extremely small and hence the data very poor.

fragmentation region, provided the positive non-scaling terms (components 1–5) are eliminated by the above exoticity criteria. The characteristic feature of this model, of course, is the energy dependence of the scaling deviation $- s^{-1/2}$ for the fragmentation region and $s^{-1/4}$ for the central region. With the high precision data presently available, it has become possible to check for these energy dependence predictions, as we shall see in the subsequent sections. We should mention here, however, that the answers seem to be in the negative.

1.3.4. Diffractive excitation

The 2-component two-body amplitude discussed earlier, did not take into account the diffractive contribution to the production amplitude,
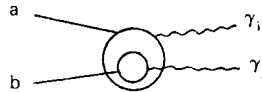
When squared this constitutes a new term in the 2nd component, representing 2-Pomeron cut. These are supposedly small relative to the Pomeron pole term, and hence neglected as a first approximation. In the 3-body amplitude, one can similarly check [35, 36] that there are diffractive contributions to the components 5–7, which are again neglected as a first approximation. In addition, however, diffractive excitations show up as two extra configurations,
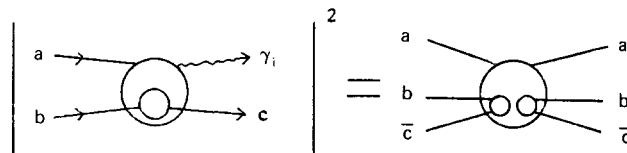
and similarly for b↔a, provided b̄c̄ or āc̄ have vacuum quantum members. These additional components (8 and 9) have to be taken into account, since they dominate the amplitude over certain kinematic regions – i.e. the triple Regge regions ($x \simeq \pm 1$). A peculiarity of the above diagram is that it corresponds to qq̄ states in the direct channel (abc̄), but vacuum exchange in the crossed channel (aā). On the basis of this, Einhorn et al. [36] have suggested that the triple Regge term PPR is negligible compared to the triple Pomeron PPP; and that the diffractive resonances are dual (at least partly) to this PPP. As we shall see in section 5, the recent data on pp → pX seem to confirm, indeed, both the features.

1.3.5. Lower lying Reggeons (φ and Baryonium)

In addition to the leading Reggeons ρ, ω, f, A_2 duality predicts the lower lying Reggeons φ (s̄s) and Baryonium (q̄q̄qq) [39–41] to show up in the K̄K and p̄p total cross-sections respectively, i.e.
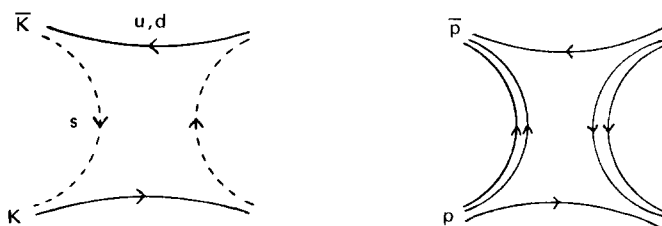
Indeed, the normal resonances ρ, ω, f, A_2 in the $\bar{K}K$ and $\bar{p}p$ amplitudes are expected to be dual to ϕ and Baryonium exchanges as one sees from the above diagrams [41, 23]. Whereas the $\bar{K}K$ total cross-section is not experimentally accessible, the $\bar{p}p$ total cross-section data seems, indeed, to show a Baryonium exchange signal [42] – but the size of the signal is quite small. As we shall see in the next section, however, the corresponding inclusive cross-sections, e.g.

$$p \xrightarrow{\ K^-\ } \Lambda \quad \text{and} \quad p \xrightarrow{\ \bar{p}\ } \pi^-$$

show large signals for ϕ and Baryonium exchanges respectively.

Let us comment on the identification of the ϕ and Baryonium exchanges with the strangeness and baryon number annihilation contributions to the respective inclusive or total cross-sections, since there has been some confusion on this issue. The strangeness annihilation contribution, necessarily corresponds to ϕ exchange as shown below. Of course, the converse is not true, as one can see by replacing
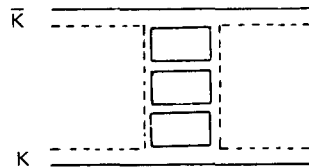
one of the normal quark loops by a strange quark. It may be reasonable to assume, however, that the latter contributions are kinematically suppressed due to the heavier K mass. Thus one may expect an approximate correspondence between the strangeness annihilation and ϕ exchange, as suggested by Inami and Miettinen [43]; and this seems to be borne out by data. There is no analogous correspondence between Baryonium exchange and baryon number annihilation, however, since the latter contributes to all – $\bar{q}\bar{q}qq$, $\bar{q}q$ and vacuum – exchanges [44]. Of course, in the colour junction model of
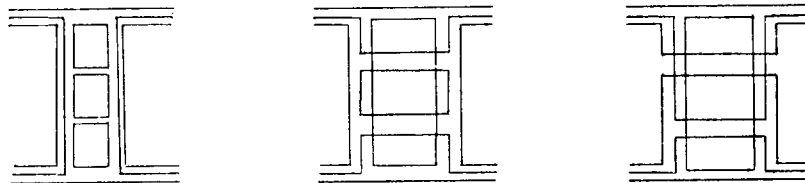
Baryoniums [45, 46], annihilation necessarily corresponds to Baryonium exchange, as shown below.
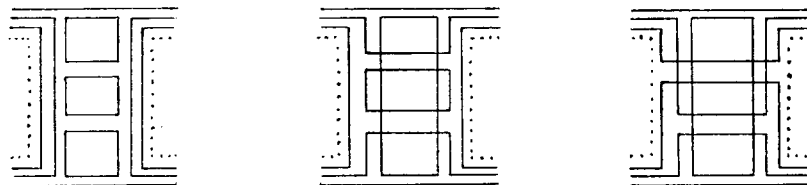
However, these Baryoniums are not all 4-quark states. In particular they contain the 0-quark and 2-junction

exchange (: :) with a high trajectory intercept $\sim\frac{1}{2}$. Thus the prediction of this model is the same as the Eylon–Harari model above [44] – i.e. unlike the strangeness annihilation cross-section the baryon number annihilation cross-section should fall slowly with energy $\sim s^{-1/2}$. This also seems to be consistent with the $\bar{p}p$ annihilation data.

1.4. Pomeron coupling constraints

If the Pomeron is a factorising pole singularity and/or the intercept is exactly at 1, then one has important constraints on the Pomeron couplings which can be tested with the inclusive data.

1.4.1. Factorisation

In the simplest dynamical model for Pomeron – i.e. the multiperipheral model [47] – the Pomeron comes out to be a factorising pole singularity. Besides it has been suggested on the basis of specific model calculations that an approximate factorisation (to $\leq 10\%$) holds for the effective Pomeron couplings in a wider class of models; in particular in eikonal models with fairly large multi-Pomeron cut corrections [48]. Thus it is important to phenomenologically test the factorisation property of the Pomeron couplings. In the 2-body case, whereas the factorisation test for elastic amplitudes is experimentally inaccessible, it has been checked for inelastic diffraction, but up to an accuracy of only 30% [49]. With the inclusive data, however, the factorisation test can be carried out for a large number of elastic (3-body) amplitudes. One can even afford to choose only exotic amplitudes, so as to suppress the Reggeon contamination. Thus, over the b-fragmentation region, the Pomeron contribution of eq. (30) is expected to factorise into

$$F_P(b \xrightarrow{a} c) = \beta_P(s/M^2, t) = \beta_{aa}^P \Gamma_{b\bar{c}}^P(s/M^2, t).\tag{1.42}$$

This means that the $b \xrightarrow{a} c$ cross-section at asymptotic energy (moderate energies for exotic processes) should be independent of 'a' when normalised by the corresponding 'ap' total cross-section

$$F(b \xrightarrow{a} c)/\sigma_{ap}^T \xrightarrow{s \to \infty} \Gamma_{b\bar{c}}^P/\beta_{pp}^P.\tag{1.43}$$

We shall see in the next section that, whereas the factorisation tests done so far were based on data compilations with a typical scatter of 25–30%, it is possible to do the test now with a single high precision experiment. And factorisation seems to be good to within 10%. One should note that apart from its theoretical significance, the factorisation relation is a useful phenomenological tool for e.g. extracting the Reggeon contribution from the inclusive cross-section data for non-exotic channels.

Of course, there are similar predictions for the central region. One gets, for instance, from eqs. (39, 40)

$$F(ab \to cX)/\sigma_{ab}^T \xrightarrow{s \to \infty} \gamma_{PP}^c(\kappa)\tag{1.44}$$

i.e. the asymptotic $ab \to cX$ central cross-section is independent of a and b when normalised by the ab total cross-section. They are not of much phenomenological use, however, since (i) the central cross-sections do not scale, even at ISR energies and (ii) the ISR cross-sections are any way limited to $pp \to cX$.

1.4.2. Pomeron-f proportionality

In the multiperipheral model for generating Pomeron from Reggeon exchanges, if one further assumes the Reggeon-particle amplitude to be dominated by Regge exchanges, as shown below,
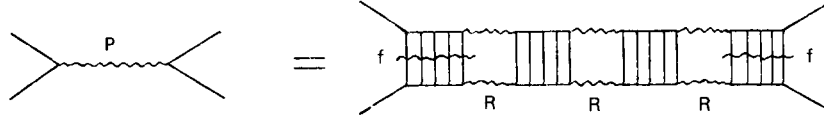
then the Pomeron coupling to the external particles, are expected to be proportional to the corresponding f couplings, i.e.

$$\beta^P_{aa}/\beta^P_{bb} = \beta^f_{aa}/\beta^f_{bb} \tag{1.45}$$

as first suggested by Carlitz, Green and Zee [50]. This prediction is evidently quite model dependent. None the less it is a powerful prediction, particularly since the Reggeon (f, A_2, ρ, ω) couplings are often interrelated by exchange degeneracy. Moreover, the prediction seems to work well in 2-body scattering, where [51]

$$\sigma^f_{\pi p}/\sigma^P_{\pi p} \simeq \sigma^f_{pp}/\sigma^P_{pp} \simeq 1/\sqrt{s}. \tag{1.46}$$

There are, of course, a large number of inclusive reactions where one can test the analogous predictions, over the fragmentation region. Reasonable success had been claimed for some of the reactions in the past [52]. As we shall see in the next section, however, the most reliable and significant one of these tests, i.e.

$$F^f(p \xrightarrow{\pi} \pi^-)/F^P(p \xrightarrow{\pi} \pi^-) = F^f(p \xrightarrow{\pi} \pi^+)/F^P(p \xrightarrow{\pi} \pi^+) \tag{1.47}$$

is off by a factor of 2. Similarly, for the triple Regge region, the Pomeron-f proportionality predicts, from eq. (46) above,

$$g_{PPP} \simeq g_{PPf} \tag{1.48}$$

and other relations arising from replacing the external Pomeron legs by f [53]. Again, this prediction (eq. (48)) seems badly off, since the PPf coupling turns out to be much smaller than PPP at small t, as we shall see in section 5.

1.4.3. Decoupling theorems

If the Pomeron is a factorising pole singularity with intercept exactly at 1, then certain Pomeron couplings are predicted to vanish as the Pomeron 4-momentum square $t \to 0$. They were first derived on the basis of the multiperipheral model, where it was shown that the asymptotic total cross-section would violate the unitarity bound unless these couplings vanish. The first such decoupling theorem was derived by Verdiev et al. [54] and Finkelstein and Kajantie [55] for the double Pomeron exchange term (described in detail in section 6). Later, Gribov and Migdal [56] and Abarbanel et al. [57] derived this, for the triple Pomeron coupling. Subsequently a more general derivation of the triple Pomeron

decoupling was given by Jones et al. [58], along with several other decoupling results. Since this derivation is quite simple and general, it would be worthwhile to describe it briefly.

It is convenient for this purpose to start with the so-called energy momentum conservation sum rule [59]

$$(p_a + p_b)^\mu \sigma_{ab}^T = \sum_c \int d^3 p_c \cdot p_c^\mu \, d\sigma/d^3 p_c. \tag{1.49}$$

Expressed in terms of the cross-section, the sum rule is a trivial consequence of energy-momentum conservation. It acquires dynamical content, however, when the total and inclusive cross-sections are related to the two and three body elastic amplitudes via unitarity, as we shall see below. Taking the difference of the C.M. energy and the longitudinal momentum components in the sum rule gives, for $s \to \infty$

$$\sigma_{ab}^T = \pi \sum_c \int dp_T^2 \int_{-1}^{0} dx \, (E_c \, d\sigma/d^3 p_c). \tag{1.50}$$

Restricting to the channel $c = b$, and the kinematic region dominated by the triple Pomeron, we have the inequality

$$\sigma_{ab}^T \geq \pi \int dp_T^2 \int_{1-\delta}^{1-M_0^2/s} d|x| \cdot F$$

$$\geq \pi \int_{t_{min} \to 0} dt \int_{1-\delta}^{1-M_0^2/s} \frac{d|x|}{1-|x|} (1-|x|)^{2\alpha'\cdot t} G_{PPP}(t) \tag{1.51}$$

where we have used eqs. (6a), (7a) and (33); and the fact that for $s \to \infty$, δ can be chosen arbitrarily small (i.e. $t_{min} \to 0$). Doing the t integration by parts gives

$$RHS = \frac{\pi G_{PPP}(0)}{2\alpha'} \int_{1-\delta}^{1-M_0^2/s} \frac{d|x|}{-(1-|x|)\ln(1-|x|)} + Const.$$

i.e.

$$\sigma_{ab}^T \geq \frac{\pi G_{PPP}(0)}{2\alpha'} \ln \cdot \ln(s/M_0^2). \tag{1.52}$$

While consistent with the Froissart bound this does violate the asymptotic unitarity bound for a factorising pole Pomeron,

$$\sigma_{ab}^T \xrightarrow{s \to \infty} Const. \tag{1.53}$$

unless the triple Pomeron coupling vanishes at $t \to 0$, i.e.

$$g_{PPP}(0) = 0. \tag{1.54}$$

More decoupling theorems have been obtained by considering the analogous energy-momentum conservation sum rule between one and two-particle inclusive cross-sections

$$(p_a + p_b - p_c)^\mu \frac{d\sigma}{d^3 p_c} = \sum_d \int d^3 p_d \cdot p_d^\mu \frac{d\sigma}{d^3 p_c \, d^3 p_d}. \tag{1.55}$$

Again, taking the difference of the C.M. energy and the longitudinal momentum components gives, for $s \to \infty$,

$$(1 - |x_c|) \frac{d\sigma}{d^3 p_c} = \pi \sum_d \int dp_{dT}^2 \int_{<0} dx_d \left(E_d \frac{d\sigma}{d^3 p_c \, d^3 p_d} \right) \tag{1.56}$$

where $x_d = 2p_d/\sqrt{s}$, which is kinematically restricted to the range $|x_d| < 1 - |x_c|$. Hence

$$(1 - |x_c|) E_c \frac{d\sigma}{d^3 p_c} \geq \pi \int dp_{dT}^2 \int_0^{1-|x_c|} d|x_d| \left(E_c E_d \frac{d\sigma}{d^3 p_c \, d^3 p_d} \right). \tag{1.57}$$

Again, we choose $c = b$ and the kinematic region dominated by triple Pomeron exchange ($x_c \simeq -1$). Then the single particle inclusive cross-section on the left is given by eq. (33), whereas the two-particle inclusive cross-section on the right is given by

$$E_c E_d \frac{d\sigma}{d^3 p_c \, d^3 p_d} = (\beta_{bc}^P(t))^2 \, \beta_{aa}^P(0) \cdot \left(\frac{\bar{M}^2}{s} \right)^{\alpha_P(0)} \cdot \left(\frac{s}{M^2} \right)^{2\alpha_P(t)} \cdot B \left(t, \bar{t}, \frac{M^2}{\bar{M}^2} \cdot \phi \right) \tag{1.58}$$
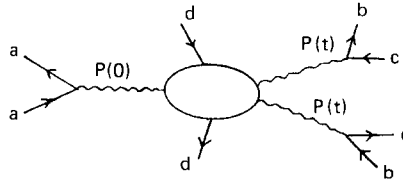
where

$$\bar{M}^2 = (p_a + p_b - p_c - p_d)^2$$
$$\bar{t} = (p_b - p_c - p_d)^2, \tag{1.59}$$

and ϕ is a Toller-like variable which drops out in the limit $t \to 0$, we are interested in. Here, B is the three-Pomeron – two-particle vertex occurring at the centre of the above diagram. From eqs. (33, 57)

and (58) one gets

$$g_{PPP}(t \to 0) \geq \pi \int dp^2_{dT} \int_0^{1-|x_c|} \frac{d|x_d|}{1-|x_c|} \left(\frac{\bar{M}^2}{M^2}\right) B\left(0, \bar{t}, \frac{M^2}{\bar{M}^2}\right)$$

$$\geq \pi \int dp^2_{dT} \int_0^1 dy \, (1-y) B(0, \bar{t}, y) \tag{1.60}$$
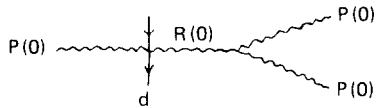
where

$$y = |x_d|/(1-|x_d|) \simeq 1 - \bar{M}^2/M^2 \tag{1.61}$$

is the Feynman variable for Pomeron $(b\bar{c}) + a \to dX$. Since, the above integrand is a positive quantity (cross-section), the vanishing of the triple Pomeron coupling implies the integrand to vanish identically, i.e.
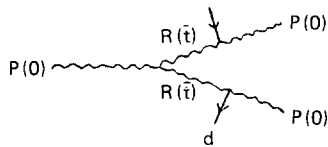
$$B(0, \bar{t}, y) = 0 \tag{1.62}$$

over the entire range of y and $\bar{t}$. Thus in the central region of particle $d(y \simeq 0, \bar{t}$ large), one gets

$$\gamma^d_{PR} \cdot g_{PPR} = 0 \tag{1.63}$$

i.e. either the Pomeron–Reggeon–$d\bar{d}$ central coupling or the PPR triple Regge coupling must vanish. Even more important is the triple Regge region of $B(y \simeq 1)$, where

$$g_{RRP}(\bar{t}) \beta^2_{PRd}(\bar{t}) = 0 \tag{1.64}$$

i.e. either the RRP triple Regge coupling or the PRd double-Regge coupling must vanish for all negative 4-momentum square $(\bar{t})$ of the Reggeon R. Moreover it seems possible to analytically continue either of these results to the mass-shell of the Reggeon $(\bar{t} = m_d^2)$ [9, 60], which leads to the extremely powerful (and embarrassing) result

$$\beta^P_{dd} = 0 \tag{1.65}$$

i.e. the Pomeron coupling to all forward elastic amplitudes must vanish.

Evidently the last mentioned result above is untenable. Fortunately, it seems, that when one takes account of the multi-Pomeron interaction in the standard perturbative approach of Gribov [56], the multi-Pomeron cuts invalidate the stronger decoupling results above (eqs. (63, 64)) [61, 62] and their

analytic continuation (eq. (65)) [63]. In contrast, the original derivation of the triple Pomeron decoupling has been shown to go through [56], in the presence of these multi-Pomeron cuts (the so-called weak coupling solution [64]). The same is true of the double Pomeron exchange (DPE) decoupling [54, 55].

Thus the decoupling predictions for the triple Pomeron and the DPE contributions are on sounder theoretical footing than the rest; and it is important to test them phenomenologically. As we shall see in sections 5 and 6, however, there is rather strong experimental evidence, that neither the triple Pomeron nor the DPE decouple at $t = 0$. Let us finally note that there is a theoretical model for the Pomeron, which can accommodate this situation. This is the so-called strong coupling solution, where the multi-Pomeron interactions are treated nonperturbatively. A detailed account of the weak and the strong coupling models is given in ref. [64]. We should simply mention here a couple of essential features of the strong coupling model. The Pomeron turns out to be a rather complicated (but still factorising) branch point singularity at $\alpha = 1$, and the asymptotic total cross-section is given by

$$\sigma_{ab}^{T} \xrightarrow{\quad s \to \infty \quad} (\ln s)^{0.38}. \tag{1.66}$$

However, this is only relevant for truly asymptotic energies, as one sees by incorporating threshold factors into the model. The thresholds for multiple Pomeron exchange are so severe that for any realistic energy range, the total cross-section is very well approximated by the zeoreth (Pomeron pole) and first order terms, of which the pole term dominates. In summary, it seems that the decoupling constraints based on asymptotic unitarity may have little phenomenological relevance at ISR or even higher energies.

1.5. Multiperipheral model

The multiperipheral model will be described in detail in the last two sections, where it will be extensively used in the analyses of central cross-section and correlation data. It would be appropriate, however, to make a few general observations about the model here. Firstly, the Pomeron coupling predictions, as noted above, were practically all based on the multiperipheral model. Secondly, and more importantly, the scaling prediction itself (both the energy independence of the inclusive cross-section in the fragmentation region and its energy and rapidity independence in the central region) was first obtained from the multiperipheral model [47], long before the work of Feynman, Yang or Mueller. Of course, the phenomenological interest in the prediction, arose only after its more general derivation in e.g. the Mueller–Regge formalism. In this context one should note that the multiperipheral model for exclusive production processes is a specific dynamical realisation of the Mueller–Regge formalism. While, the validity of the multiperipheral model ensures that of the Mueller–Regge scheme, the latter is expected to be valid for a much wider class of dynamical models. Naturally the predictions, following from the Mueller–Regge formalism are considered more reliable than the multiperipheral model predictions in general†. But for the same reason, the former are comparatively fewer in number and limited in scope, even for inclusive phenomenology. For instance, the multi-

† Another reason why the scaling prediction of the multiperipheral model in the mid-sixties was not considered a serious phenomenological proposition, was that the model as then applied to direct pion production, was known to have some serious phenomenological limitations. Most of them have been overcome in the modern version – i.e. the multiperipheral cluster model [65].

peripheral model predicts the nature and position of the Pomeron singularity [65], which have to be assumed in the Mueller–Regge formalism. More importantly, the multipheral model predicts the energy scales, where the asymptotic Regge behaviour for the fragmentation and central cross-sections (eqs. (30) and (39)) are expected to set in, and the type of threshold rise expected at lower energies. The latter is analogous to the threshold rise for the total cross-section, but stretched over a considerably larger energy range, particularly for the central cross-section, as we shall see in section 7. This seems to be the most plausible interpretation for the observed central cross-section rise. The effect can be incorporated into the Mueller–Regge formalism in terms of daughter trajectory contributions to eq. (39), but the formalism has, of course, little predictive value for this purpose. Similar effects are also expected in the central correlation data, for which the Mueller–Regge formalism would again be inadequate. Finally, things like semi-inclusive correlation are, of course, beyond the scope of Mueller–Regge formalism.

It is evident from the above observations, that the Mueller–Regge formalism, while extremely useful for multiparticle phenomenology, cannot be a substitute for an explicit dynamical model for particle production, like the multiperipheral model. It is in this context that the tests of multiperipheral model and the determination of the model parameters with the central cross-section and correlation data (sections 7 and 8) are very significant.

2. Fragmentation region (large M^2)

In the Mueller–Regge formalism this corresponds to the single Regge region; and the fragmentation cross-section $F(b \xrightarrow{a} c)$ can be approximated by the Regge exchanges in $a\bar{a}$, i.e.

$$F(b \xrightarrow{a} c) = \beta_P + \sum \beta_R s^{\alpha_R - 1}$$

$$R = \rho, \omega, f, A_2 \qquad \alpha_R \simeq \tfrac{1}{2}$$

(2.1)
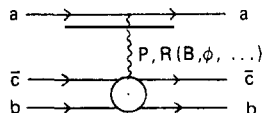
plus possible contributions from lower trajectories – e.g. Baryonium B exchange in $p \xrightarrow{\bar{p}} \pi$ or ϕ exchange in $p \xrightarrow{K^-} \Lambda$.

The phenomenology of the above fragmentation cross-sections is carried out in this section. As discussed at length in the introduction, the main features we would be studying are the following:

(i) signals for the lower lying trajectory exchanges, notably the Baryonium exchange signal in $p \xrightarrow{\bar{p}} \pi^{\pm}$;

(ii) exchange degeneracy (EXD) prediction for the leading Reggeons R and the early scaling criteria;

(iii) Pomeron factorisation;

(iv) Pomeron–f proportionality;

(v) possible deviation from scaling arising from kinematic effects i.e. the choice of scaling variables.

A detailed analysis of the high precision BNL–Pennsylvania data [68] on $p \to \pi$, is carried out in the first subsection. The following subsection presents compilations of the older data on $p \to \pi$, and the resulting phenomenology. The third subsection is devoted to the analysis of heavier fragments ($p \to K$, ρ, Λ, Δ, Σ_{1385}), which is again based on data compilations. The last one deals with the limited high energy data available on double fragmentation.

2.1. $p \to \pi$ (BNL–Pennsylvania data)

The BNL–Pennsylvania data is an invaluable piece of data for the single Regge analysis. With the same spectrometer and the same kinematic bite for the detected pion, they cover both the BNL and FNAL energies ($P_{lab} = 4$–$250 \, \text{GeV}/c$) and all the beam particles (p, $\bar{p}$, $\pi^{\pm}$, $K^{\pm}$). Thus, for the first time, one has a sufficiently large energy range with a sufficiently small point to point systematic error to do a quantitative Mueller–Regge analysis. The quoted error bars, corresponding to the statistical and the point to point systematic errors added in quadrature, are $\pm 5\%$ for the π^{+} beam and $\pm 3\%$ for the π^{-} and proton beams†. Unfortunately their kaon beam data have poor statistics; and for a meaningful phenomenology we have to supplement these by interpolations of kaon data from other sources.

The kinematic bite corresponds to the following ranges of the lab. momentum and angle of the detected particle;

$$0.3 \le p \le 0.6$$

$$59.4° \le \theta + \left(\frac{1 \, \text{GeV}/c}{p}\right) 3.4° \le 64.4°. \tag{2.2}$$

This corresponds roughly to a lab. rapidity y and p_T bite

$$0.6 \lesssim y \lesssim 0.7, \qquad 0.2 \lesssim p_T \lesssim 0.5. \tag{2.3}$$

Thus the measured inclusive cross-sections correspond to

$$\sigma(b \xrightarrow{a} c) = \int_{0.3}^{0.6} \int_{1.036-0.059/p}^{1.123-0.059/p} \frac{d\sigma}{dp \, d\theta} \, dp \, d\theta. \tag{2.4}$$

This is, of course, the same as the invariant cross-section $d\sigma/dy \, dp_T^2$, integrated over the invariant phase space element $dy \, dp_T^2$ corresponding to eq. (3) above.

As mentioned above, we shall be using the $p \xrightarrow{K^{\pm}} \pi^{-}$ data from other sources, integrated over the kinematic cut of eq. (4). These are the bubble chamber data for K^{-} beam at 10, 16 [69] and 14 GeV/c [70] and for K^{+} beam at 8, 16 [71] and 12 GeV/c [72]. Of these the 14 GeV/c K^{-} data and the 12 GeV K^{+} data are given as double distributions, from which the cross-section σ (eq. (4)) were evaluated using eq. (1.26). For the rest only the p_T^2 integrated distributions are available; and in evaluating the cross-section σ we assumed exponential p_T^2 dependence along with the quoted values of $\langle p_T^2 \rangle$.

2.1.1. Cross-section differences

The cleanest quantities for Regge analysis are, of course, the difference of particle and antiparticle induced inclusive cross-sections

$$\Delta_{ab}(c) = \sigma(b \xrightarrow{\bar{a}} c) - \sigma(b \xrightarrow{a} c) \tag{2.5}$$

which filters out the Pomeron and the even C Reggeon exchanges. Thus one expects

---

† In addition there is an overall normalisation error of 3%.

$$\Delta_{\pi p}(\pi^-) = \beta_\rho s^{\alpha_\rho - 1} \sim s^{-1/2} \tag{2.6}$$

$$\Delta_{Kp}(\pi^-) = \beta_{\rho,\omega} s^{\alpha_{\rho,\omega} - 1} \simeq \Delta_{\pi p}(\pi^-) \tag{2.7}$$

$$\Delta_{pp}(\pi^-) = \beta_{\rho,\omega} s^{\alpha_{\rho,\omega} - 1} + \beta_B s^{\alpha_B - 1} \simeq 2\Delta_{\pi p}(\pi^-) + \beta_B s^{\alpha_B - 1}. \tag{2.8}$$

The approximate relations amongst the leading Reggeon R contributions to the three processes follow from the 2-body coupling relations

$$\beta_{KK}^\omega \simeq \beta_{KK}^\rho \simeq \beta_{KK}^f \simeq \beta_{KK}^{A_2} \simeq \tfrac{1}{2}\beta_{\pi\pi}^\rho \simeq \tfrac{1}{2}\beta_{\pi\pi}^f = \tfrac{1}{2}\beta_\pi$$

$$\beta_{NN}^\rho \simeq \tfrac{1}{3}\beta_{NN}^\omega \simeq \tfrac{1}{3}\beta_{NN}^f \simeq \beta_{NN}^{A_2} = \tfrac{1}{2}\beta_\pi \tag{2.9}$$

and the degeneracy of the lower vertices (see eq. (1.42))

$$\Gamma_{p\pi^+}^\rho = \Gamma_{p\pi^+}^\omega = \Gamma_{p\pi^+}^f = \Gamma_{p\pi^+}^{A_2} = \Gamma_{p\pi^+}. \tag{2.10}$$

The 2-body coupling relations follow from duality and the so-called universality hypothesis; and in any case have been checked with the 2-body data [51]. The degeneracy of the lower vertices follows from the early scaling criterion I of subsection 1.3.3 ($ab\bar{c}$ exotic, $b\bar{c}$ non-exotic [37, 38]), which seems to be a good first approximation. Essentially identical relations hold for the cross-section differences $\Delta_{\pi p,pp}(\pi^+)$ whereas $\Delta_{Kp}(\pi^+)$ is expected to vanish (see table 3)†.

The BNL–Penn. data for $\Delta_{\pi p,pp}(\pi^-)$ are shown on a $s^{-1/2}$ plot in fig. 1 along with the $\Delta_{Kp}(\pi^-)$ points interpolated from the bubble chamber data. Before going into quantitative fits we should note the following features: (1) The quality of the $\Delta_{\pi p}(\pi^-)$ data is at least as good as the corresponding total cross-section difference, with which the first quantitative Regge fits were done [73]. It is roughly linear on the $s^{-1/2}$ plot. (2) The $\Delta_{pp}(\pi^-)$ points over the FNAL energy range are, to a good approximation, double the corresponding $\Delta_{\pi p}(\pi^-)$ points. There is a clear excess, however, at lower energies, which is very suggestive of a low lying trajectory exchange. The signal stands out in spite of the poor statistics of the antiproton data. (3) The $\Delta_{Kp}(\pi^-)$, obtained from the data compilation, is inadequate for a quantitative Mueller–Regge analysis‡. However, it is roughly equal to the $\Delta_{\pi p}(\pi^-)$.

The BNL–Penn. data on $\Delta_{\pi p,pp}(\pi^+)$, shown in fig. 2, are again consistent with the features 1 and 2 above. However, the uncertainties are much larger, due to the π^+ identification problem. The solid lines are the fits to the $\Delta_{\pi p,pp}(\pi^\pm)$ data with eqs. (6) and (8). The corresponding ρ and Baryonium B Regge parameters are shown in table 1 below. The α_ρ, estimated from the $\Delta_{\pi p}(\pi^-)$ data, is of course, a little low; which may be attributed to subasymptotic effects. The effect seems too small, however, to confuse the Baryonium exchange signal§ in $\Delta_{pp}(\pi^-)$.

Let us conclude this analysis with a few observations: (1) Qualitative indications of all the features noted above, including the anomalous component in $\Delta_{pp}(\pi^-)$ were seen from earlier data [74]; but no quantitative analyses were so far possible. (2) Baryonium exchange signals have been noted in a number

---

† Although the $\Gamma_{p\pi^-}^{\rho,f}$ vertices are not required a priori to be degenerate, such a degeneracy seems to be implied by the early scaling observed for $p \xrightarrow{\pi^-} \pi^+$ as we shall see below.

‡ This is typical, in fact, of the state of the game prior to the BNL–Penn. data.

§ Although there are other candidates for low lying exchange as e.g. Regge cuts, there is no natural reason for them to show up only in baryon–antibaryon processes.
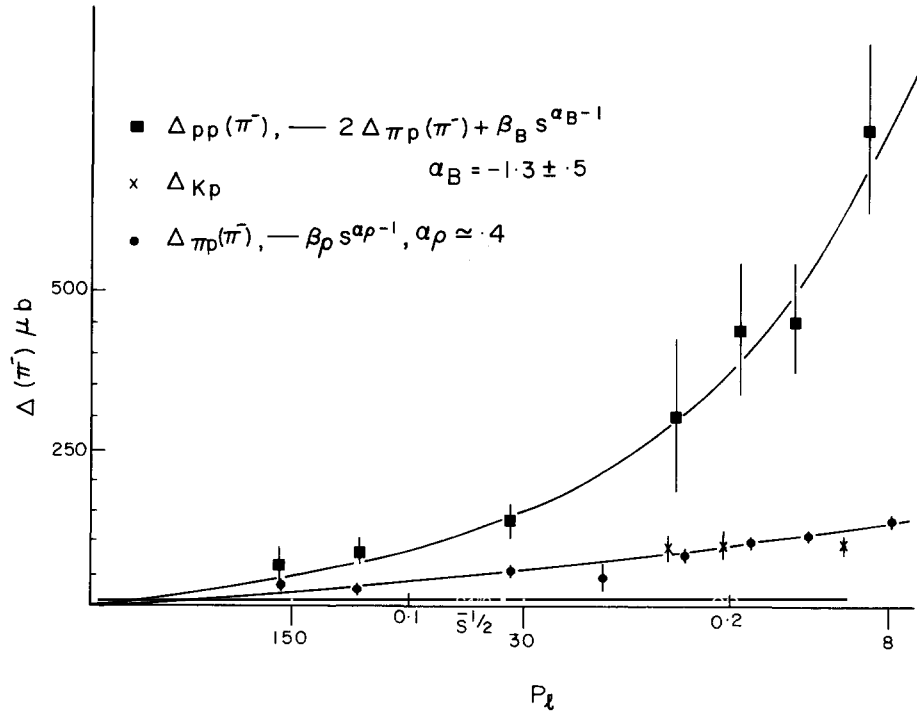
Fig. 2.1. The inclusive cross-section differences $\Delta_{\pi p,pp}(\pi^-)$ from the BNL–Penn. data [68] and $\Delta_{Kp}(\pi^-)$ from the data of refs. [69–72]. The fits are described in table 1.
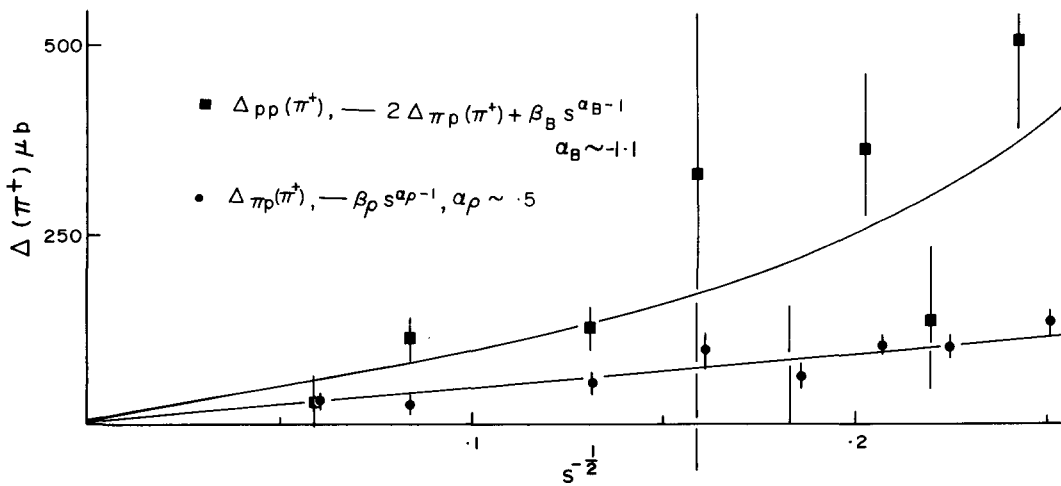
Fig. 2.2. The inclusive cross-section differences $\Delta_{\pi p,pp}(\pi^+)$ from the BNL–Penn. data [68]. The fits are described in table 1.

Table 2.1

Fits to the inclusive cross-section differences: $\Delta_{\pi p}(\pi) = \beta_\rho \cdot s^{\alpha_\rho - 1}$, $\Delta_{pp}(\pi) = 2\Delta_{\pi p}(\pi) + \beta_B \cdot s^{\alpha_B - 1}$

Process	β_ρ, β_B (mb)	α_ρ, α_B	χ^2/ν
$\Delta_{\pi p, pp}(\pi^-)$	0.76, 300	0.37, -1.3	6.3/11
$\Delta_{\pi p, pp}(\pi^+)$	0.49, 61	0.49, -1.1	16.3/12

of baryon–antibaryon processes [42, 75, 76]; but nowhere was the signal as pronounced as in $\Delta_{pp}(\pi^-)$. (3) From this $\Delta_{pp}(\pi^-)$ data one can in fact obtain a fairly reliable bound on ω–Baryonium mixing $(\theta_{\omega-B} \lesssim 15°)$ [77].

2.1.2. Cross-sections at FNAL energies

Let us now study the individual inclusive cross-sections. We shall restrict here to the FNAL energy range, where the Mueller–Regge predictions are most reliable. Moreover, we shall normalise the inclusive cross-section by the asymptotic total cross-section

$$f(b \xrightarrow{a} c) = \sigma(b \xrightarrow{a} c)/\sigma_{ap}^T \tag{2.11}$$

to facilitate the Pomeron factorisation test. For the asymptotic total cross-section we choose the values at 200 GeV/c [78], i.e.

$$\sigma_{pp,\pi p,Kp}^T = 39, 24, 20 \text{ mb}. \tag{2.12}$$

The normalised cross-sections of the BNL–Penn. data are shown on a $s^{-1/2}$ plot in fig. 3. The straight lines represent fits with eq. (1), assuming Pomeron factorisation, exchange degeneracy a la the exoticity criterion I [37, 38], and the leading Reggeon intercept $\alpha_R = \frac{1}{2}$. The magnitudes of the Reggeon couplings to the pion and antiproton induced processes, have not been constrained, however. The resulting Pomeron and Reggeon coupling parameters are shown in table 2 below. The error bars correspond to an increase of the total χ^2 by 1 unit.

From the fits of fig. 3 and the corresponding coupling parameters of table 2 one should note the following features:

(1) All the exotic processes (a la criterion I) show scaling over the FNAL range ($P_{lab} = 30$–250 GeV/c)

Table 2.2

Fits to $p \xrightarrow{\pi^\pm, p, \bar{p}} \pi^-$ and $p \xrightarrow{\pi^\pm, p, \bar{p}} \pi^+$ assuming $f(p \xrightarrow{\pi^\mp p} \pi^\mp) = A$,

$$f(p \xrightarrow{\pi^\mp, \bar{p}} \pi^\mp) = A + B_{\pi, p} s^{-1/2}$$

Process	$A(\times 10^3)$	$B_\pi(\times 10^3)$	$B_p(\times 10^3)$	χ^2/ν
$p \xrightarrow{\pi^\pm, p, \bar{p}} \pi^-$	6.69 ± 0.07	17.3 ± 1.4	24.6 ± 3.0	10.7/11
$p \xrightarrow{\pi^\pm, p, \bar{p}} \pi^+$	11.57 ± 0.11	16.5 ± 2.4	28.0 ± 3.8	5.1/11
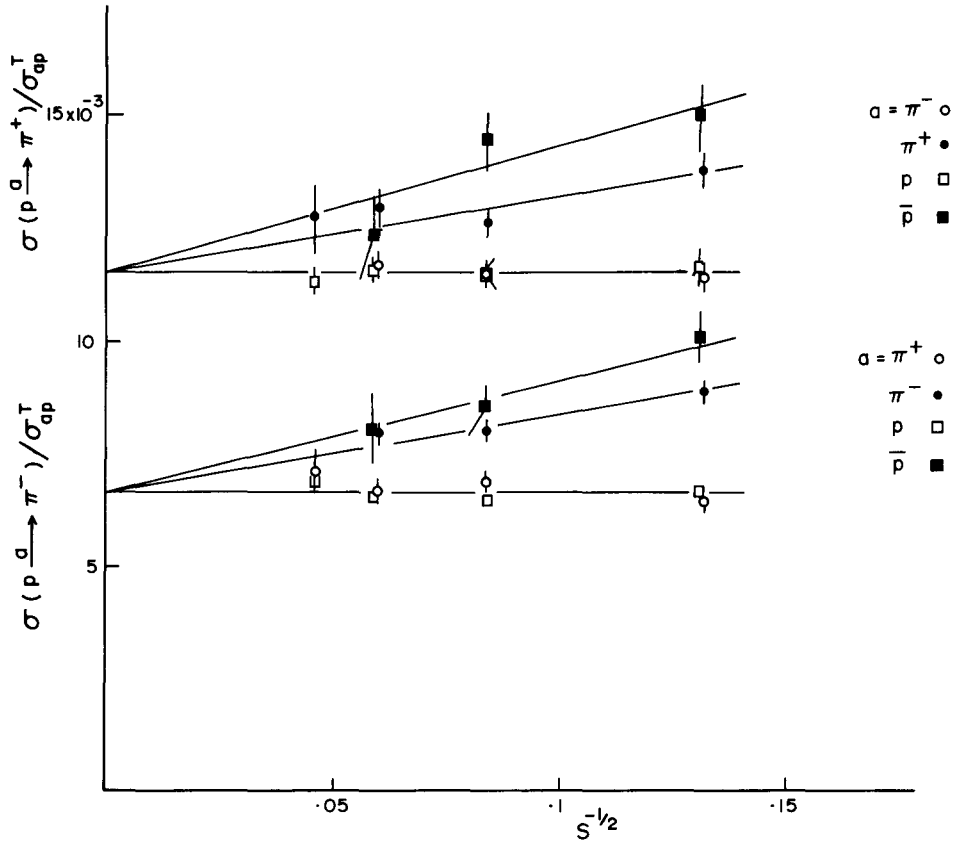
Fig. 2.3. The normalised inclusive cross-sections from the BNL–Penn. data [68] over the FNAL energy range. The fits are described in table 2.

to within 1 σ ($< \pm 5\%$) – i.e. scaling seems to hold to an accuracy of 10%. Note that these include the processes p $\xrightarrow{\text{p}}$ $\pi^{\pm}$ (ac non-exotic) and p $\xrightarrow{\pi^+}$ π^- (ab non-exotic) and thus confirm the criterion I [37, 38] to be a reasonable first approximation. It also includes the process p $\xrightarrow{\pi^-}$ π^+ (abc non-exotic), mentioned earlier, where early scaling is not required by the duality constraints. It does not conflict with the criterion I, however, which is only a sufficient criterion for early scaling.

(2) One should note that the observed scaling to within 10% accuracy over the FNAL range, only implies EXD to within 40% accuracy, i.e.

$$\frac{\beta_T - \beta_V}{\beta_T + \beta_V} < 0.4, \qquad (2.13)$$

T, V standing for the leading Tensor and Vector trajectories. This is because the scale is set by the fall of the non-exotic cross-sections over the same range (fig. 3). It may appear that going down to lower energies would give a more precise estimate on EXD. However, this is plagued by kinematic scale breaking effects as we shall see later.

(3) All the early scaling cross-sections are seen to satisfy Pomeron factorisation to again within 1σ – i.e. Pomeron factorisation holds to within 10%.

(4) It may be noted here that the previous tests of early scaling and Pomeron factorisation were all

based on data compilations; and they often went down to 8 GeV/c. As we shall see later, there is a typical scatter of ~25% in the data compilations and there is a further uncertainty of equally large magnitude coming from the kinematic scale breaking effects at the low energy end.

(5) The relative magnitudes of the leading Reggeon couplings to the pion and antiproton induced reactions are in reasonable agreement with eqs. (6) and (8) above – i.e.

$$B_\pi/B_p \simeq \sigma_{pp}^T/2\sigma_{\pi p}^T \simeq 0.8.\tag{2.14}$$

(6) However, the Pomeron–f proportionality prediction seems to be off by a factor of 2. More precisely from Pomeron–f proportionality and ρ–f exchange degeneracy one expects the relative magnitudes of the Reggeon and Pomeron couplings in $p \xrightarrow{\pi} \pi^-$ and $p \xrightarrow{\pi} \pi^+$ to be equal

$$\frac{B_\pi}{2A}(\pi^-) = \frac{B_\pi}{2A}(\pi^+) \simeq \left\langle\frac{M^2}{s}\right\rangle^{-1/2} \quad \text{from two body analysis}$$

$$1.3\pm0.1 \quad 0.7\pm0.1 \quad 1.1 \qquad \text{(Expt).}\tag{2.15}$$

Thus the model seems to be at best qualitatively valid. Even so it is significant that the ratio of nonscaling to scaling contributions for inclusive cross-sections are roughly similar to that for total cross-sections.

2.1.3. Cross-sections at BNL energies

Let us finally study the inclusive cross-sections over the PS energy range. The normalised cross-sections $f(p \xrightarrow{a} \pi)$ are shown on a $s^{-1/2}$ plot in fig. 4, down to a lab. momentum of 4 GeV/c. In addition to the BNL–Penn. data, the interpolated bubble chamber data for $K^\pm$ beam [69–72] are also shown. One evidently sees a striking deviation from scaling at the low energy end for $p \xrightarrow{p} \pi^-$, and the effect seems to be at least as large for $p \xrightarrow{K^+} \pi^-$. The $p \xrightarrow{\pi^+} \pi^-$ data, however, shows very little deviation from scaling down to the lowest energy. Since this is a very significant effect in the 10 GeV/c range, where a good deal of Mueller–Regge phenomenology have been done in past, let us investigate it in detail.

Firstly one notices from the high precision $p \xrightarrow{p} \pi^-$ data that it is clearly nonlinear on the $s^{-1/2}$ plot – i.e. the nonscaling term is not simply proportional to $s^{-1/2}$. Therefore it cannot be attributed to exchange degeneracy breaking, as in the Tye–Veneziano scheme [35].

It seems most likely a kinematic effect. More precisely there is a kinematic effect of this magnitude arising from the choice of scaling variables. This can be seen by computing the M^2/s, t interval corresponding to the fixed p, θ cut of eq. (2). For $p \xrightarrow{p} \pi^-$, the interval is

$$M^2/s = 0.819\text{–}0.838, \quad t = 0.28 \text{ to } M^2/s = 0.634\text{–}0.672, \quad t = -0.27 \text{ at } 8\,\text{GeV}/c$$

$$M^2/s = 0.835\text{–}0.855, \quad t = 0.28 \text{ to } M^2/s = 0.660\text{–}0.701, \quad t = -0.27 \text{ at } 30\,\text{GeV}/c$$

$$\tag{2.16}$$

with little further variation at higher energies; and they are very similar for $p \xrightarrow{\pi,K} \pi^-$. Now the M^2/s distribution for $p \to \pi^-$ is so steep that the modest downward slide of the M^2/s cut from 30 to 8 GeV/c brings down the cross-section by 30% – assuming, of course, that the latter scales for fixed M^2/s and t. For a quantitative estimate we parametrise the shape of the $\underline{p \xrightarrow{p,\pi^+,K^+} \pi^-}$ fragmentation cross-sections,

Fig. 2.4. The normalised inclusive cross-sections $p \rightarrow \pi^-$ from the BNL–Penn. data [68] over the full energy range. Some interpolated bubble chamber data for $p \xrightarrow{K^\pm} \pi^-$ [69–72] and $p \xrightarrow{\gamma} \pi^-$ [81] are also been added, as indicated in brackets. The curve shows the expected kinematic deviation from scaling, assuming exact scaling in M^2/s and t as per eq. (17).

assuming scaling in M^2/s and t, as

$$\frac{d\sigma}{\pi \, dt \, dM^2/s} = \left(\frac{\sqrt{s}}{2p_{\text{in}}}\right) F$$

$$= 4.8 \exp[(-16 + 6.67t)(0.87 - M^2/s)] + 19.6 \exp[(-8.35 + 1.83t)(1.04 - M^2/s)]. \quad (2.17)$$

This corresponds to a fit to the $16 \, \text{GeV}/c$ $p \xrightarrow{\pi^+} \pi^-$ data of ABBCCHW coll. [79], over the bulk of the target fragmentation region ($M^2/s = 0.3$–0.9 and practically the full range of t). Integrating the above cross-section (eq. (17)) over the fixed p, θ cut of eq. (4) using eqs. (1.4), (1.5) and (1.26), one gets the energy dependence curve† (practically identical for the three beams p, π^+ and K^+) shown in fig. 4. Thus assuming exact scaling in M^2/s, t gives a significant kinematic scale breaking effect for fixed p, θ (or y_L, p_T) interval of eq. 2(3). The corresponding kinematic scale breaking effects for the fixed intervals of (p_L, p_T), (x, p_T) and (y, p_T), typical of data compilations, are shown in fig. 6.

† The $\sqrt{s}/2p_{\text{in}}$ factor in the Jacobian has negligible contribution to the energy dependence. It arises almost entirely from the variation of the M^2/s interval with energy.

Before going into comparison with data, one should note from the size of the effect in figs. 4 and 6, that the scaling behaviour at PS energies is rather sensitive to the choice of scaling variable. Exact scaling in one set of variables corresponds to a 30% deviation in another over the range 10–30 GeV/c. It arises primarily from the steep M^2/s (or x) dependence of the $p \to \pi^-$ fragmentation cross-sections. This phenomenon does not seem to have received adequate attention in the past. One exception is the ref. [71], where it was noticed that the 8 and 16 GeV/c $p \xrightarrow{K^+} \pi^-$ data were consistent with scaling at fixed M^2/s, but showed appreciable deviation at fixed y.

Let us next look at the comparison with the data points of fig. 4. One sees that the kinematic scale breaking effect arising from the choice of M^2/s and t as scaling variables is similar in shape and size to the observed effect for $p \xrightarrow{p} \pi$ and perhaps also $p \xrightarrow{K^+} \pi^-$. However, it cannot reproduce the $p \xrightarrow{\pi^+} \pi^-$ data, which seem to show a much smaller scaling deviation. Of course, one can empirically construct scaling variables, which would give a smaller deviation for the pion induced reaction, compared to kaon or proton. It seems to us more attractive, however, to attribute the observed excess for $p \xrightarrow{\pi^+} \pi^-$ to the positive nonscaling component 4, arising from a non-exotic ab system [36a] – i.e. the criterion II of section 1.3.3. We have checked that the excess can be fitted with a $s^{-1/2}$ term to within one standard deviation of the data points. Its magnitude is roughly 30% of the dominant nonscaling component (criterion I), as measured from $p \xrightarrow{\pi^-} \pi^-$.

We should emphasise that, whatever be its origin, there is a 30% deviation from the factorisation relation between $p \xrightarrow{\pi^+} \pi^-$ and $p \xrightarrow{p} \pi^-$ (or $p \xrightarrow{K^+} \pi^-$) around 10 GeV/$c$. Again this phenomenon has escaped the past phenomenological analyses, since they were based on data compilations with a typical uncertainty of 25–30%. This deviation has serious implications on the phenomenology of Reggeon (R) exchanges, which had been carried out in the past assuming Pomeron factorisation. A notable example is the relation between $p \xrightarrow{\gamma} \pi^-$ and $p \xrightarrow{\pi^+} \pi^-$ (or $p \xrightarrow{K^+} \pi^-$) as studied in ref. [80]; i.e.

$$f(p \xrightarrow{\gamma} \pi^-) = f(p \xrightarrow{\pi^+} \pi^-) + \frac{(\beta^f_{\gamma\gamma} + \beta^{A_2}_{\gamma\gamma})}{2\beta^\rho_{\pi\pi}} \cdot \frac{\beta^P_{\pi\pi}}{\beta^P_{\gamma\gamma}} [f(p \xrightarrow{\pi^-} \pi^-) - f(p \xrightarrow{\pi^+} \pi^-)]$$

$$\simeq f(p \xrightarrow{\pi^+} \pi^-) + 1.05[f(p \xrightarrow{\pi^-} \pi^-) - f(p \xrightarrow{\pi^+} \pi^-)] \tag{2.18}$$

$$f(p \xrightarrow{\gamma} \pi^-) = f(p \xrightarrow{K^+} \pi^-) + \frac{(\beta^f_{\gamma\gamma} + \beta^{A_2}_{\gamma\gamma})}{4\beta^\rho_{KK}} \cdot \frac{\beta^P_{KK}}{\beta^P_{\gamma\gamma}} [f(p \xrightarrow{K^-} \pi^-) - f(p \xrightarrow{K^+} \pi^-)]$$

$$\simeq f(p \xrightarrow{K^+} \pi^-) + 0.85[f(p \xrightarrow{K^-} \pi^-) - f(p \xrightarrow{K^+} \pi^-)]. \tag{2.19}$$

The 9.3 GeV/c $p \xrightarrow{\gamma} \pi^-$ cross-section [81] (normalised with a $\sigma^T_{\gamma p} = 115\,\mu b$) is shown in fig. 4. One evidently sees that it satisfies the relation (19) but the relation (18) is very badly broken†. It is also evident that the $p \xrightarrow{\gamma} \pi^-$ cross-section cannot satisfy both the eqs. (18) and (19), because there is a conflict between the two, arising from the breakdown of factorisation. One may note however that the corresponding relation between the $p \xrightarrow{\pi^+} \pi^-$ and the $p \xrightarrow{K^+} \pi^-$ cross-section differences [83] (i.e. eq. (7)) seems to agree with data.

Finally one should note from fig. 4 that the deviation from scaling (i.e. eq. (1)) for the 10 GeV/c $p \xrightarrow{p} \pi^-$ cross-section is still a small effect, when compared to the $p \xrightarrow{\bar{p},p} \pi^-$ cross-section difference. To

---

† The deviation from eq. (18) is, indeed, so large that it shows up even in the data compilations of figs. 7, 8 (or fig. 1 of ref. [82]).
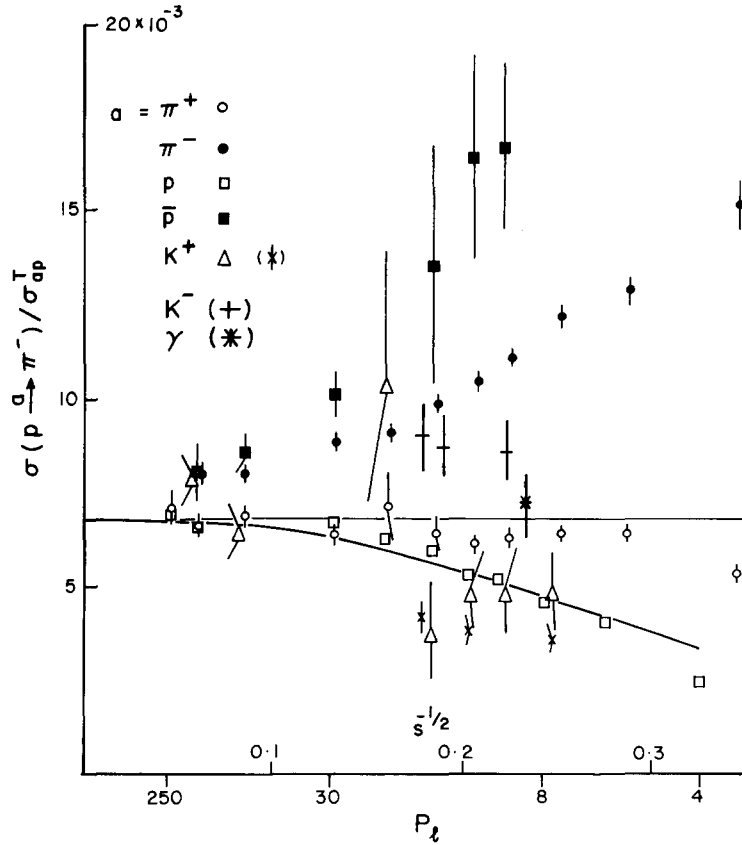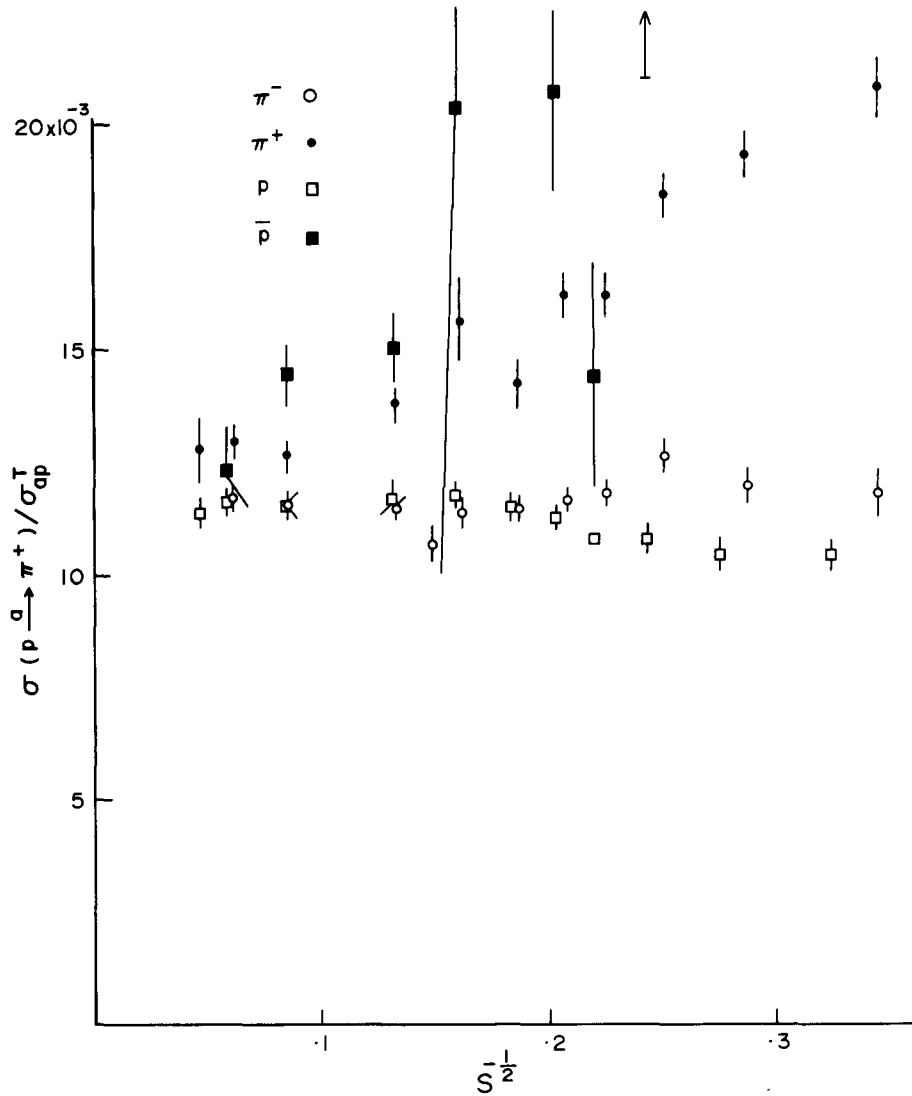
Fig. 2.5. The normalised inclusive cross-sections $p \to \pi^+$ from the BNL-Penn. data [68] over the full energy range.

that extent the Mueller–Regge phenomenology of the latter, carried out in fig. 1, should be, at least qualitatively, reliable.

The BNL–Penn. cross-sections for $p \to \pi^+$ are shown over the full energy range in fig. 5. The one distinctive feature of the $p \to \pi^+$ cross-section, is that the deviation from scaling is much weaker than the $p \to \pi^-$ case. This can be qualitatively understood in terms of the M^2/s dependence of the former cross-sections being considerably less steep than the latter [71]†.

---

† Ref. [71] gives the M^2/s single dist. for $p \xrightarrow{K^-} \pi^+$. Assuming this dist. to be independent of t, we have estimated the kinematic scale breaking effect analogous to the one estimated earlier for $p \to \pi^-$. It turns out to be roughly a half of the latter, whereas experimentally it seems to be about a quarter.

2.2. p → π (data compilations)

This subsection is devoted to the compilation of all the available data on p → π fragmentation, prior to the BNL–Penn. data. As we shall see, the scatter in these data compilations are so large that it is hard to draw any quantitative conclusions based on them. The best one can hope for is to check the consistency of the results, obtained from the BNL–Penn. data above, with these data compilations.

The fragmentation cross-sections are usually given as single (p_T integrated) distributions in one of the longitudinal variables – p_L, x or y. A compilation of the cross-sections over a fixed interval of p_L (=−0.4 to +0.2) has already been given in refs. [82, 84]. We shall give here the corresponding compilations over fixed intervals of $x(=−1$ to $−0.3)$† and $y(=−0.8$ to $+0.4)$. The limits have been chosen simply to correspond to those of p_L interval above for $p_T = \langle p_T \rangle$.

The reason for separate compilations for the different choices of the longitudinal variable are two-fold, as mentioned in subsection 1.1. Firstly, it is not possible to transform a single distribution given in one longitudinal variable to that in another (e.g. $d\sigma/dx$ to $d\sigma/dy$), since the relation between the two involves p_T. An approximate transformation, wherein one simply replaces p_T by $\langle p_T \rangle$, has sometimes been used in the past. However, we have explicitly checked with the p $\xrightarrow{\text{p}}$ π⁻ data of Blobel et al. [85], who give the single distributions in both x and y, that the error involved in this is much too large. Thus our compilations over the x and the y intervals only include data given in terms of the respective variables. The second reason is that the s dependence over the PS energy range is expected to be rather sensitive to the choice of the scaling variables, as we saw in the last section. This is illustrated in fig. 6, where the kinematic scaling deviations for the fixed p_L, x and y intervals above are shown for p → π⁻, assuming exact scaling in M^2/s and t (i.e. eq. (17))‡. In this case the deviation is evidently much smaller for the fixed y than for the fixed x interval, and hence the former choice of the longitudinal variable would have a distinct advantage. One may note that, whether or not M^2/s and t are the right scaling variables, the energy dependence over the PS range (8–30 GeV/c) are expected to be appreciably different for the three intervals above.
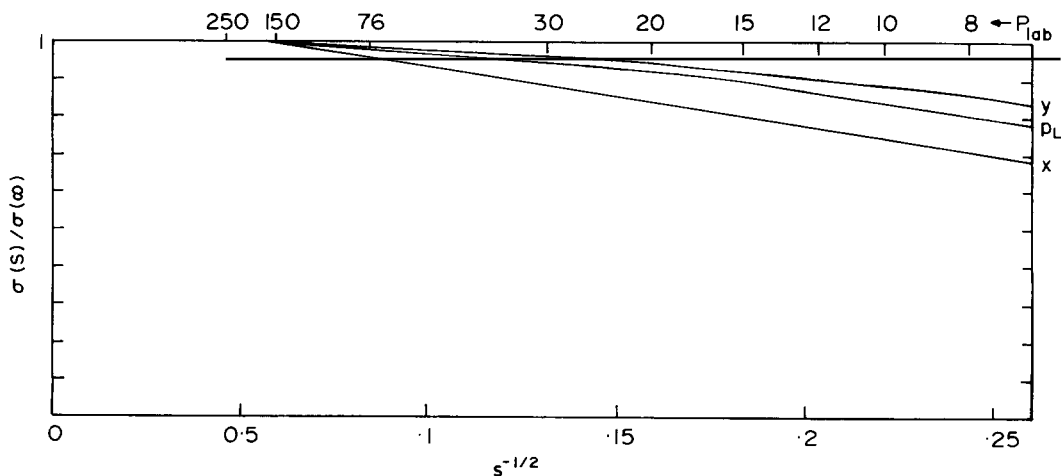
Fig. 2.6. The expected kinematic rise of the p → π⁻ cross-section for fixed intervals of $y(−0.8$ to $0.4)$, $p_L(−0.4$ to $0.2)$ and $x(−0.9$ to $0.3)$, assuming exact scaling in M^2/s and t, as per eq. (17).

† Here we use the definition $x = 2p_L/\sqrt{s}$. Naturally x_{min} is a little larger than $−1$ at moderate s. It makes little difference in practice, however, since the cross-sections are strongly damped at this end.

‡ The corresponding scaling deviations for p → π⁺ are expected to be roughly half these amounts.

The compilations are based on the $p \to \pi^{\pm}$ data of refs. [85–91], where the $s^{-1/2}$ values are indicated in bracket to help the identification of the data points. The figs. 7 and 8 show the compilations of $p \to \pi^-$ cross-sections over the fixed y and x intervals respectively. The 2 solid lines are simply eye ball fits to the exotic cross-sections $p \xrightarrow{p,\pi^+,K^+} \pi^-$ and the non-exotic cross-section $p \xrightarrow{\pi^-} \pi^-$, assuming Pomeron factorisation, EXD and a $\alpha_R = \frac{1}{2}$. The dashed line is simply drawn with a 20% higher slope than in $p \xrightarrow{\pi^-} \pi^-$ to correspond to the cross-sections $p \xrightarrow{K^-,\bar{p}} \pi^-$ via eqs. (7), (8), (11) and (12). Thus these lines are essentially identical to the three lines of fig. 3. On a rough qualitative level there seems to be an overall consistency of the high energy data points with the corresponding lines – i.e. with Pomeron factorisation, EXD (a la criterion I), $\alpha_R = \frac{1}{2}$ and the 2-body coupling relations (eq. (9)). There is also a clear signal of an upward deviation of the low energy $p \xrightarrow{\bar{p}} \pi^-$ points (Baryonium exchange) in fig. 8. Besides, there are indications that the low energy $p \xrightarrow{K^{\pm}} \pi^-$ points show downward deviations and the $p \xrightarrow{\gamma} \pi^-$ shows a deviation from eq. (18), as in the case of fig. 4. However, the scatter in the data points are evidently too large to draw any quantitative conclusions.

The corresponding compilations of the $p \to \pi^+$ cross-sections are shown in figs. 9 and 10 for the fixed y and x intervals. The solid lines again are eye-ball fits to the exotic cross-sections $p \xrightarrow{p,K^+} \pi^+$ and the non-exotic cross-section $p \xrightarrow{\pi^+} \pi^+$, and the dashed line is drawn with a slope 20% higher than the latter

Fig. 2.7. Compilation of the $p \to \pi^-$ cross-sections [85–91] over a fixed interval of $y(-0.8$ to $0.4)$. The solid lines are eye ball fits to the exotic cross-sections $p \xrightarrow{p,\pi^+K^+} \pi^-$ and the nonexotic cross-section $p \xrightarrow{\pi^-} \pi^-$; and the dashed line is the prediction for the high energy $p \xrightarrow{\bar{p},K^-} \pi^-$ cross-sections.
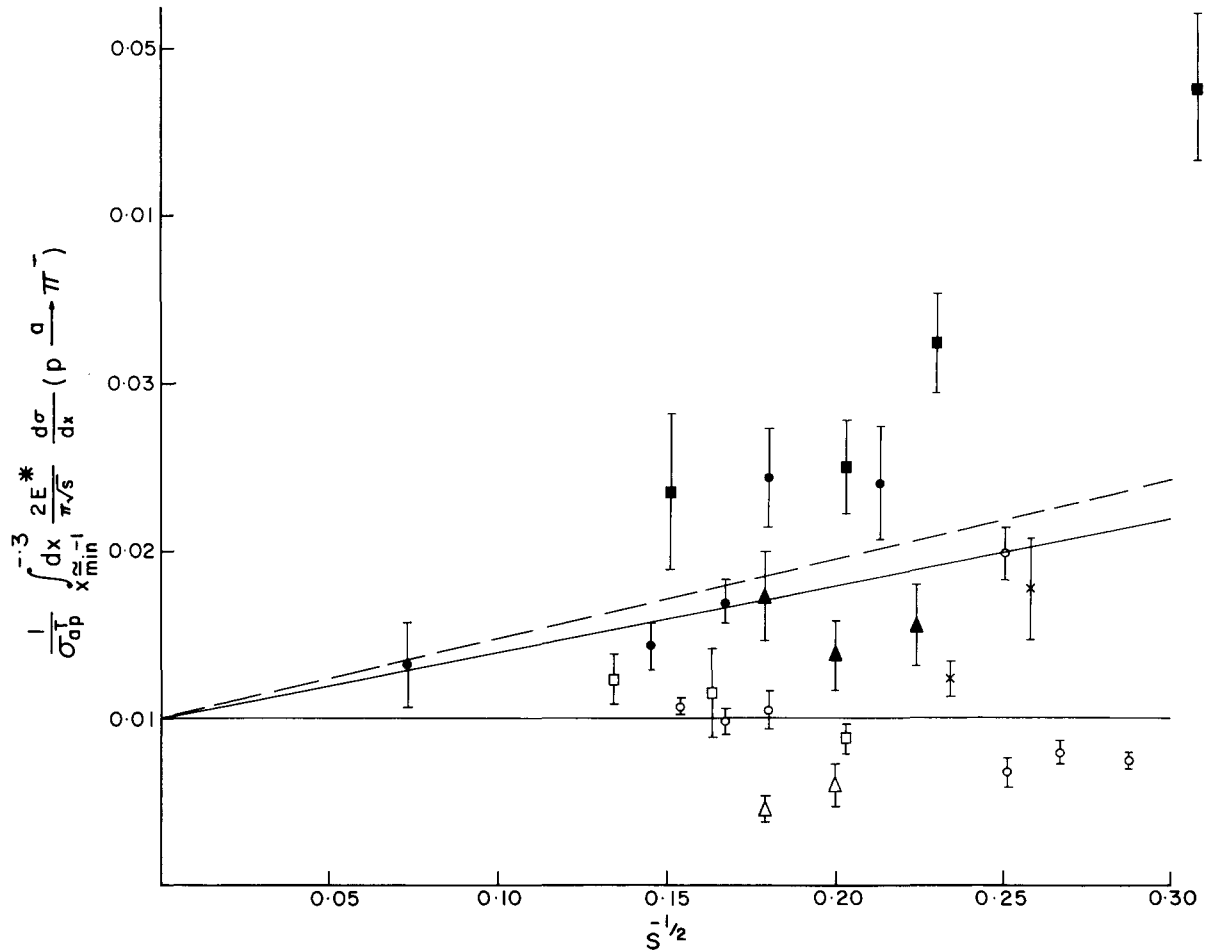
Fig. 2.8. Compilation of the $p \to \pi^-$ cross-sections [85–91] over a fixed interval of $x(-1$ to $-0.3)$. The lines and the data symbols are identical to those of fig. 7.

to correspond to the high energy $p \xrightarrow{\bar{p}} \pi^+$ cross-sections. Moreover, the non-exotic cross-section $p \xrightarrow{\pi^-} \pi^+$, as noted earlier, seems to show early scaling (fig. 5). And one expects from this and factorisation that the nonexotic cross-sections $p \xrightarrow{K^-,\gamma} \pi^+$ should also lie on the flat line [80, 83]. Unfortunately one sees from the compilations of figs. 9 and 10 that the uncertainty in these $p \to \pi^+$ data are even larger than the corresponding $p \to \pi^-$ data, primarily due to the π^+ identification problem. Thus it is hard to draw even qualitative conclusions in this case. At most, one can say that within the large uncertainty of these data compilations, there is no inconsistency with the features mentioned above (or with fig. 5).

From the $p \to \pi^-$ data, with comparatively lesser uncertainties, one can make a fairly useful compilation of the particle–antiparticle cross-section differences (eq. (5)), given some discretion in the choice of data points, of course. Fig. 11 shows such a compilation†, for the fixed p_L interval of

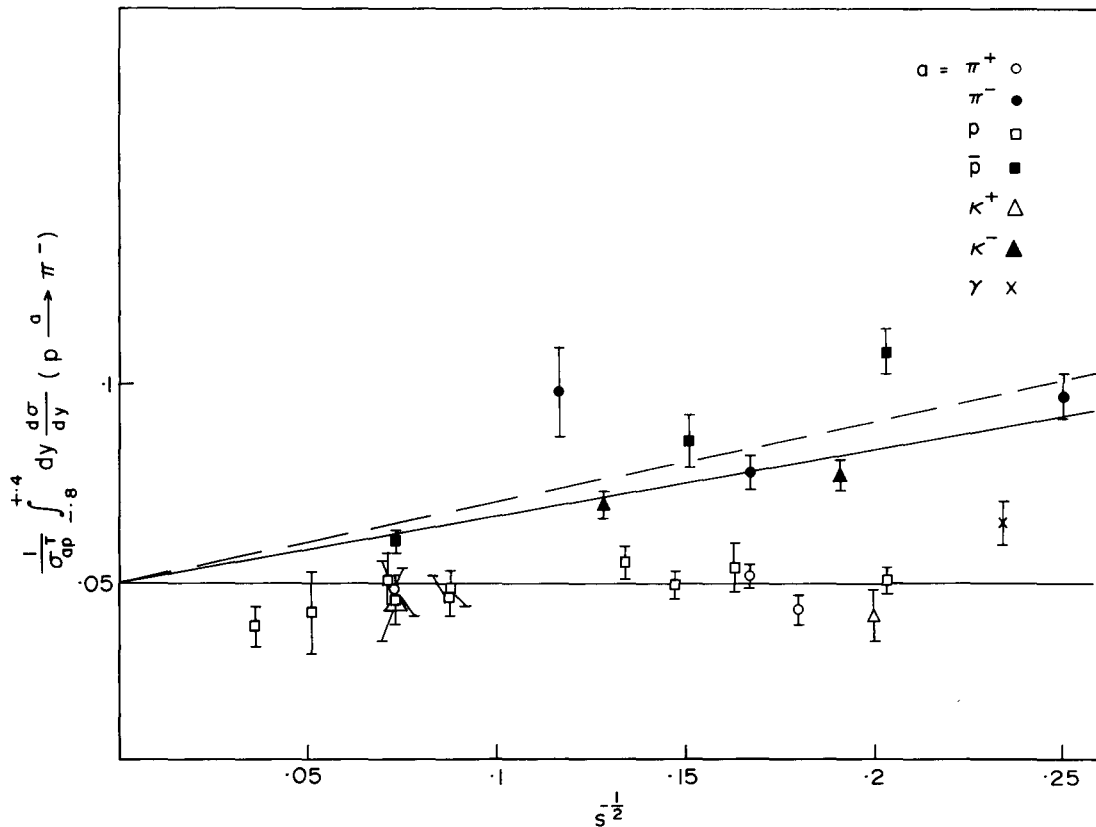† A similar compilation is given in ref. [92].
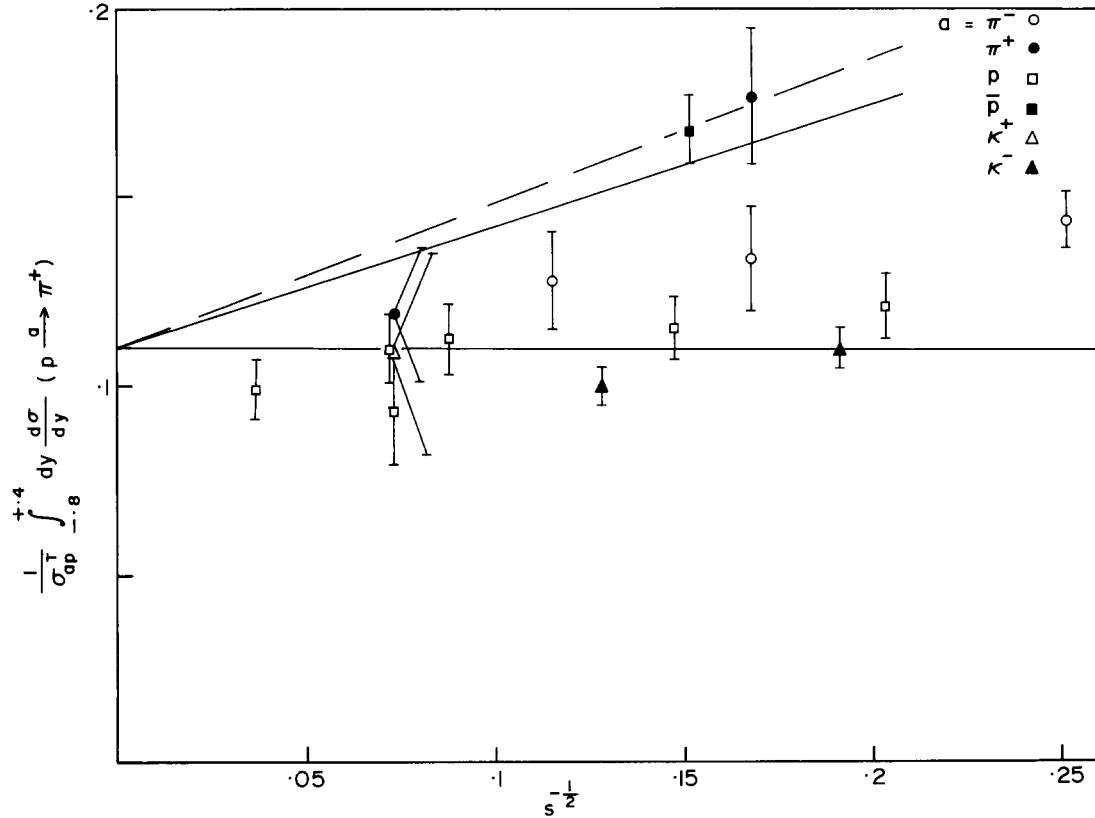
Fig. 2.9. Compilation of the $p \rightarrow \pi^+$ cross-sections [85–90] over a fixed interval of $y(-0.8$ to $0.4)$. The solid lines are eye ball fits to the exotic cross-sections $p \xrightarrow{p,K^+} \pi^+$ and the nonexotic cross-section $p \xrightarrow{\pi^+} \pi^+$; and the dashed line is the prediction for the high energy $p \xrightarrow{\bar{p}} \pi^-$ cross-section. The early scaling of $p \xrightarrow{\pi^-} \pi^+$, implies the $p \xrightarrow{K^-,\gamma} \pi^+$ cross-sections to lie on the flat line as well.

Whitmore, i.e. for

$$\Delta_{ab}(c) = \sigma(b \xrightarrow{\bar{a}} c) - \sigma(b \xrightarrow{a} c)$$

$$\sigma = \int\limits_{-0.4}^{0.2} E \frac{d\sigma}{dp_L} dp_L. \qquad (2.20)$$

The $\Delta_{\pi p, Kp}(\pi^-)$ points are taken from the compilation of ref. [82], and the corresponding $\Delta_{pp}(\pi^-)$ points have been estimated from refs. [87, 88]. One sees that the πp points are consistent with the $s^{-1/2}$ behavior and roughly equal to Kp (eqs. (6, 7)) as noted in ref. [82] and also that the high energy pp point is roughly twice as large (eq. (8)) as noted in ref. [92]. These serve as consistency checks for the analogous features observed in the last subsection (fig. 1). Lastly, the low energy pp points show a clear excess which can be consistently described by the same Baryonium trajectory $(\alpha_B \simeq -1.3)$ as in fig. 1, as illustrated by the curved line.

Evidently the last consistency check, involving the Baryonium exchange signal and trajectory
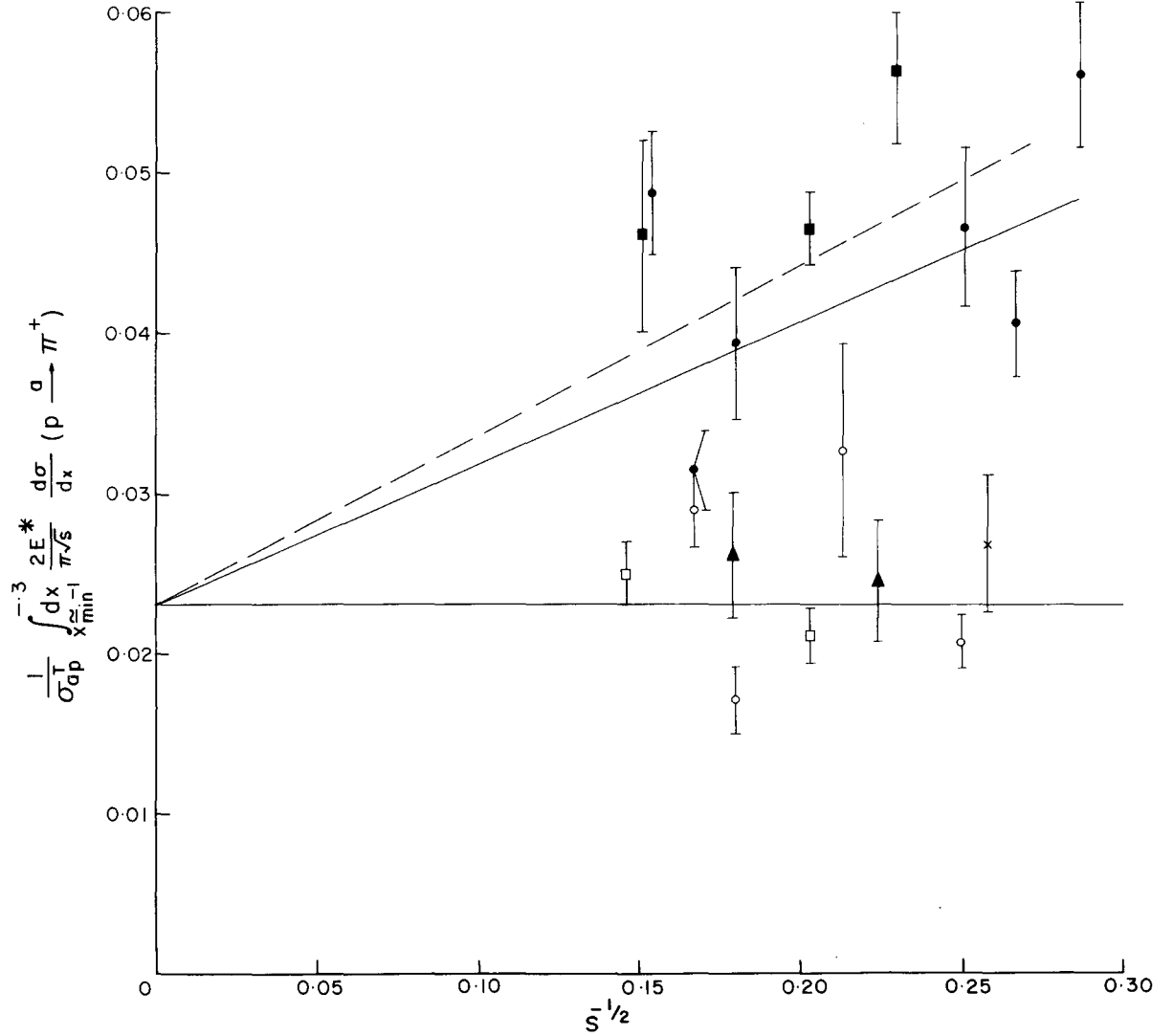
Fig. 2.10. Compilation of the $p \to \pi^+$ cross-sections [85–91] over a fixed interval of $x(-1$ to $-0.3)$. The lines and the data symbols (γX) are identical to those of fig. 9.

parameter is very significant. To pursue it further we have checked the energy dependence of the cross-section

$$F(p \xrightarrow{\bar{p}} \pi^-) = \frac{2E^*}{\sqrt{s}} \cdot \frac{d\sigma}{dx}(p \xrightarrow{\bar{p}} \pi^-)$$

over a range of x values (< -0.15). From eqs. (1, 6, 8 and 11), one expects

$$F^s(p \xrightarrow{\bar{p}} \pi^-) = [1 - 2(\beta^P_{\pi\pi}/\beta^P_{pp})(s/s_1)^{-1/2}] \cdot F(p \xrightarrow{P} \pi^-)$$
$$+ 2F^{s1}(p \xrightarrow{\pi^-} \pi^-) \cdot (s/s_1)^{-1/2} + c(x) \cdot s^{\alpha_B - 1} \tag{2.21}$$
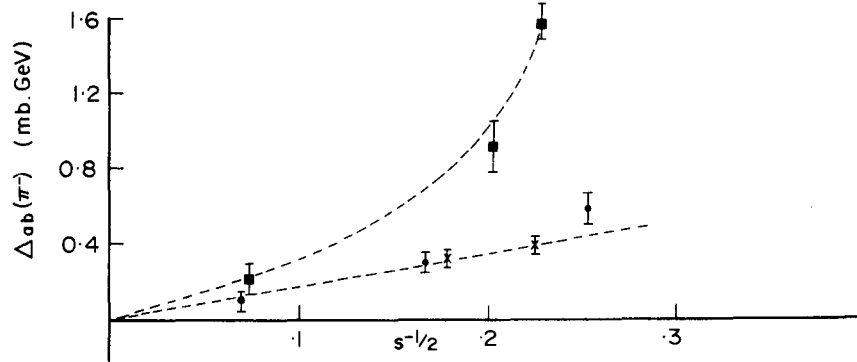
Fig. 2.11. Compilation of the inclusive cross-section differences $\Delta_{\pi p, Kp, pp}(\pi^-)$ over a fixed interval of p_L (eq. (20)). The data points for $\pi p(\bullet)$ and Kp($\times$) are from ref. [82] and pp(■) from refs. [85, 86]. The dashed lines show that both πp and Kp points are consistent with the same straight line $a \cdot s^{-0.5}$, whereas the pp points are consistent with $2a \cdot s^{-0.5} + b \cdot s^{-2.3}$ (as per eqs. (6–8)).

where $\beta^P_{\pi\pi}/\beta^P_{pp} \simeq 0.62$ (eq. (12)). The available x distributions for $p \xrightarrow{\bar{p}} \pi^-$ are shown in fig. 12. They are the 4.6 and 9.1 GeV/c data of Gregory et al. and the 22.4 GeV/c data of Boos et al. [86]. For the RHS we use the 16 GeV/c $p \xrightarrow{\pi^-} \pi^-$ data [93], and the 12 and 24 GeV/c $p \xrightarrow{p} \pi^-$ data of Blobel et al. [85]; in order to take care of a slow energy dependence in $p \xrightarrow{p} \pi^-$ we use 12 GeV/c data for predicting the 4.6 and 9.1 GeV $p \xrightarrow{\bar{p}} \pi^-$, and the 24 GeV/$c$ data for the 22.4 GeV/c $p \xrightarrow{\bar{p}} \pi^-$. The prediction from the first 2 terms (P + R) of eq. (21) is shown by dashed lines. There is evidently a systematic discrepancy with the low energy data, which seems to go down rapidly with energy. Fitting the discrepancy with the 3rd term (Baryonium exchange) at 4.6 and 9.1 GeV/c gives the solid lines shown in fig. 12. It corresponds to a $\alpha_B = -0.7 \pm 0.5$. We should add, however, that using the 8.25 GeV/c $p \xrightarrow{K^-} \pi^-$ data [94] instead of 16 GeV/c $p \xrightarrow{\pi^-} \pi^-$ data one gets an equally good fit to the $p \xrightarrow{\bar{p}} \pi^-$, but with a $\alpha_B = -0.01 \pm 0.3$. In a summary the $p \xrightarrow{\bar{p}} \pi^-$ data compilation seems to support the Baryonium exchange signal; and within rather large uncertainties (including those associated with the choice of input data) it is also consistent with the Baryonium trajectory estimate of the last subsection.

2.3. Heavier fragments $(p \rightarrow K^0, \rho^0, \Lambda, \Sigma^+_{1385}, \Delta^{++})$

This subsection is devoted to the compilation of inclusive K^0, ρ^0, Λ, Σ^+_{1385} and Δ^{++} production data [95–103] and the related phenomenology. The Λ, K^0 and Σ^+_{1385} cross-sections are evaluated over a fixed interval of $x(-0.8$ to $-0.4)$ and the ρ^0 cross-section over a fixed interval of y (0.6 to 0.8); since most of the respective data were given in the corresponding variables. In some cases, however, we have used a transformation between the x and y distributions ($d\sigma/dx$ to $d\sigma/dy$ and vice-versa) assuming $p_T = \langle p_T \rangle$, in spite of our earlier cautions to the contrary. The reasons are firstly the scarcity of these data points and secondly that the uncertainties in these data are much larger any way†.

It is evident from the above remarks that the quality of these data are, if at all, inferior to the $p \rightarrow \pi$ data compilations of the last subsection. But these are the best one has for the reactions under study. Therefore we have carried out quantitative fits to these data (figs. 13–16) with the Mueller–Regge formulae.

† Besides, we have explicitly checked for a few cases that the error involved in this transformation are smaller here than for the π cross-section, because the $\langle p_T \rangle$ is less than the rest mass of these heavier fragments.
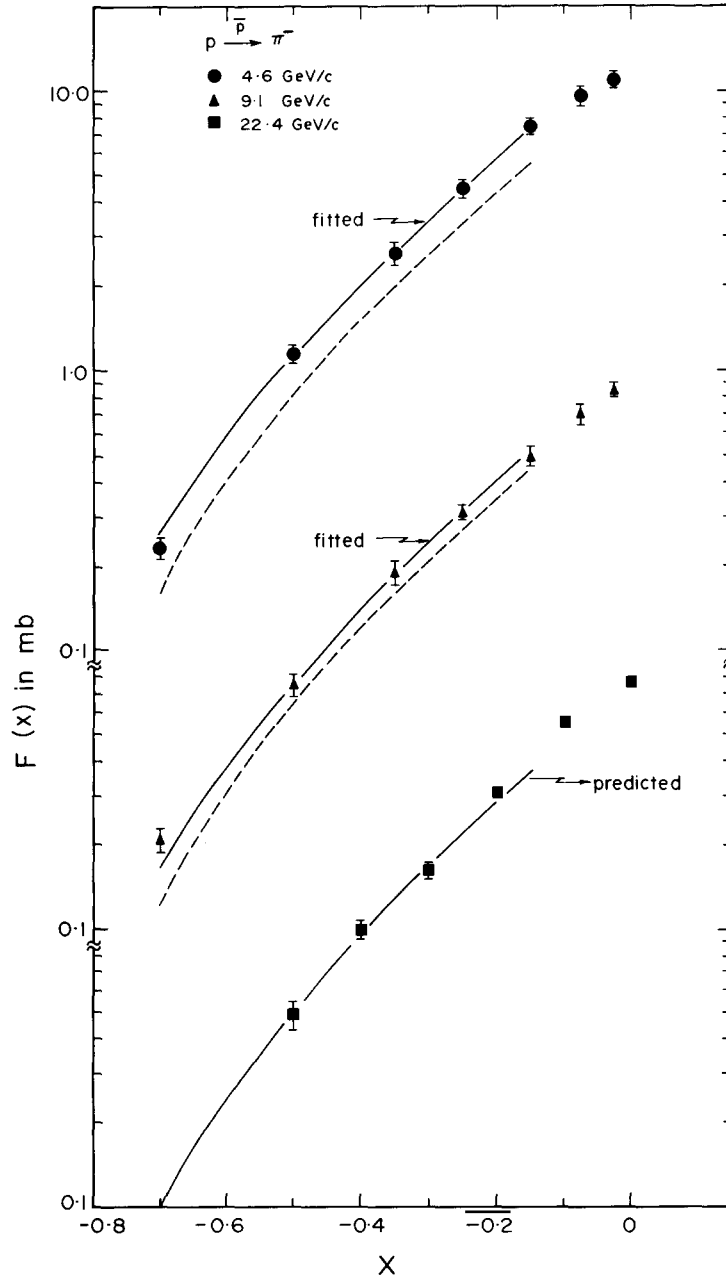
Fig. 2.12. The invariant cross-section $f(x)$ is plotted as a function of x for process $p \xrightarrow{\bar{p}} \pi^-$ at 4.6, 9.1 and 22.4 GeV/c. The dashed curves are predictions for 4.6 and 9.1 GeV/c data points from factorization hypothesis. The curves labelled as fitted are obtained by adding the Baryonium contribution. The curve labelled as predicted at 22.4 GeV/c is obtained by adding the Baryonium contribution, as deduced from 4.6 and 9.1 GeV/c data, to the normal contribution from factorization.

2.3.1. Formalism

The cross-sections plotted in figs. 13–16 are the normalised inclusive cross-sections corresponding to eq. (11), i.e.

$$f(b \xrightarrow{a} c) = \sigma(b \xrightarrow{a} c)/\sigma_{ap}^{T} \qquad (2.22)$$

where the ap total cross-sections are again taken from eq. (12). The Mueller–Regge formula used is essentially that eq. (1), i.e.

$$\sigma(b \xrightarrow{a} c) = \beta_P(b \xrightarrow{a} c) + \beta_R(b \xrightarrow{a} c) \cdot s^{-1/2} \qquad (2.23)$$

plus the ϕ contribution in

$$p \xrightarrow{K^-} \Lambda, \quad p \xrightarrow{K^+} K^0 \quad \text{and} \quad p \xrightarrow{K^-} \Sigma_{1385}^+; \quad \text{i.e.}$$

$$\beta_\phi(b \xrightarrow{a} c)s^{\alpha_\phi - 1} \qquad (2.23a)$$

with

$$\alpha_\phi = 0$$

and the Baryonium contribution in $p \xrightarrow{\bar{p}} K^0$ and $p \xrightarrow{\bar{p}} \rho^0$, i.e.

$$\beta_B(b \xrightarrow{a} c)s^{\alpha_B - 1} \qquad (2.23b)$$

with

$$\alpha_B = -\tfrac{1}{2}.$$

The choice of Baryonium intercept is somewhat ad hoc; but as we shall see, with the quality of data available here, there is hardly any Baryonium exchange signal.

For the leading Reggeon contribution we use the exchange degeneracy relations analogous to eq. (10). These follow from the exoticity criterion I, which we have seen to be a reasonable first approximation. We also use the 2-body coupling relations of eq. (9). The resulting Reggeon contributions β_R for the processes under consideration are shown in table 3 along with those for $p \to \pi^\pm$. One should note that the net Reggeon contribution β_R in $p \xrightarrow{a} \Lambda$ are given by a single parameter. The same is true for $p \xrightarrow{a} K^0$ and $p \xrightarrow{a} \Sigma^+$.

The Pomeron contributions are represented by the exotic cross-sections. There is a definite trend for these exotic cross-sections to rise with energy. There seems to be an indication, in fact, that the cross-section rise for these heavier fragments (in particular K^0 and Λ) may be more substantial than that observed earlier for pions. The very fact of the fragment mass dependence of the rise would suggest, of course, that it may be a kinematic effect – e.g. the one arising from transformation between different scaling variables, as considered in the earlier sections. In particular it would be very instructive to check if exact scaling in M^2/s and t would again correspond to a rise of the observed magnitude for the fixed interval of x considered here. We have not been able to estimate this, however, in the absence of the double distribution data for these processes†. Moreover, the quality of these data compilations is too poor to determine the shape of the cross-section rise. We have, therefore, assumed the simplest (i.e.

---

† In this context we feel the double distribution data, in M^2/s and t, for the Λ and K^0 cross-sections would be very useful.

Table 2.3

The net Reggeon contribution β_R (R = ρ, ω, f, A₂) to the various inclusive cross-sections

Fragmentation process	a	β_R	a	β_R	a	β_R
p $\xrightarrow{a}$ π⁻	π⁻	$2\beta_\pi \cdot \Gamma_{p\pi^+}$	K⁻	$2\beta_\pi \cdot \Gamma_{p\pi^+}$	p̄	$4\beta_\pi \cdot \Gamma_{p\pi^+}$
	π⁺	Exotic	K⁺	Exotic	p	Exotic
p $\xrightarrow{a}$ π⁺	π⁻	$\beta_\pi(\Gamma^f_{p\pi^-} - \Gamma^\rho_{p\pi^-})$	K⁻	$\beta_\pi(\Gamma^f_{p\pi^-} - \Gamma^\rho_{p\pi^-})$	p̄	$\beta_\pi(3\Gamma^f_{p\pi^-} - \Gamma^\rho_{p\pi^-})$
	π⁺	$\beta_\pi(\Gamma^f_{p\pi^-} + \Gamma^\rho_{p\pi^-})$	K⁺	Exotic	p	Exotic
p $\xrightarrow{a}$ K⁰	π⁻	$2\beta_\pi \cdot \Gamma_{p\bar{K}^0}$	K⁻	$2\beta_\pi \cdot \Gamma_{p\bar{K}^0}$	p̄	$4\beta_\pi \cdot \Gamma_{p\bar{K}^0}$
	π⁺	Exotic	K⁺	Accidental EXD	p	Exotic
p $\xrightarrow{a}$ ρ⁰	π⁻	$\beta_\pi(\Gamma^\omega_{p\rho} + \Gamma^\rho_{p\rho})$	K⁻	$\beta_\pi(\Gamma^\omega_{p\rho} + \Gamma^\rho_{p\rho})$	p̄	$\beta_\pi(3\Gamma^\omega_{p\rho} + \Gamma^\rho_{p\rho})$
	π⁺	$\beta_\pi(\Gamma^\omega_{p\rho} - \Gamma^\rho_{p\rho})$	K⁺	Exotic	p	Exotic
p $\xrightarrow{a}$ Λ	π⁻	$2\beta_\pi \cdot \Gamma_{p\bar\Lambda}$	K⁻	$2\beta_\pi \cdot \Gamma_{p\bar\Lambda}$	p̄	$4\beta_\pi \cdot \Gamma_{p\bar\Lambda}$
	π⁺	Exotic	K⁺	Exotic	p	Exotic
p $\xrightarrow{a}$ Δ⁺⁺	π⁻	Exotic	K⁻	Exotic	p̄	$\beta_\pi(\Gamma^\rho_{p\bar\Delta} - \Gamma^\omega_{p\bar\Delta})$
	π⁺	$2\beta_\pi \cdot \Gamma^\rho_{p\bar\Delta}$	K⁺	$\beta_\pi(\Gamma^\rho_{p\bar\Delta} + \Gamma^\rho_{p\bar\Delta})$	p	$2\beta_\pi(\Gamma^\rho_{p\bar\Delta} + \Gamma^\omega_{p\bar\Delta})$
p $\xrightarrow{a}$ Σ⁺	π⁻	Exotic	K⁻	$2\beta_\pi \cdot \Gamma_{p\bar\Sigma}$	p̄	$2\beta_\pi \cdot \Gamma_{p\bar\Sigma}$
	π⁺	$2\beta_\pi \cdot \Gamma_{p\bar\Sigma}$	K⁺	Exotic	p	Exotic

linear) parametrisation for these rising cross-sections. This corresponds to the Pomeron contribution

$$f_P(b \xrightarrow{a} c) = \beta_P(b \xrightarrow{a} c)/\sigma^T_{ap} = A_{bc} - B_{abc}s^{-1/2}. \tag{2.24}$$

Thus the Pomeron factorisation is a priori assumed only for the limiting contribution.

2.3.2. Comparison with data

The compilations of the inclusive Λ, K⁰, Σ^+_{1385} and ρ production data are fitted to the Mueller–Regge formulae (eqs. (22–24)) above in figs. 13–16.

(1) p→Λ (fig. 13): Amongst the processes considered here this has by far the best data. The most remarkable feature of this data is, of course, the huge φ exchange signal in p $\xrightarrow{K^-}$ Λ. The approximate equality between the leading Reggeon contributions to the normalised p $\xrightarrow{\pi^-,\bar{p}}$ Λ cross-sections, as predicted by the EXD constraints above, is satisfied within the uncertainty of these data. The normalised exotic cross-sections p $\xrightarrow{p,K^+}$ Λ remain roughly equal down to the lowest energy, which implies factorisation for the effective Pomeron contribution. It may be added here that this factorisation test has been carried out over a wide range of M^2/s and t, with impressive success, using the 19 GeV/c p $\xrightarrow{p}$ Λ and 16 GeV/c p $\xrightarrow{K^+}$ Λ data [103]. Finally, the third exotic cross-section p $\xrightarrow{\pi^+}$ Λ seems to lie a little higher, as in the p→π⁻ case discussed earlier, and the excess may again be attributed to the smaller nonscaling component 4, a la the exoticity criterion II. But one should bear in mind that the observed excess here is comparable to the scatter in these data points.

(2) p→K⁰ (fig. 14): Again the φ exchange signal is quite clear in p $\xrightarrow{K^+}$ K⁰, particularly since one expects no leading Reggeon R contribution here from the EXD constraints†. In contrast, there seems to

† It should be recalled that the φ exchange signals in both p $\xrightarrow{K^-}$ Λ and p $\xrightarrow{K^+}$ K⁰ were first observed by Inami and Miettinen [43], on the basis of earlier data compilations.
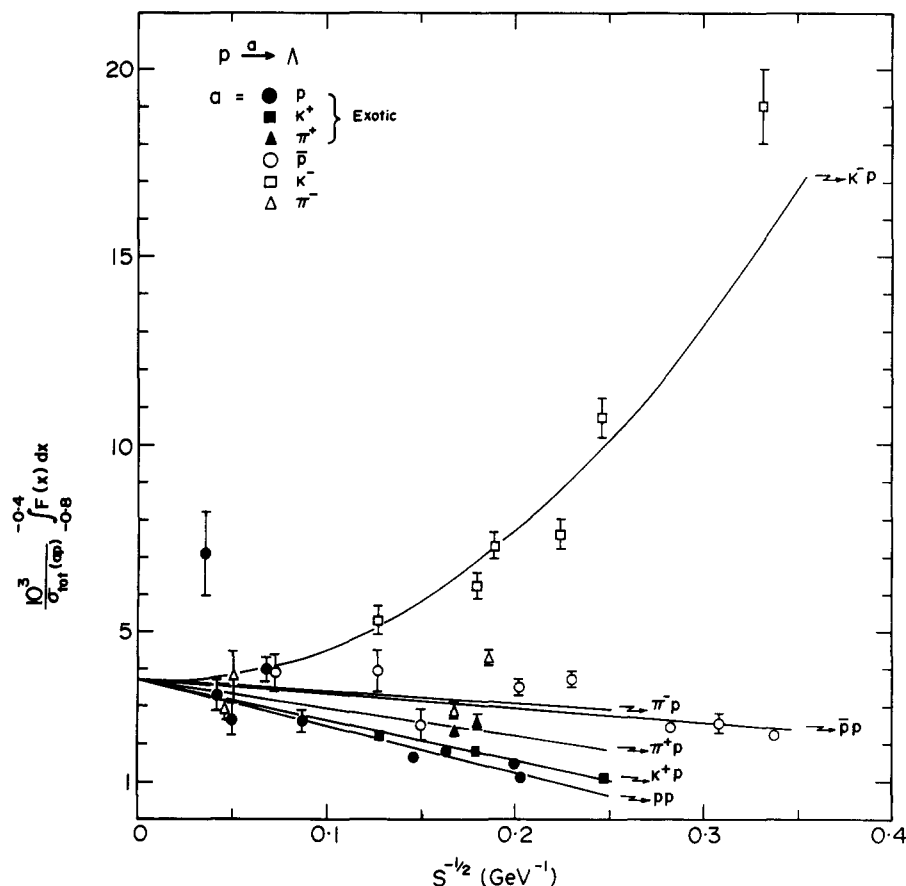
Fig. 2.13. The normalized invariant cross-sections for the processes p $\xrightarrow{a}$ Λ are plotted as a function of $s^{-1/2}$. The fitted curves are based on factorization hypothesis as discussed in the text.

be very little Baryonium exchange signal in p $\xrightarrow{p}$ K^0 over the relevant range of $P_{lab}(>4\,\text{GeV}/c)$. The Reggeon contribution to the 3 normalised cross-sections p $\xrightarrow{\pi^-,K^-,\bar{p}}$ K^0 seem to be approximately equal as expected from EXD. The equality between the normalised exotic cross-sections p $\xrightarrow{p,\pi^+}$ K^0, as expected from Pomeron factorisation, is compatible within the rather large uncertainty of these data points.

(3) p→Σ^+_{1385} (fig. 15): The only feature one can possibly deduce from the few data points available here, is the ϕ exchange signal in p $\xrightarrow{K^-}$ Σ^+_{1385}.

(4) p→ρ^0 (fig. 16): The quality of data available here is evidently too poor to draw any meaningful conclusions about the features mentioned above.

(5) p→Δ^{++}: The available data for these processes are inadequate to study the energy dependence. However, a fairly impressive test of Pomeron factorisation has been made, using the 16 GeV/c data for the two exotic cross-sections p $\xrightarrow{\pi^-,K^-}$ Δ^{++} [102]. This is shown in fig. 17.

2.4. Double fragmentation cross-sections

In previous subsections we discussed the energy dependence of one particle distributions in the framework of Mueller–Regge formalism. The Regge singularities that appear in 2-body processes are
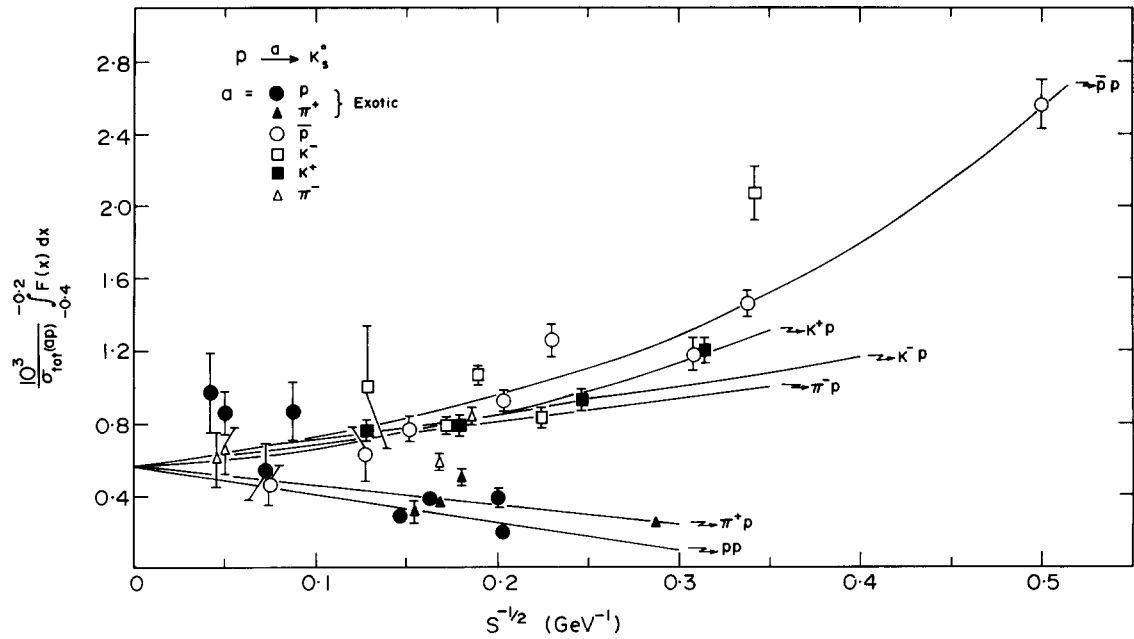
Fig. 2.14. The invariant cross-sections for $p \xrightarrow{a} K_s^0$ versus $s^{-1/2}$. The details are as in fig. 4.
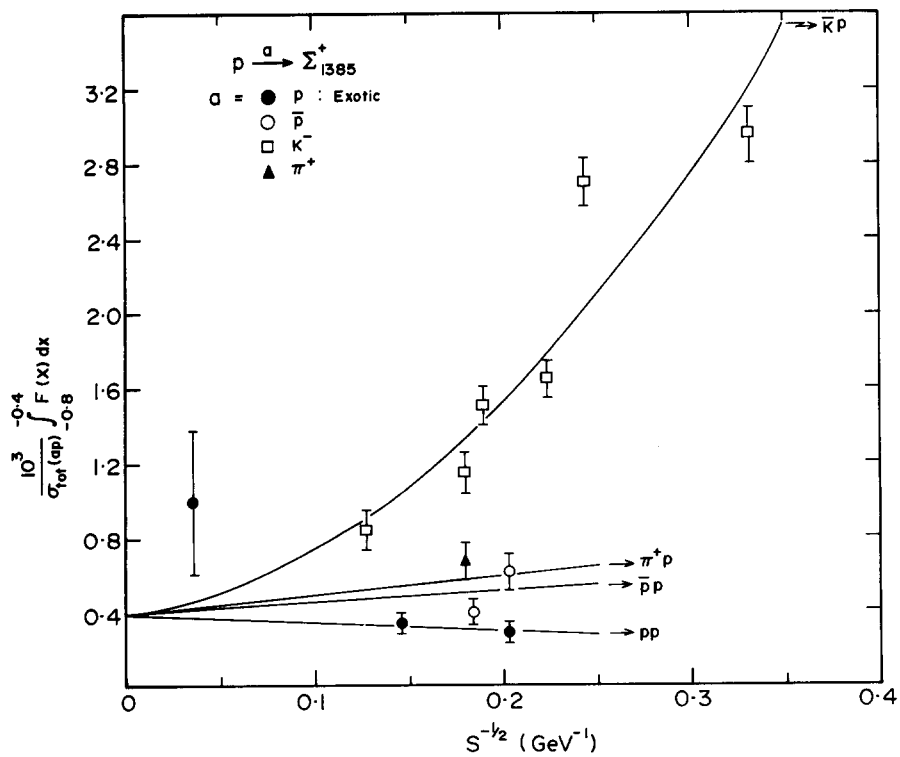
Fig. 2.15. The invariant cross-sections for $p \xrightarrow{a} \Sigma^+$ (1385) versus $s^{-1/2}$. The details are as in fig. 4.
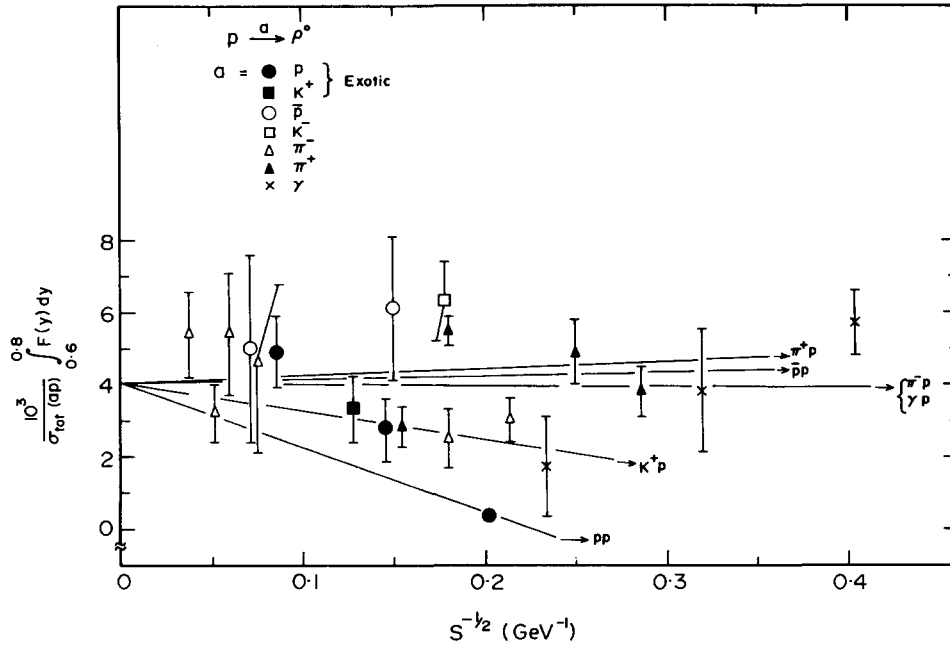
Fig. 2.16. The invariant cross-sections for $p \xrightarrow{a} \rho^0$ versus $s^{-1/2}$. The details are as in fig. 4.
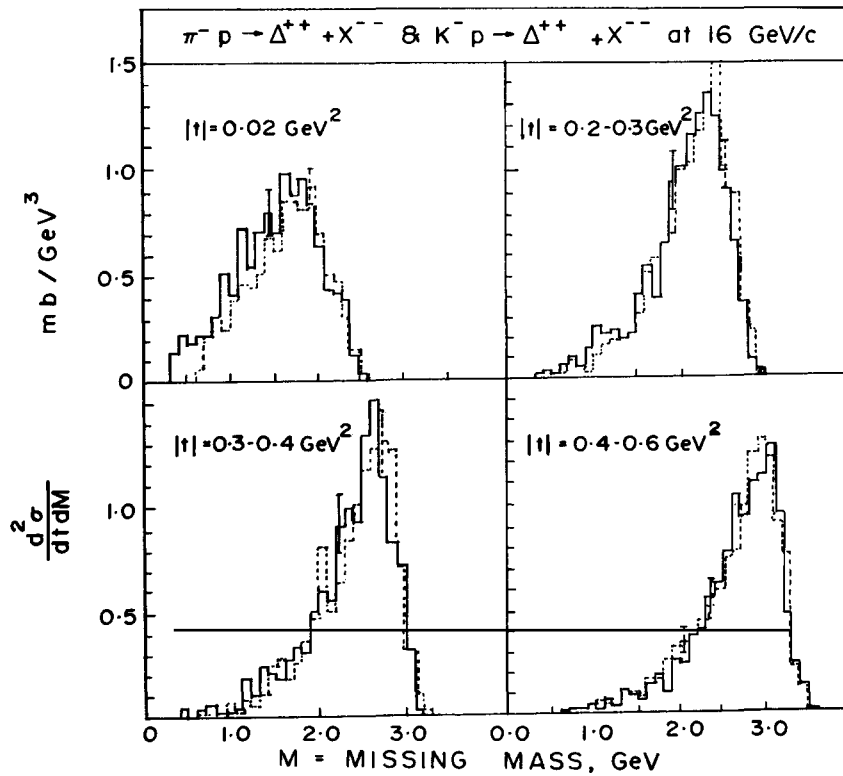
Fig. 2.17. Plots of $d^2\sigma/dt\,dM$ for different t-intervals are shown for the π^- reaction (full line) and the K^- reaction (dotted line). The K^- distributions are multiplied by $\sigma_{tot}(\pi^- p)/\sigma_{tot}(K^- p) = 1.19$. The figure is taken from Bosetti et al. [102].

also able to describe single-particle inclusive processes. Further simplification is achieved through factorisation hypothesis which enables one to identify Regge residues of non-fragmenting vertices with the corresponding 2-body processes. This procedure can be extended to two-particle inclusive processes where one particle is in the fragmentation region of the target and the other particle is in the fragmentation region of the projectile. Extending the factorisation hypothesis one can in principle determine completely the two-particle distributions in terms of single-particle distributions [104], see fig. 18. This is clear from the expression of the cross-section for the double fragmentation process $(b \to c|d \leftarrow a)$ which can be written as

$$E_c E_d \frac{d\sigma}{d^3 p_c d^3 p_d} (b \to c|d \leftarrow a) = \Gamma^P_{bc}(x_c, p_{Tc}) \, \Gamma^P_{ad}(x_d, p_{Td}) + \sum_{R=\rho,\omega,f,A_2} \Gamma^R_{bc}(x_c, p_{Tc}) \cdot \Gamma^R_{ad}(x_d, p_{Td}) \cdot s^{-1/2}.$$

(2.25)

Test of factorisation through double fragmentation distributions has been carried out [105] using data of $(p \to \pi^-|\pi^- \leftarrow p)$ and $(\bar{p} \to \pi^+|\pi^- \leftarrow p)$ at $100 \, \text{GeV}/c$, in terms of rapidity distributions after integration over transverse momenta. From the relations between the Regge residues as discussed earlier, we can write the double fragmentation distributions for the above two processes,

$$\frac{d^2\sigma}{dy_f \, dy_b} (pp \to \pi^-_f \pi^-_b) = \Gamma^P_{p\pi^+}(y_f) \, \Gamma^P_{p\pi^+}(y_b)$$

(2.26)

$$\frac{d^2\sigma}{dy_f \, dy_b} (\bar{p}p \to \pi^+_f \pi^-_b) = \Gamma^P_{p\pi^+}(y_f) \Gamma^P_{p\pi^+}(y_b) + 4\Gamma^R_{p\pi^+}(y_f) \cdot \Gamma^R_{p\pi^+}(y_b) \cdot s^{\alpha_R - 1}$$

(2.27)

where y_f and y_b refer to the rapidity of the forward and backward pion. Single-particle distributions for $p \xrightarrow{p} \pi^-$ and $p \xrightarrow{\bar{p}} \pi^-$ can be written down from table 3.

To test Pomeron factorisation, we re-write eq. (26) in terms of one-particle distributions resulting in the following expression,

$$\frac{d^2\sigma}{dy_f \, dy_b} (pp \to \pi^-_f \pi^-_b) = \frac{1}{\sigma_{tot}(pp)} \cdot \frac{d\sigma}{dy_f} (pp \to \pi^-_f) \cdot \frac{d\sigma}{dy_b} (pp \to \pi^-_b).$$

(2.28)

The two sides of this equation at $100 \, \text{GeV}/c$ are shown in fig. 19(a). In the double fragmentation region, $y_f > 1$ and $y_b < -1$, they are in good agreement within experimental uncertainty of $\sim 15\%$.
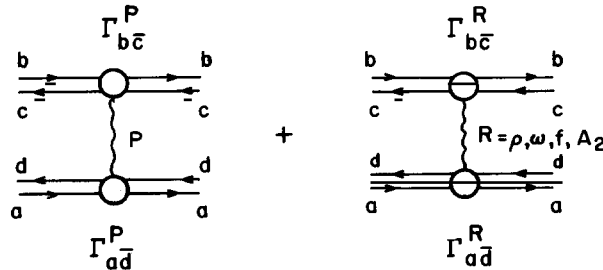
Fig. 2.18. Two particle inclusive diagrams where on particle 'c' is in the fragmentation region of 'b' and the other particle 'd' is in the fragmentation region of 'a'.
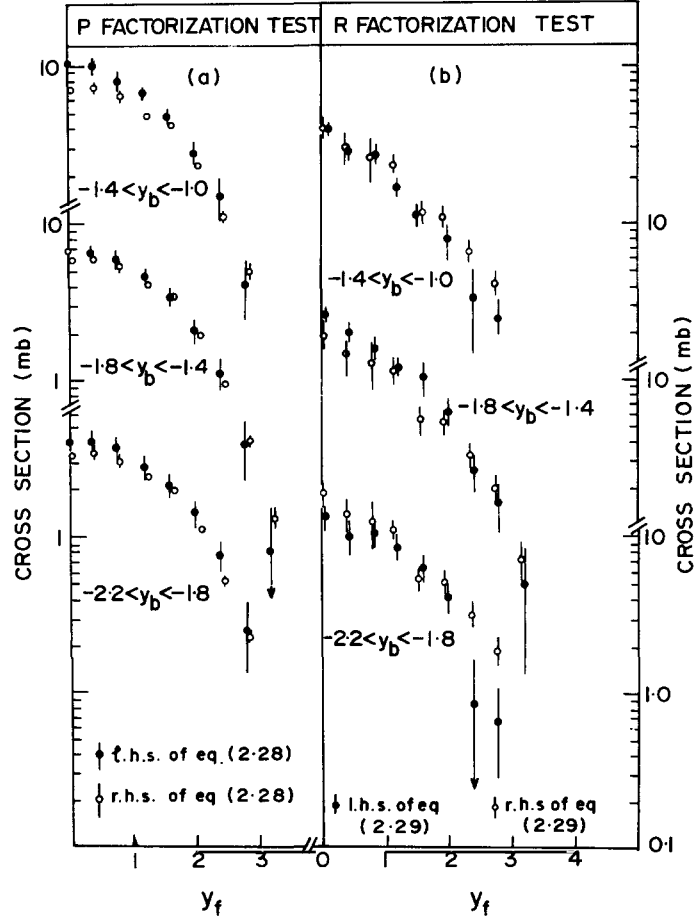
Fig. 2.19. Factorization test from double and single pion production using 100 GeV data of pp and p̄p: (a) test of Pomeron factorization and (b) test of Reggeon factorization. The figure is taken from ref. [105].

In order to test Reggeon factorisation the Pomeron term from eqs. (26) and (27) is eliminated by taking their difference and then re-writing it in terms of one-particle distributions one gets,

$$\left[\frac{d^2\sigma}{dy_f\,dy_b}(\bar{p}p\to\pi_f^+\pi_b^-)-\frac{d^2\sigma}{dy_f\,dy_b}(pp\to\pi_f^-\pi_b^-)\right]\cdot 4\beta_\pi^2\cdot s^{\alpha_R-1}$$

$$=\left[\frac{d\sigma}{dy_f}(\bar{p}p\to\pi_f^+)-\frac{d\sigma}{dy_f}(pp\to\pi_f^-)\right]\cdot\left[\frac{d\sigma}{dy_b}(\bar{p}p\to\pi_b^-)-\frac{d\sigma}{dy_b}(pp\to\pi_b^-)\right].\tag{2.29}$$

The two sides of this equation are shown in fig. 19(b) and are seen to be in agreement for $y_f > 1$ within experimental uncertainty of ~30%.

Thus the factorisation hypothesis gives a satisfactory understanding of the two-particle distributions in terms of one-particle distributions.

2.5. Summary

From the high precision BNL–Penn. data [68] on $p \xrightarrow{\pi,p,\bar{p}} \pi$ one obtains the following quantitative results:

(1) The $\pi^{\pm}$ induced cross-section differences are well described by ρ exchange with a conventional intercept ($\alpha(0) \simeq 0.4$–0.5); but the corresponding p, $\bar{p}$ induced cross-section differences show an appreciable contribution from a lower trajectory exchange ($\alpha(0) \simeq -1$), which may be identified as Baryonium.

(2) Within the FNAL range of $P_{lab.} = 30$–250 GeV/c, the exotic cross-sections $p \xrightarrow{p,\pi^+} \pi^-$ and $p \xrightarrow{p} \pi^+$ (a la criterion I [37, 38]) show scaling to within the experimental accuracy of 10%. The same is true for $p \xrightarrow{\pi^-} \pi^+$, where early scaling is not a priori expected. One should note that the test of scaling to within 10% accuracy over this range corresponds to a test of exchange degeneracy to only within 40% accuracy.

(3) The Pomeron factorisation predictions between these scaling cross-sections are again satisfied to within the experimental accuracy of 10%.

(4) The remaining cross-sections $p \xrightarrow{\pi^-,\bar{p}} \pi^-$ and $p \xrightarrow{\pi^+,\bar{p}} \pi^+$ show a nonscaling component $\sim s^{-1/2}$, as expected for the leading Reggeon R exchanges. The relative magnitudes of the nonscaling components in π and $\bar{p}$ induced cross-sections are also in agreement with the exchange degeneracy relation, following from the exoticity criterion I above. From this and the observation (2) above it appears that the exoticity criterion I is at least a good first approximation.

(5) The f–Pomeron proportionality prediction between the two processes $p \to \pi^-$ and $p \to \pi^+$ is off by a factor of 2.

(6) The exotic cross-section $p \xrightarrow{p} \pi^-$ shows an appreciable (negative) deviation from scaling at lower energies – about 30% at 8 GeV/c. The effect seems to be at least as large for $p \xrightarrow{K^+} \pi^-$, if one supplements the (rather poor) BNL–Penn. data for this process by interpolations from other measurements. In contrast the $p \xrightarrow{\pi^+} \pi^-$ data shows a much smaller scaling deviation. It may be added, however, that the $p \xrightarrow{K^{\pm}} \pi^-$ cross-section difference, estimated from the interpolated data, is roughly equal to the $p \xrightarrow{\pi^{\pm}} \pi^-$ cross-section difference in agreement with the exchange degeneracy prediction.

(7) The scaling deviation is clearly seen to be a nonlinear effect on the $s^{-1/2}$ plot. Hence it cannot be attributed to exchange degeneracy breaking [35]. It is most likely a kinematic effect. More precisely, one can show by using the $p \to \pi^-$ double distribution, that scaling at fixed M^2/s and t corresponds to a scale breaking effect of the right shape and size for the experimental cut of fixed p_L, p_T (or y, p_T). This would suggest M^2/s and t to be the most appropriate choice of scaling variables. In any case the exercise demonstrates how sensitive the scaling phenomenon over the PS energy range is to the choice of scaling variable.

(8) This prescription for scaling deviation cannot, of course, account for the observed difference between the $p \xrightarrow{p,K^+} \pi^-$ cross-sections on one hand and the $p \xrightarrow{\pi^+} \pi^-$ on the other. An attractive interpretation of this phenomenon is in terms of the exoticity criterion II [36a], where a positive (but small) nonscaling component is expected for $p \xrightarrow{\pi^+} \pi^-$, since the incident system ab is nonexotic. In any case, the observed difference between the two processes, has serious implication for the Mueller–Regge phenomenology in the 10 GeV/c range, based on factorisation.

(9) The corresponding scaling deviations for $p \to \pi^+$ are much smaller, which can be qualitatively understood in terms of the M^2/s (or x) distribution for this process being considerably less steep than $p \to \pi^-$.

(10) In the context of the above observations, the absence of the $p \xrightarrow{K} \pi$ data of matching precision to the BNL–Penn. data on $p \xrightarrow{p,\pi} \pi$ seems to us an important gap. An extension of the latter data over a

wider range of y, would also be very helpful – e.g. for a detailed investigation into the scaling deviation.

The compilations, based on the available p → π data, show a typical scatter of about 25%. Within this uncertainty it is consistent with all the features noted above. In fact qualitative indications of many of these features are clearly visible in these data compilations. In view of the rather large uncertainty, however, they do not seem very useful for a quantitative analysis.

For the heavier fragments (K^0, Λ, Σ_{1385}^+, ρ etc.) the data compilations have even a larger scatter. Still one can clearly see the ϕ exchange signals in p$\xrightarrow{K^-}$ Λ, p$\xrightarrow{K^-}$ Σ_{1385}^+ and p$\xrightarrow{K^+}$ K^0. Another noteworthy feature, particularly visible in the Λ and K^0 data, is that the exotic cross-sections seem to show a more substantial rise with energy than for π. Of course the very fact of its fragment mass dependence indicates the rise to be a kinematic effect, like the one mentioned above. For a quantitative estimate of this effect, one needs the double distribution, which are not so far available for these processes. Also the data compilations are evidently inadequate to determine the shape or even the quantitative size of the cross-section rise. A single counter measurement for the Λ and K^0 cross-section, spanning a large energy range would be very useful for this purpose as also for a quantitative analysis of ϕ exchange.

Lastly, we have discussed double fragmentation processes, and the factorisation hypothesis is found to be good within ~20% from two-pion production in pp and p̄p interactions at 100 GeV/c.

3. Triple Regge (TR) analysis (non-diffractive reactions)

In the inclusive reaction b$\xrightarrow{a}$c the triple Regge (TR) limit is a special case of the single Regge limit, namely, the region near the phase space boundary (see figs. 1.1 and 1.2). Specifically, the kinematic region for the triple Regge is,

$$t = (p_b - p_c)^2 \to \text{small}$$

$$s = (p_a + p_b)^2 \to \text{large}$$

$$M^2 = (p_a + p_b - p_c)^2 \to \text{large}$$

$$s/M^2 \to \text{large}. \tag{3.1}$$

In fig. 1 is shown the TR diagram. The spin averaged inclusive cross-section for the production of particle 'c' can be written as [16],

$$\frac{d^2\sigma}{dt \, d(M^2/s)} = \frac{1}{s} \sum_{ijk} G_{ijk}(t) \cdot (s/M^2)^{\alpha_i(t)+\alpha_j(t)} \cdot (M^2)^{\alpha_k(0)}$$

$$= \sum_{ijk} G_{ijk}(t) \cdot s^{\alpha_k(0)-1} \cdot (M^2/s)^{\alpha_k(0)-\alpha_i(t)-\alpha_j(t)} \tag{3.2}$$

where $G_{ijk}(t)$ is given by (note that one has to add the graph by interchanging $i \leftrightarrow j$ in fig. 1),

$$G_{ijk}(t) = \frac{1}{16\pi(2s_a+1)(2s_b+1)} \cdot \left[\sum_{\lambda_b\lambda_c} \beta^i_{\lambda_b\lambda_c}(t)\beta^j_{\lambda_b\lambda_c}(t)\right] \cdot \left[\sum_{\lambda_a} \beta^k_{\lambda_a\lambda_a}(0)\right][2\text{Re}\{\xi^*_i(t) \cdot \xi_j(t)\}] \cdot g_{ijk}(t, t, 0). \tag{3.3}$$
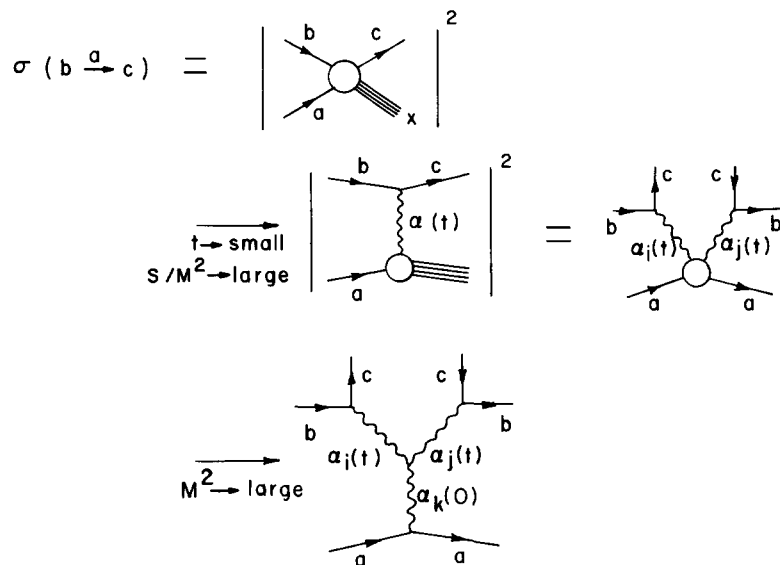
Fig. 3.1. Illustration of the triple Regge limit.

For the case of $\alpha_i(t) = \alpha_j(t)$ we should replace $2\mathrm{Re}\,\xi_i^*\xi_j$ by $|\xi_i(t)|^2$ as then there will be only one graph. s_a and s_b are the spins of particles 'a' and 'b'; λ_i are the helicities; α_i and $\beta^i_{\lambda_b\lambda_c}$ are the usual Regge trajectory functions and the coupling of Regge pole i to the quasi two-body system $b\bar{c}$; $\xi_i(t)$ is the signature factor,

$$\xi_i(t) = [\tau_i + \exp(-\mathrm{i}\,\pi\alpha_i(t))]/[-\sin\pi\alpha_i(t)] \tag{3.4}$$

where τ_i is the signature of the Regge trajectory. g_{ijk} refers to the triple Regge coupling.

The Regge residues and signature factors severely constrain the nature of Regge trajectories that can be exchanged. The following rules may be remembered [106, 107]:

The cross-section vanishes if any one of the following conditions is valid,

(i) if $\alpha_i(t)$ and $\alpha_j(t)$ are exchange degenerate and have opposite signature;

(ii) if $\alpha_k(0)$ has unnatural parity;

(iii) if $\alpha_i(t)$ and $\alpha_j(t)$ have opposite naturality.

A trajectory is called a natural trajectory (N) if $\tau P = +1$, where P is the parity of the trajectory, and an unnatural trajectory (U) if $\tau P = -1$. Because of the above rules the cross-section can be written as the sum of a natural and an unnatural parity component,

$$\sigma = \sigma^N + \sigma^U. \tag{3.5}$$

We have summarised in table 1 the properties of some of the important trajectories which are used in the following sections.

In subsections 3.1 to 3.3 are presented the TR analysis to extract the ordinary meson-, strange meson- and baryon-trajectories from the experimental data. In subsection 3.4 we discuss the role of absorptive corrections in a TR analysis. We discuss in subsection 3.5 the finite mass sum rules and its applications.

Table 3.1
Regge trajectory functions as deduced from Chew–Frautschi plot

Trajectory	Signature	Naturality τP	$\alpha(t)$
π	+1	−1	$\left.\begin{array}{c} \\ \end{array}\right\}$ $-0.013 + 0.67t$
B	−1	−1	
ρ	−1	+1	$\left.\begin{array}{c} \\ \end{array}\right\}$ $0.46 + 0.89t$
A_2	+1	+1	
ω	−1	+1	$\left.\begin{array}{c} \\ \end{array}\right\}$ $0.39 + 0.99t$
f	+1	+1	
ϕ	−1	+1	$\left.\begin{array}{c} \\ \end{array}\right\}$ $0.18 + 0.79t$
f'	+1	+1	
K	+1	−1	$\left.\begin{array}{c} \\ \end{array}\right\}$ $-0.18 + 0.72t$
K_A	−1	−1	
K^*	−1	+1	$\left.\begin{array}{c} \\ \end{array}\right\}$ $0.37 + 0.79t$
K^{**}	+1	+1	
N_α	+1	+1	$-0.4 + t$
N_γ	−1	+1	$-0.35 + 0.8t$
Δ_δ	−1	−1	$0.10 + 0.92t$
Λ_α	+1	+1	$-0.71 + 0.97t$
Σ_α	+1	+1	$-0.76 + 0.89t$
Σ_δ	−1	−1	$-0.25 + 0.91t$

3.1. Ordinary meson trajectories

The intercepts of natural meson trajectories ρ, ω and A_2 are well-known from the total cross-section data; the trajectory functions for ρ and A_2 are also known from two-body reactions. The unnatural meson trajectories π, B etc. are not that well-known. In this subsection we shall present experimental data to see whether these trajectories where they are expected to be dominant can explain the inclusive distributions.

3.1.1. π-trajectory from $\pi^- \xrightarrow{P} \rho^0$

The π-trajectory was extracted by studying the density matrix element of $\rho^0 \to \pi^+\pi^-$ in the inclusive reaction,

$$\pi^- + p \to \rho^0 + X \tag{3.6}$$

at 15 GeV/c [108]. The density matrix element ρ_{00} is non-zero if the above reaction is dominated by pion exchange. The projection of the inclusive cross-section, $\rho_{00}\, d^2\sigma/dt\, dM^2$, is studied in the context of
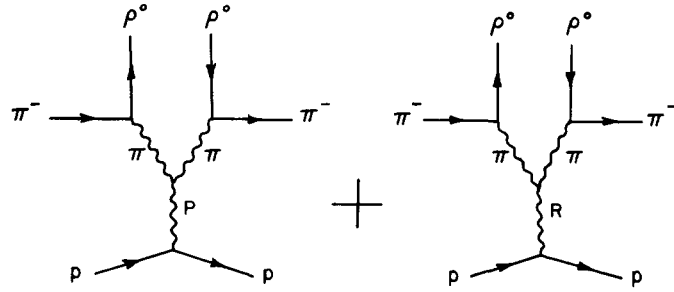
Fig. 3.2. TR diagram for $\pi^- \xrightarrow{\text{p}} \rho^0$.

the triple Regge model, see fig. 2,

$$\rho_{00} \frac{\text{d}^2\sigma}{\text{d}t \, \text{d}M^2} = s^{2\alpha_\pi(t)-2} \cdot [G_{\pi\pi\text{P}}(t) \cdot (M^2)^{1-2\alpha_\pi(t)} + G_{\pi\pi\text{R}}(t) \cdot (M^2)^{0.5-2\alpha_\pi(t)}] \tag{3.7}$$

where the intercepts of the Pomeron and Reggeon in the $\text{p}\bar{\text{p}}$ vertex are taken to be 1 and 0.5 respectively. In this case the triple Regge couplings, $G_{\pi\pi\text{P}}$ and $G_{\pi\pi\text{R}}$, can be explicitly written in terms of πp total cross-sections. The experimental distribution for $\rho_{00} \, \text{d}^2\sigma/\text{d}t \, \text{d}M^2$ was fitted by expression (7), shown in fig. 3, for $|t| \leq 1.1$ $(\text{GeV}/c)^2$. The π-trajectory thus deduced from the fit was,
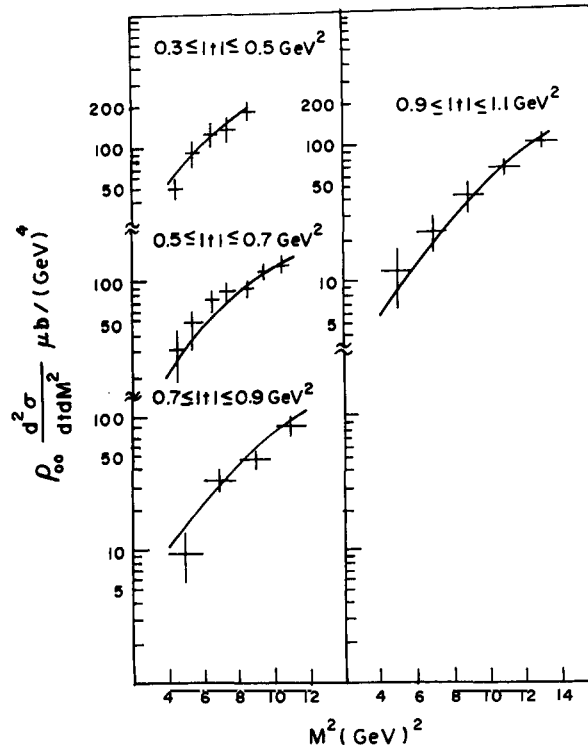
Fig. 3.3. Double differential cross-section $\rho_{00} \, \text{d}^2\sigma/\text{d}t \, \text{d}M^2$ for the reaction $\pi^- \xrightarrow{\text{p}} \rho^0$. The solid lines represent the results of TR analysis [108].

$$\alpha_\pi(t) = -(0.12 \pm 0.07) + (0.78 \pm 0.21)t \tag{3.8}$$

which is in good agreement with the expected pion trajectory (see table 1).

3.1.2. π, ρ and A_2 trajectories from $p \xrightarrow{a} \Delta^{++}$ (1232)

The triple Regge diagram for the process $p \xrightarrow{a} \Delta^{++}$ is shown in fig. 4. In the $a\bar{a}$ vertex there are basically two types of exchanges, one due to the Pomeron and the other due to high lying meson trajectories $R = \rho$, ω, f, A_2. In the $p\bar{\Delta}^{++}$ vertex the basic exchange is due to meson trajectories with $I = 1$, i.e. $R = \pi$, ρ, A_2. The separation of the P from the R trajectory in the $a\bar{a}$ vertex is possible if we use the exoticity criterion of $ab\bar{c}$ as discussed in subsection 1.3.3. If 'a' is π^- or K^- the system $ab\bar{c}$ is exotic and hence we will have only the Pomeron term,

$$\frac{d^2\sigma}{dt\,d(M^2/s)} = G_{RRP}(t) \cdot (M^2/s)^{1-2\alpha_R(t)} \tag{3.9}$$

where the summation over $R = \pi$, ρ, A_2 is implied. In the case of 'a' being π^+ or K^+ both the P and R terms at the $a\bar{a}$ vertex will contribute and the invariant cross-section can be written as

$$\frac{d^2\sigma}{dt\,d(M^2/s)} = G_{RRP}(t) \cdot (M^2/s)^{1-2\alpha_R(t)} + G_{RRR}(t) \cdot (M^2/s)^{\alpha_R(0)-2\alpha_R(t)} \cdot s^{\alpha_R(0)-1}. \tag{3.10}$$

The best way to determine the RRR term will be to take differences of the invariant cross-sections, at a fixed value of s, with 'a' $= K^-$ and K^+ (or π^- and π^+),

$$\frac{d^2\sigma(p \xrightarrow{K^+} \Delta^{++})}{dt\,d(M^2/s)} - \frac{d^2\sigma(p \xrightarrow{K^-} \Delta^{++})}{dt\,d(M^2/s)} = G_{RRR}(t) \cdot (M^2/s)^{\alpha_R(0)-2\alpha_R(t)} \cdot s^{\alpha_R(0)-1}. \tag{3.11}$$

We shall now discuss the experimental data. These data will be grouped into two classes, (a) with incident beam momenta $<30\,\text{GeV}/c$ [102, 109–112] and (b) with incident momenta $>100\,\text{GeV}/c$ [113, 114] and they are described below.

(a) *Incident beam momenta* $<30\,\text{GeV}/c$:
From the reaction $p \xrightarrow{K^-} \Delta^{++}$, where $ab\bar{c}$ is exotic, it has been possible to deduce the intercept of the
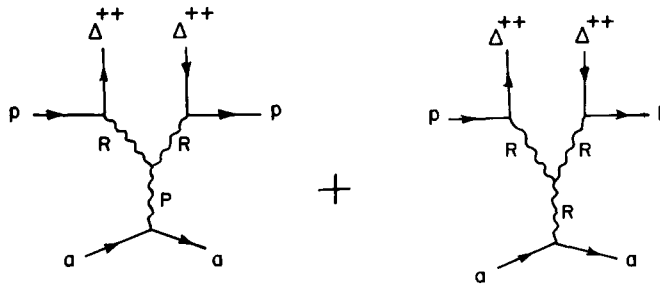
Fig. 3.4. TR diagram for $p \xrightarrow{a} \Delta^{++}$.
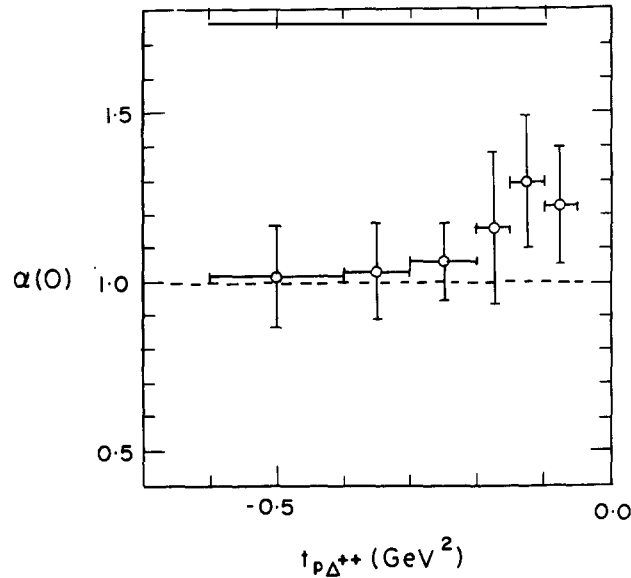
Fig. 3.5. Estimation of the Pomeron intercept from $p \xrightarrow{K^-} \Delta^{++}$ at 10 and 16 GeV/c [102].

Pomeron by comparing the data [102] at 10 and 16 GeV/c. This is shown in fig. 5. It is seen that the Pomeron intercept is consistent with unity.

The Regge trajectory at the $p\bar{\Delta}^{++}$ vertex, i.e. $\alpha_R(t)$, has also been determined and the experimental results are displayed in fig. 6 for the exotic reactions $p \xrightarrow{\pi^-} \Delta^{++}$ at 15 GeV/c [111] and $p \xrightarrow{K^-} \Delta^{++}$ at 14.3 GeV/c [110]. Two sets of data points are seen to be in good agreement. In the same figure we have
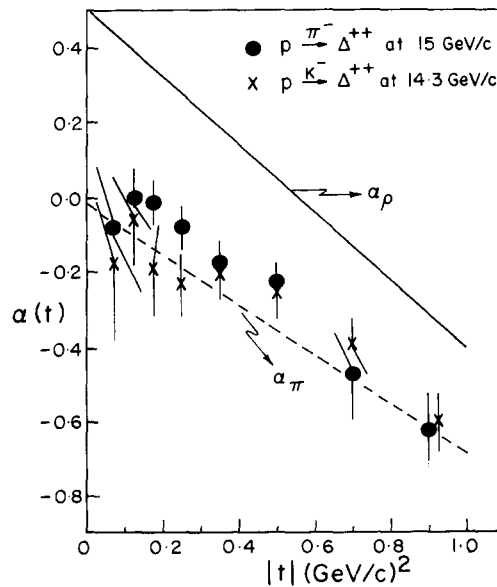
Fig. 3.6. Regge trajectory as obtained from $p \xrightarrow{\pi^-} \Delta^{++}$ at 15 GeV/c [111] and $p \xrightarrow{K^-} \Delta^{++}$ at 14.3 GeV/c [110]. The solid and the dotted lines represent the ρ and π trajectories respectively.

shown the pion trajectory, $\alpha_\pi(t) = 0.013 + 0.67t$, by the dashed line and the ρ trajectory, $\alpha_\rho(t) = 0.5 + 0.9t$, by the full line. It is seen that the data points are in good agreement with the pion trajectory over the full $|t|$ range studied†.

The importance of the RRR term was studied [112] through eq. (11) by taking the difference of the experimental structure functions from K^+ and K^- data at 16 GeV/c. In order to smooth out the resonance structure the first moment of the RRR term and of the difference of the experimental distributions were used. The experimental distributions as seen from fig. 7 are well described by the RRR term.

(b) *Incident beam momenta* >100 GeV/c:

In fig. 8 is shown the trajectory as deduced from $\mathrm{p} \xrightarrow{\pi^-} \Delta^{++}$ from the combined data at 100, 200 and 360 GeV/c [113]. The high energy data also reveals the dominance of the pion trajectory. Some contribution from the high lying ρ trajectory cannot be ruled out for $|t| > 0.4$ (GeV/$c)^2$.

Comparison with two body reactions $\mathrm{pp} \to \mathrm{n}\Delta^{++}, \Delta^{++}\Delta^0$

Recently two experiments conducted at the ISR for the exclusive reactions $\mathrm{pp} \to \mathrm{n}\Delta^{++}$ [115] and $\mathrm{pp} \to \Delta^{++}\Delta^0$ [116] revealed that the energy dependence of the cross-section for these two reactions changes drastically at the ISR energies. The compilation of data as presented in [116] is shown in fig. 9, $\sigma p_{\mathrm{lab}}^2$ versus p_{lab}. For the pion exchange the dependence of $\sigma \propto p_{\mathrm{lab}}^{-2}$ is expected while $\sigma \propto p_{\mathrm{lab}}^{-1}$ is expected for ρ, A_2 exchanges. It is seen from the figures that the data up to about 400 GeV/c are consistent with the dominance of pion exchange, whereas beyond 400 GeV/c the dominance of ρ, A_2 exchanges are seen. The dominance of the pion exchange as seen from the inclusive data below 400 GeV/c is in good agreement with the exclusive data.
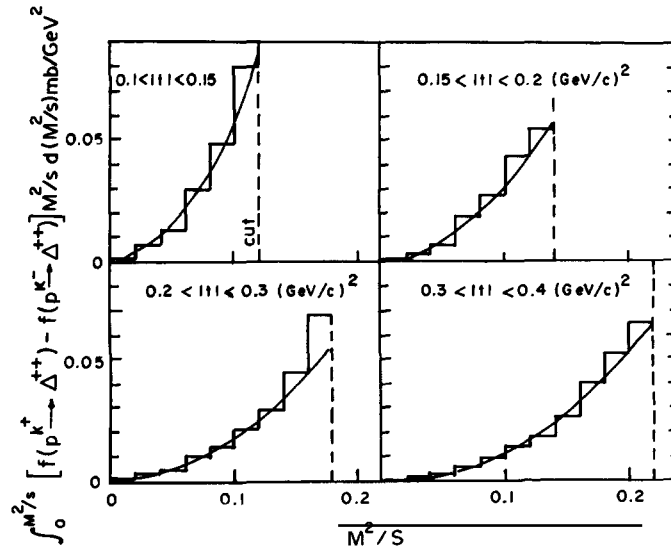
Fig. 3.7. The first moment of the difference of the inclusive cross-section, eq. (11), versus M^2/s is shown for four t bins. The curves are the results of the fits with the RRR triple-Regge term [112].

† It may be noted that the authors [110, 111] concluded that the pion trajectory is dominant only for $|t| < 0.3$ (GeV/$c)^2$; it is because they treated the pion trajectory as $\alpha_\pi(t) = 0.0 + t$.
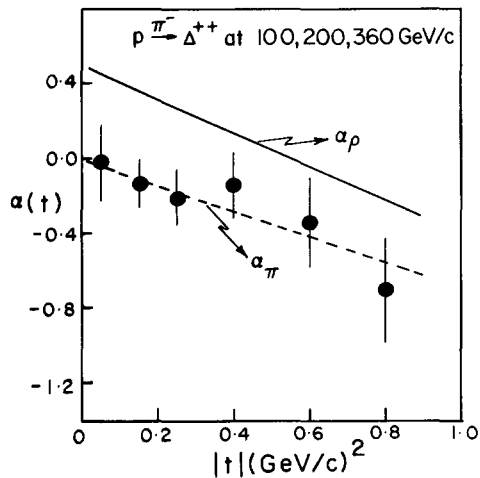
Fig. 3.8. Regge trajectory as obtained from p $\xrightarrow{\pi^-}$ Δ^{++} at 100, 200 and 360 GeV/c [113]. The solid and the dotted lines represent the ρ and π trajectories respectively.

3.1.3. ρ and A_2 trajectories from $\pi^{\pm} \xrightarrow{p} \pi^0, \eta$

The following two reactions have been studied [117] to extract ρ and A_2 trajectories from fragmentation of $\pi^{\pm}$ into π^0 and η respectively,

$$\pi^{\pm} + p \rightarrow \pi^0 + X \tag{3.12}$$
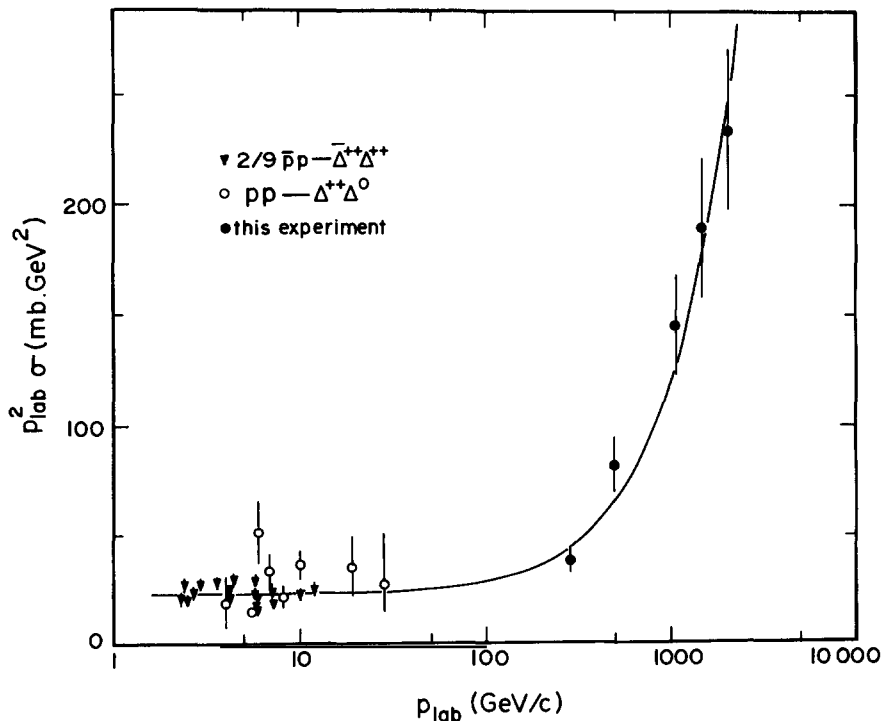
Fig. 3.9. The variation of σp_{lab}^2 with p_{lab} for $pp \rightarrow \Delta^{++}\Delta^0$. The figure is taken from ref. [116].

$$\pi^{\pm} + p \rightarrow \eta + X.$$ (3.13)

The beam momentum was 100 GeV/c. The kinematic regions used were $0 < -t \leq 4$ (GeV/c)^2 and $x \gtrsim 0.7$; here $|t|$ refers to the 4-momentum transfer from the incident $\pi^{\pm}$ to the fragmented $\pi^0(\eta)$ particle.

The TR diagrams for the reaction (12) are shown in fig. 10. The dominant contribution at the $\bar{p}p$ vertex arises from the Pomeron exchange and a small contribution from the meson trajectories, $f \pm \rho$ (note that the ρ trajectory has opposite sign for the $\pi^{\pm}$ beams). The ρ contribution is found to be negligible as the cross-sections from the π^+ and π^- beams are almost equal; and it may also be reasonable to neglect f at such high energies. Hence the invariant cross-section, eq. (2), can be written with $x \approx 1 - M^2/s$, as,

$$\frac{d^2\sigma}{dt\,dx} = G_{\rho\rho P}(t) \cdot (1 - x)^{1-2\alpha_\rho(t)}.$$ (3.14)

The ρ trajectory as obtained from the x-dependence of the cross-section at different $|t|$ values is shown in fig. 11. There is a strong indication that the trajectory flattens off to ≈ -0.5 for $|t| > 1$ (GeV/c)^2.

The ρ trajectory has also been extracted from the s-dependence of the exclusive channel

$$\pi^- + p \rightarrow \pi^0 + n$$ (3.15)

and there are two different experiments, one in the energy range 20 to 200 GeV with $|t| < 1.4$ GeV^2 [118] and the other in the range 15 to 40 GeV with $|t| < 2.0$ GeV^2 [119]. The smooth curves through their data points are shown in fig. 11 as dashed line and dot-dashed line respectively. They are not in good agreement with each other over the common t-range. However, the high statistics experiment in the range 15 to 40 GeV [119] does not show any deviation from linearity up to $|t| = 2.0$ GeV^2 and thus in disagreement with the inclusive data.†

In the case of reaction (13) the dominant TR graph is A_2A_2P. The A_2 trajectory as deduced from the x dependence of the cross-section at different t values is shown in fig. 12. Here also the A_2 trajectory flattens off at ≈ -0.5 for $|t| \geq 1.5$ (GeV/c)^2. The data on the exclusive channel

$$\pi^- + p \rightarrow \eta + n$$ (3.16)

exist in the energy range 15 to 100 GeV [120, 121]. The A_2 trajectory as deduced from the high statistics
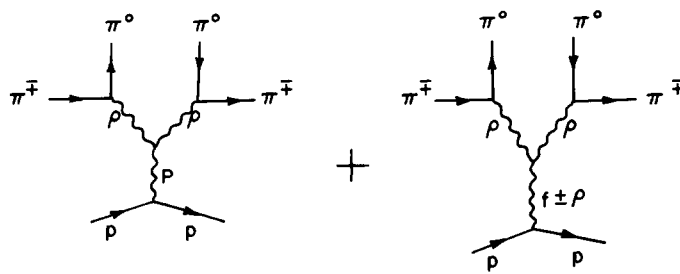
Fig. 3.10. TR diagram for the reaction $\pi^+ \xrightarrow{p} \pi^0$.

† The flattening of the effective ρ-trajectory in the inclusive data, has been recently interpreted in terms of a combination of triple Regge and hard scattering contributions (D. Beavis, B.R. Desai and D. Keim, UCR preprint, 1980).
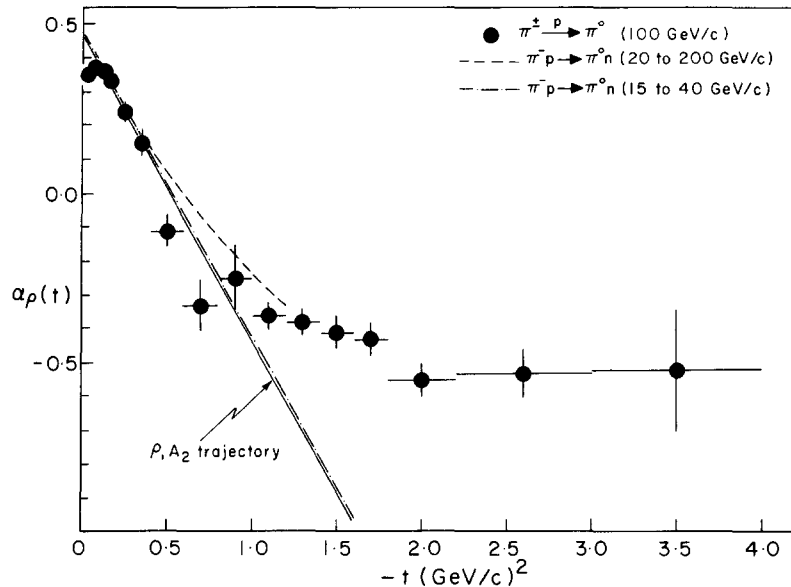
Fig. 3.11. ρ trajectory as deduced from $\pi^\pm \xrightarrow{p} \pi^0$ at 100 GeV/c [117]. Results from two-body reaction $\pi^-p \to \pi^0 n$ are also shown as dashed line [118] and dot-dashed line [119]. The solid line refers to the expected ρ, A_2 trajectory.

data [120] is shown in fig. 12. It is seen that the A_2 trajectory from the exclusive channel also shows a flattening effect beyond $|t| \gtrsim 0.7$ $(\mathrm{GeV}/c)^2$.

3.2. Strange meson trajectories

Here the well established natural trajectories are $K^*(890)$ and $K^{**}(1430)$. Among the unnatural
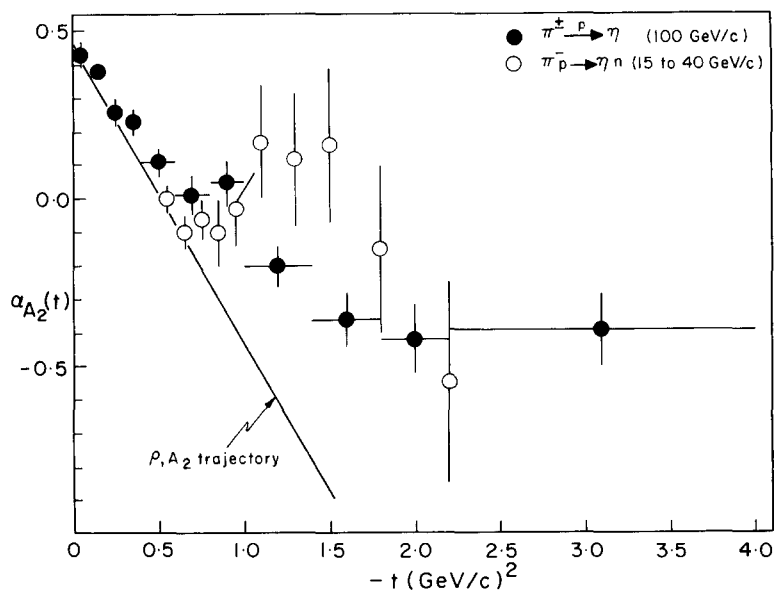
Fig. 3.12. A_2 trajectory as deduced from $\pi^\pm \xrightarrow{p} \eta$ at 100 GeV/c [117]. Results from two-body reaction $\pi^-p \to \eta n$ [120] are also shown as open circles for comparison. The solid line refers to the expected ρ, A_2 trajectory.

trajectories the only well established is the K and there is indication for the existence of $K_A(1280)$ in the Q region. These strange meson trajectories are responsible for the reactions $p \xrightarrow{a} \Lambda$ and $p \xrightarrow{a} \Sigma^+(1385)$. In the $a\bar{a}$ vertex there will be contributions, in general, from both the Pomeron and the meson trajectories. We shall discuss below only those experimental data where only one trajectory is dominant in the $a\bar{a}$ vertex as this will lead to a better determination of the effective kaon trajectory (experimental data from $p \xrightarrow{\bar{p}} \Lambda$ [122], $p \xrightarrow{\pi^-} \Lambda$ [123] and $p \xrightarrow{K^-} \Sigma^+_{1385}$ [124] will not therefore be discussed).

3.2.1. $p \xrightarrow{p} \Lambda$

Since $a\bar{b}\bar{c}$ is exotic in this reaction the Pomeron term only will dominate the $a\bar{a}$ vertex. The invariant cross-section can therefore be written as,

$$\frac{d^2\sigma}{dt\, d(M^2/s)} = G(t) \cdot (M^2/s)^{1-2\alpha_{eff}(t)} \tag{3.17}$$

where the intercept of the Pomeron is taken as unity and $\alpha_{eff}(t)$ represents the effective kaon trajectory for the $p\Lambda$ vertex. The latter is determined in the usual way by studying (M^2/s) versus t plots. In table 2 is listed the effective kaon trajectory as determined from the experimental data at 12, 19, 24 and 69 GeV/c [125–127]. From the table it seems that the unnatural kaon trajectory $(\alpha_K(0) \approx -0.3)$ is the dominant contributor at lower energies and there is an indication that the contribution from the natural K^* trajectory $(\alpha_{K^*}(0) \approx 0.3)$ becomes important at higher incident energies. An alternative and perhaps more plausible interpretation of this energy dependence of $\alpha_{eff}(t)$ is in terms of the scaling deviation observed for this process at low energies (subsection 2.3). One may interpret the rising cross-section at low energies in terms of an effective Pomeron intercept >1 or in terms of a change of variable as discussed below. In either case it would correspond to a lowering of the α_{eff} of eq. (17) at low energies in agreement with table 2.

3.2.2. $p \xrightarrow{K^+} \Lambda$

In this reaction $a\bar{b}\bar{c}$ is exotic and therefore the Pomeron exchange will be the dominant term in the $K^+\bar{K}^+$ vertex. A study of this reaction has been made by the same group [128] at two momenta 8.2 and 16 GeV/c and therefore a separate TR analysis to the two momenta as well as a combined analysis were made. In order to combine data at different energies it may be appropriate to write the kinematical factors explicitly and with this the TR expression becomes,

$$E\frac{d\sigma}{d^3p} \equiv \frac{2p^*_{inc}}{\pi\sqrt{s}} \cdot \frac{d^2\sigma}{dt\, d(M^2/s)} = G(t) \cdot (M^2/s)^{1-2\alpha_{eff}(t)}. \tag{3.18}$$

Table 3.2
Effective kaon trajectory as determined from $p \xrightarrow{\bar{p}} \Lambda$

p_{lab} (GeV/c)	$\alpha_{eff}(t)$	Upper limit of $\|t\|$ used in GeV^2
12	$-(0.54 \pm 0.07) + (0.89 \pm 0.08)t$	3.6
19	$-(0.38 \pm 0.11) + (1.15 \pm 0.07)t$	4.0
24	$-(0.09 \pm 0.04) + (1.04 \pm 0.05)t$	3.6
69	$+(0.20 \pm 0.22) + (0.93 \pm 0.08)t$	11.0

From the separate analysis of 8.2 GeV/c and 16 GeV/c data they find the intercept of the effective kaon trajectory as $-(0.50 \pm 0.14)$ and $-(0.22 \pm 0.11)$ respectively; the trajectory points are shown in fig. 13(a). As the threshold for the reaction $K^+ + p \rightarrow \Lambda + X$ is $M_{th}^2 = 4m_K^2$, the authors argue that the above discrepancy in the intercept arises due to not using the proper variable and they suggest that M^2 should be replaced by $M^2 - M_{th}^2$. The effective kaon trajectories as deduced after this modification are, fig. 13(b),

$$\alpha_{eff}(t) = -(0.06 \pm 0.32) + (0.86 \pm 0.32)t, \quad \text{at } 8.2 \text{ GeV}/c$$

$$\alpha_{eff}(t) = -(0.10 \pm 0.21) + (0.77 \pm 0.13)t, \quad \text{at } 16 \text{ GeV}/c. \tag{3.19}$$

The agreement between the two sets of trajectories are good. It may also be noted that the change in the variable from M^2 to $M^2 - M_{th}^2$ increases the intercept of the effective trajectory.

From the combined data at 8.2 and 16 GeV/c, the effective kaon trajectory is found to be,

$$\alpha_{eff}(t) = -(0.12 \pm 0.15) + (0.77 \pm 0.11)t \tag{3.20}$$

which is close to the kaon trajectory.

3.2.3. $p \xrightarrow{K^-} \Lambda$

The inclusive production of Λ in this reaction can be subdivided into two parts [43]: (i) strangeness annihilation process of the type

$$K^- + \text{'}K^{+\text{'}} \rightarrow \text{pions} \tag{3.21}$$

where the leading Regge trajectory, fig. 14, is expected to be the exchange degenerate ϕ-f' trajectory,
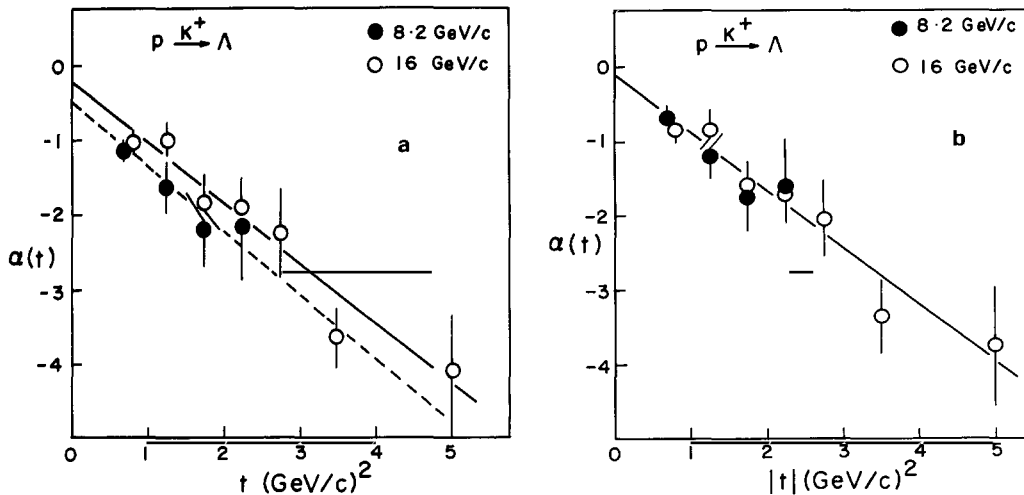
Fig. 3.13. Regge trajectory as deduced from $p \xrightarrow{K^+} \Lambda$ at 8.2 and 16 GeV/c [128]. (a) The TR fits were made with M^2 as the variable. The solid and dotted lines are fits to the trajectory points of 16 and 8.2 GeV/c respectively. (b) The TR fits were made with $M^2 - M_{th}^2$ as the variable. The solid line represents the results of the TR fit to the combined data 8.2 and 16 GeV/c.
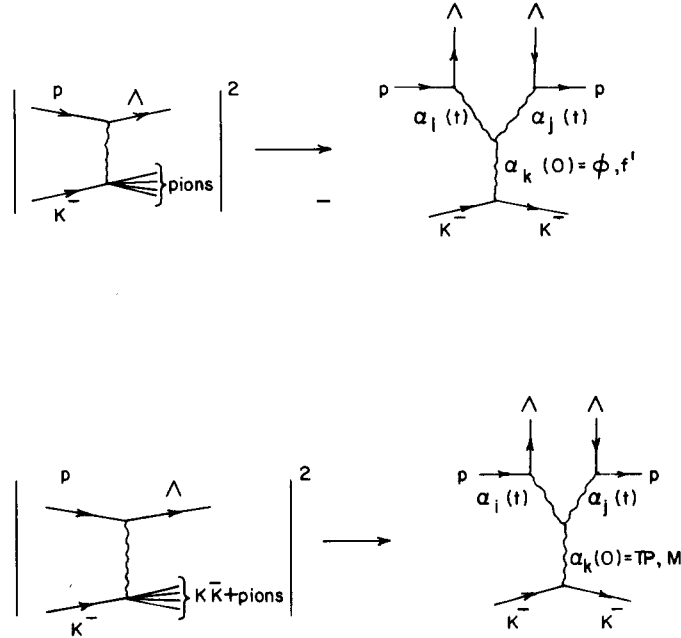
Fig. 3.14. TR diagrams for the strangeness annihilation and non-annihilation processes in $p \xrightarrow{K^-} \Lambda$.

and (ii) strangeness nonannihilation process of the type

$$K^- + \text{'}K^{+}\text{'} \rightarrow \bar{K}K + \text{pions} \tag{3.22}$$

where the leading trajectories are expected to be the Pomeron and the ordinary meson trajectories (see subsection 1.3.5). At low energies the reaction (21) is the dominant one. This can be inferred from the ratio $\sigma(K^-p \rightarrow \Lambda + \text{pions})/\sigma(K^-p \rightarrow \Lambda + K\bar{K} + \text{pions})$ which is ≈ 9 at $4.2\,\text{GeV}/c$ [129] and is ≈ 4 at $8.25\,\text{GeV}/c$ [130]. Also the energy dependence of the cross-section for $K^- + p \rightarrow \Lambda + \text{pions}$ is $\sim s^{-0.9 \pm 0.1}$ which is suggestive of the dominance of ϕ, f' trajectories [130], while the cross-section for $K^- + p \rightarrow \Lambda + K\bar{K} + \text{pions}$ is continuously increasing from $\approx 0.4\,\text{mb}$ at $4\,\text{GeV}/c$ to $\approx 1.7\,\text{mb}$ at $32\,\text{GeV}/c$ [131] which is suggestive of the dominance of the Pomeron trajectory.

The TR analyses were carried out at $4.2\,\text{GeV}/c$ [129, 132] and $8.25\,\text{GeV}/c$ [133]. In the former case the TR analysis was performed separately for the processes (21) and (22), and to take care of the copious production of resonances the first moment integral was used,

$$I_1(x, t) = \int_0^x \left(\frac{\nu}{s}\right) \cdot \frac{\mathrm{d}^2\sigma}{\mathrm{d}t\,\mathrm{d}(\nu/s)} \cdot \mathrm{d}(\nu/s) \tag{3.23}$$

with

$$\frac{\mathrm{d}^2\sigma}{\mathrm{d}t\,\mathrm{d}(\nu/s)} = G(t) \cdot s^{\alpha_k(0)-1} \cdot (\nu/s)^{\alpha_k(0)-2\alpha_{\text{eff}}(t)} \tag{3.24}$$

and

$$\nu = M^2 - t - m_K^2.$$ (3.25)

At a given s one thus determines $\alpha_k(0) - 2\alpha_{eff}(t)$ for different t-values. At 8.25 GeV/c the analysis was carried out by fitting the data of $d^2\sigma/dt\, d(M^2/s)$ versus M^2/s (i.e. replacing $\nu \to M^2/s$ in eq. (24)). The value of $\alpha_k(0)$ was determined by fitting $(E/\pi p_{max})d\sigma/dx$, or the equivalent $d\sigma/d(M^2/s)$, at different energies to the $s^{\alpha_k(0)-1}$ in the target fragmentation region. For the reaction (21) this procedure yielded,

$$\alpha_k(0) = 0.078 \pm 0.013$$ (3.26)

which is consistent with the ϕ-f' trajectory coupling to the $K\bar{K}$ vertex.

The effective kaon trajectories were thus deduced to be,

$$\alpha_{eff}(t) = -(0.05 \pm 0.04) + (1.02 \pm 0.02)t, \quad \text{at 4.2 GeV/}c \text{ and } |t| < 1.0 \text{ GeV}^2$$

$$\alpha_{eff}(t) = -(0.15 \pm 0.04) + (0.86 \pm 0.04)t, \quad \text{at 8.25 GeV/}c \text{ and } |t| < 1.5 \text{ GeV}^2$$ (3.27)

which lie between the K and K^* trajectories.

The TR analysis of the reaction (22) did not yield any conclusive result at 4.2 GeV/c because of the high mass threshold of $M^2 = 4m_K^2$.

3.2.4. Energy dependence of Λ cross-section in pp and $\bar{p}p$ interactions

An attempt has been made [134] to understand the high energy behaviour of the inclusive Λ production cross-section in pp and $\bar{p}p$ interactions. The dominant trajectories at the non-fragmenting vertex were taken as the Pomeron and the odd signature ω^0 trajectory with intercept as 0.4. With this the invariant cross-section for $p \xrightarrow{a} \Lambda$ becomes,

$$\frac{d^2\sigma}{dt\, d(M^2/s)} = \frac{\sqrt{s}}{2p_{inc}^*} \cdot G(t)(M^2/s)^{1-2\alpha_{eff}(t)} \pm s^{-0.6} \cdot (M^2/s)^{0.4-2\alpha_{eff}(t)}$$ (3.28)

where the positive and the negative sign are to be used for the case of 'a' = $\bar{p}$ and 'a' = p respectively. It was shown that the central production of Λ is small, namely $\sigma_{\bar{\Lambda}}/\sigma_{\Lambda}$ is 9% in pp interactions, and therefore the Λ is basically produced through fragmentation process. The inclusive cross-section was calculated by integrating eq. (28) over t and M^2/s and thus stretching triple Regge formalism to cover the complete fragmentation region. By making a simultaneous fit to the pp and $\bar{p}p$ data, see fig. 15, the effective trajectory was found to be,

$$\alpha_{eff}(t) = -(0.2 \pm 0.1) + (0.8 \pm 0.1)t$$ (3.29)

which is in good agreement with the effective kaon trajectory deduced from the conventional TR analysis. It is also to be noted that the energy dependence of Λ production in pp and $\bar{p}p$ interactions are well reproduced.
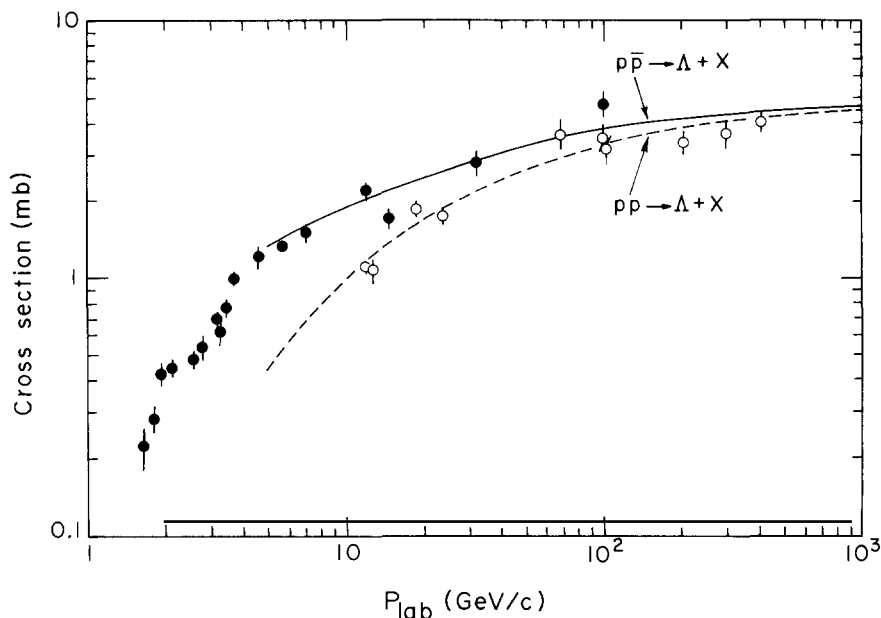
Fig. 3.15. Production cross-section of Λ in pp and $\bar{p}p$ interactions. The solid and dotted lines refer to the energy dependence expected for $\bar{p}p$ and pp interactions respectively [134].

3.2.5. K^*, K^{**} trajectories from $K^\pm \to \pi^0(\eta)$, $\pi^\pm \to K^\pm$

The following reactions have been studied at 100 GeV/c [135],

$$K^\pm + p \to \pi^0 + X \qquad K^\pm + p \to \eta + X \tag{3.30}$$

and an important point to note that only the *natural trajectories* K^* and K^{**} are allowed in the $K\pi^0(\eta)$ vertex. The reactions with the K^+ beam are exotic. The effective Regge trajectories as deduced from π and η data are in agreement with each other and also with the K^*, K^{**} trajectory. In fig. 16 is shown the $\alpha(t)$ as deduced from the η data.

Measurements of inclusive $K^\pm$ production using Fermilab Single Arm Spectrometer in $\pi^+ \xrightarrow{\ p\ } K^+$
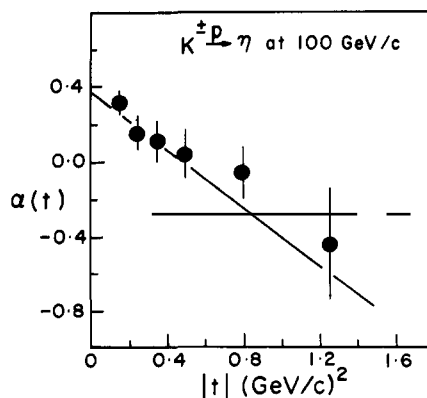
Fig. 3.16. Regge trajectory as obtained from $K^\pm \xrightarrow{\ p\ } \eta$ at 100 GeV/c [135]. The solid line refers to the exchange degenerate K^*, K^{**} trajectory.

and $\pi^- \xrightarrow{P} K^-$ in the energy range 50 to 140 GeV also yielded the K*, K** trajectory as [136] 0.20 ± 0.06 and 0.25 ± 0.06 for the t range −0.1 to −0.6.

3.3. Baryon trajectory

In this case the most of the data exist in the form of two classes namely, p $\xrightarrow{a}$ mesons (π or K) [70, 81, 135–140] and K $\xrightarrow{P}$ strange baryons (Λ or Ξ) [128, 132, 133, 141, 142]. In the first case we have data right from 9.3 GeV to the ISR energies while in the second case only low energy data exist in the range 4 to 16 GeV. Besides there is some FNAL data [136] on $\pi^+ \xrightarrow{P} p$ and $\pi^- \xrightarrow{P} \bar{p}$. These data are discussed below.

3.3.1. p $\xrightarrow{P} \pi^\pm$, K$^+$

Since this is an exotic channel there will be Pomeron dominance in the p$\bar{p}$ vertex. The exchange trajectory for the p$\bar{\pi}^+$ vertex will be Nucleon or Δ while for the p$\bar{\pi}^-$ vertex it will be only Δ trajectory. In case of the vertex p$\bar{K}^+$ the exchanged trajectory will be Λ or Σ.

Several analyses have been made at 19.2 GeV/c [137–139] and the effective trajectories for the p$\bar{\pi}$ and p$\bar{K}^+$ vertices as deduced from these analyses are in good agreement with each other and we quote the trajectories in table 3 as obtained in [138]. We have also listed the two exotic exchanges from p $\xrightarrow{P} K^-$ and p $\xrightarrow{P} \bar{p}$. It is seen from the table that the effective trajectories as obtained from the data are much lower than the expected leading trajectories. Same conclusion was reached from the study of non-exotic channels p $\xrightarrow{\gamma} \pi^-$ at 9.3 GeV/c [81] and p $\xrightarrow{K^-} \pi^\pm$ at 14.3 GeV/c [70].

At high energies there are three experiments: (i) at 100 GeV/c [135] with p $\xrightarrow{P} \pi^0$, (ii) at 50–175 GeV/c [136] with p → π^+, K$^+$, and (iii) at the ISR energy, $\sqrt{s}$ = 45 GeV/c [140], with p $\xrightarrow{P} \pi^\pm$, K$^+$. The (missing mass)^2 distributions from the ISR experiment is shown in fig. 17. The distributions were fitted with the expression,

$$\frac{d^2\sigma}{dt\, d(M^2/s)} = G(t) \cdot (M^2/s)^{1-2\alpha_{eff}(t)} \tag{3.31}$$

for $M^2 < 600$ GeV^2 (i.e. $x > 0.7$) and $|t| < 1.5$ (GeV/c)^2. The effective trajectories as deduced from these fits are shown in fig. 18. It is seen from the figure that the effective trajectory for p $\xrightarrow{P} \pi^+$ and p $\xrightarrow{P} K^+$ are in good agreement with the nucleon and the $\Lambda(\Sigma)$ trajectory respectively, whereas the $\alpha_{eff}(t)$ for p $\xrightarrow{P} \pi^-$ is still much below the Δ trajectory. The effective trajectory from p $\xrightarrow{P} \pi^0$ at 100 GeV/c is in agreement with the nucleon trajectory. The effective trajectories as deduced from

Table 3.3
Effective baryon trajectories as extracted from pp reactions at
19.2 GeV/c

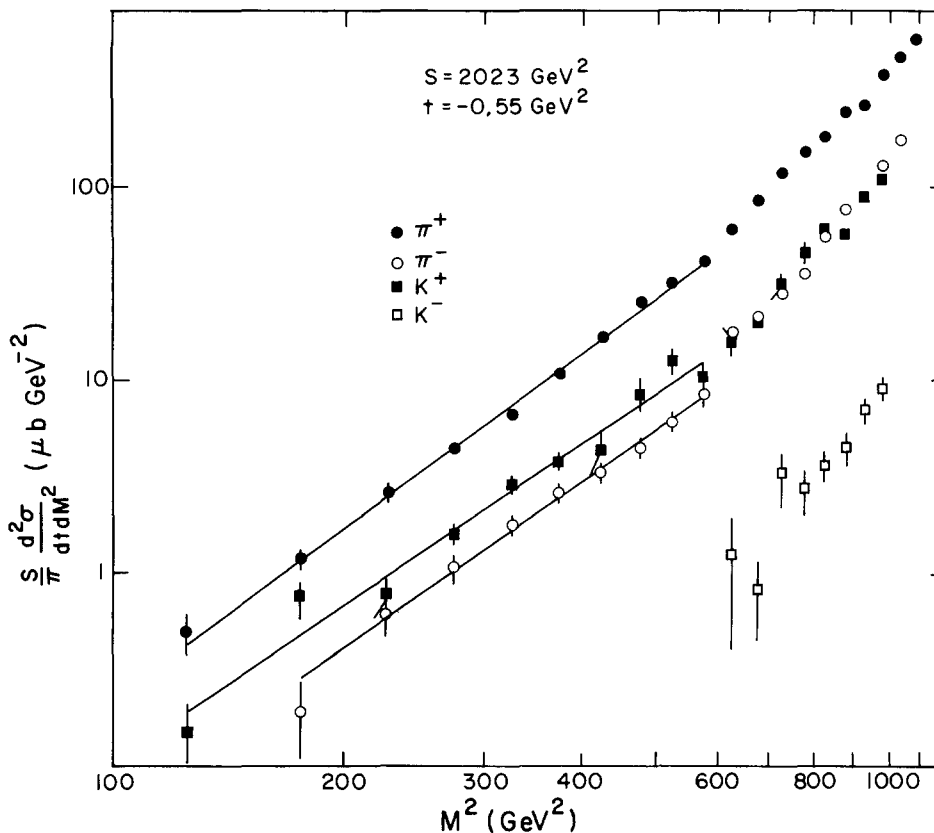| Reactions	$\alpha_{eff}(t)$	Expected leading trajectory
p + p → π^+ + X	−1.32 + 0.53t	N$_\alpha$
p + p → π^- + X	−2.0 + 0.78t	Δ_δ
p + p → K$^+$ + X	−1.11 + 0.63t	Σ_δ, Λ_α
p + p → K$^-$ + X	−3.55 + 0.7t	exotic
p + p → $\bar{p}$ + X	−5.7 + 0.7t	exotic

Fig. 3.17. Missing-mass square distribution from $p \xrightarrow{p} \pi^+(\pi^-, K^+, K^-)$ at $\sqrt{s} = 45$ GeV and with $t = -0.55$ GeV^2. The solid lines are TR fits to the data [140].
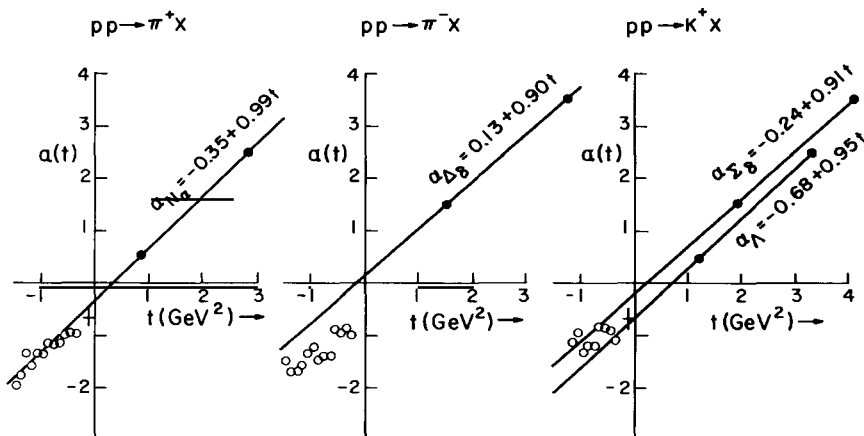

Fig. 3.18. Effective trajectories as obtained from inclusive meson production at ISR with $\sqrt{s} = 45$ GeV [140].

$p \to \pi^+$ and $p \to K^+$, over $t = -0.2$ to 0.2, using the Fermilab Single Arm Spectrometer [136] are -0.65 ± 0.15 and -0.65 ± 0.20 respectively, which are in good agreement with the ISR data.

It is to be noted from the table 3 and fig. 18 that the intercepts of all the three trajectories from $p \xrightarrow{p} \pi^{\pm}$, K^+ (i.e. the N, Δ and Λ trajectories) are raised by ≈ 0.8 in going from $19 \, \text{GeV}/c$ to the ISR energies. In particular the N and Λ trajectories are raised to the value as expected from the Chew–Frautschi plot (table 1).

It should be mentioned here that the anomalously low baryon trajectories, as obtained from the baryon $\to$ meson data at PS energies, has exercised theorists for a long time. The most plausible explanation seems to be a kinematic one, due to Chan Hong-Mo [7, 8], suggesting that the triple Regge behaviour should set in late for a heavy particle b fragmenting into a light one c. This follows from the multiperipheral production amplitude shown below. The triple Regge diagram corresponds to the sum
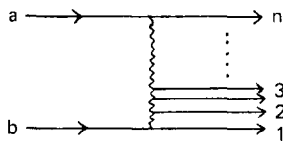
of all graphs, where the detected particle c is the 1st one in the multiperipheral chain – i.e. has the lowest momentum transfer relative to b. Such graphs are expected to be dominant for t close to $t_{\min}$; i.e. for small negative t (where most of these analyses have been made) and $m_b \lesssim m_c$. However, for $m_b \gg m_c$, $t_{\min}$ has a significant positive value (~ 0.6 for $p \to \pi$). Thus for small negative t, which is an appreciable distance away from $t_{\min}$, the graphs corresponding to $c = 2, 3, 4, \ldots$ on the multiperipheral chain should be significant. Of course, at very large $s (\gg M^2)$, these graphs would vanish for any finite t, and the triple Regge formula would be restored. In this context it is reassuring that there is a distinct improvement in the trajectory estimate from the FNAL and ISR data, at least for the nucleon exchange $(p \to \pi^+)$ and $p \to K^+$. However, the effective Δ trajectory is still below the expected value.

3.3.2. $K^- \xrightarrow{p} \Lambda$

The exchanged trajectory mediating $K^- \bar{\Lambda}$ vertex is the antinucleon which leads to off-shell antinucleon elastic scattering at the lower vertex (proton). The latter as discussed in subsection 1.3.5 is expected to have a strong contribution from the low-lying baryonium trajectory. The intercept of the trajectory at the lower vertex was obtained [133] by fitting the invariant $f(x)$ distribution to the expected power law $s^{\alpha_k(0)-1}$ in the kaon fragmentation region and its value is found to be: $\alpha_k(0) = 0.05 \pm 0.02$. The effective trajectory for the $K^- \bar{\Lambda}$ vertex is obtained from,

$$\frac{d^2\sigma}{du \, d(M^2/s)} = G(u) \cdot s^{\alpha_k(0)-1} \cdot (M^2/s)^{\alpha_k(0)-2\alpha_{\text{eff}}(u)} \tag{3.32}$$

in the usual way (here u is the square of the 4-momentum transfer from K^- to Λ). The values of $\alpha_{\text{eff}}(u)$ as deduced from $4.2 \, \text{GeV}/c$ [132] and $8.25 \, \text{GeV}/c$ [133] with the value of $\alpha_k(0)$ as given above are

$$\alpha_{\text{eff}}(u) = -(0.40 \pm 0.06) + (0.98 \pm 0.07)u, \quad \text{at } 4.2 \, \text{GeV}/c$$

$$\alpha_{\text{eff}}(u) = -(0.43 \pm 0.07) + (0.79 \pm 0.06)u, \quad \text{at } 8.25 \, \text{GeV}/c. \tag{3.33}$$

They are in good agreement with the nucleon trajectory. The analysis at 14.3 GeV/c [141] is also in agreement with the nucleon trajectory.

3.3.3. $\pi^+ \xrightarrow{P} p$ and $\pi^- \xrightarrow{P} \bar{p}$

Finally the effective nucleon trajectory as estimated from the FSASF data† [136] on $\pi^+ \xrightarrow{P} p$ and $\pi^- \xrightarrow{P} \bar{p}$ are -0.50 ± 0.10 and -0.55 ± 0.15 respectively, over the range $u = -0.2$ to -0.6.

3.4. Role of absorptive corrections

The importance of including absorptive cut corrections in the triple Regge analyses has been stressed by several authors [143–146]. However, it is extremely difficult to isolate the absorptive cut effects from the inclusive cross-sections, since they seem to be very similar in shape to the corresponding pole terms [147–149]. As regards the relative magnitudes of the absorptive cut and the pole terms, the existing estimates for the vector–tensor (ρ, A_2, K^*, K^{**}) exchange processes [107, 149] suggest the cut terms to be only about 30% of the corresponding pole terms at small t ($|t| \le 0.4$). On the other hand for pion exchange processes like $p \to \Delta^{++}$, the absorptive cut contribution at small t seems to be relatively more significant [150]. This is analogous to the two-body scattering case, where the absorptive cuts are known to be more significant for pion exchange than for vector–tensor exchanges, at small t.

In order to check the above estimates with the inclusive cross-section data, one needs a reasonable prescription for the size of the Pole term – i.e. the magnitude of the triple Regge coupling $G(t)$. For the pion exchange process $p \xrightarrow{P} \Delta^{++}$, this has been obtained by extrapolation from the near by pion pole [150, 151]. It turns out to be almost a factor of 2 higher than the cross-section data, as one sees from fig. 19 [151]; and the discrepancy can be understood in terms of the absorptive cut correction [150]. For the other exchanges, however, one has no reasonable estimate of the size of the triple Regge pole term. The best test for the adequacy of the pole prescription would be a factorisation test for the two external Reggeons (fig. 1). More precisely one should test if the triple Regge couplings g_{ijk} obtained from different
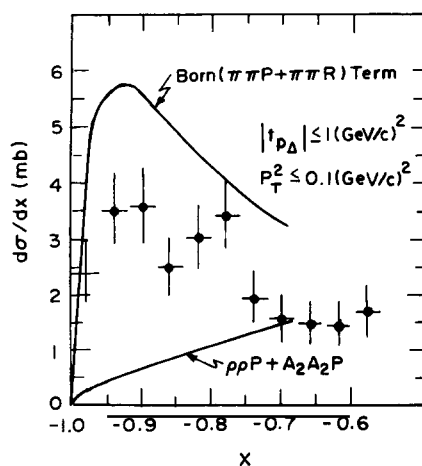
Fig. 3.19. $d\sigma/dx$ distribution for $p \xrightarrow{P} \Delta^{++}$ at 205 GeV/c. The top curve is the total contribution expected from $\pi\pi P$, $\rho\rho P$ and A_2A_2P terms [151].

---

† The FSASF data on the beam fragmentation processes considered in this and the preceding subsections, seems to contain a wealth of information for nondiffractive triple Regge analysis. Unfortunately the data has remained practically unutilised so far (apart from a very sketchy TR analysis by the collaboration [136]), and also inaccessible.

fragmentation vertices $b \rightarrow c$ and the corresponding two-body couplings $(\beta_{bc}^{i})^2$ are equal. Thus one can do a triple Regge factorisation test amongst the π exchange processes $p \rightarrow \Delta^{++}$, $\pi^- \rightarrow \rho^0$ and $\gamma \rightarrow \pi^+$; the ρ, A_2 exchange processes $\pi^- \rightarrow \pi^0$, $K^- \rightarrow K^0$ and $\pi^- \rightarrow \eta$; the nucleon exchange processes $p \rightarrow \pi^+$, $\pi^+ \rightarrow p$ and $K^- \rightarrow \Lambda$ etc. For a meaningful test, of course, one needs data over the FNAL energy range, and preferably a single experiment covering the different beam particles†. In the absence of such data, one may make the following tentative conclusions, on the basis of the absorptive cut calculations mentioned above [149, 150].

Incorporation of absorptive cuts into the triple Regge formalism is not expected to affect the shape of the inclusive cross-sections appreciably. It may alter the magnitude of the pion exchange cross-sections by as much as a factor of 2, whereas for most other processes its effect is expected to be only about 30%, at small t $(|t| < 0.4)$.

3.5. Finite Mass Sum Rules (FMSR)

The formula (2) discussed above is valid only when M^2 is sufficiently large. At low M^2 there will be resonances which are not described by the formula (2). In two body scattering the ideas of duality led to the finite energy sum rules (FESR) which relate the integral over the low energy resonance region to the parameters of the high energy Regge exchange (fig. 20a). A natural extension of the two body scattering to the inclusive reaction is to relate the low M^2 resonance region to the high M^2 triple-Regge
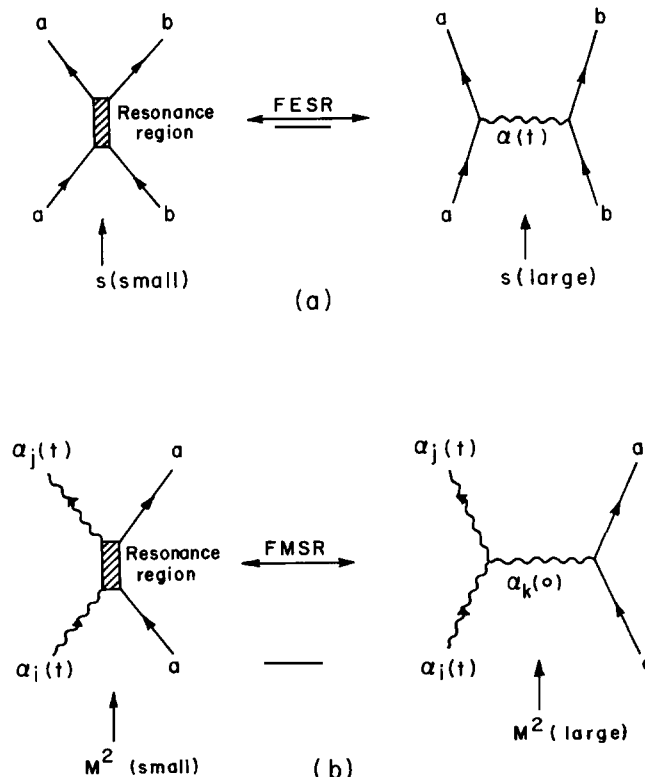
Fig. 3.20. (a) Illustration of duality in particle–particle scattering. (b) Illustration of duality in Reggeon–particle scattering.

† Again the FSASF experiment on beam fragmentation [136] seems to be very well suited for this purpose.

parameters through sum rules for the Reggeon particle scattering amplitude [19–22], (for details see subsection 1.2.2). In this case the dispersing variable is ν ($\nu = M^2 - t - m_a^2$) or the missing mass M^2 rather than the incoming energy s and hence the name finite mass sum rules (FMSR). It essentially means that the large M^2 triple-Regge terms of formula (2) when extrapolated to small M^2 is expected to reproduce in an average sense the low M^2 resonance region (fig. 20b). For the FMSR one needs to consider both the right and left hand cuts of the Reggeon–particle amplitude as in the two-body case. The following FMSR has been derived,

$$
\int_0^x d\nu \cdot \nu^n \left[\frac{d^2\sigma}{dt\, d(M^2/s)} (b \xrightarrow{a} c) + (-1)^{n+1} \cdot \frac{d^2\sigma}{dt\, d(M^2/s)} (c \xrightarrow{a} b) \right]
$$

$$
= \sum_{ijk} G_{ijk}(t) [1 + (-1)^{n+1} \tau_i \tau_j \tau_k] \cdot s^{\alpha_i(t)+\alpha_j(t)-1} \cdot \frac{X^{a(t)+n+1}}{a(t)+n+1} \tag{3.34a}
$$

where, $a(t) = \alpha_k(0) - \alpha_i(t) - \alpha_j(t)$. If a combination which is symmetric in ν is taken for the Reggeon–particle scattering, then the contribution from residues of the nonsense wrong signature fixed poles has to be included in the sum rule. This provides a method of estimating the fixed pole residue which can give some idea on the size of the Regge cuts for two-body scattering. Some attempts have been made [25, 152] to estimate the fixed pole residue which will not be discussed here. However, it is worth mentioning that if the Reggeon–particle scattering is exotic in the s or u channel the fixed pole contribution vanishes for the resonant part of the amplitude.

Several applications [25, 53, 75, 152–156] of FMSR have been made in the study of inclusive reactions, namely to estimate the triple Regge couplings and to relate quasi two-body reactions through superconvergence relations and semi-local duality. The basic hypothesis is the extension of the two component duality of Harari–Freund to Reggeon–particle scattering; this associates the background (BG) and the resonance part (Res) of the missing mass integral with the Pomeron (P) and Reggeon (R) components of the triple-Regge terms respectively. The FMSR can thus be rewritten as,

$$
\int_0^x d\nu\, \nu^n \left[\frac{d^2\sigma^{BG,Res}}{dt\, d(M^2/s)} (b \xrightarrow{a} c) + (-1)^{n+1} \cdot \frac{d^2\sigma^{BG,Res}}{dt\, d(M^2/s)} (c \xrightarrow{a} b) \right]
$$

$$
= \sum_{ijk} G_{ijk}(t) \cdot [1 + (-1)^{n+1} \tau_i \tau_j \tau_k] \cdot s^{\alpha_i(t)+\alpha_j(t)-1} \cdot \frac{X^{\alpha_{P,R}(0)-\alpha_i(t)-\alpha_j(t)+n+1}}{\alpha_{P,R}(0) - \alpha_i(t) - \alpha_j(t) + n + 1}. \tag{3.34b}
$$

3.5.1. Superconvergence relations

It is possible to construct FMSR through a combination of inclusive cross-sections such that the triple Regge term on the right-hand side of eq. (34) vanishes. This is done by writing a linear combination of elastic Reggeon–particle amplitudes which corresponds to exotic quantum number exchange in the $a\bar{a}$ channel. As a result one would get a sum rule involving several resonance production cross-sections.

An attempt was made [154] for a combination of $\rho^{\pm}p$ scattering amplitude through the zeroth-moment sum rule for the difference of $\pi^+ p \to \pi^0 X$ and $\pi^0 p \to \pi^+ X$; from isospin symmetry the cross-sections for $\pi^0 p \to \pi^+ X$ and for $\pi^- p \to \pi^0 X$ are the same. This corresponds to $I = 1$ exchange in the

---

† Again the FSASF experiment on beam fragmentation [136] seems to be very well suited for this purpose.

$\bar{p}p$ channel. In view of the smallness of the non-flip $\rho^0 p\bar{p}$ coupling the triple Regge term in eq. (34) is suppressed. This leads to the following relation,

$$\int dM^2 \left[(d^2\sigma/dt \, dM^2)_{\pi^+ p \to \pi^0 X} - (d^2\sigma/dt \, dM^2)_{\pi^- p \to \pi^0 X} \right] \approx 0. \tag{3.35}$$

The prominent resonances in the ρp channels are N and Δ and therefore eq. (35) can be written as,

$$(d\sigma/dt)_{\pi^+ p \to \pi^0 \Delta^{++}} - (d\sigma/dt)_{\pi^- p \to \pi^0 n} - (d\sigma/dt)_{\pi^- p \to \pi^0 \Delta^0} \approx 0. \tag{3.36}$$

Using the isospin symmetry in eq. (36) yields the following relation,

$$(d\sigma/dt)_{\pi^+ p \to \pi^0 \Delta^{++}} = \tfrac{3}{2}(d\sigma/dt)_{\pi^- p \to \pi^0 n}. \tag{3.37}$$

The experimental result at 8 GeV/c is shown in fig. 21 and it is seen that the relation (37) is well satisfied by the data.

Applying identical consideration to $K^- p \to \bar{K}^0 X$, one gets the relation,

$$(d\sigma/dt)_{K^- p \to \bar{K}^0 n} = 2(d\sigma/dt)_{K^- p \to \bar{K}^0 \Delta^0} \tag{3.38}$$

which seems to be satisfied equally well by the 13 GeV/c data for the two processes [155], as shown in fig. 22.

Another superconvergent relation has been written [25] by taking the combination of the $\rho\pi$
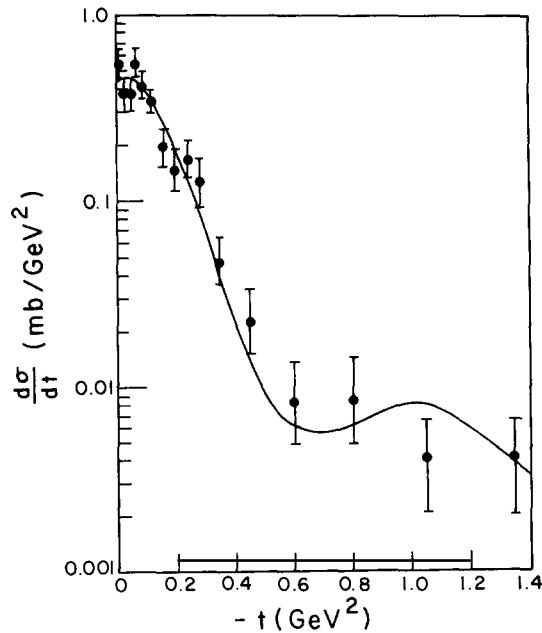
Fig. 3.21. $d\sigma/dt$ versus t for $\pi^+ p \to \pi^0 \Delta^{++}$ at 8 GeV/c. The solid curve refers to $\tfrac{3}{2} d\sigma/dt$ for $\pi^- p \to \pi^0 n$ at the same momentum [154].
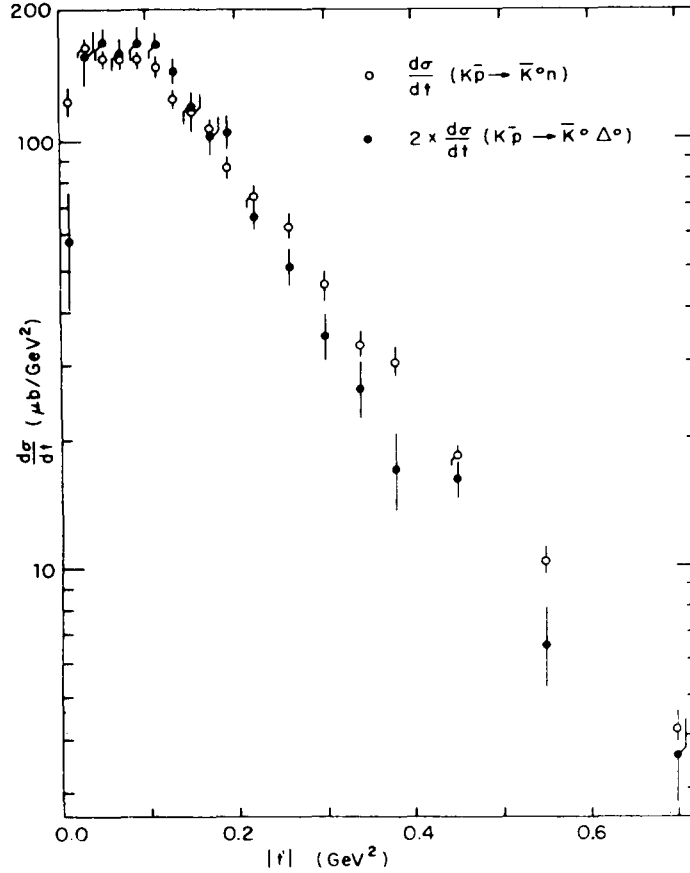
Fig. 3.22. Test of superconvergence relation: $(d\sigma/dt)_{K^-p\to\bar{K}^0n} = 2(d\sigma/dt)_{K^-p\to\bar{K}^0\Delta^0}$.

amplitudes as,

$$A_{\rho^-\pi^+} + A_{\rho^+\pi^+} - 2A_{\rho^0\pi^+} \tag{3.39}$$

which corresponds to a pure $I = 2$ exchange in the crossed $\pi\pi \to \rho\rho$ channel. From this the following first-moment sum rule has been derived for the natural parity exchange in π^-p interactions,

$$(-t)\frac{d\sigma}{dt}(\pi^-p\to\pi^0n) + (m_{A_2}^2 - t - m_\pi^2)\frac{d\sigma}{dt}(\pi^-p\to A_2^0n) = (m_\omega^2 - t - m_\pi^2)\frac{d\sigma}{dt}(\pi^-p\to\omega n). \tag{3.40}$$

The experimental result at $7\,\text{GeV}/c$ is shown in fig. 23. The agreement between the left-hand and the right-hand side of the eq. (40) is very good.

3.5.2. Semi-local duality

Semi-local duality suggest that the leading Regge exchange in Reggeon–particle scattering when extrapolated to low M^2 values will yield in an average sense the resonance contributions. The averaging is to be done on resonance contributions over a typical range of $\sim 1\,\text{GeV}^2$. From eq. (34b) one can
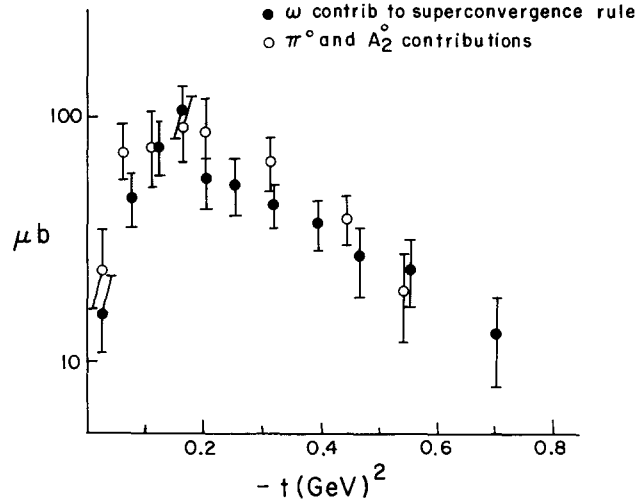
Fig. 3.23. Test of superconvergence relation (40) at 7.5 GeV/c [25].

therefore write the average resonance production cross-section as,

$$\left\langle \frac{d\sigma^{Res}}{dt \, dM^2} \right\rangle \sim (M^2)^{\alpha_R(0)-2\alpha_i(t)}.$$ (3.41)

This clearly brings out the dependence of the resonance production cross-section on resonance mass for a given exchange trajectory α_i at fixed s and t. Similarly, the background contribution [153, 156] will be given by replacing $\alpha_R(0)$ by $\alpha_P(0)$ in eq. (41). There are four important cases where the semi-local duality has been successfully tested [25, 75, 157–165]: (a) forward production of meson resonances, (b) ratio of unnatural to natural parity exchange, (c) antishrinkage in resonance production, and (d) backward production of meson resonances.

(a) *Forward production of meson resonances*:
To test eq. (41) it is necessary to isolate a particular exchange trajectory $\alpha_i(t)$. For the reactions,

$$\pi^- + p \to (\rho^0, f^0, g^0)n$$ (3.42a)

$$K^- + p \to (K^{*0}, K^{**0})n$$ (3.42b)

it is known from the energy dependence and density matrix measurements that the π-exchange dominates these production cross-sections at small t. Since the crossed channel Reggeon–particle scattering is exotic in the above cases the contribution from fixed poles vanishes and therefore eq. (34b) can be written for both odd and even n,

$$\int_0^x d\nu \, \nu^n \frac{d\sigma_\pi^{Res}}{dt \, dM^2} [\pi^-(K^-)p \to X^0 n] = f(t) \cdot s^{2\alpha_\pi(t)-2} \cdot X^{0.5-2\alpha_\pi(t)+n+1}$$ (3.43)

where $\alpha_R(0)$ is taken as 0.5. In figs. 24 and 25 are shown the experimental values for reactions (42a) and
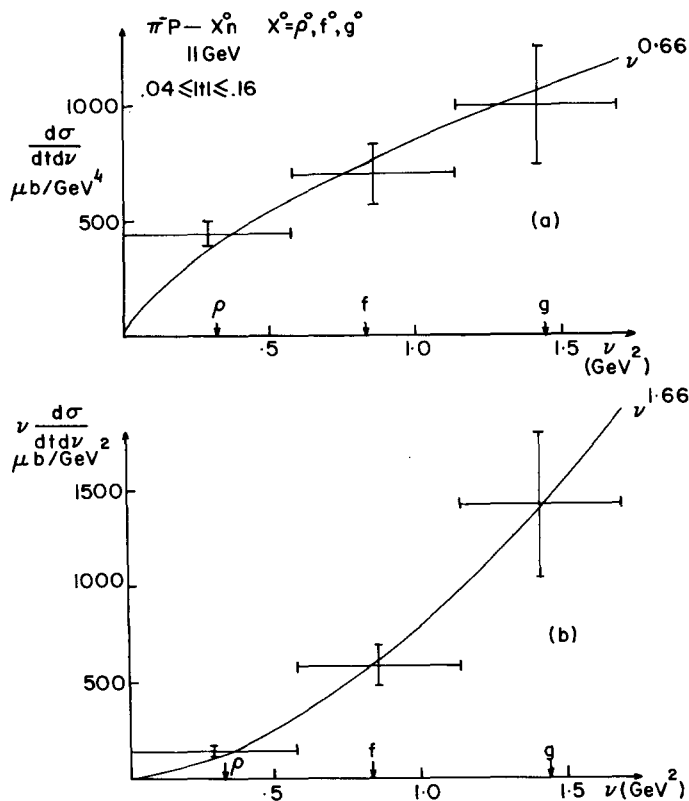
Fig. 3.24. The zeroth and the first moment of the double differential cross-section of $\pi^- p \to (\rho^0, f^0, g^0)n$ at 11 GeV/c for $0.04 < |t| < 0.16$. The solid curves are the expected distributions from π exchange [25].
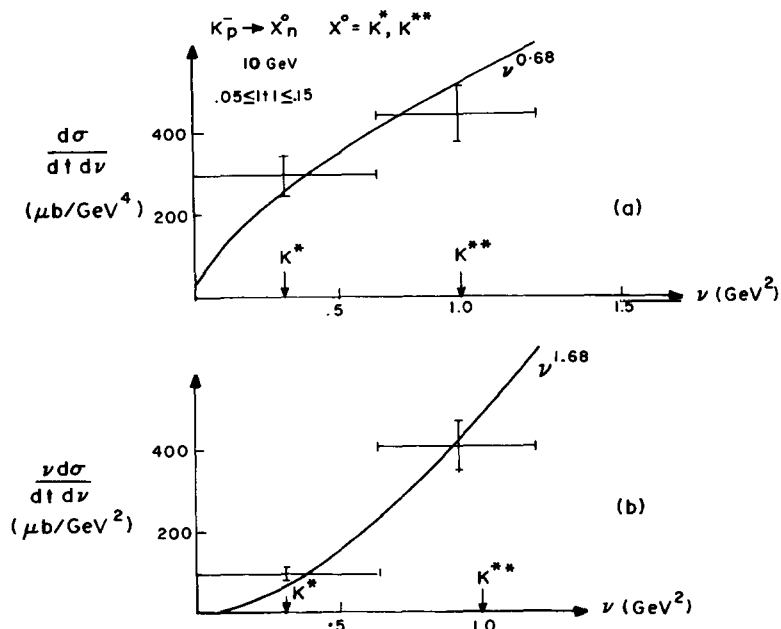
Fig. 3.25. The zeroth and the first moment of the double differential cross-section of $K^- p \to (K^*, K^{**})n$ at 10 GeV/c for $0.05 \le |t| \le 0.15$. The solid curves are the expected distributions from π exchange [25].

(42b) and are compared with the Regge contribution [25]. From the figures it is concluded that semi-local duality works very well. The resonances produced through f, ω exchanges are also in agreement with semi-local duality.

(b) *Ratio of unnatural to natural parity exchange*:

Eq. (41) can be rewritten in terms of the ratio of exchange contributions due to natural and unnatural parity Regge poles as

$$R = (d\sigma/dt)_{UNP}/(d\sigma/dt)_{NP} \sim (M^2)^{2(\alpha_N(t)-\alpha_U(t))} \sim M^2 \tag{3.44}$$

for low $|t|$ values because $\alpha_N(0) \approx 0.5$ and $\alpha_U(0) \approx 0.0$; i.e. unnatural parity exchanges dominates the production of higher mass resonances.

In fig. 26 is shown the ratio NP/UNP, i.e. $1/R$, for the reactions

$$\pi^+ + p \rightarrow \rho^0 + [\Delta^{++}(1236), \Delta^{++}(1880)]$$

$$\rightarrow \omega + [\Delta^{++}(1236), \Delta^{++}(1880)] \tag{3.45}$$

at 7.1 GeV/c. The dotted curves in the figure for $\Delta^{++}(1880)$ have been obtained [157] by using relation (44) from the solid curves which describe the production of $\Delta^{++}(1236)$.
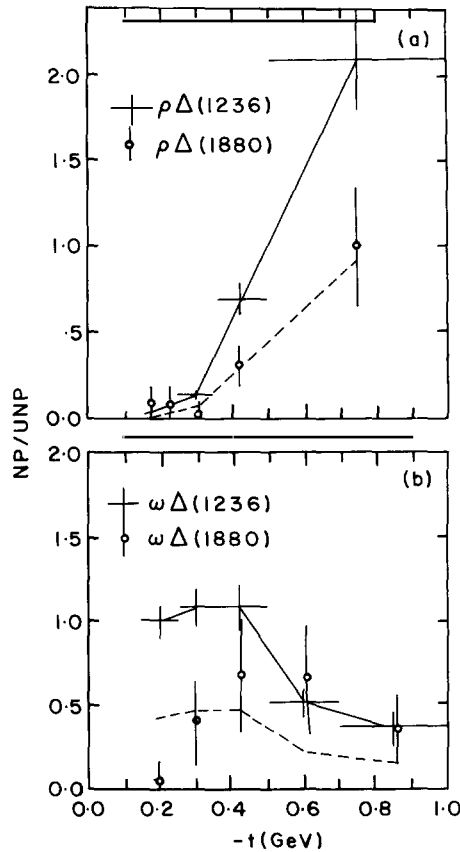
Fig. 3.26. NP/UNP for $\Delta^{++}(1236)$ and $\Delta^{++}(1880)$ in association with (a) ρ^0 and (b) ω from π^+p reactions. The solid lines represent eyeball fits to the $\Delta^{++}(1236)$ reactions and the dotted lines represent the predictions for the $\Delta^{++}(1880)$ reactions.
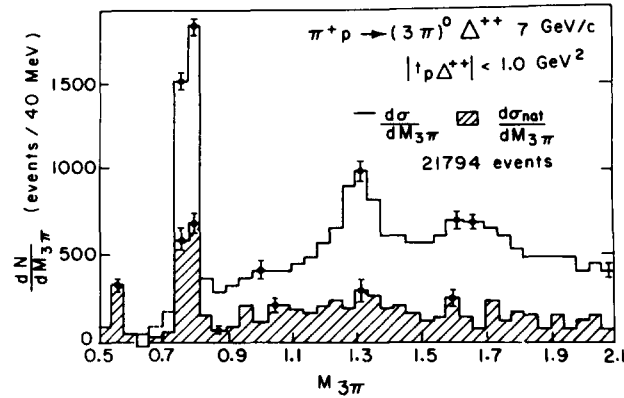
Fig. 3.27. Natural and unnatural parity contributions to the production of ω, A_2 and $\omega^*(1670)$ from $\pi^+ p \to (3\pi)^0 \Delta^{++}$ at 7 GeV/c.

Fig. 27 shows the natural and unnatural parity contributions to ω, A_2^0 and $\omega^*(1670)$ production from the reaction

$$\pi^+ + p \to (3\pi)^0 + \Delta^{++}$$

(3.46)

at 7 GeV/c [158]. The suppression of the natural to unnatural parity ratio with increasing resonance mass is clearly visible.

Fig. 28 shows the ratio R for the production of ω, A_2^0 and $\omega^*(1670)$ from the reaction,

$$\pi^- + p \to (\pi^+ \pi^- \pi^0) + n$$

(3.47)
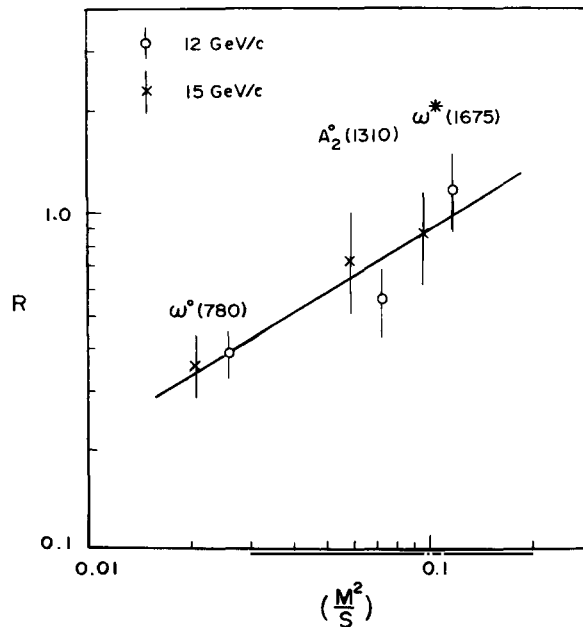
Fig. 3.28. The ratio R = UNP/NP as a function of M^2/s for ω, A_2^0 and ω^* production from $\pi^- p$ reactions.

at 12 and 15 GeV/c [159]. From this CERN OMEGA spectrometer data the difference between the unnatural and natural exchange trajectories has been found to be,

$$\alpha_N(t) - \alpha_U(t) = (0.50 \pm 0.17) + (0.62 \pm 0.55)t. \tag{3.48}$$

(c) *Antishrinkage in resonance production*:
The t-dependence of eq. (41) can be written as

$$d\sigma/dt \sim \exp\{(B - 2\alpha_i' \ln M^2)t\} \tag{3.49}$$

i.e., one expects a logarithmic antishrinkage with the increasing resonance mass. There are clear indications of this antishrinkage in all the resonance production data mentioned above. The best data for a quantitative comparison, is of course the high statistics CERN OMEGA spectrometer data [159], shown in fig. 29.

(d) *Backward production of meson resonances*:
The backward production of meson resonances, namely in $\pi \xrightarrow{p} p$, would lead us to study Reggeised antibaryon–baryon scattering which according to duality should proceed via baryonium
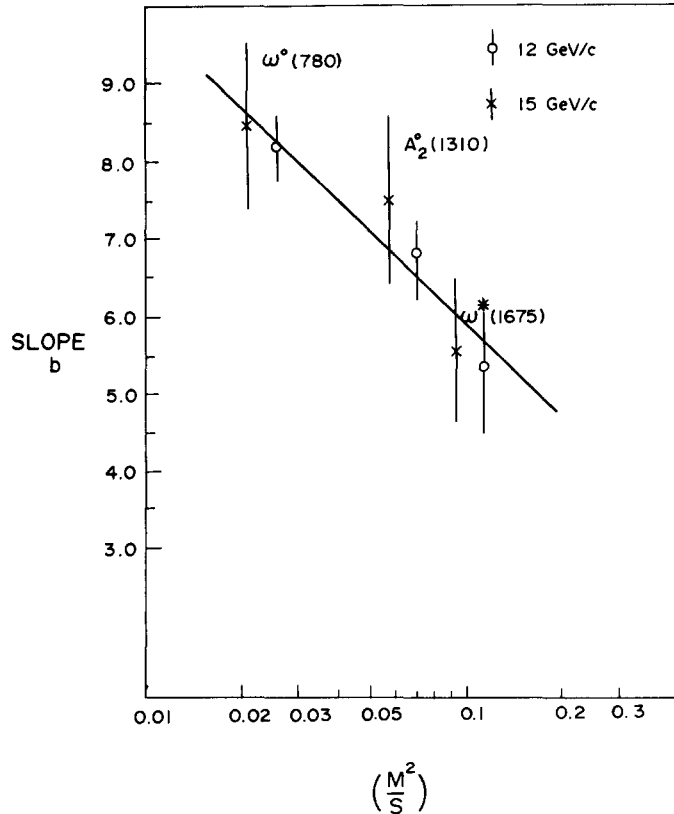
Fig. 3.29. The slope $b(=B - 2\alpha' \ln M^2/s)$ as a function of M^2/s for ω, A_2^0 and ω^* production from π^-p reactions.

exchange. Such an attempt was made [75] by studying the reaction,

$$\pi^- + p \to p + X^-$$ (3.50)

where the leading exchange in the $\pi^- \bar{p}$ vertex is the $\bar{\Delta}$. According to eq. (41) the background and resonance parts should behave like $(M^2)^{1-2\alpha_\Delta(u)}$ and $(M^2)^{\alpha_B(0)-2\alpha_\Delta(u)}$. From the actual behaviour of the resonance production cross-section the value of $\alpha_B(0)$ has been estimated. The experimental values of the resonance production cross-section at 16 GeV/c is shown in fig. 30 for $u \approx -0.2$ (the value of α_Δ at $u \approx -0.2$ is ≈ 0). The background is consistent with the M^2 dependence, whereas the resonance part behaves like $(M^2)^{-0.5}$. The fit to the resonance data yielded $\alpha_B(0) = -0.5 \pm 0.3$ for the dual trajectory which is very much lower than the intercept of the normal meson trajectory of $+0.5$. This analysis lends support to the duality idea that the meson resonances in baryon–antibaryon scattering are dual to exotic exchange. Similar analyses of the experimental data for $K^-(\pi^-) \xrightarrow{\text{p}} \Lambda$ are also consistent with the above conclusion.

3.6. Summary

In this section we presented the triple Regge analysis of the inclusive reactions $b \xrightarrow{a} c$ to see to what extent the expected leading Regge trajectories can account for the missing-mass-square distributions. We have stressed on those reactions where the system $ab\bar{c}$ is exotic; this leads to the dominance of the Pomeron term over the meson term in the $a\bar{a}$ vertex and hopefully one can ignore the latter contribution in the first approximation. The following conclusions can be drawn from the experimental data:

(i) The expected dominance of the π trajectory is seen in the inclusive cross-section $\rho_{00} \, d^2\sigma/dt \, dM^2$ for the reaction $\pi^- \xrightarrow{\text{p}} \rho^0$ at 15 GeV/c. The dominance of the pion trajectory is also seen in the Δ^{++} production from proton fragmentation. It is interesting to note that the energy dependence of the
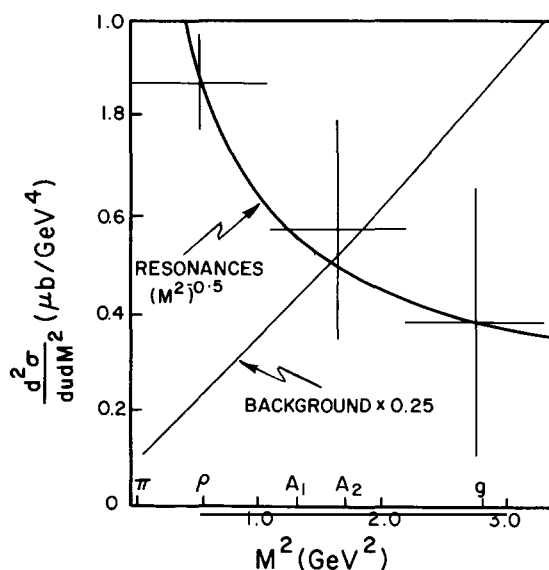
Fig. 3.30. Resonance and background cross-sections for $\pi^- p \to pX^-$ at 16 GeV/c. The fitted curve to the resonance corresponds to $\alpha_R(0) = -0.5$ and to the background it corresponds to $\alpha_R(0) = 1.0$ [75].

two-body cross-sections of $pp \to \Delta^{++}\Delta^0$ and $pp \to \Delta^{++}n$ reveals the dominance of the π-exchange up to about 400 GeV in agreement with the inclusive data; and beyond 400 GeV the dominance of ρ, A_2 exchanges are seen.

(ii) There is a strong indication from the inclusive data of $\pi^\pm \xrightarrow{P} \pi^0, \eta$ at 100 GeV/c that the ρ and A_2 trajectories flatten off ≈ -0.5 for $|t| \gtrsim 1 \, (\text{GeV}/c)^2$. The A_2 trajectory as deduced from two-body reaction $\pi^- p \to \eta n$ in the range 15 to 40 GeV also shows a break in the trajectory from linearity beyond $|t| > 0.7 \, (\text{GeV}/c)^2$, whereas the ρ trajectory as deduced by the same group from $\pi^- p \to \pi^0 n$ does not show any deviation from linearity up to $|t| = 2.0 \, (\text{GeV}/c)^2$ in disagreement with the inclusive data $\pi^\pm \xrightarrow{P} \pi^0$.

(iii) The effective kaon trajectory as deduced from $p \xrightarrow{a} \Lambda$ lies between K and K^* trajectories. For the strangeness annihilation process of the type $K^- + 'K^{+'} \to$ pions in the reaction $p \xrightarrow{K^-} \Lambda$ the leading trajectory coupling to the $K\bar{K}$ vertex is consistent with the exchange degenerate ϕ-f' trajectory.

(iv) The baryon trajectory has been deduced from $p \xrightarrow{a}$ mesons and $K \xrightarrow{P}$ strange baryons. In the low energy region ($p_{\text{lab}} \lesssim 20 \, \text{GeV}/c$) the effective baryon trajectories as obtained from the former reaction are much lower than the expected leading trajectories, whereas in the latter case they are in good agreement with the expected leading trajectories. The new data at ISR energies for $p \xrightarrow{P} \pi^+$ and $p \xrightarrow{P} K^+$ are in good agreement with the nucleon and the $\Lambda(\Sigma)$ trajectory respectively, but the problem still exists with the ISR data of $p \xrightarrow{P} \pi^-$ where the trajectory intercept is still much below the expected Δ trajectory.

In general the absorptive corrections are neglected in the TR analysis. The need for it is seen through the reaction $p \xrightarrow{P} \Delta^{++}$ which is dominated by the π exchange. It is interesting to note that the inclusion of absorptive corrections changes only the normalization and therefore it is difficult to isolate its effects. The best way to look for these effects seems to be through the triple Regge factorisation test between different fragmenting vertices. For this purpose beam fragmentation data over the FNAL energy range, covering several beam particles, would be highly useful. In the absence of such data one may tentatively conclude on the basis of specific cut calculations, that at small t the cuts have about a 30% effect in vector–tensor exchange and a somewhat larger effect in π exchange processes.

We have discussed some of the applications of the FMSR through which the utility of the low M^2 resonance region becomes clear, in an average sense, in the TR analysis. There exist good evidences for semi-local duality and in a special case like Reggeised antibaryon–baryon scattering the analysis led to the determination of the intercept of the Baryonium trajectory.

4. Polarization in inclusive reactions

It was realised pretty early in the inclusive game that the single and triple Regge analyses described earlier for the unpolarized cross-sections can be extended to the polarization measurements. Moreover the polarization measurements can give information on the underlying Regge exchanges, which are not accessible to the unpolarized cross-sections. Thus there has been a long standing theoretical interest in the inclusive polarization [166, 167]. It was only during the last 4–5 years, however, that inclusive polarization data of any significance has emerged. Of course, the polarization data is still very fragmentary and mostly restricted to the low energy region.

The formalism and the predictions for the inclusive polarization are described in the following subsection. In the next two subsections we compare these predictions with the inclusive polarization data – first

for Λ-polarization, where most of the available data is concentrated; and then for the remaining data. The last one summarises the essential results.

4.1. Formalism and predictions

We shall concentrate on the aspects of polarization formalism, which are relevant to the analysis of the available data. A more detailed account of the formalism can be found in refs. [106, 107, 168]. We shall restrict to the polarization measurements with spin $\frac{1}{2}$ particles. It is convenient to define the spin projections λ_a, λ_b, λ_c along the transversity axis $\hat{n}$, which is normal to the production plane, i.e.

$$\hat{n} = p_a \times p_c / |p_a \times p_c|.$$ (4.1)

Then the polarization of the detected particle P_c is defined as

$$P_c \sigma = \frac{1}{(2s_a + 1)(2s_b + 1)} \sum_{\lambda_a \lambda_b} [\sigma^{\uparrow\uparrow}_{\lambda_a\lambda_b,\lambda_a\lambda_b} - \sigma^{\downarrow\downarrow}_{\lambda_a\lambda_b,\lambda_a\lambda_b}]$$ (4.2)

where the first and the second terms are simply the measured inclusive cross-sections with the spin of the detected particle c lying along and opposite to the transversity axis. More precisely, in terms of the production amplitude f shown in fig. 1a, we have

$$\sigma^{\lambda_c\lambda_c}_{\lambda_a\lambda_b,\lambda_a\lambda_b} = \frac{1}{16\pi s} \sum_x |f^x_{\lambda_c,\lambda_a\lambda_b}(s, t, M^2)|^2.$$ (4.3)

(a)   (b)

(c)   (d)
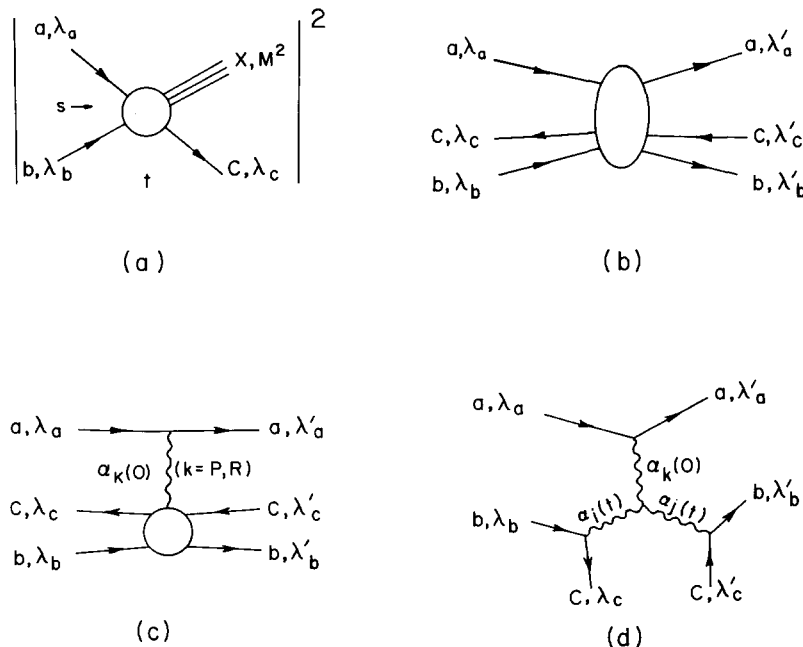
Fig. 4.1. (a) Inclusive cross-section for specific spin projection; (b) the corresponding 3-body Mueller amplitude; (c) single Regge expansion of the Mueller amplitude; (d) triple Regge expansion.

In this notation, the unpolarized inclusive cross-section

$$\sigma = s \frac{d\sigma}{dt\, dM^2} = \frac{1}{(2s_a + 1)(2s_b + 1)} \sum_{\lambda_a \lambda_b \lambda_c} \sigma^{\lambda_c \lambda_c}_{\lambda_a \lambda_b, \lambda_a \lambda_b}$$

$$= \frac{1}{16\pi s(2s_a + 1)(2s_b + 1)} \sum_{\lambda_a \lambda_b \lambda_c} \sum_x |f^x_{\lambda_c, \lambda_a \lambda_b}(s, t, M^2)|^2. \tag{4.4}$$

Similarly the polarization asymmetries for the incident particles are defined as

$$P_a \sigma = \frac{1}{2(2s_b + 1)} \sum_{\lambda_b \lambda_c} [\sigma^{\lambda_c \lambda_c}_{\uparrow \lambda_b, \uparrow \lambda_b} - \sigma^{\lambda_c \lambda_c}_{\downarrow \lambda_b, \downarrow \lambda_b}] \tag{4.2a}$$

$$P_b \sigma = \frac{1}{2(2s_a + 1)} \sum_{\lambda_a \lambda_c} [\sigma^{\lambda_c \lambda_c}_{\lambda_a \uparrow, \lambda_a \uparrow} - \sigma^{\lambda_c \lambda_c}_{\lambda_a \downarrow, \lambda_a \downarrow}]. \tag{4.2b}$$

With the simultaneous polarization measurements of the incident and the detected particles one can construct additional polarization parameters R, R', A, A' and D [106, 168], which shall not be discussed here.

Now, Mueller's optical theorem for the inclusive cross-section with specific spin projections (eq. (3)) gives

$$F_{\lambda_a \lambda_b \lambda_c, \lambda_a \lambda_b \lambda_c} = \sum_x |f^x_{\lambda_c, \lambda_a \lambda_b}(s, t, M^2)|^2 \tag{4.5}$$

where F is the M^2 discontinuity of the forward 3-body amplitude for ab$\bar{c}$ (fig. 1b). Substituting this in eqs. (2, 2a, 2b, 3) give

$$P_c \sigma = \frac{1}{16\pi s(2s_a + 1)(2s_b + 1)} \sum_{\lambda_a \lambda_b} [F_{\lambda_a \lambda_b \uparrow, \lambda_a \lambda_b \uparrow} - F_{\lambda_a \lambda_b \downarrow, \lambda_a \lambda_b \downarrow}] \tag{4.6}$$

$$P_a \sigma = \frac{1}{16\pi s \cdot 2(2s_b + 1)} \sum_{\lambda_b \lambda_c} [F_{\uparrow \lambda_b \lambda_c, \uparrow \lambda_b \lambda_c} - F_{\downarrow \lambda_b \lambda_c, \downarrow \lambda_b \lambda_c}] \tag{4.6a}$$

$$P_b \sigma = \frac{1}{16\pi s \cdot 2(2s_a + 1)} \sum_{\lambda_a \lambda_c} [F_{\lambda_a \uparrow \lambda_c, \lambda_a \uparrow \lambda_c} - F_{\lambda_a \downarrow \lambda_c, \lambda_a \downarrow \lambda_c}]. \tag{4.6b}$$

It is useful to rewrite these amplitudes in the more familar notation of helicity frame (s-channel). Using

$$|\uparrow\rangle = \frac{1}{\sqrt{2}}(-i|+\rangle + |-\rangle)$$

$$|\downarrow\rangle = \frac{1}{\sqrt{2}}(-|+\rangle + i|-\rangle) \tag{4.7}$$

where $\pm$ refer to helicity projection $\pm\frac{1}{2}$, give

$$P_c\sigma = \frac{-i}{16\pi s(2s_a + 1)(2s_b + 1)} \sum_{\lambda_a\lambda_b} [F_{\lambda_a\lambda_b^+,\lambda_a\lambda_b^-} - F_{\lambda_a\lambda_b^-,\lambda_a\lambda_b^+}] \tag{4.8}$$

$$P_a\sigma = \frac{i}{16\pi s \cdot 2(2s_b + 1)} \sum_{\lambda_b\lambda_c} [F_{+\lambda_b\lambda_c,-\lambda_b\lambda_c} - F_{-\lambda_b\lambda_c,+\lambda_b\lambda_c}] \tag{4.8a}$$

$$P_b\sigma = \frac{i}{16\pi s \cdot 2(2s_a + 1)} \sum_{\lambda_a\lambda_c} [F_{\lambda_a^+\lambda_c,\lambda_a^-\lambda_c} - F_{\lambda_a^-\lambda_c,\lambda_a^+\lambda_c}]. \tag{4.8b}$$

Finally the unpolarized cross-section is given by

$$\sigma = \frac{1}{16\pi s(2s_a + 1)(2s_b + 1)} \sum_{\lambda_a\lambda_b\lambda_c} F_{\lambda_a\lambda_b\lambda_c,\lambda_a\lambda_b\lambda_c}. \tag{4.9}$$

The single Regge and triple Regge expansions for $F_{\lambda_a\lambda_b\lambda_c,\lambda_a'\lambda_b'\lambda_c'}$, valid over the b-fragmentation region $(b \xrightarrow{a} c)$ and large M^2, are illustrated in figs. 1c and 1d. It is evident from these figures and eq. (8a), that polarization at the nonfragmenting vertex (P_a) corresponds to the forward helicity flip coupling $\beta_{+-}^{P,R}(0)$; and hence it should vanish identically for a factorising pole exchange $(\beta_{+-}^{pole}(t) \propto \sqrt{t})$. This was first pointed out by Abarbanel and Gross [166]. We shall see below, however, that one expects interesting polarization (P_a) effects arising from Regge cuts, as first suggested by Phillips, Ringland and Worden [167]. In contrast, the polarizations at the fragmenting vertex (P_c, P_b) are expected to get finite contributions from the single and triple Regge pole exchange diagrams. In fact, it has been suggested on the basis of absorptive cut calculations [107], that the dominant contribution to these polarizations are expected to come from pole exchange. Therefore it is appropriate to discuss the polarization predictions for the fragmenting and the nonfragmenting vertices separately.

4.1.1. Polarizations at the fragmenting vertex

Let us first look at the single Regge predictions. It is evident from the discussions of sections 1 and 2 that the exchange degeneracy and the Pomeron factorisation properties of the 3-body amplitude are expected to hold for the individual helicity configurations – i.e. for $F_{\lambda_a'\lambda_b'\lambda_c',\lambda_a\lambda_b\lambda_c}$ of fig. 1c. As a result one has the following predictions for P_b and P_c, which should be valid over the bulk of the b-fragmentation region – i.e. excluding the vicinity of $|x| = 1$ (low M^2).

(1) For exotic processes (abc̄ exotic and bc̄ nonexotic), the polarizations $P_{b,c}$ should be independent of energy and also independent of the incident particle 'a' [167]. Interesting examples are the target polarization asymmetry P_b in

$$p \xrightarrow{p,K^+,\pi^+} \pi^- \quad \text{and} \quad p \xrightarrow{p,K^+,\pi^+} \Lambda$$

and the recoil Λ polarization P_c for the latter set of reactions. It may be added that the kinematic scale breaking effects are expected to cancel out, at least partly, from the ratios P_b and P_c.

(2) At a given energy, the polarizations $P_{b,c}$ are expected to be independent of 'a' for a set of nonexotic reactions too, where the relative Reggeon to Pomeron contributions are predicted to be approximately equal by the exchange degeneracy and the 2-body coupling relations of table 2.3. These are, of course, the processes, for which the normalised cross-sections were predicted to be equal, in reasonable agreement with data (see section 2). Notable examples are

$$p \xrightarrow{\pi^-, K^-, \bar{p}} \pi^- \quad \text{and} \quad p \xrightarrow{\pi^-, K\bar{N}A, \bar{p}} \Lambda$$

where NA refers to the strangeness nonannihilation component. In particular, there is a reasonable amount of Λ polarization data now for the latter set of processes, with which the predicted equality can be tested. Finally one may note that, using f–Pomeron proportionality as a crude first approximation (which may be meaningful, since the polarization data are rather crude), would suggest the polarization for the above nonexotic processes to be roughly independent of energy.

(3) The annihilation component $p \xrightarrow{K\bar{A}} \Lambda$ is also expected to have an energy independent polarization. Let us now proceed to the triple Regge analysis. The triple Regge diagram of fig. 1d gives

$$F_{\lambda'_a \lambda'_b \lambda'_c, \lambda_a \lambda_b \lambda_c} = [\beta^j_{\lambda'_c \lambda_b} \beta^i_{\lambda_c \lambda_b} \xi^*_j \xi_i + \beta^i_{\lambda'_c \lambda_b} \beta^j_{\lambda_c \lambda_b} \xi^*_i \xi_j] \cdot \beta^k_{\lambda'_a \lambda_a} g_{ijk} \left(\frac{s}{M^2}\right)^{\alpha_i + \alpha_j} \cdot (M^2)^{\alpha_k(0)}. \tag{4.10}$$

Substituting this in eqs. (8, 8b, 9), one gets

$$P_c \sigma = \frac{1}{16\pi s(2s_a+1)(2s_b+1)} \sum_{\lambda_b} [\beta^j_{+\lambda_b} \beta^i_{-\lambda_b} - \beta^j_{-\lambda_b} \beta^i_{+\lambda_b}] \cdot 2\text{Im}\,\xi^*_j \xi_i \sum_{\lambda_a} \beta^k_{\lambda_a \lambda_a} g_{ijk} (s/M^2)^{\alpha_i + \alpha_j} (M^2)^{\alpha_k(0)} \tag{4.11}$$

$$P_b \sigma = \frac{1}{16\pi s \cdot 2(2s_a+1)} \sum_{\lambda_c} [\beta^j_{\lambda_c+} \beta^i_{\lambda_c-} - \beta^j_{\lambda_c-} \beta^i_{\lambda_c+}] \cdot 2\text{Im}\,\xi^*_j \xi_i \sum_{\lambda_a} \beta^k_{\lambda_a \lambda_a} \cdot g_{ijk} (s/M^2)^{\alpha_i + \alpha_j} \cdot (M^2)^{\alpha_k(0)} \tag{4.12}$$

$$\sigma = \frac{1}{16\pi s(2s_a+1)(2s_b+1)} \sum_{\lambda_b \lambda_c} \beta^j_{\lambda_c \lambda_b} \beta^i_{\lambda_c \lambda_b} \cdot 2\text{Re}\,\xi^*_j \xi_i \cdot \sum_{\lambda_a} \beta^k_{\lambda_a \lambda_a} \cdot g_{ijk} (s/M^2)^{\alpha_i + \alpha_j} (M^2)^{\alpha_k(0)}. \tag{4.13}$$

Further, parity invariance relates the 2-body helicity couplings

$$\beta^i_{\lambda \lambda'} = \eta^i (-1)^{\lambda - \lambda'} \beta_{-\lambda - \lambda'} \tag{4.14}$$

where $\eta^i(=\pm 1)$ is the naturality of the trajectory.

From eqs. (11, 12, 14) one sees that the polarized cross-sections $P_{b,c}\sigma$ vanish in each of the following situations:

(i) if α_i and α_j have opposite naturality;

(ii) if α_k has unnatural parity;

(iii) if α_i and α_j have the same phase, including the particular $i = j$;

(iv) if the two couplings are exchange degenerate, in particular if

$$\beta^i_{+-}/\beta^i_{++} = \beta^j_{+-}/\beta^j_{++}.$$

The first two conditions, of course, hold for the unpolarized cross-section σ as well. Thus there are no natural–unnatural parity interference terms in either the unpolarized or the polarized cross-section; and one can write eqs. (11–14) as

$$P_c \sigma = P^N \sigma^N + P^U \sigma^U \tag{4.15}$$

$$P_b \sigma = P^N \sigma^N - P^U \sigma^U \tag{4.16}$$

$$\sigma = \sigma^N + \sigma^U. \tag{4.17}$$

If the polarizations P_b and P_c are equal (opposite), it means the polarized cross-sections are dominated by natural (unnatural) parity exchanges. We may add here that one can also estimate the relative size of the two exchanges in σ, if one knows the double polarization parameter [106, 168]

$$D = (\sigma_N - \sigma_U)/(\sigma_N + \sigma_U). \tag{4.18}$$

In contrast to the first two conditions, the conditions (iii) and (iv) are complimentary to those for the unpolarized cross-sections, as enumerated in the last section. In particular the polarized cross-sections get contribution only from the $i \neq j$ terms; and therefore provide a useful probe for these interference terms.

One interesting example is the target polarization asymmetry in $p_\uparrow \xrightarrow{P} p$. Here the dominant triple Regge contributions to $P_b \sigma$ at large x are expected to come from the interference terms $\rho P \rho$ and $A_2 P A_2$ [106, 169]. Thus the target polarization asymmetry data for $p_\uparrow \xrightarrow{P} p$, should be helpful for the triple Regge analysis of diffraction, to be discussed in the next section. Unfortunately the quality of data so far available is too poor to be of any practical help.

A second and phenomenologically more significant example is $p \xrightarrow{P} \Lambda$, for which we have reasonable data on recoil Λ polarization P_c. The process being exotic, one expects only Pomeron exchange in the $a\bar{a}$ channel. The main natural and unnatural parity contributions to the unpolarized cross-section, as discussed in the last section, are

$$\sigma^N \to K^* K^* P, K^{**} K^{**} P$$

$$\sigma^U \to KKP, K^A K^A P. \tag{4.19}$$

The corresponding contributions for the polarized cross-section are

$$P^N \sigma^N \to K^* K^{**} P$$

$$P^U \sigma^U \to KK^A P, KK^B P. \tag{4.20}$$

However, the $K^* K^{**} P$ term vanishes for an SU(3) singlet Pomeron; and it should also be suppressed by the condition (iv). The same arguments apply to the $KK^B P$ term. Therefore, it is reasonable to neglect these terms in eq. (20), so that the dominant contribution to the polarized cross-section $P_c \sigma$ comes from $KK^A P$. It then follows trivially from eqs. (11–20) that

$$P_\Lambda \propto \frac{C'_U (M^2)^{-2\alpha_K}}{C_U (M^2)^{-2\alpha_K} + C_N (M^2)^{-2\alpha_K}} \propto \frac{C'_U}{C_U + (C_N/M^2)} \tag{4.21}$$

i.e. the recoil Λ polarization is expected to go down with decreasing M^2 (increasing $|x|$). This is evidently a significant triple Regge prediction, which can be checked with the available P_Λ data.

4.1.2. Polarization at the nonfragmenting vertex

As noted earlier, the polarization at the nonfragmenting vertex P_a corresponds to helicity flip coupling at the a$\bar{a}$ vertex (fig. 1c), and hence it is predicted to vanish at moderate M^2 for factorising pole exchanges [166]. This is analogous to the 2-body reactions $\gamma p \to \pi^+ n$, $pn \to np$ and $\pi^- p \to \rho^0 n$, where a factorising pion pole exchange is required to vanish in the forward direction, as it corresponds to helicity flips at the two vertices†. None-the-less, the reactions are known to show forward pion exchange peaks; and they have been successfully accounted for by the absorptive cut model (πP cut) [170]. This has led Phillips, Ringland and Worden [167] to suggest a finite polarization at the nonfragmenting vertex P_a, arising from absorptive cuts. Since Pomeron (and also f, ω) have negligible helicity flip coupling the dominant contribution to P_a is expected to come from the absorptive ρ cut (ρP cut). This immediately leads to the 2 predictions below.

(1) Energy dependence − At fixed M^2/s (or x)

$$P_a \propto s^{-1/2}. \tag{4.22}$$

(2) Mirror symmetry −

$$P_a(b \xrightarrow{p} c) = -P_a(b \xrightarrow{n} c)$$

and

$$P_a(\pi^+ \xrightarrow{p} \pi^+) = -P_a(\pi^- \xrightarrow{p} \pi^-) \tag{4.23}$$

where the latter prediction follows from G parity − i.e. a ρ, coupling to the $p\bar{p}$ vertex, requires an odd number of ρ to couple to the $\pi\pi$ system (fig. 1c). This prediction is phenomenologically significant, since there is some proton polarization data for $\pi^\pm \xrightarrow{p} \pi^\pm$. Further, there has been predictions of the M^2/s (or x) dependence of $P_a(\pi^\pm \xrightarrow{p} \pi^\pm)$ corresponding to various absorptive cut diagrams in the triple Regge region. We shall simply reproduce the diagrams along with the corresponding x and s dependence from the works of Paige and Sidhu [107] (fig. 2a) and of Soffer and Wray [171] (fig. 2b). They exhibit explicitly, of course, the energy dependence and the mirror symmetry properties mentioned above.

4.2. The Λ-polarization data

There is a significant amount of polarization data available now for inclusive Λ production, since the Λ polarization is easily measured through its decay distribution. These are presented below, and compared with the Mueller−Regge predictions.

4.2.1. Energy and x dependence

(1) Let us first consider the exotic process

$$p \xrightarrow{p} \Lambda.$$

---

† Note that angular momentum conservation requires the overall helicity flip to be zero in the forward direction. This can be achieved through a compensation between the two helicity flips, but only for a nonfactorising exchange mechanism.
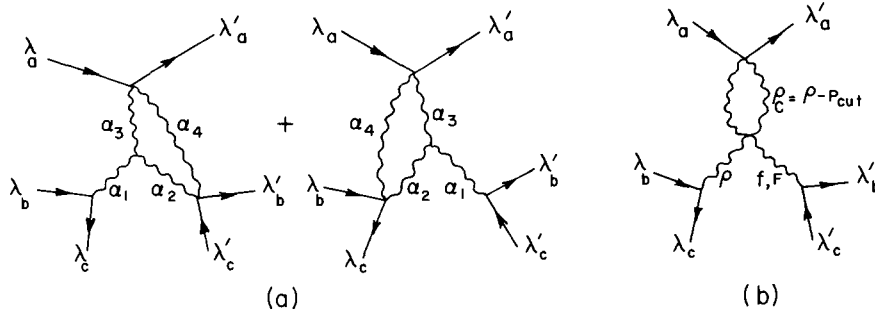
Fig. 4.2. Absorptive ρ-cut contribution to the polarization at the nonfragmentating vertex $\pi^\pm \xrightarrow{p\uparrow} \pi^\pm$. The diagrams (a) and (b) are considered in refs. [107] and [171] respectively.

The recoil Λ polarization data at $6\,\text{GeV}/c$ [172] and $19\,\text{GeV}/c$ [173] are shown as a function of x in fig. 3c. It is seen to be energy independent, in agreement with the Mueller–Regge prediction. This is also evident from fig. 4, which shows the energy dependence of polarization integrated over $x = -1$ to -0.8. There is, of course, very little polarization outside this region. The corresponding value for P_Λ in $p \xrightarrow{K^+} \Lambda$, which is also exotic, is -0.1 ± 0.3 from the $32\,\text{GeV}/c$ data [174]. Unfortunately, the uncertainty is too large to make a meaningful test of the factorisation prediction.

One may compare the observed x dependence of fig. 3c, with the triple Regge prediction of eq. (21). There seems to be a clear discrepancy here – whereas P_Λ is predicted to go down with decreasing M^2 (i.e. $|x| \to 1$) the data shows the opposite trend. The discrepancy is particularly intriguing since the corresponding unpolarized cross-section was seen to be in reasonable agreement with the triple-Regge prediction (section 3). Hence it calls for a more detailed investigation. The $6\,\text{GeV}/c$ data [172] measures simultaneously the target proton and the recoil Λ polarizations. For the triple Regge region of interest $(x = -1$ to $-0.8)$ it gives [175]

$$P_c = 0.42 \pm 0.08, \qquad P_b = -0.21 \pm 0.07, \qquad D = -0.39 \pm 0.21 \tag{4.24}$$

which corresponds, via eqs. (15–18), to

$$P^N = 0.11 \pm 0.06, \qquad P^U = 0.32 \pm 0.06, \qquad \sigma^N/\sigma^U = 0.44 \pm 0.22. \tag{4.25}$$

Thus it suggests that unnatural parity exchanges dominate not only the polarized cross-section (eq. (20)), but the unpolarized one (eq. (19)) as well – i.e. $C_U \gg C_N$ in eq. (21). Consequently one expects only a marginal decrease of P_Λ towards $|x| \to 1$. But it still cannot account for the increase towards $|x| \to 1$, seen
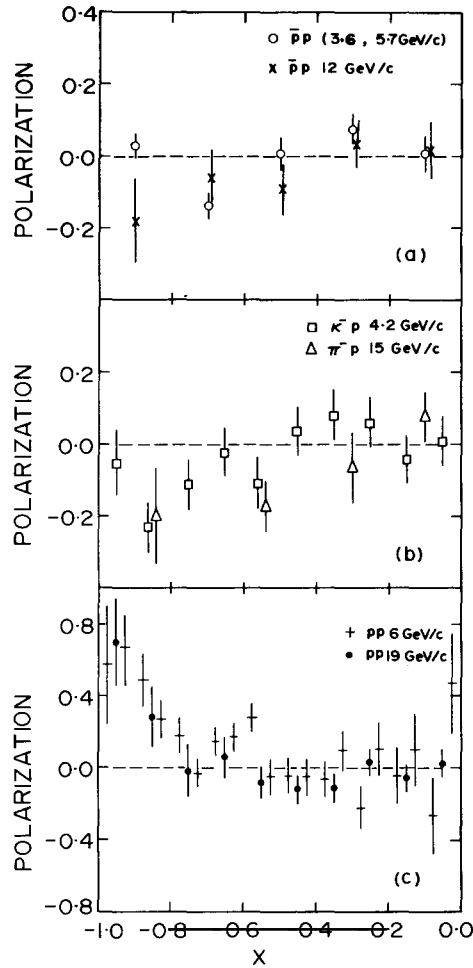
Fig. 4.3. The dependence of the polarization of Λ on x is shown for: (a) $\bar{p}p$ data at 3.6, 5.7, 12 GeV/c; (b) K^-p (nonannihilation) data at 4.2 GeV/c, π^-p at 15 GeV/c; (c) pp data at 6 and 19 GeV/c.

for the P_Λ data of fig. 3c. Moreover, the discrepancy cannot be accounted for by the absorptive cuts, at least in its simple form considered so far [107] since they give extremely small polarization ($P_\Lambda < 5\%$). Thus the inclusive polarization data seems to suggest that the cuts are significant and qualitatively different from the simplest absorption prescription. One may note an interesting parallel with 2-body reactions like $\pi^-p \to \pi^0n$, which shows substantial polarization, in disagreement with the simplest pole or pole plus absorptive cut model predictions; and on the basis of which identical conclusions have been drawn [170, 176].

(2) Let us next consider the nonexotic processes

$$p \xrightarrow{\pi^-, K\bar{N}\Lambda, \bar{p}} \Lambda.$$

As discussed in subsection 4.1.1 above, these polarizations are expected to be roughly equal. This seems to be in agreement with the Λ polarization data for $\bar{p}p$ [177, 178, 180], π^-p [179] and K^-p
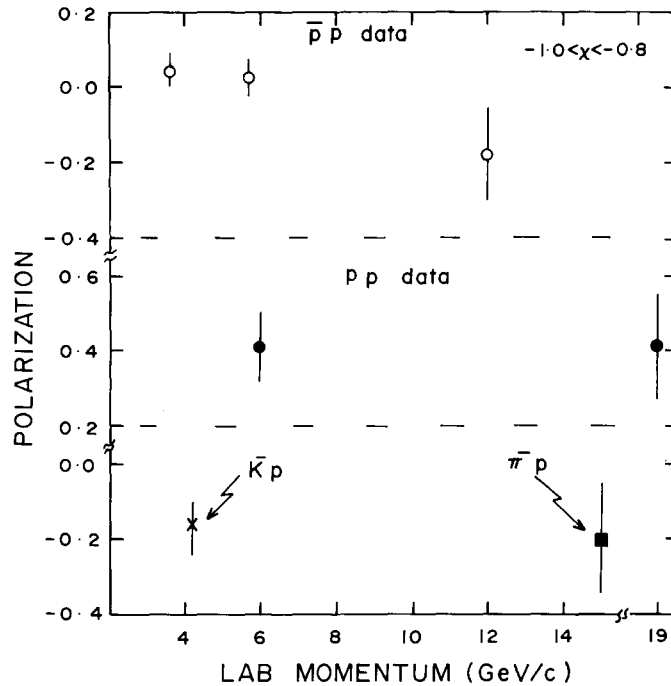
Fig. 4.4. The energy dependence of the polarization is shown for the region $-1.0 < x < -0.8$ from $\bar{p}p$, pp, K^-p (strangeness nonannihilation) and π^-p data.

(nonannihilation) [180] shown in figs. 3(a, b) and 4. In this context, it is worth noting that these polarizations are very different from those of $p \xrightarrow{p} \Lambda$ (fig. 3) and of $p \xrightarrow{K\bar{\Lambda}} \Lambda$ (fig. 5). Within the limited energy range and the rather large uncertainties associated with these polarization data, they are consistent with a rough energy independence. As regards the x dependence, the quality of data is evidently too poor here to make any meaningful comparison with the triple Regge predictions.
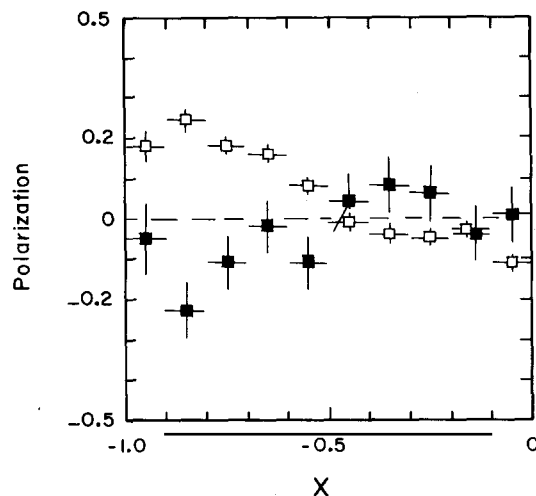
Fig. 4.5. The P_Λ versus x plot for the strangeness annihilation process $K^- + p \rightarrow \Lambda + pions$ and strangeness nonannihilation process $K^- + p \rightarrow \Lambda + K\bar{K} + pions$ at 4.2 GeV/c: $\square$ and $\blacksquare$ for strangeness annihilation and nonannihilation respectively.

(3) Let us finally consider the strangeness annihilation process

$$p \xrightarrow{K\bar{\Lambda}} \Lambda.$$

Unfortunately the separation between the strangeness annihilation and nonannihilation components has been done only with the 4.2 GeV/c data [180]. The two components are shown in fig. 5; and are evidently very different. The corresponding polarized cross-sections are shown against M^2 in fig. 6. The annihilation component is seen to be dominated by the resonances π, ρ, ω, f, A_2. It is tempting to identify this feature with the duality prediction that the annihilation component, corresponding to ϕ exchange, is dual to these normal resonances, whereas the nonannihilation component is dual to ϕ, f' and the background.

Since, the annihilation and the nonannihilation components of

$$p \xrightarrow{K^-} \Lambda$$

have not been separated in the higher energy data [174, 181–185], the net Λ polarization is shown against P_{lab} in fig. 7a. There is a discernible decrease in P_Λ and perhaps a change of sign in going from 4 to 32 GeV/c; which can be understood as follows. As discussed in subsection 4.1.1 above, the annihilation and the nonannihilation component are each expected to give a roughly energy in-dependent polarization. However, their signs are opposite, as one sees from the 4.2 GeV/c data $-P_\Lambda^A \simeq 0.2$ and $P_\Lambda^{NA} \simeq -0.2$. Now, the nonannihilation component is rapidly increasing with energy – it is about 10% at 4.2 GeV/c and 60% at 32 GeV/c. One therefore expects the net polarization P_Λ to show a decrease from 0.2 to a slightly negative value over this range; which seems to be in agreement with data. In concluding this analysis we should stress the need for separating the strangeness annihilation components in these $p \xrightarrow{K^-} \Lambda$ data [174, 181–185].

(4) Fig. 7b shows the momentum dependence of P_Λ from kaon fragmentation

$$K^- \xrightarrow{p} \Lambda$$

from the above experiments [174, 180–185], for the corresponding triple Regge region $x > 0.8$. The
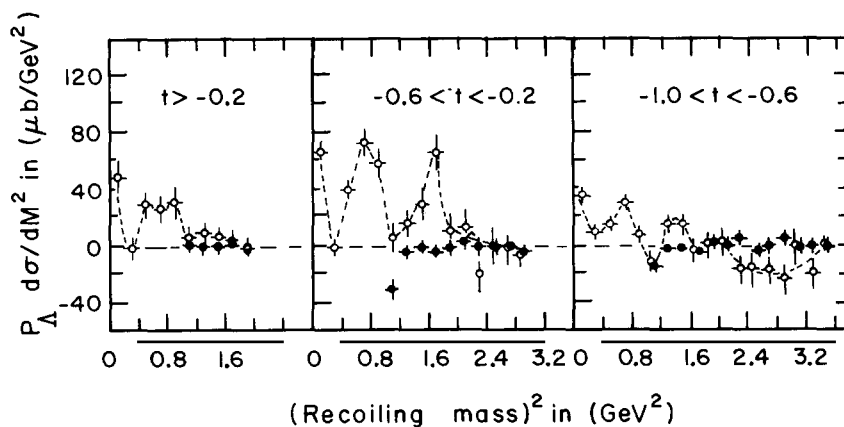
Fig. 4.6. $P_\Lambda \, d\sigma/dM^2$ versus M^2; $\bigcirc$ and $\bullet$ for strangeness annihilation and nonannihilation respectively, for $p \xrightarrow{K^-} \Lambda$.
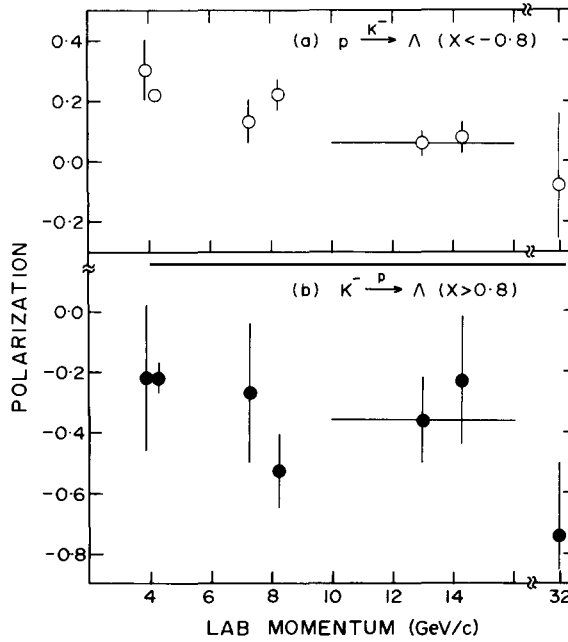
Fig. 4.7. The momentum dependence of P_Λ from $K^- + p \to \Lambda + X$: (a) with $x < -0.8$ and (b) with $x > 0.8$.

leading triple Regge terms expected are, of course, $\bar{N}_i \bar{N}_j P$ and $\bar{N}_i \bar{N}_j R$. However, the line reversed process $K^+ \xrightarrow{\text{p}} \bar{\Lambda}$, corresponding to the triple Regge term $N_i N_j P$ (since it is exotic), seems to have much smaller cross-section [182]. Thus one may expect the process $K^- \xrightarrow{\text{p}} \Lambda$ to be dominated by the Reggeon exchange term alone and hence an energy independent polarization [182]. This seems to be consistent with the data, within their rather large uncertainties. For the line reversed process $K^+ \xrightarrow{\text{p}} \bar{\Lambda}$, polarization measurements exist at 13 GeV/c [186] and 32 GeV/c [174]. For $x > 0.3$, the values of $P_{\bar{\Lambda}}$ are -0.3 ± 0.2 and -0.4 ± 0.2 respectively – i.e. independent of energy, again within large uncertainties.

4.2.2. p_T dependence

The recoil Λ polarization for the target fragmentation region $(x < -0.2)$ is plotted against its transverse momentum in fig. 8, for

$$p \xrightarrow{\text{p,}\bar{\text{p}}\text{,}\pi^-\text{,}K\bar{N}\Lambda} \Lambda.$$

This includes the 24 GeV/c pp data and ISR data at $\sqrt{s} = 53, 62$ GeV/c [187] in addition to those discussed earlier. For the sake of comparison, the P_Λ data from nuclear targets [188–190] are also shown in the same figure. The P_Λ data from the strangeness annihilation process

$$p \xrightarrow{K\bar{\Lambda}} \Lambda$$

is shown separately in fig. 9.

All these P_Λ data evidently show strong p_T dependence, as first pointed out in ref. [189]. One can, however, see some striking similarity amongst the strangeness nonannihilation processes shown in fig. 8.
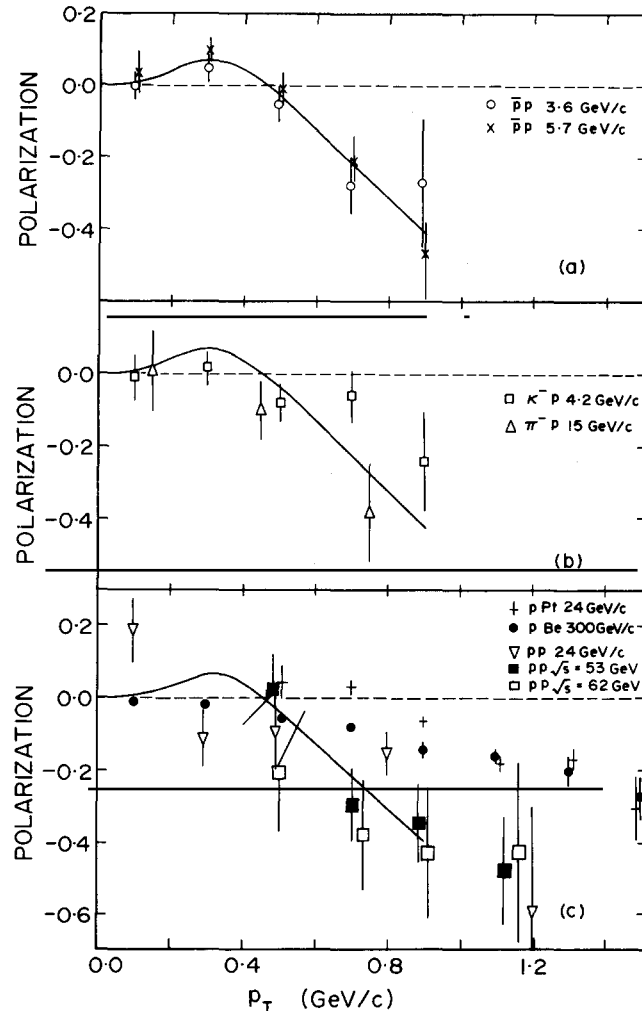
Fig. 4.8. The Λ polarization is shown as a function of the transverse momentum of Λ from: (a) p̄p data at 3.6 and 5.7 GeV/c; (b) K⁻p (strangeness nonannihilation) at 4.2 GeV/c and π⁻p at 15 GeV/c; (c) pp data at 24 GeV/c and √s = 53, 62 GeV/c along with the pPt data at 24 GeV/c and pBe data at 300 GeV/c. The smooth curve represents the trend of the combined p̄p data at 3.6 and 5.7 GeV/c.

For small $p_T(<0.4)$ all the polarizations are small except for pp. More strikingly, they all become increasingly negative at large p_T; and in fact for $p_T > 0.4$, all the P_Λ data on proton target seem to have roughly the same shape and magnitude irrespective of the type and energy of the incident particle. The nuclear target data show a similar trend but a weaker p_T dependence than the proton target data. This is perhaps understandable, since the nuclear effects, in general, decrease the polarization.

As regards theoretical interpretation of the above systematics, one realises, of course, that the Mueller–Regge model is of little use here. Firstly the Regge models have little predictive value for the p_T dependence (i.e. t dependence), which is hidden in the residue functions; and secondly they are not reliable at large p_T any way. An empirical model has been suggested to explain these polarizations at high energies, using diquarks as dynamical entities [191]. In this model the Λ polarization stems from the production mechanism of the s-quark, the structure of Λ being $(ud)_0 s$, where the $(ud)_0$ pair
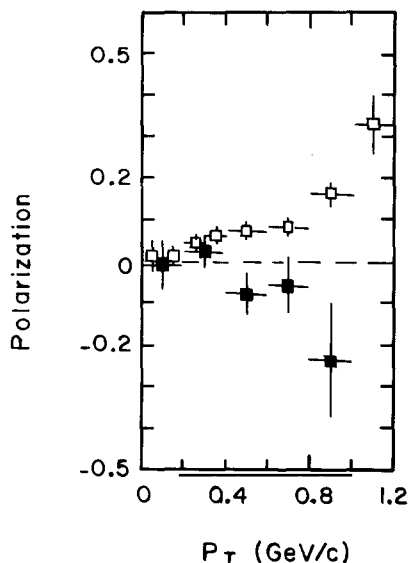
Fig. 4.9. P_Λ versus p_T for the strangeness annihilation □ and nonannihilation ■ components in p $\xrightarrow{K^-}$ Λ.

corresponds to $I = S = 0$. This model predicts the Λ-polarizations of approximately the correct magnitude. But the insensitivity of the Λ-polarization on incident energy, as observed experimentally from 3.6 GeV/c to the ISR energies, will be difficult to account for in this model.

4.3. Other polarization data

We discuss here the limited inclusive polarization data available for processes other than Λ production.

4.3.1. $p_\uparrow \xrightarrow{p} p$

The target polarization asymmetry P_b data available for this process at 6 GeV/c [192] is shown in fig. 10. As discussed in subsection 4.1.1 above, this provides a useful probe for the interference terms between diffractive and nondiffractive exchanges (i.e. the triple Regge terms $\rho P \rho$ and $A_2 P A_2$) [169]. As we see from this figure the polarization is rather small (essentially consistent with zero) over the triple Regge region of interest. This is consistent with the triple Regge analysis of the p $\xrightarrow{p}$ p cross-section, discussed in the next section, which suggests the nondiffractive contribution to be dominated by pion exchange and hence a negligible interference term between the two. For a quantitative estimate of the interference term, of course, one needs polarization data at higher energies and of substantially higher precision.

4.3.2. $\pi^\pm \xrightarrow{p\uparrow} \pi^\pm$

The target polarization asymmetry P_a available for this process at 8 GeV/c [193] is shown in fig. 11. This is the polarization effect at the nonfragmenting vertex, discussed in subsection 4.1.2, which is extremely interesting, as it probes the effect of cuts in inclusive reaction. The data seems to agree with the mirror symmetry prediction of the ρ-cut models (eq. (23)). It should be noted, however, that nonzero polarization is seen essentially at a single mass point (apart from the elastic point, of course). It
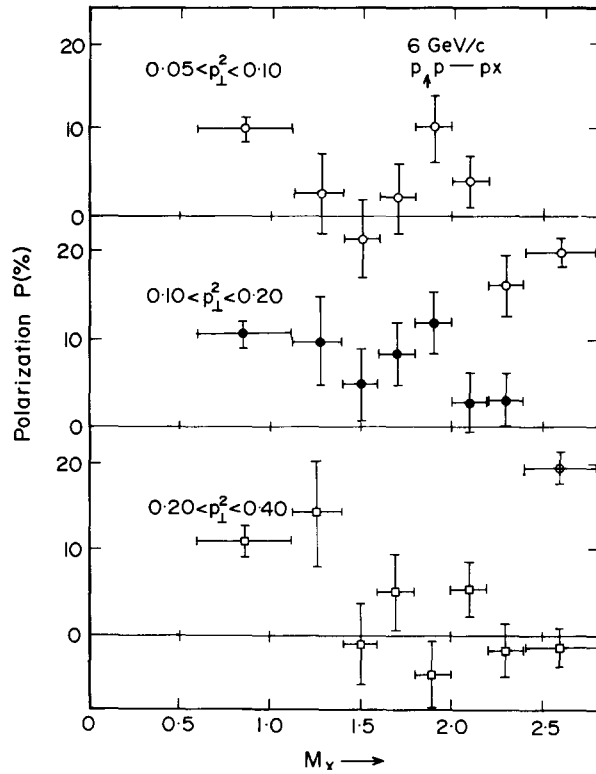
Fig. 4.10. The target polarization asymmetry data for $p_\uparrow \xrightarrow{p} p$ at 6 GeV/c [192]. The lowest mass (M_X) point is the elastic polarization.
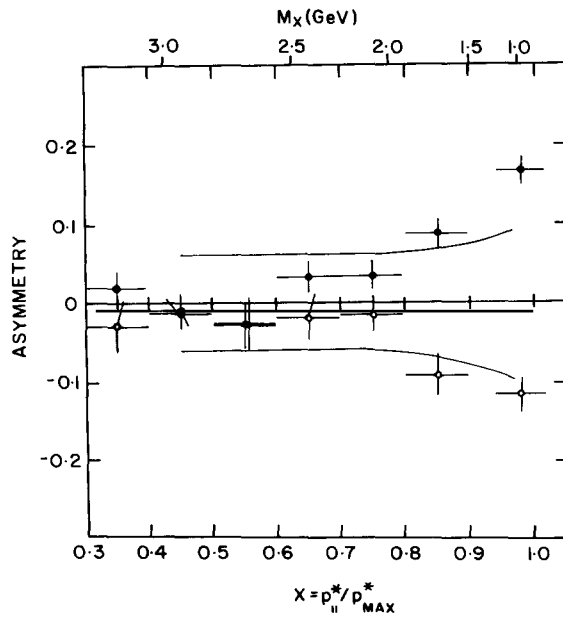
Fig. 4.11. Results on asymmetry P_a of the inclusive reactions $\pi^\pm + p(\uparrow) \to \pi^\pm$ at 8 GeV/c [193]. Data points ● for $\pi^+ p \to \pi^+$, ○ for $\pi^- p \to \pi^-$; ▲ and □ for elastic points in π^+ and π^-. Curves in the figure correspond to ref. [171] as shown in fig. 4.2 (b).

should be emphasised that nonzero polarization for the elastic or the individual resonance contributions in the missing mass channel do not imply Regge cut exchange. It is only when these individual resonance contributions to P_a are additive, does it imply (via duality) a finite polarization effect building up at large M^2, and hence Regge cut exchange [167]. To check this point it is essential to have data with finer mass resolution. It is equally important to have data at higher energies in order to check the $s^{-1/2}$ energy dependence (eq. (22)), predicted by the ρ-cut exchange†. The three features mentioned above (mirror symmetry, no significant oscillations in M^2 and $s^{-1/2}$ energy dependence) are common to all absorptive ρ-cut graphs. In contrast the predicted x distribution are very different for different graphs as shown in fig. 2. Thus a precise x-distribution data would be able to distinguish between the contending graphs. In short, the available data on P_a gives an encouraging hint for ρ-cut exchange; but it is essential to have more detailed data for a convincing answer.

4.4. Summary

Let us summarise the essential features of the inclusive polarization data.

(1) The recoil Λ polarization for the exotic process $p \xrightarrow{P} \Lambda$ is independent of energy, in agreement with the Mueller–Regge prediction. However, the x-dependence seems to be in striking disagreement with the triple Regge prediction; and it seems it cannot be resolved by including absorptive Regge cuts. This point is evidently very significant; and it needs further experimental and phenomenological investigation.

(2) The recoil Λ polarization for the $p \xrightarrow{\bar{p}, \pi^-, K\bar{N}} \Lambda$ data seem to be roughly equal, as implied by factorisation, exchange degeneracy and the 2-body coupling relations. The agreement is particularly impressive when one contrasts the P_Λ for the above processes with those for $p \xrightarrow{P} \Lambda$ or the strangeness annihilation process $p \xrightarrow{K\bar{A}} \Lambda$. In this context, it seems desirable to separate the annihilation and nonannihilation components in the $p \xrightarrow{K^-} \Lambda$ data, which is presently available only at 4.2 GeV/c.

(3) There seems to be a striking empirical systematics in the p_T dependence of the Λ polarization. All the P_Λ data on proton target (except for the strangeness annihilation process $p \xrightarrow{K\bar{A}} \Lambda$) have roughly the same shape and size for $p_T > 0.4$, irrespective of the energy and type of the incident particle. The P_Λ data on nuclear targets also show a similar behavior, but the p_T dependence is less steep.

(4) The limited polarized target asymmetry data available for $p_\uparrow \xrightarrow{P} p$ is consistent with negligible interference between diffractive and nondiffractive exchanges – i.e. the triple Regge terms $P\rho\rho$ and $PA_2A_2 \simeq 0$.

(5) The limited polarized target asymmetry data available for the nonfragmenting vertex $\pi^\pm \xrightarrow{p\uparrow} \pi^\pm$ gives an encouraging hint for the ρ-cut exchange; but it is essential to have a more detailed data for a convincing answer.

5. Triple Regge analysis (diffraction)

This section is devoted to a detailed triple Regge analysis of diffractive excitation and extraction of the relevant triple Regge terms PPP and PPR. Of course, these triple Regge exchanges are known to be of special theoretical significance for a number of reasons.

---

† It should be pointed out in this context that the vanishing of P_a for factorising pole exchange has been proved only for the leading order term in s [166, 167].

(1) It is important to know whether a finite triple Pomeron term exists, since it is the first nontrivial step in the multiple Pomeron exchange, as suggested by the t-channel Regge picture of diffraction.

(2) It is equally important to know whether the triple Pomeron term PPP (if it exists) vanishes at $t = 0$, as required in the conventional pole or weak cut models of Pomeron [56, 64] (see subsection 1.4.3).

(3) The relative magnitudes of the PPP and PPf couplings would be able to distinguish between the predictions of ref. [36] ($G_{PPf} \ll G_{PPP}$) based on topological considerations, and ref. [50] ($G_{PPf} = G_{PPP}$) based on f-P proportionality (see subsections 1.3.4 and 1.4.2).

(4) One can also find out if the diffractively produced resonances are dual to PPP as predicted by the topological considerations [36] or to PPf as predicted by f-P proportionality [50].

(5) Finally the knowledge of PPP and PPR parameters are useful in estimating the diffractive contribution to the pionisation cross-section and more importantly to correlation, as we shall see in the last two sections.

5.1. Earlier results

Naturally the triple Regge phenomenology of diffraction has received a good deal of attention from the very beginning. Some of the early works are listed in refs. [194–197]. But a detailed quantitative analysis was possible only after the arrival of the FNAL and ISR data [198–203] on

$$pp \rightarrow pX. \tag{5.1}$$

No single experiment of this lot was adequate, however, for a complete triple Regge analysis. Moreover, there were significant inconsistency problems between them – in particular between the Columbia–Stonybrook data [203] and the others. Hence the triple Regge analyses were necessarily based on compilations of different data; and there were significant quantitative disagreements [169, 204–208], arising from one's choice of the input data. Thus two global data fits by Field and Fox [169] and by Roberts and Roy [208] gave significantly different results – i.e. a PPP coupling significantly larger (smaller) than PPR for the RR (FF) fits (fig. 4) – since the FF fit included the C-S data, whereas it was excluded in the RR fit, in view of its inconsistency with the other data†. The disagreement was particularly serious at small $|t|$, where the only high energy data available at this stage were the bubble data of refs. [200–202], apart from the C-S counter data. This disagreement was reflected, of course, in the corresponding estimates of the diffractive cross-section rise (table 4). None-the-less a near unanimity had been reached at this stage about such general features, as the presence of a sizeable scaling component PPP and the PPP coupling not vanishing at $t = 0$ [169, 204–208].

There have been several experimental developments in the subsequent years, which seem to support the RR solution rather strongly. Firstly the C-S collaboration have extended their data to a wider range of s and t, which enables them to do a complete triple Regge analysis with their own data [209]. And the result is exactly the opposite of all the other experiments – i.e. inelastic diffraction is completely saturated by the nonscaling component PPR. Their result is compared with those of RR and FF fits in table 1 below. It clearly illustrates the incompatibility of the C-S result with that of the other experiments and helps one to understand the quantitative discrepancy between RR and FF solutions.

---

† Although there were other minor differences between the two fits, we have checked that the disagreement was almost entirely due to the C-S data.

Table 5.1
Break up of the diffraction peak ($|x| > 0.9$) at 300 GeV/c

	PPP	PPR	Nondiffraction background
RR [208]	75%	15%	10%
FF [169]	51%	34%	15%
C-S [209]	0%	64%	36%

In fact the M^2 dependence observed in the C-S experiment† is even steeper than the PPR, a more satisfactory description being given by the empirical formula

$$\frac{d\sigma}{dt\,dM^2} = 6.3\,e^{6.3t}\left[\frac{15 \pm 0.5}{s} + \frac{2.9 \pm 0.1}{M^{3.7\pm0.1}}\right]. \tag{5.2}$$

Secondly there have been two other counter experiments at FNAL – the DRRF [210] and the FSASF [211] experiments – each of which suggest a dominant PPP cont. at small t. The DRRF experiment has a rather restricted range of t and x for a complete TR analysis, and also their normalisation has some quantitative problem as we shall discuss later. On the other hand, the FSASF experiment covers the relevant range of t and x; and is adequate for a complete TR analysis even though its energy range is limited (essentially 70–140 GeV/c).

5.2. Detailed fit to the FSASF data and comparison with earlier data

We have done a detailed triple Regge fit to the FSASF data along with 24 GeV/c data of the BHM bubble chamber [212] and the CERN counter [213] groups‡. The PS data (24 GeV/c) has been added as a check on the energy dependence; but the essential result – i.e. the separation of the PPP and PPR components – follows from the x dependence of the FSASF data alone, as we shall see below.

The TR diagram for the reaction (1) is shown in fig. 1. Since the formalism has been described in detail in sections 1 (subsection 1.2.2c,d) and 3, it need not be repeated here. We should simply note that a meaningful separation of the PPP and PPR components requires the use of the FMSR integrals, since the FNAL data has a limited energy range. For it is clear from eq. (8) below, that such a separation requires analysing the diffractive peak ($\nu/s \simeq 1 - x < 0.05$) over either a large range of s (i.e. going down to the PS energy) or a large range of ν/s (going down to 0.01–0.02 say). In either case one hits the resonance region, and hence the necessity of the FMSR.

We fit the first moment FMSR integral

$$I(s,r) = \int_0^r (\nu/s)\frac{d\sigma}{dt\,d(\nu/s)}\,d(\nu/s) \tag{5.3}$$

† It may be noted that this experiment was done on polypropene and carbon targets, from which the proton target data was obtained by subtraction.

‡ The two sets of 24 GeV/c data agree in the t and M^2 distributions but the counter data has around 10% higher normalisation. Since its quoted normalisation uncertainty is also 10%, and the bubble chamber experiments have generally more reliable normalisation, we have scaled down the counter data by 10% as in the RR analysis.
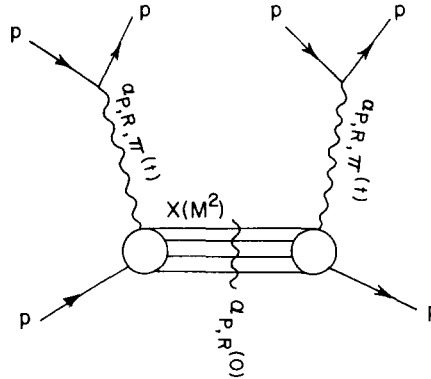
Fig. 5.1. Triple Regge diagram for $pp \to pX$.

over the low missing mass region, and the function

$$F(s, \nu/s) = (\nu/s) \frac{d\sigma}{dt\, d(\nu/s)} \tag{5.4}$$

at some high missing mass points, where

$$\nu = M^2 - m^2 - t. \tag{5.5}$$

For most of the t range of interest, the r and ν/s variables where $I(s, r)$ and $F(s, \nu/s)$ are fitted respectively are indicated below.

s	r	ν/s
46.8	0.04, 0.06	0.08, 0.10
130.7	0.02, 0.03, 0.04, 0.06	0.094
260.6	0.01, 0.02, 0.03, 0.04, 0.06	0.097
324.9	0.01, 0.02, 0.03	–
	(all together 18 points)	

We generally use the 6 term formulae

$$I(s, r) = G_{PPP} \frac{r^{3-2\alpha_P}}{(3-2\alpha_P)} + G_{PPR} \frac{r^{2.5-2\alpha_P}}{(2.5-2\alpha_P)\sqrt{s}} + G_{RRP} \frac{r^{3-2\alpha_R}}{(3-2\alpha_R)}$$

$$+ G_{RRR} \frac{r^{2.5-2\alpha_R}}{(2.5-2\alpha_R)\sqrt{s}} + G_{\pi\pi P} \frac{r^{3-2\alpha_\pi}}{(3-2\alpha_\pi)} + G_{\pi\pi R} \frac{r^{2.5-2\alpha_\pi}}{(2.5-2\alpha_\pi)\sqrt{s}} \tag{5.6}$$

and

$$F\left(s, \frac{\nu}{s}\right) = G_{PPP} \left(\frac{\nu}{s}\right)^{2-2\alpha_P} + G_{PPR} \left(\frac{\nu}{s}\right)^{1.5-2\alpha_P} \cdot \frac{1}{\sqrt{s}} + G_{RRP} \left(\frac{\nu}{s}\right)^{2-2\alpha_R}$$

$$+ G_{RRR} \left(\frac{\nu}{2}\right)^{1.5-2\alpha_R} \cdot \frac{1}{\sqrt{s}} + G_{\pi\pi P} \left(\frac{\nu}{s}\right)^{2-2\alpha_\pi} + G_{\pi\pi R} \left(\frac{\nu}{s}\right)^{1.5-2\alpha_\pi} \cdot \frac{1}{\sqrt{s}} \tag{5.7}$$

with

$$\alpha_R = 0.5 + t \quad \text{and} \quad \alpha_\pi = -0.02 + t. \tag{5.8}$$

The results for $t = 0.05$ are shown in the following table (set I). For comparison we have also shown a 4 term fit, where both vector–tensor and pion exchanges are described by a single effective trajectory α_R, left free (set II) – as followed by RR. The low value of the resulting α_R is suggestive of a very significant π contribution. Of course whether one treats the vector–tensor and the pion exchanges separately or through a single effective trajectory makes little difference to the diffraction parameters as one sees from this table. However, treating them separately has the advantage of reducing the interference term ambiguity, since π and P do not interfere and RP interference is bounded by a Schwarz inequality

$$\sigma_{\text{PfP+fPP}} \leq 2 \cos \frac{\pi}{2} (\alpha_P - \alpha_R) \sqrt{\sigma_{\text{PPP}} \, \sigma_{\text{ffP}}} \lesssim \sqrt{\sigma_{\text{PPP}} \cdot \sigma_{\text{ffP}}} \tag{5.9}$$

where $\sigma = d\sigma/dt \, d\nu$. To estimate the size of the ambiguity we have repeated the 6 term fit with an interference term added at the above maximal value (set III). We see that it makes little difference to the diffractive TR parameters G_{PPP} and G_{PPR}. This is an extremely significant result since there is no reliable estimate of the precise values of the interference terms. The closest one can get to a phenomenological estimate is through the polarization asymmetry data for $pp_\uparrow \to pX$ discussed in the last section (fig. 4.10) or the inclusive cross-section difference

$$\sigma(\pi^- p \to \pi^- X) - \sigma(\pi^- p \to \pi^+ X) \tag{5.10}$$

for which the FSASF data is shown in fig. 2. The dominant TR term for both is the interference term $\rho P\rho$. But the quality of these data are evidently inadequate for a quantitative estimate of $\rho P\rho$; and besides there is no quantitatively reliable way of connecting this to the interference term of present interest, i.e. fPP. None-the-less, it is reassuring that both these data are at least consistent with a negligibly small interference term (≈ 0), in agreement with our present analysis.

On the basis of the above experience we have extended the set I fit (6 terms and no interference added) to other t values. Here we have fixed

$$\alpha_P = 1 + 0.25t \tag{5.11}$$

Table 5.2

(In) sensitivity of the diff. TR couplings G_{PPP} and G_{PPR} to the parametrisation of the nondiff. terms and the interference term ambiguity, as explained in the text. The couplings are in mb/GeV^2 units ($t = -0.05$)

Fit	χ^2/ν	α_P	G_{PPP}	G_{PPR}	G_{RRP}	G_{RRR}	$G_{\pi\pi P}$	$G_{\pi\pi R}$
I	$\dfrac{9.6}{11}$	0.995 ± 0.003	3.94 ± 0.20	0.43 ± 0.13	6.6 ± 5.1	26 ± 16	559 ± 110	72 ± 182
II	$\dfrac{9.9}{13}$	Fixed 0.995	4.02 ± 0.12	0.49 ± 0.13	425 ± 49	265 ± 126	($\alpha_R = 0.01 \pm 0.02$)	
III	$\dfrac{9.6}{12}$	Fixed 0.995	3.67 ± 0.15	0.55 ± 0.13	3.2 ± 1.5	4.7 ± 11.6	499 ± 69	295 ± 200
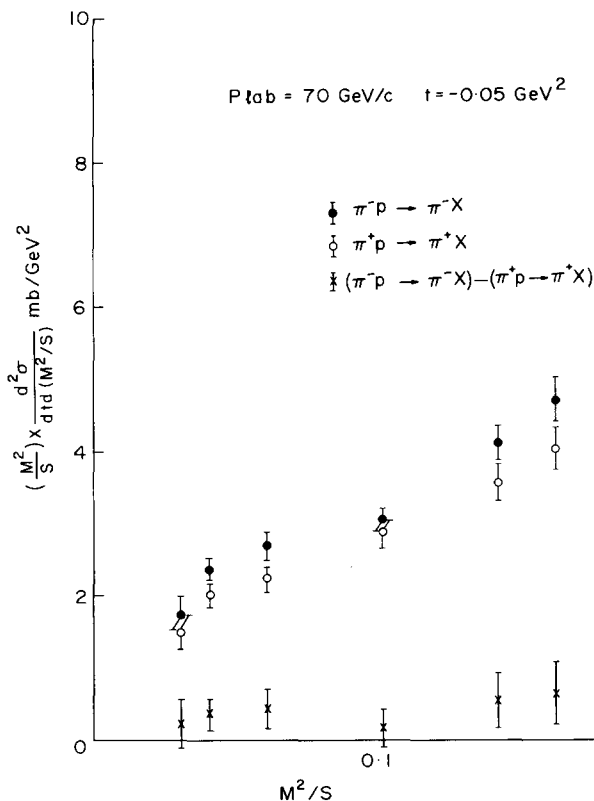
Fig. 5.2. FSASF data on the diffractive processes $\pi^\pm p \to \pi^\mp X$ and the corresponding cross-section difference. The latter measures the triple Regge interference term $\rho P \rho$.

as suggested by 2 body data (we have also repeated the fit with $\alpha'_P = 0.4$, as will be discussed later). The resulting couplings are shown in the following table.

Of course, the nondiffractive parameters, as determined from this fit have rather large uncertainties. It should be noted, however, that the $\pi\pi P$ coupling is consistent with the form

$$G_{\pi\pi P} = \frac{1}{4\pi} \cdot \frac{g_{\pi N}^2}{4\pi} \cdot \sigma_T^\infty(\pi N) \cdot \frac{(-t)}{(t - \mu^2)^2} = \frac{14.5 \times 21}{4\pi} \cdot \frac{(-t)}{(t - 0.02)^2} \tag{5.12}$$

suggested by an extrapolation from on-shell πN scattering [214] which also agrees with the $pn \to px$ data over the available range $0.15 < |t|$ [215, 216]. Only at $t = -0.05$ does the present estimate of $G_{\pi\pi P}$ show an excess (fig. 3). But as indicated in the table below, this excess can be traded off for a moderate G_{RRP} without affecting the χ^2 of the fit or the diffractive parameters appreciably.

The diffractive parameters G_{PPP} and G_{PPR} are determined quite precisely. These are compared with the fits of RR and FF in fig. 4. Evidently, the FSASF data favour the RR fit rather strongly – in particular a $G_{PPP} \gg G_{PPR}$ at small t. Also shown are fits to the present coupling estimates in the form

$$G_{PPP} = 4.74 \, e^{14.8t} + 2.23 \, e^{3.1t} \quad \text{with} \quad \chi^2/\nu = 0.9/3, \tag{5.13}$$

$$G_{PPR} = 3.45[e^{4.3t} - e^{10.4t}] \quad \text{with} \quad \chi^2/\nu = 4.3/4. \tag{5.14}$$

Table 5.3
The TR couplings (in mb/GeV^2) for the 6 terms fit of eqs. (6, 7)

$-t$	χ^2/ν	G_{PPP}	G_{PPR}	G_{RRP}	G_{RRR}	$G_{\pi\pi P}$	$G_{\pi\pi R}$
0.05	$\frac{9.5}{12}$	4.24 ± 0.24	0.51 ± 0.18	$.15 \pm 5$	27 ± 18	619 ± 112	21 ± 150
$\Big($0.05	$\frac{10.3}{12}$	3.80 ± 0.13	0.73 ± 0.15	44 ± 5	1 ± 10	167	$259 \pm 200\Big)$†
0.1	$\frac{2.8}{12}$	2.74 ± 0.11	1.16 ± 0.12	38 ± 5	0 ± 9	124 ± 60	0 ± 116
0.15	$\frac{1.9}{12}$	1.89 ± 0.08	1.13 ± 0.10	35 ± 5	15 ± 11	104 ± 62	4 ± 153
0.2	$\frac{9.2}{12}$	1.43 ± 0.07	0.92 ± 0.10	35 ± 4	22 ± 11	47 ± 44	0 ± 147
0.25	$\frac{4.1}{9}$	1.11 ± 0.24	0.94 ± 0.12	21 ± 5	41 ± 12	49 ± 45	0 ± 139
0.35	$\frac{8.6}{11}$	0.80 ± 0.06	0.70 ± 0.07	23 ± 5	20 ± 16	133 ± 98	0 ± 88
0.45	$\frac{8.6}{11}$	0.54 ± 0.03	0.47 ± 0.05	22 ± 4	46 ± 15	34 ± 56	0 ± 105

† Fit obtained by restricting $G_{\pi\pi P}$ to <300.
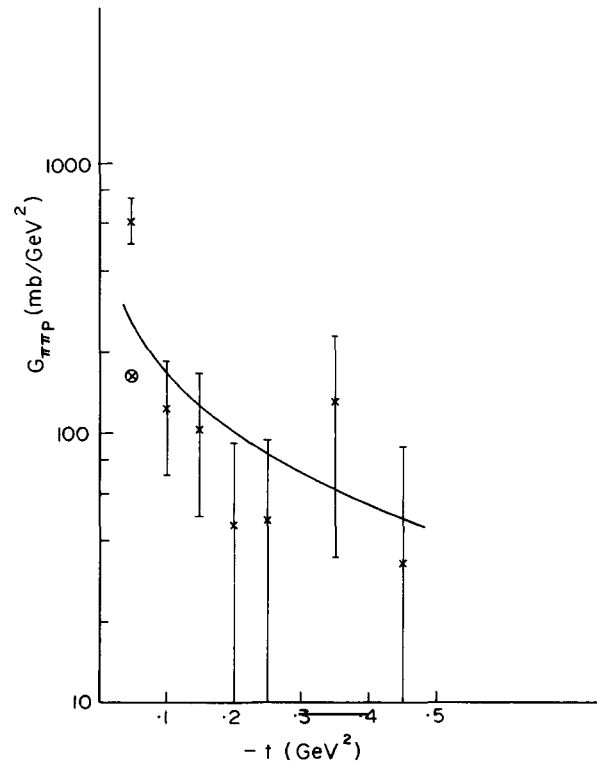
Fig. 5.3. The $\pi\pi P$ triple Regge couplings of table 3 compared with extrapolation formula (eq. (12)) of Bishari [214]. The point × corresponds to the constrained solution, shown in brackets in table 3.
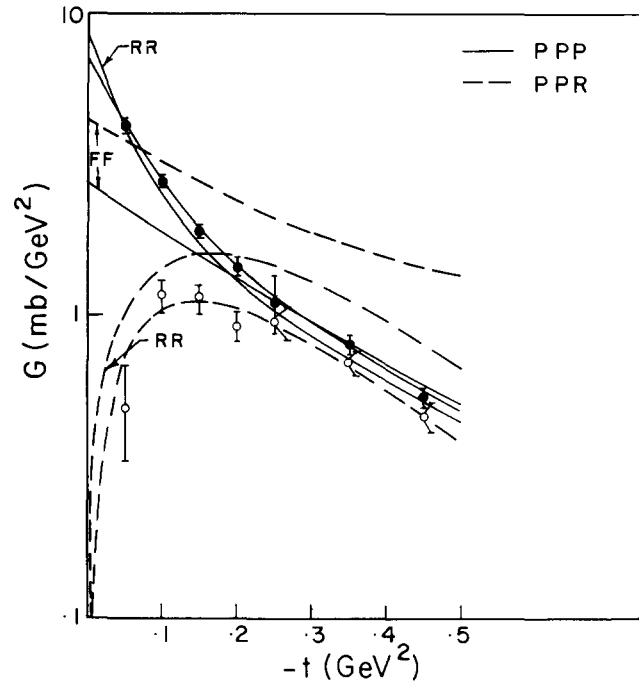
Fig. 5.4. The diffractive triple Regge couplings G_{PPP} and G_{PPR} of the present fit. For comparison the results of the FF [169] and RR [208] fits are also shown.

The G_{PPP} can also be fitted by a quadratic exponent

$$G_{PPP} = 6.22\, e^{(8.9t+7.86t^2)}$$ (5.13a)

but with a somewhat larger χ^2/ν (=5.3/4). We should note that identical TR parameters have been independently obtained from these data by Roberts [217].

The energy dependence of the 1st moment $I(s, r = 0.06)$ is shown against the inputed data points for $-t = 0.05$, 0.1 and 0.15 in fig. 5. Fig. 6 compares the $I(s, r = 0.04)$ at $-t = 0.05$ of the present fit with those of RR and FF fits. In addition to the inputed FSASF and the BHM data points, the 200 GeV/c ANL-FNAL [202] data and the 20 GeV/c data of Edelstein et al. [218], are also shown. Comparison of the FSASF and the low energy data points evidently suggests a very small nonscaling term PPR unlike the FF fit. We shall see below that the same result also follows from the FSASF data alone, when one looks at the missing mass dependence.

The $F(s, \nu/s)$ data are plotted against ν/s for $-t = 0.05$, 0.1 and 0.15 in the figs. 7, 8 and 9. Also shown are the cross-section (solid line) and the diffractive contribution (dashed line) of the present fit, for the central FSASF energy of $s = 261$. The fit has, of course, very little energy dependence, particularly at $-t = 0.05$ (≤ 5 percent over the FSASF energy range). In the region $\nu/s < 0.04$, dominated by diffraction, the FSASF data is flat, as required by a dominant scaling term PPP. Of course the resonance bumps lie appreciably above the scaling curve. This must not, however, be interpreted in terms of a nonscaling contribution PPR†. For this exactly compensates for the fact that the inelastic

---

† This point should be stressed as several experimental papers have tried to interpret the energy dependence observed over the very low missing mass region, in terms of the nonscaling component PPR.
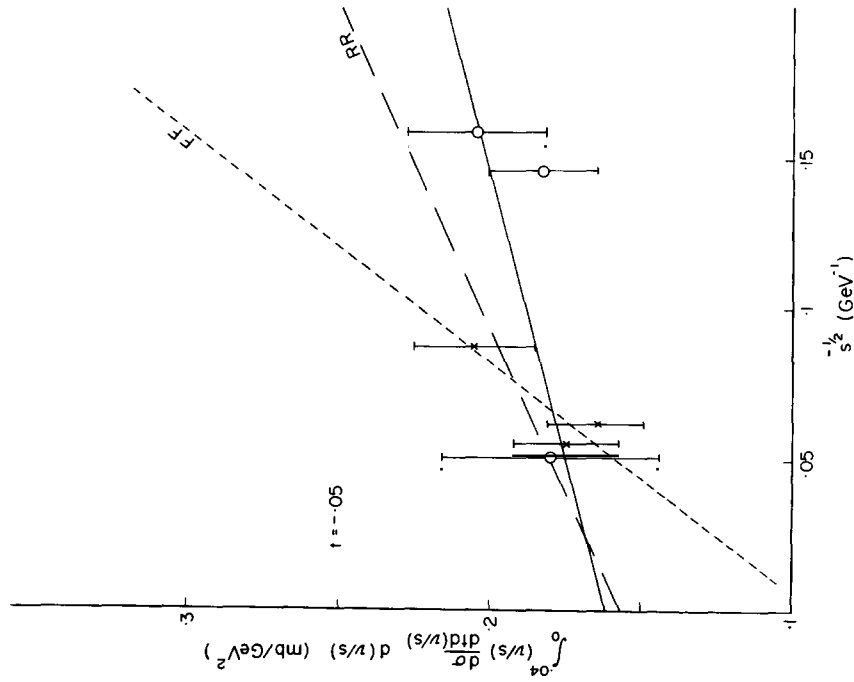
Fig. 5.6. The 1st moment integral $I(s, r = 0.04)$ of the present fit compared with the FF and RR fits at $-t = 0.05$. In addition to the inputed FSASF and BHN data points, those of the 200 GeV/c ANL-FNAL data and 20 GeV/c data of Edelstein et al. are also shown.
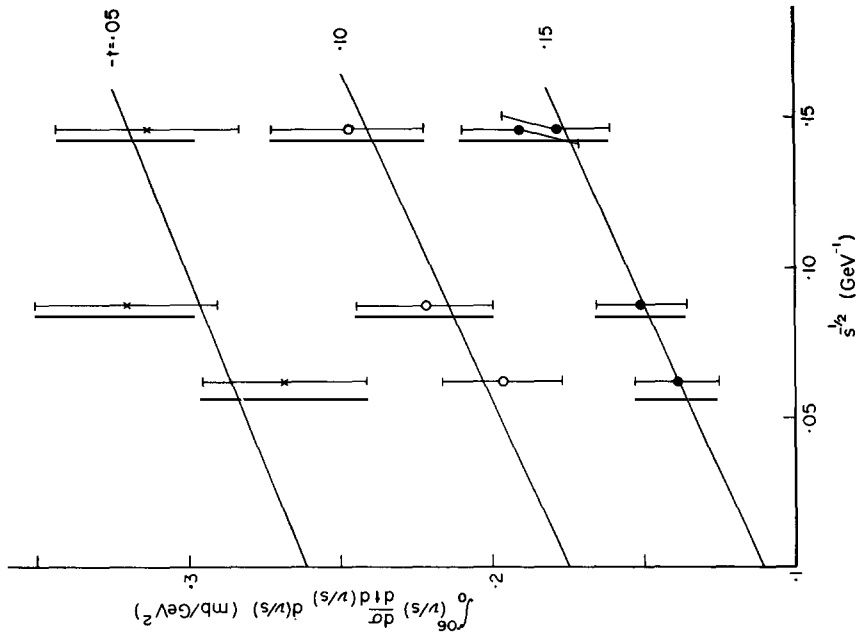
Fig. 5.5. The present fit compared with the inputed data for the 1st moment integral $I(s, r = 0.06)$ at $-t = 0.05$, 0.1 and 0.15.
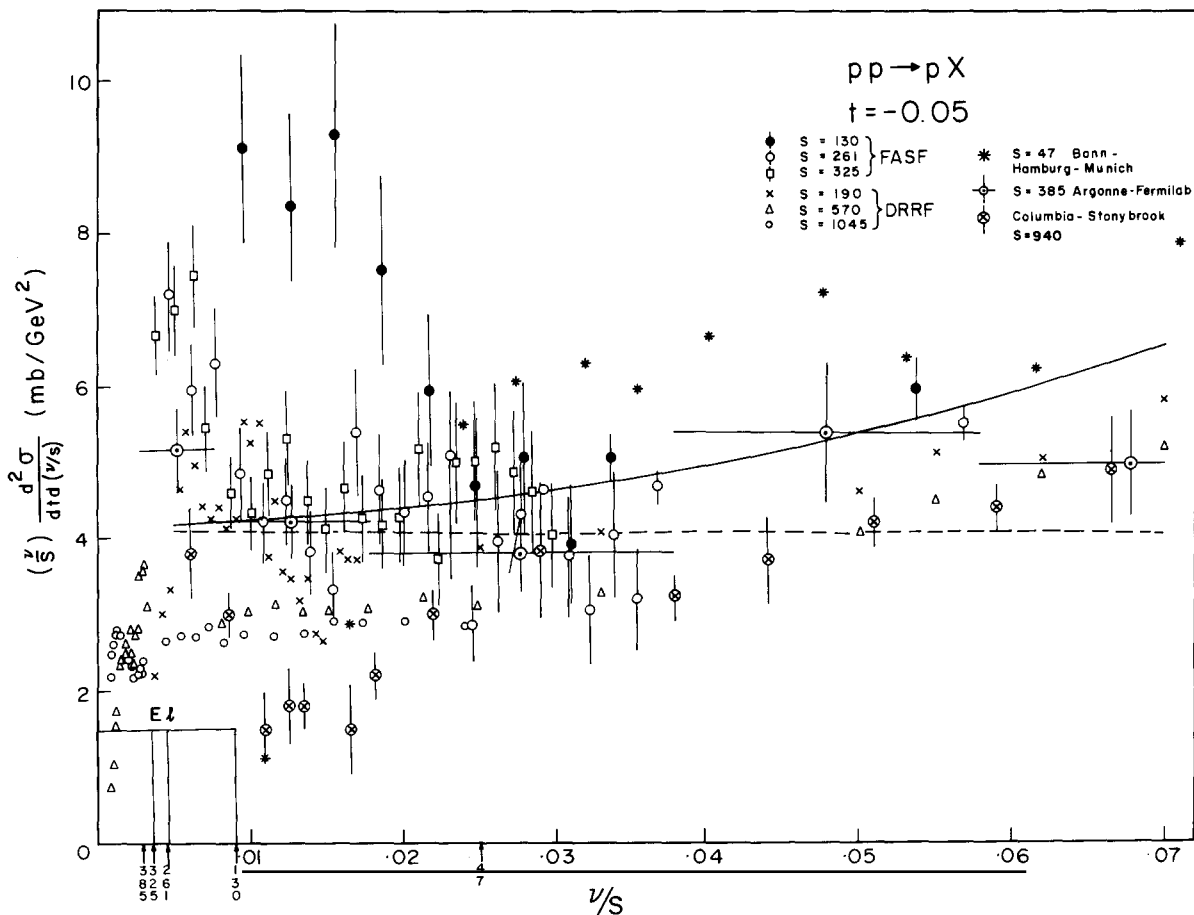
Fig. 5.7. The ν/s dependence of the present fit compared with the available data at $-t = 0.05$. The diffractive component (PPP + PPR) is shown separately by the dashed line.

threshold is a nonscaling quantity – it goes down like s^{-1}. The effect is particularly significant at low t, since, the elastic cont. is suppressed by the $(-t)/s$ factor. This contribution is shown at the bottom left corner-spread over the sub-threshold region. The excess in the resonance region compensates the short fall of the elastic contribution, so that the first moment integral is well matched by a flat scaling term at all energies. This is separately illustrated in fig. 10 where the low mass integrals $(0 < \nu < 2.6)$ are seen to agree with our PPP dominated fit to within 10–15 percent. On the other hand a sizeable PPR contribution, as in the FF fit, would over shoot all the data points, and most of them by 30–40 percent.

In addition to the inputed data we have shown the ANL-FNAL data [202] at $s = 385$ and the ISR data [198] at $s = 550$ in figs. 7–9. They agree with the FSASF data both in shape and normalisation. At $-t = 0.05$, we also show the C-S data (interpolated from the $-t = 0.037$ and 0.066 points using their quoted slope of 6.3) [219] and the DRRF data [210]. The DRRF data points are estimated from pd→dx data using factorisation; but the $s = 190$ and 570 points have been extended beyond $\nu/s = 0.017$ and 0.025 using their pp→px data at $s = 290$ and 700 respectively. This agrees in shape with the FSASF data – i.e. a flat cross-section for $\nu/s < 0.04$ which also matches with the integral over the low mass region $(0 < \nu < 2.6)$. In contrast to all these data the C-S data, has a pronounced dip in the
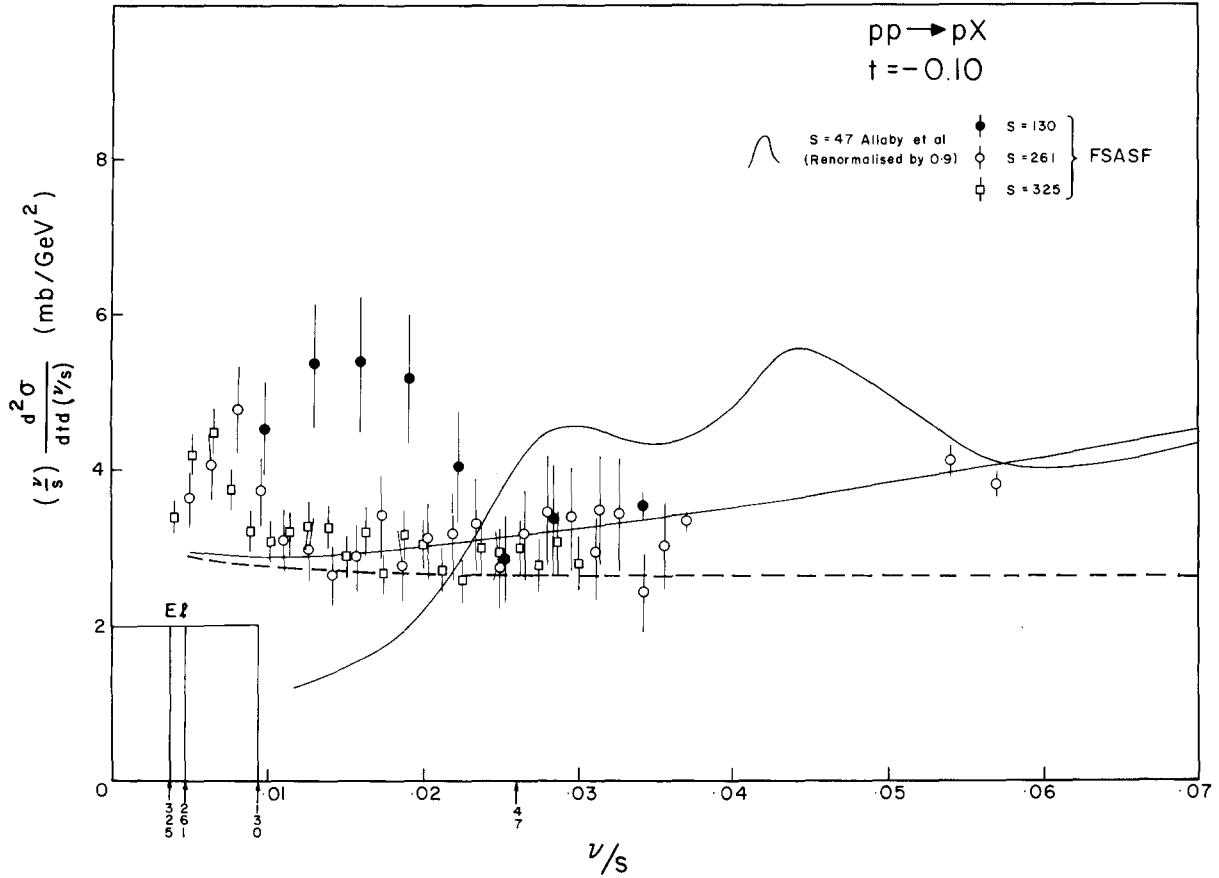
Fig. 5.8. Same as fig. 7, for $-t = 0.1$.

0.02 < ν/s < 0.03 region, a flat extrapolation from which will also far under shoot the low mass integral. This clearly shows why they need a dominant PPR term.

Finally we should comment on the energy dependence of the DRRF data which seems to fall by 20 percent from $s = 190$ to 1045. It seems to us that this has nothing to do with the relative size of the scaling and nonscaling components of diffraction (i.e. PPP versus PPR†). For it shows a fall of this magnitude for a fixed M^2 bite as well (as also for the individual diff. resonances), where the energy dependence can only come from nondiffractive exchanges. The integral over the low missing mass region $(0 < \nu < 2.6)$ is shown in fig. 10 against s^{-1}. Although a sufficiently large nondiffractive exchange can accommodate a 20 percent fall in the $s = 190$ to 1045 range, the resulting extrapolation would far overshoot the low energy data, as it corresponds to a s^{-1} (vector–tensor exchange) or faster (pion exchange) energy dependence. Thus, in the conventional Regge framework it is hard to reconcile such a rapid decrease over the FNAL energy range with the near constancy of the diffractive cross-section between PS and FNAL energies. Moreover it seems to be inconsistent with the compilation of bubble chamber data over the FNAL energy range [200, 202], although they have limited statistics. Therefore

† To check this explicitly we have fitted the ν/s dist. of the DRRF data (fig. 7) to eqs. (6,7). At each energy we get a G_{PPP}/G_{PPR} ratio of about 10, in agreement with the FSASF fit.
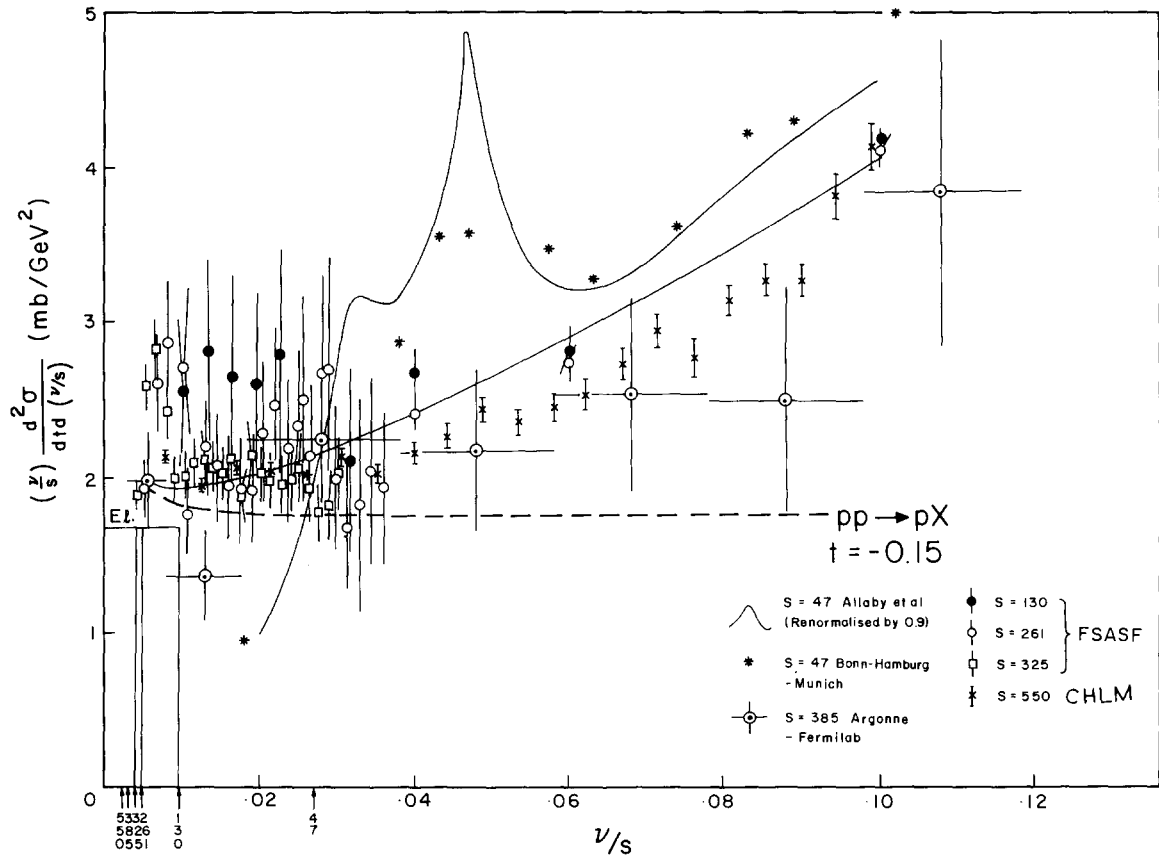
Fig. 5.9. Same as fig. 7, for $-t = 0.15$.

we feel that this energy dependence may be largely attributed to an energy dependent normalisation error of ~15 percent. One should note that the quoted normalisation error for the $pd \to dx$ cross-section, arising from extrapolation to $t = 0$ (optical theorem point), is 12 percent, and factorisation has been tested to a 15 percent accuracy only. Since a good part of these uncertainties can be energy dependent, a net energy dependent uncertainty of 15 percent is quite plausible. None-the-less the effect seems to us sufficiently intriguing to warrant a high statistics measurement of the $pp \to pX$ cross-section (like the FSASF) over the full FNAL energy range.

Before closing this section we would like to make a factorisation test with the FSASF data on

$$\pi^+ p \to \pi^+ X. \tag{5.15}$$

For $v/s < 0.03$, the inclusive cross-sections (1) and (15), are expected to be dominated by the diffractive component (see fig. 7) and hence Pomeron factorisation implies

$$\frac{d\sigma}{dt\, d(v/s)} (\pi^+ p \to \pi^+ X) \Big/ \frac{d\sigma}{dt\, d(v/s)} (pp \to pX) = \frac{d\sigma}{dt} (\pi p \to \pi p) \Big/ \frac{d\sigma}{dt} (pp \to pp). \tag{5.16}$$

The ratio of the 2 inclusive cross-sections from the FSASF expt. are compared with the corresponding
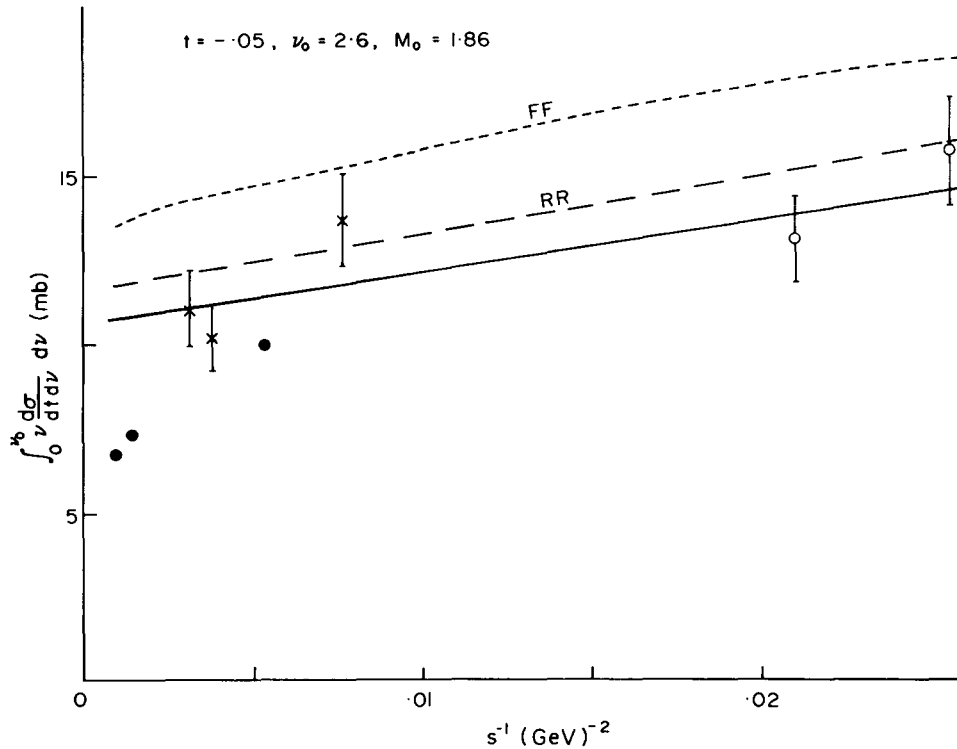
Fig. 5.10. The low mass integral $(0 < \nu < 2.6)$ of the present fit shown against the FSASF (×), DRRF (●) and the low energy data (○) of BHM and Edelstein et al.

elastic cross-section ratios in fig. 11, at $-t = 0.05$, 0.15, 0.25 [217]. Thus whereas the $\pi p \to \pi X$ data is inadequate for an independent TR analysis it is reassuring that it is at least consistent with the Pomeron factorisation prediction.

5.3. Consequences

The main results of the foregoing triple Regge analysis – i.e. (1) a nonvanishing triple Pomeron coupling at $t = 0$ $(G_{PPP}(0) \neq 0)$ and (2) dominance of the triple Pomeron component in diffraction $(G_{PPP} \gg G_{PPR})$ – have several consequences of interest to the theoretical models for Pomeron.

5.3.1. Nonvanishing triple Pomeron coupling $(G_{PPP}(0) \neq 0)$

As discussed in the first section (subsection 1.4.3), this result implies that the simple pole model for Pomeron exchange or the pole plus cut model a la the standard perturbative Gribov calculus [56] are inconsistent with the asymptotic unitarity constraint. It therefore favours the so-called strong coupling solution to the Gribov calculus [64], where the multi-Pomeron cuts are treated nonperturbatively. However, the threshold suppression for the multi-Pomeron exchanges are so severe, that over any realistic energy range the total cross-section can be approximated by the Pomeron pole and the first order cut terms as in the standard perturbative approach [220, 221].
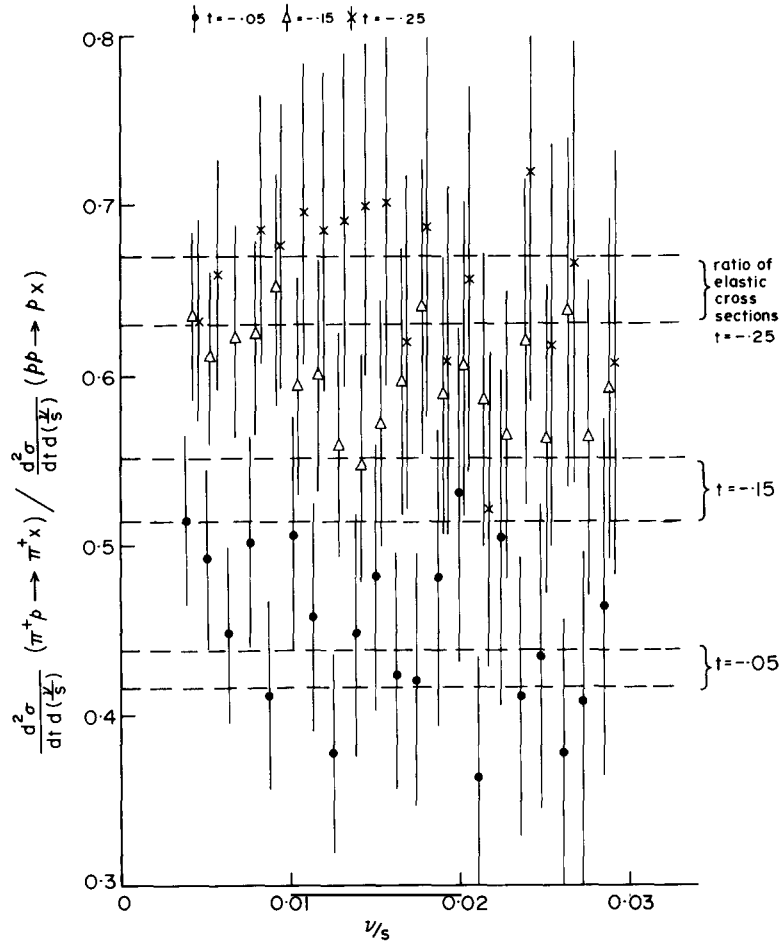
Fig. 5.11. The factorisation prediction between the diffractive processes pp→pX and πp→πX compared against the FSASF data [217].

5.3.2. Diffractive cross-section rise
The integral diffractive excitation cross-section

$$\sigma^{D} = 2 \int\limits_{1.2}^{0.2s} d\nu \int\limits^{t_{min}} dt \frac{d\sigma^{D}}{d\nu\, dt}$$ (5.17)

calculated from the present fit is shown for the two extreme ISR energies ($s = 360$ and 3600) in the following table, along with the RR and FF results. To check the sensitivity of the diffractive cross-section rise on the input Pomeron slope we have repeated the triple Regge analysis with a

$$\alpha_{P} = 1 + 0.4t.$$ (5.18)

Table 5.4

The inelastic diffraction cross-section σ^D(mb) from the present fit shown for the ISR energy range ($s = 360$–3600). The RR and FF results are also shown for comparison

s		σ_{PPP}	σ^{PPR}	σ^D
	FF	3.60	2.52	6.12
	RR	5.64	1.29	6.93
360	Present fit	5.84	0.84	6.68
	Present fit ($\alpha'_P = 0.4$)	6.11	1.0	7.11
	FF	5.06	2.18	7.24
	RR	8.37	1.14	9.51
3600	Present fit	8.62	0.75	9.37
	Present fit ($\alpha'_P = 0.4$)	8.77	0.78	9.55

The resulting couplings can be parameterised as

$$G_{PPP} = 4.69\, e^{19.3t} + 3.23\, e^{2.9t} \tag{5.19}$$

$$G_{PPR} = 7.74[e^{3.4t} - e^{5.9t}] \tag{5.20}$$

and the corresponding cross-sections are shown in the same table. The diffractive cross-section rise is evidently insensitive to the choice of α'_P. One gets a rise of 2.7 mb with $\alpha'_P = 0.25$ and 2.4 mb with $\alpha'_P = 0.4$, which are close to the RR estimate of 2.6 mb†, but more than double the FF value of 1.1 mb. To this of course, one should add the double diffraction cont.

$$\frac{d\sigma^{DD}}{dt\,d\nu\,d\nu'} = \frac{d\sigma^D}{dt\,d\nu} \cdot \frac{d\sigma^D}{dt\,d\nu'} \bigg/ \frac{d\sigma^{El}}{dt} \tag{5.21}$$

integrated over t, ν and ν'. This gives a further rise of $\simeq 1$ mb over the same energy range. Thus the net diffractive cross-section seems to rise by 3.5 mb over the ISR range, which is numerically close to the observed rise in the total inelastic cross-section over this range.

Thus the nondiffractive cross-section

$$\sigma^{ND} = \sigma^T - \sigma^{El} - \alpha^D \tag{5.22}$$

which corresponds to the cross-section for production of final states with no large rapidity gap, seems to remain approximately constant. Whether or not it implies a constant multiperipheral cross-section σ^B, which defines the bare Pomeron pole exchange, is of course model dependent. In the simple minded 2 component model, which is assumed in most of the multiperipheral model calculations,

$$\sigma^B = \sigma^{ND} \to \text{const.}$$

† This corresponds to a rise of $\simeq 1$ mb over the FNAL range ($s = 200$–800), which agrees with the rise estimated from a compilation of the bubble chamber data [222]. None-the-less, one still needs a high precision counter measurement of the diffractive cross-section rise. It will be very useful in this respect, if the FSASF measurement is extended to cover the full FNAL energy range and the CHLM measurement at ISR is extended to cover the full range of t.

i.e.

$$\alpha_P(0) \simeq 1. \tag{5.23}$$

On the other hand, in the Gribov calculus model [220, 221], which is theoretically more attractive,

$$\sigma^B = \sigma^{ND} + 2(\sigma^D + \sigma^{E1}) \to \text{Rising}$$

i.e.

$$\alpha_P(0) > 1. \tag{5.24}$$

These models are discussed in greater detail in section 7.

5.3.3. Dual property of diffractive resonances

The result $G_{PPP} \gg G_{PPR}$ is evidently in agreement with the prediction of ref. [36] based on topological considerations, and in disagreement with the P-f proportionality prediction [50]. This is in agreement with an earlier analysis by Inami and Roberts [52]. Moreover the PPR coupling, as estimated here, is too small to describe the resonance contribution to the low M^2 integral. For instance, at $-t = 0.05$, the PPR contribution to the integral

$$I = \int\limits_0^{2.6} \nu \frac{d\sigma}{dt\, d\nu} d\nu \tag{5.25}$$

shown in fig. 10 is only 15–20 percent. Since the elastic contribution itself is $\simeq 20$ percent and the N*(1400) contribution is much bigger at this t value, one cannot evidently saturate the resonance contribution by PPR. In fact in most resonance and background separation analyses [213, 218] the former constitutes the major part of this integral, and seems therefore to get substantial contribution from the PPP term.

This result is in agreement with the previous analyses of refs. [206 and 169] for $pp \to pX$ and the analysis of ref. [197] for $\pi p \to pX$. We should comment, however, on a recent triple Regge analysis by Hidaka [223] which arrives at just the opposite conclusion – i.e. diffractive resonances in $pp \to pX$ are dual to PPR. It is based on a limited set of data and on a very restricted kinematic range ($s > 200$, $\nu/s \gtrsim 0.04$ and $0.2 < -t < 0.4$); and obtains $G_{PPR} \simeq 2G_{PPP}$. We have followed through this analysis closely. It seems to us clear that the kinematic ranges, as we have stressed earlier, are too restricted to permit a meaningful separation between PPP and PPR.

Finally Hoyer and Thacker [224] have observed an interesting correlation between the t dependence of elastic and N*(1400) production cross-sections, which strongly supports a duality between the diffractive resonances and PPP. In the first moment integral of eq. (25) above, i.e.

$$(-t)\frac{d\sigma}{dt}(pp \to pp) + (\nu_{N^*})\frac{d\sigma}{dt}(pp \to pN^*(1400)) \simeq G_{PPP}(t) \cdot \bar{\nu} \tag{5.26}$$

the steep N*(1400) slope compensates the suppression of the elastic contribution at small t in such a way

that the two together match the t dependence of $G_{PPP}(t)$, as obtained from large M^2 fits, over a very wide region.

Thus there seems to be rather strong evidences, suggesting that the diffractive resonances are largely dual to the triple Pomeron exchange as predicted in ref. [36].

5.3.4. Other consequences

It is evident from eqs. (7) and (17) above that,

$$\frac{d\sigma^D(PPP, PPR)}{d(\ln M^2)} = C_P, C_R \exp\{-\tfrac{1}{2}\ln M^2\} \tag{5.27}$$

$$\sigma^D(PPP, PPR) = \int_{M_0^2}^{rs} [C_P, C_R \exp\{-\tfrac{1}{2}\ln M^2\}] \, d(\ln M^2) \tag{5.28}$$

where $C_{P,R}$ are constants and the t_{min} cut-off in eq. (17) provides an effective cut-off for the diffractive excitation mass at $r \cdot s$ ($r \sim 0.1$). Thus, whereas a PPR dominance would essentially correspond to a fixed mass range for diffractive excitation, the observed PPP dominance of diffraction implies that the mass range increases indefinitely with the incident energy. Indeed, the diffractive cross-section rise noted earlier, comes entirely from the production of these higher mass clusters with increasing energy, as evident from eq. (28). This has two interesting consequences – (i) a logarithmic increase of average diffractive multiplicity [225, 226] and (ii) a diffractive contribution to the pionisation cross-section [227].

(i) Pomeron factorisation would imply that the diffractive cluster decays are identical to the nondiffractive ones, i.e.

$$\langle n(M^2)\rangle_D = a \ln M^2 \tag{5.29}$$

where a is the coff. of the $\ln s$ multiplicity rise for nondiffractive events (≈ 2 for charged pions). More importantly, the average diffractive multiplicities of the FNAL bubble chamber data [202] are in agreement with eq. (29). Approximating $n(M^2)$ by its average value, one gets from eqs. (27, 29)

$$d\sigma^D/dn = C_p/a. \tag{5.30}$$

Thus, one expects a flat diffractive multiplicity distribution over the range $0 < n < a \ln rs$ – i.e. essentially stretching up to the Poisson peak for the nondiffractive part. It corresponds to an average diffractive multiplicity

$$\langle n \rangle_D = \tfrac{1}{2}a \ln rs \to \tfrac{1}{2}a \ln s \tag{5.31}$$

i.e. a $\ln s$ rise similar to the nondiffractive case, but with half its coefficient.

(ii) The CM rapidity of a cluster of mass M is

$$y(M^2) = \tfrac{1}{2}\ln M^2/s. \tag{5.32}$$

Then it follows from eq. (27) that the diffractive clusters populate the CM rapidity space uniformly from
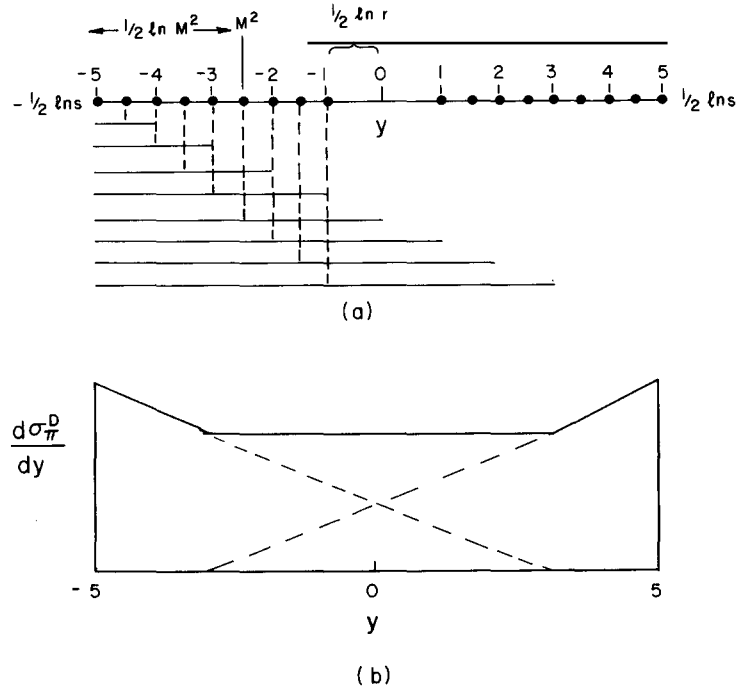
Fig. 5.12. (a) Rapidity distribution of the diffractively excited clusters (●) and their decay pions (——). (b) The resulting pionisation cross-section.

$y \simeq \pm\frac{1}{2}\ln s$ to $\mp\frac{1}{2}\ln r$ (fig. 12a). Moreover a cluster of mass M is spaced at distance $\frac{1}{2}\ln M^2$ from the end. Again like the nondiffractive case, the decay pions are expected to be uniformly distributed over a rapidity range $\pm\frac{1}{2}\ln M^2$, as indicated in fig. 12a. Adding the decay pions from the two sides (beam and target excitation) one gets the pionisation cross-section illustrated in fig. 12b. It evidently shows a central plateau. But since $\sigma^D \simeq \frac{1}{4}\sigma^{ND}$ and less than half the events populate the central region, the diffractive contribution to the pionisation cross-section is expected to be only $\lesssim\frac{1}{8}$.

The two effects described above are discussed in greater detail in sections 7 and 8.

5.4. Summary

(1) The FSASF data on diffractive excitation is adequate for a complete triple Regge analysis on its own, in spite of a limited energy range. It gives a nonvanishing triple Pomeron coupling at $t = 0$ (i.e. $G_{PPP}(0) \neq 0$), and also a dominant triple Pomeron component in diffraction (i.e. $G_{PPP} \gg G_{PPR}$).

(2) These results are in quantitative agreement with the earlier data, with the single exception of the C-S data. Indeed the triple Regge parameters, resulting from the FSASF data, are practically identical to those estimated earlier [208], from a global data compilation excluding the C-S data.

(3) The C-S data, which is also adequate now for a complete triple Regge analysis on its own, gives exactly the opposite result–i.e. no triple Pomeron component in diffraction ($PPP = 0$). However, the weight of experimental evidence now is overwhelmingly against this result. To that extent the triple Regge fits, based on data compilations including the C-S points (e.g. ref. [169]), should also be treated with caution.

(4) The DRRF data on pd → dX gives PPP and PPR parameters, in quantitative agreement with (1) and (2) above. But it shows a 20% drop in normalisation over the FNAL range, which persists for individual diffractive resonances like N*(1400); and it seems hard to account for in the conventional Regge picture of diffraction. However, the experiment has rather large normalisation uncertainty.

(5) The PPR component from these estimates turn out to be too small to account for the diffractive resonance contribution to the FMSR, at least at small $|t|$. Thus the diffractive resonances seem to be largely dual to (triple) Pomeron exchange, as predicted in ref. [36].

(6) The dominance of the PPP component implies a significant rise of the diffractive excitation cross-section with energy – by ~2.5 mb over the ISR range and ~1 mb over the FNAL range. The latter is in agreement with the FNAL bubble chamber data, within their limited statistics.

(7) Finally we should emphasise the necessity of a high precision counter measurement of the diffractive cross-section rise over the FNAL (and preferably the ISR) energy range. In this context it will be very useful if the FSASF measurement are extended over the full FNAL energy range and/or the CHLM measurement at ISR are extended to lower $|t|$ range. The latter seems to be in progress [228].

6. Double Pomeron exchange

A very interesting class of diffractive excitation is the so-called Double Pomeron Exchange (DPE).
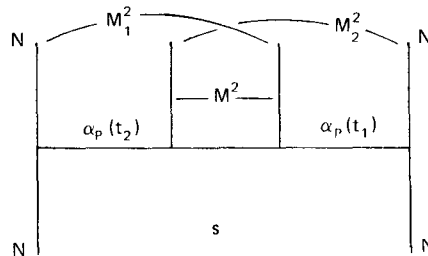
The theoretical interest in this process, as mentioned in subsection 1.4.3, dates back to 1964. It was first observed by Verdiev et al. [54] and then by Finkelstein and Kajantie [55], that a multiple Pomeron recurrence processes (of which the DPE is the 1st nontrivial step) asymptotically violates the Froisart bound. Two ways out of this contradiction have been suggested. The first, which was favoured by Verdiev et al., was for the internal vertex to vanish as $t_1, t_2 \rightarrow 0$. The second alternative, which was favoured by Finkelstein and Kajantie was to do away with the factorising Pomeron pole hypothesis. In particular it was suggested that there are no recurrence of the Pomeron exchange (DPE ≡ 0). This would be a natural consequence, for instance, in the optical model approach to hadron diffraction, where the Pomeron is just a synonym for the optical absorption of hadron in the s-channel, as opposed to a distinct t-channel exchange. Thus experimental evidence for or against DPE is of considerable importance in deciding the nature of the Pomeron. Of course, similar constraints, apply for the triple Pomeron exchange, as discussed in the last section; but DPE is evidently a more explicit example of Pomeron recurrence.

During the last 3–4 years a clear experimental evidence for DPE has emerged, as we shall see below.

6.1. Formalism

In terms of the above diagram

$$\frac{d\sigma^{DPE}}{dt_1\,dt_2\,d(M_1^2/s)\,d(M_2^2/s)} = \gamma_P(t_1)\,\gamma_P(t_2)\left(\frac{M_1^2}{s}\right)^{1-2\alpha_P(t_1)}\left(\frac{M_2^2}{s}\right)^{1-2\alpha_P(t_2)}\cdot\sigma_{PP}(M^2, t_1, t_2)\tag{6.1}$$

and the single diffractive background

$$\frac{d\sigma^{BG}}{dt_1\,dt_2\,d(M_1^2/s)\,d(M_2^2/s)} = \gamma_P(t_1)\,\gamma_R(t_2)\left(\frac{M_1^2}{s}\right)^{1-2\alpha_P(t_1)}\left(\frac{M_2^2}{s}\right)^{1-2\alpha_R(t_2)}\cdot\sigma_{PR}(M_1^2, t_1, t_2) + (1\leftrightarrow 2)\tag{6.2}$$

where the subscript R stands collectively for all the leading Meson exchanges. We also have the approx. equality

$$\frac{M_1^2}{s}\cdot\frac{M_2^2}{s}\simeq\frac{M^2}{s}\qquad\text{for } M^2\ll\langle P_{T\pi}^2\rangle\simeq 0.1.\tag{6.3}$$

Of course, the eq. (1) for the DPE cross-section can give only such general properties as the lack of correlation between the 2 outgoing protons (figs. 2 and 3 below). For a quantitative estimate of this quantity – its size and its dependence on the central cluster mass and rapidity as well as the incoming energy and momentum transfers – one has to invoke a model for $\sigma_{PP}(M^2, t_1, t_2)$. A standard practice has been to approximate the PP cross-section by the leading Regge behaviour, so that it is immediately related to the triple Regge couplings estimated in the last section.
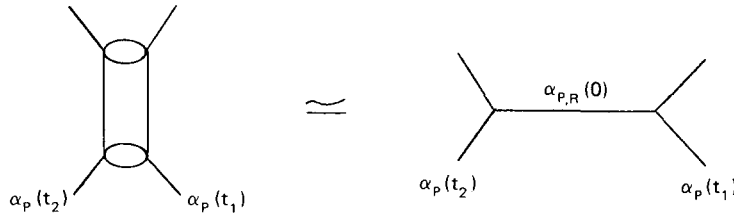
One has, of course, to bear in mind that the cross-section σ_{PP} corresponds to an even crossing amplitude and it peaks in the very low energy region $(M\simeq 0.5)$. Thus extrapolating the Regge contributions down to such low energies assumes a semilocal duality in Pomeron–Pomeron scattering which has not been adequately tested for any Reggeon–Reggeon scattering[†] [229]. None-the-less, let us proceed to calculate the DPE cross-section; we get

$$\frac{d\sigma^{DPE}}{dt_1\,dt_2\,d(M_1^2/s)\,d(M_2^2/s)} = \frac{G_{PPP}(t_1)\,G_{PPP}(t_2)}{\sigma_{PP}^P}\left(\frac{M_1^2}{s}\right)^{1-2\alpha_P(t_1)}\cdot\left(\frac{M_2^2}{s}\right)^{1-2\alpha_P(t_2)}\tag{6.4}$$

[†] The corresponding semilocal duality for Pomeron–proton or Pomeron–pion scattering seems to work down to the lowest resonance (N*(1400) or A₁) but not down to the Born term (p or π) [204, 197].

where G_{PPP} is precisely the triple Pomeron coupling of the last section and $\sigma_{\text{pp}}^{\text{P}}$ is the Pomeron contribution to the pp total cross-section ($\simeq 40$ mb). We have neglected the PPR contribution, since it is much smaller than the PPP. Following similar considerations for σ_{PR} we get

$$\frac{d\sigma^{\text{BG}}}{dt_1 \, dt_2 \, d(M_1^2/s) \, d(M_2^2/s)} = \frac{G_{\text{PPP}}(t_1) \, G_{\text{RRP}}(t_2)}{\sigma_{\text{pp}}^{\text{P}}} \left(\frac{M_1^2}{s}\right)^{1-2\alpha_{\text{P}}(t_1)} \cdot \left(\frac{M_2^2}{s}\right)^{1-2\alpha_{\text{R}}(t_2)} + (1 \leftrightarrow 2). \tag{6.5}$$

Now the analyses of the last section immediately tell us that in order for the DPE signal to dominate over the single diffractive background we must have†

$$M_1^2/s, M_2^2/s < 0.05. \tag{6.6}$$

Then the relation (3) above implies that for a reasonable bite of M^2, we must have $s > 400$. Thus the DPE signal is expected to show up only at FNAL and ISR energies; and the energy dependence can be studied only at the ISR. In fact all 3 experiments which show clear signals for DPE, which will be discussed below, are ISR experiments [230–232].

One may note that the rough magnitude of the DPE cross-section can already be obtained from eq. (4) above, i.e.

$$\sigma^{\text{DPE}}(M_{1,2}^2/s < 0.05) \simeq \sigma^{\text{D}}(M_1^2/s < 0.05) \cdot \sigma^{\text{D}}(M_2^2/s < 0.05)/\sigma_{\text{pp}}^{\text{P}} \simeq 2 \times 2/40 \text{ mb}. \tag{6.7}$$

The actual prediction is however a factor of 3 lower as we see below.

The predicted DPE cross-section and the BG are shown on a M_1^2/s and M_2^2/s plot in fig. 1 for $s = 940$ along with the experimental scatter plot [230]. For simplicity we have approximated the G_{PPP} by a single exponential

$$G_{\text{PPP}}(t) = A_{\text{P}} \, e^{B_{\text{P}}t} = 6.2 \, e^{7.9t}$$

and

$$\alpha_{\text{P}}(t) = 1 + 0.25t. \tag{6.8}$$

Since, the BG is relatively small over the region of interest and since a reliable separation between the vector–tensor and the pionic cont. to G_{RRP} is not provided by the single diffraction data, we have approximated the meson exchange by a single effective trajectory [208], with

$$G_{\text{RRP}}(t) = A_{\text{R}} \, e^{B_{\text{R}}t} = 200 \, e^{4.6t}$$

$$\alpha_{\text{R}}(t) = 0.2 + 0.5t. \tag{6.9}$$

The estimate of BG may be reliable to within a factor of 2, say. The central cluster decay seems to be dominated by the 2 pion mode for the region of interest $-M_{1,2}^2/s < 0.05$, i.e. $M < 1.5$. Hence we have multiplied the cross-sections (4) and (5) by $\frac{2}{3}$ to take care of the $\pi^0\pi^0$ mode, i.e.

$$\sigma_{\text{ch}}^{\text{DPE,BG}} = \frac{2}{3}\sigma^{\text{DPE,BG}} \tag{6.10}$$

† The nondiffractive background is negligible over this region and hence we shall ignore it.
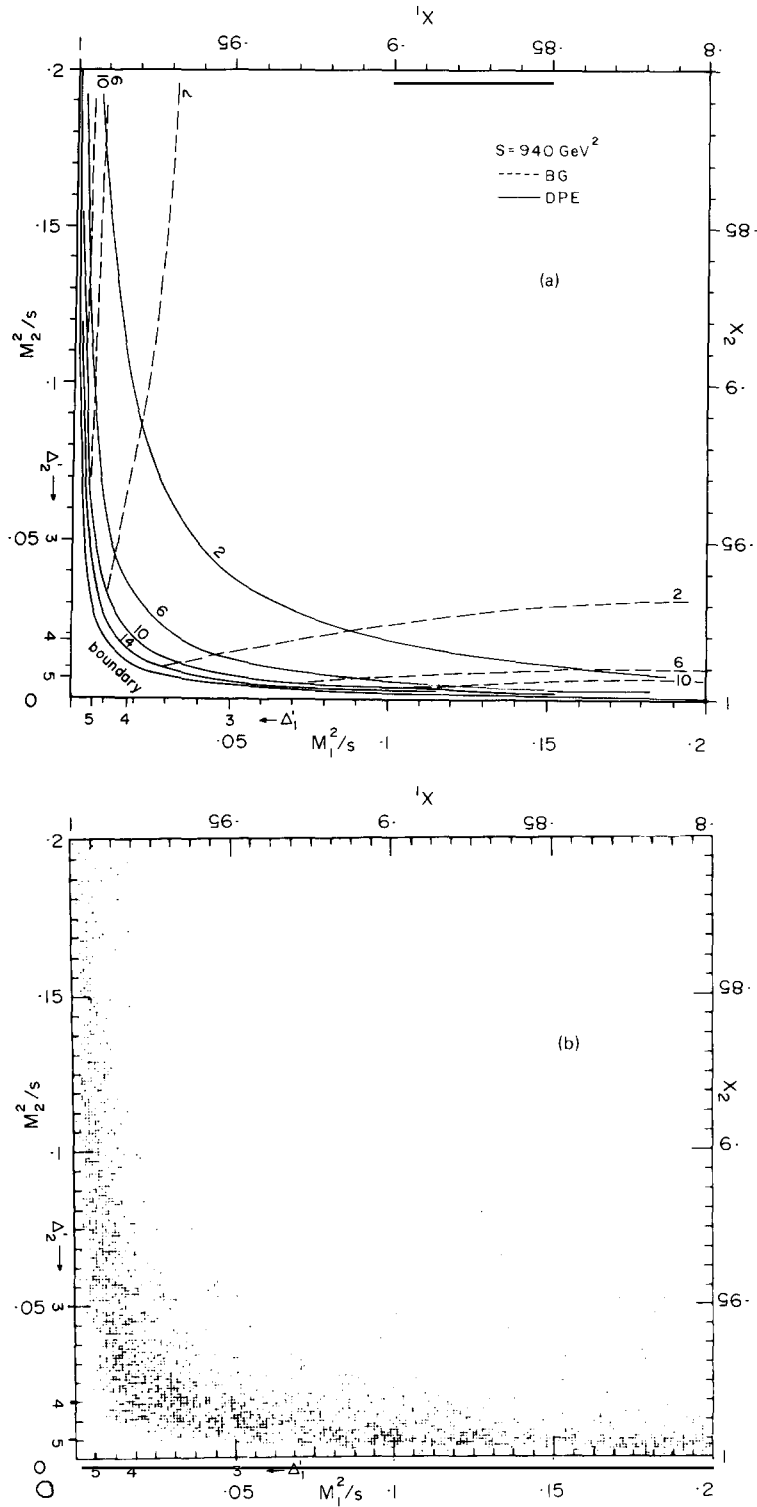
Fig. 6.1. (a) The DPE and BG contributions to $d\sigma_{ch}/d(M_1^2/s)\,d(M_2^2/s)$. The kinematic boundary corresponds to $s = 940\,\mathrm{GeV}^2$ ($\Delta_M^{min} = 0.5$). (b) The CCHK data for $d\sigma_{ch}/d(M_1^2/s)\,d(M_2^2/s)$ at 940 GeV^2. The $\Delta_M^{min} = 0.5(0)$ corresponds to a boundary point $\Delta_{1,2}^* = 4.25\ (4.5)$ or $M_{1,2}^2/s = 0.014\ (0.011)$. The data favours $\Delta_M^{min} = 0.5$.

to compare with the $pp \rightarrow pp\pi^+\pi^-$ data. Thus the quantities plotted are

$$\frac{d\sigma_{ch}^{DPE}}{d(M_1^2/s)\,d(M_2^2/s)} = \frac{2}{3}\left(\frac{A_P^2}{40}\right) \cdot \left(\frac{M_1^2}{s} \cdot \frac{M_2^2}{s}\right)^{-1}$$

$$\cdot \frac{\exp\{[B_P - 2\alpha'_P \ln(M_1^2/s)]t_1^{min} + [B_P - 2\alpha'_P \ln(M_2^2/s)]t_2^{min}\}}{[B_P - 2\alpha'_P \ln(M_1^2/s)][B_P - 2\alpha'_P \ln(M_2^2/s)]}$$ (6.4a)

and

$$\frac{d\sigma_{ch}^{BG}}{d(M_1^2/s)\,d(M_2^2/s)} = \frac{2}{3}\left(\frac{A_P A_R}{40}\right)\left(\frac{M_1^2}{s}\right)^{-1}\left(\frac{M_2^2}{s}\right)^{1-2\alpha_R(0)}$$

$$\cdot \frac{\exp\{[B_P - 2\alpha'_P \ln(M_1^2/s)]t_1^{min} + [B_R - 2\alpha'_R \ln(M_2^2/s)]t_2^{min}\}}{[B_P - 2\alpha'_P \ln(M_1^2/s)][B_R - 2\alpha'_R \ln(M_2^2/s)]} + (1 \leftrightarrow 2).$$ (6.5a)

Finally the kinematic boundary has been chosen as

$$\frac{M_1^2}{s} \cdot \frac{M_2^2}{s} \simeq \frac{M^2}{s} < \frac{0.2}{s}$$ (6.11)

in accordance with the experimental plot. This corresponds to an effective threshold in the central cluster production at

$$M \simeq 0.45$$ (6.11a)

which is also evident from the experimental M distribution (fig. 5b). It is essential to take care of this threshold in estimating the DPE cross-section as eq. (4) increases sharply with decreasing M. One sees from fig. 1a that

$$\sigma_{ch}^{DPE}(M_{1,2}^2/s < 0.05) \sim 20\,\mu b \quad \text{i.e.} \quad \sigma^{DPE}(M_{1,2}^2/s < 0.05) \sim 30\,\mu b$$ (6.7a)

which is about a third of the naive estimate of eq. (7) above. The reason simply is that the kinematic boundary (11) above severely cuts off the lower ends of the M_1^2/s and M_2^2/s distributions.

Since the DPE experiments use rapidity cuts let us recast the above formulae in the rapidity variables indicated in the following diagram.
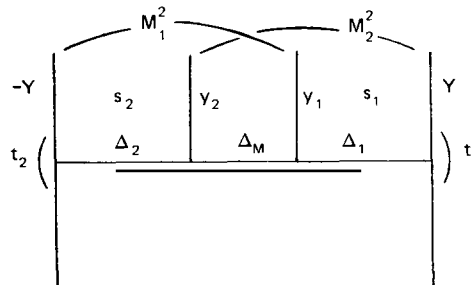
One can easily derive the following approximate relations

$$\Delta_1 = Y - y_1 \simeq \ln(s_1/\mu_T m_T) \tag{6.12a}$$

$$\Delta_2 = y_2 - (-Y) \simeq \ln(s_2/\mu_T m_T) \tag{6.12b}$$

$$\Delta_M = y_1 - y_2 \simeq \ln(M^2/\mu_T^2) \tag{6.12c}$$

which are valid as long as the rapidity differences are not too small (at least $>\frac{1}{2}$). This constraint is guaranteed for $\Delta_{1,2}$ by the experimental cuts. Although there is no explt. cut on Δ_M, the effective threshold cut-off (eq. (11a)) corresponds to a

$$\Delta_M^{min} \simeq \tfrac{1}{2}. \tag{6.11b}$$

Now

$$2Y = \ln(s/m_T^2) = \Delta_1 + \Delta_2 + \Delta_M \tag{6.13}$$

gives

$$s_1 s_2 = \mu_T^4 s/M^2. \tag{6.13a}$$

Similarly one can derive

$$\ln(M_1^2/\mu_T m_T) = 2Y - \Delta_1$$

$$\ln(M_2^2/\mu_T m_T) = 2Y - \Delta_2 \tag{6.14}$$

which give

$$M_1^2 s_1 = M_2^2 s_2 = \mu_T^2 s. \tag{6.14a}$$

From (13a) and (14a) the relation (3) above follows. Moreover using (14a) one gets (with $\langle \mu_T \rangle \simeq 0.35$, $\langle m_T \rangle \simeq 1$)

$$\Delta'_{1,2} \equiv \ln(s/M_{1,2}^2) = \ln(s_{1,2}/\mu_T m_T) + \ln(m_T/\mu_T) \simeq \Delta_{1,2} + 1. \tag{6.15}$$

Finally, the rapidity of the central cluster is given by

$$y_c \equiv \frac{y_1 + y_2}{2} = \frac{\Delta_2 - \Delta_1}{2}. \tag{6.16}$$

Of course, all practical applications of the above relations involve averaging over the transverse momenta, i.e. substituting μ_T and m_T by their average values. There may however be appreciable smearing effects near the boundaries of some of the rapidity cuts.

We shall consider 3 types of rapidity cuts relevant to the DPE experiments at ISR. The analysis here, closely follows the work of Desai et al. [233], with one important numerical difference, however. These authors use the triple Pomeron coupling of ref. [169], which is smaller than the present fit by a factor 1.5, as discussed in the last section. Hence their DPE estimate is smaller by a factor of 2 in normalisation. This seems to have been compensated, however, by their neglect of the threshold cut-off for cluster mass (eqs. (11a, b)), so that their integrated DPE cross-sections are very similar to ours [234].

(I) $\Delta_{1,2} > 3$ i.e. $\Delta'_{1,2} > 4$: Using eq. (15) the cross-sections (4a) and (5a) can be rewritten as

$$\frac{d\sigma_{ch}^{DPE}}{d\Delta'_1 d\Delta'_2} = \frac{2}{3}\left(\frac{A_P^2}{40}\right)\frac{\exp\{(B_P + 2\alpha'_P \Delta'_1)t_1^{min} + (B_P + 2\alpha'_P \Delta'_2)t_2^{min}\}}{(B_P + 2\alpha'_P \Delta'_1)\cdot(B_P + 2\alpha'_P \Delta'_2)} \tag{6.17}$$

$$\frac{d\sigma_{ch}^{BG}}{d\Delta'_1 d\Delta'_2} = \frac{2}{3}\left(\frac{A_P A_R}{40}\right)\frac{\exp\{-\Delta'_2(2 - 2\alpha_R(0))\}\cdot\exp\{(B_P + 2\alpha'_P \Delta'_1)\cdot t_1^{min} + (B_R + 2\alpha'_R \Delta'_2)\cdot t_2^{min}\}}{(B_P + 2\alpha'_P \Delta'_1)\cdot(B_R + 2\alpha'_R \Delta'_2)}$$
$$+ (1\leftrightarrow 2). \tag{6.18}$$

The integrated cross-sections

$$\sigma_{ch}^{DPE,BG} = \int_4^{\ln s - 2 - \Delta_M^{min}} d\Delta'_1 \int_4^{\ln s + 2 - \Delta_M^{min} - \Delta'_1} d\Delta'_2 \frac{d\sigma_{ch}^{DPE,BG}}{d\Delta'_1 d\Delta'_2} \tag{6.19}$$

where the integration limits easily follow from eqs. (13) and (15). It corresponds to the shaded triangle below.
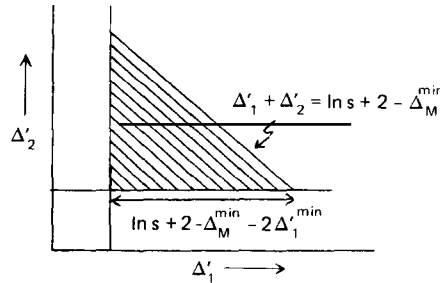
One can then easily see the gross features of the DPE cross-section and BG as functions of energy. Neglecting the t^{min} effect and the Pomeron slope, the integrand (17) becomes a constant. Hence the DPE cross-section is essentially given by the area of the triangle

$$\sigma_{ch}^{DPE} \propto (\ln s + 2 - \Delta_M^{min} - 2\Delta_1^{'min})^2. \tag{6.20}$$

On the other hand since (18) is strongly peaked at $\Delta_{2,1}^{'min}$, the integral is essentially proportional to twice the base of the triangle

$$\sigma_{ch}^{BG} \propto (\ln s + 2 - \Delta_M^{min} - 2\Delta_1^{'min}). \tag{6.21}$$

In either case the threshold is (with $\Delta_M^{min} \simeq \frac{1}{2}$) at $\ln s \simeq 6.5$ i.e. $s \simeq 700\,\text{GeV}^2$.

(II) $|y_{1,2}| < y^{max}(=1)$: For this it is convenient to use the variables y_c and Δ_M. One has

$$\frac{d\sigma}{dy_c\, d\Delta_M} = \frac{d\sigma}{d\Delta_1\, d\Delta_2} = \frac{d\sigma}{d\Delta_1'\, d\Delta_2'} \cdot \qquad (6.22)$$

The integrated cross-sections with the above rapidity cut are given by

$$\sigma_{ch}^{DPE,BG} = \int_{\Delta_M^{min}/2 - y^{max}}^{y^{max} - \Delta_M^{min}/2} dy_c \int_{\Delta_M^{min}}^{2(y^{max} - |y_c|)} d\Delta_M\, \frac{d\sigma_{ch}^{DPE,BG}}{dy_c\, d\Delta_M} \qquad (6.23a)$$

or alternatively by

$$\sigma_{ch}^{DPE,BG} = \int_{\Delta_M^{min}}^{2y^{max}} d\Delta_M \int_{\Delta_M/2 - y^{max}}^{y^{max} - \Delta_M/2} dy_c \frac{d\sigma_{ch}^{DPE,BG}}{dy_c\, d\Delta_M}. \qquad (6.23b)$$

Again one can easily see the energy dependence of $\sigma_{ch}^{DPE,BG}$ under the same approximations as above, where the DPE integrand (17) becomes a constant and the BG integrand (18) $\propto \exp\{-\Delta_2^{min}(2 - 2\alpha_R(0))\}$ i.e. $\exp\{-\ln s(1 - \alpha_R(0))\}$. Since the integration region is now independent of s we see that σ_{ch}^{DPE} is essentially a constant whereas σ_{ch}^{BG} goes down like $s^{-1+\alpha_R(0)}$. Of course, this cut merges with the cut I above for $\ln s = 8$ ($s \simeq 3000$ GeV^2) which is the top ISR energy. At lower energies the advantage of cut I is that it keeps the DPE signal to BG ratio large, whereas that of cut II is that it gives a larger cross-section and a larger kinematic range to study things like the cluster mass M and rapidity y_c dependence.

(III) $|y_{1,2}| < y^{max}(=1.5)$: The formulae (22) and (23) are applicable here, with $y^{max} = 1.5$ instead of 1.

From (23a) and (23b) one obtains the distribution in the cluster rapidity y_c and the cluster mass M. They are

$$\frac{d\sigma^{DPE,BG}}{dy_c} = \int_{\Delta_M^{min}}^{2(y^{max} - |y_c|)} d\Delta_M\, \frac{d\sigma^{DPE,BG}}{dy_c\, d\Delta_M} \qquad (6.24a)$$

$$\frac{d\sigma^{DPE,BG}}{dM} = \frac{2}{M} \int_{\Delta_M/2 - y^{max}}^{y^{max} - \Delta_M/2} dy_c\, \frac{d\sigma^{DPE,BG}}{dy_c\, d\Delta_M}. \qquad (6.24b)$$

6.2. Results and comparison with data

The three ISR experiments showing DPE signal are by the ARCGM [232], CHOV [231] and CCHK [230] groups. The latter two experiments use the split field magnet, and hence can measure all the momenta. The CCHK experiment is the most thorough one, spanning 5 energy points and a number of alternative cuts – in particular cut I (sample E) and cut II (sample B) and one corresponding to cut III at $s = 940$ GeV^2 (sample C). The CHOV experiment uses cut II and covers 2 energy points. The ARCGM experiment uses cut III and covers 4 energy points, but with a very limited t-bite. Besides this

experiment does not have momentum measurement for the outgoing particles†. None-the-less, having three experiments over the same energy range helps a good deal in cross-checking the results; and there seems to be general agreement amongst all the three, within their quoted uncertainties. Let us compare these data with the DPE predictions.

6.2.1. Correlation and t-dependence

A characteristic feature of the DPE signal is the lack of correlation between the 2 outgoing protons. This follows simply from eq. (1), i.e. does not require the duality assumption for the σ_{PP}. Fig. 2 shows the $\Delta\phi$ (azimuthal angle difference for the 2 outgoing protons) distribution of the CCHK data (cut II) at $s = 940\,\text{GeV}^2$. Evidently there is no azimuthal correlation between the 2 outgoing protons. This also agrees with the CHOV data at $s = 2025\,\text{GeV}^2$. However the $530\,\text{GeV}^2$ CHOV data seems to show an appreciable correlation. If confirmed, this would suggest a significant BG cont. at this energy. This would also explain the difference between the CCHK and the CHOV cross-sections at $530\,\text{GeV}^2$ (fig. 4), since the latter has been corrected for the observed correlation.

Fig. 3(a, b) shows the lack of correlation between the momentum transfers t_1 and t_2 for the above CCHK data. An uncorrelated exponential distribution

$$\mathrm{d}\sigma/\mathrm{d}t_1\,\mathrm{d}t_2 = e^{bt_1}\,e^{bt_2} \tag{6.25a}$$

can be re-expressed as

$$\frac{\mathrm{d}\sigma}{\mathrm{d}(t_1 + t_2)\,\mathrm{d}(t_1 - t_2)} = \tfrac{1}{2}\,e^{(b(t_1 + t_2))}. \tag{6.25b}$$

The resulting single distributions are

$$\frac{\mathrm{d}\sigma}{\mathrm{d}t_1} = \int_{-\infty}^{0} e^{b(t_1 + t_2)}\,\mathrm{d}t_2 = e^{bt_1}/b \tag{6.26a}$$

$$\frac{\mathrm{d}\sigma}{\mathrm{d}(t_1 + t_2)} = \tfrac{1}{2}\int_{t_1+t_2}^{-(t_1+t_2)} e^{b(t_1+t_2)}\,\mathrm{d}(t_1 - t_2) = -(t_1 + t_2)\,e^{b(t_1+t_2)}. \tag{6.26b}$$
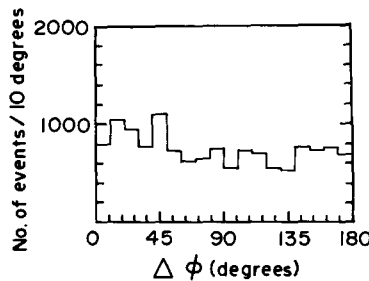
Fig. 6.2. Azimuthal correlation data for the 2 outgoing protons (CCHK experiment, cut II, $s = 940\,\text{GeV}^2$).

† Thus their measurement of t and the rapidity differences are only approximate.
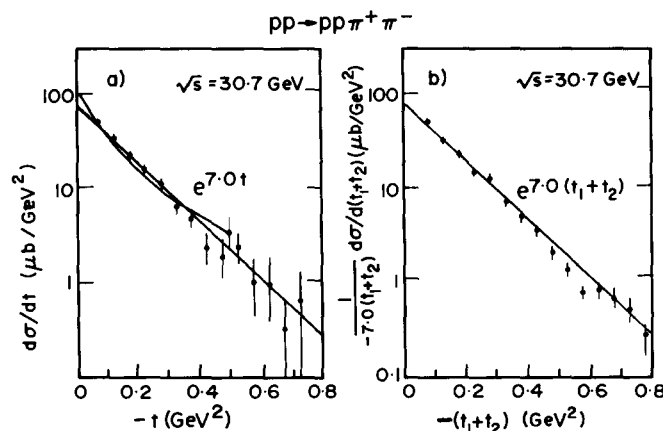
Fig. 6.3. The momentum transfer distributions of the CCHK data (cut II) at $940\,\text{GeV}^2$. The curved line in (a), shows the prediction from the PPP coupling of fig. 5.4.

The figures 3(a, b) demonstrate the equality between $d\sigma/dt_1$ and $(1/-b(t_1 + t_2))\,d\sigma/d(t_1 + t_2)$. This has also been verified with the CHOV and the ARCGM data.

Provided one makes the duality hypothesis for σ_{PP}, one can predict the $t_{1,2}$ dependence as well, i.e. from eq. (4). This is shown by the curved line in fig. 3a, with the G_{PPP} parametrisation of the last section (fig. 5.4). For the range $(0 > t > -0.5\,\text{GeV}^2)$ over which G_{PPP} was fitted the prediction is compatible with the experimental t_1 distribution. One may note in particular that the distribution shows no sign of a turnover as $t \rightarrow 0$.

6.2.2. Size and energy dependence

The predicted DPE and BG cross-sections are shown in table 1 for all the 3 cuts and for $\Delta_M^{min} = 0$ and 0.5. It is evidently sensitive to the choice of Δ_M^{min}. Since the experimental $\Delta_{1,2}$ distribution (fig. 1b) and M distribution (fig. 5b) suggest an effective threshold around $\Delta_M^{min} = 0.5$, the comparison with data should be done for this choice. This is shown in fig. 4. In view of the approximation involved, the agreement is quite impressive. The size of the cross-section and the energy dependence for the cuts II, III help to discriminate between the DPE and BG contributions. Both of them support the DPE to be the main contribution. One should note that for the cuts II and III, the energy dependence predictions for DPE and BG do not involve the duality assumption.

6.2.3. Cluster rapidity y_c and mass M dependence

The predicted y_c dependence of the DPE and BG contributions for cut II (eq. (24a)) are shown in fig. 5a along with the CCHK data. Again there is general agreement. One may note, however, that the peaking at $y_c = 0$ is largely a kinematic effect – the range of Δ_M integration goes down linearly with increasing y_c (eq. (24a)). This effect overwhelms the characteristic dynamical features of a central plateau and valley for the DPE and BG respectively. To discriminate between the shapes of the DPE signal and the BG one must have the y_c distribution for a fixed Δ_M bite, and also higher statistics than presently available.

The predicted M dependence of the DPE signal and BG (eq. (24b)) are shown in fig. 5b. Here we have chosen cut III, since the range for cut II $(0.45 < M < 0.9)$ is too small to study the shape. The data shown in this figure is the $940\,\text{GeV}^2$ CCHK data sample C $(\Delta_{1,2} > 2)$ which is essentially equivalent to
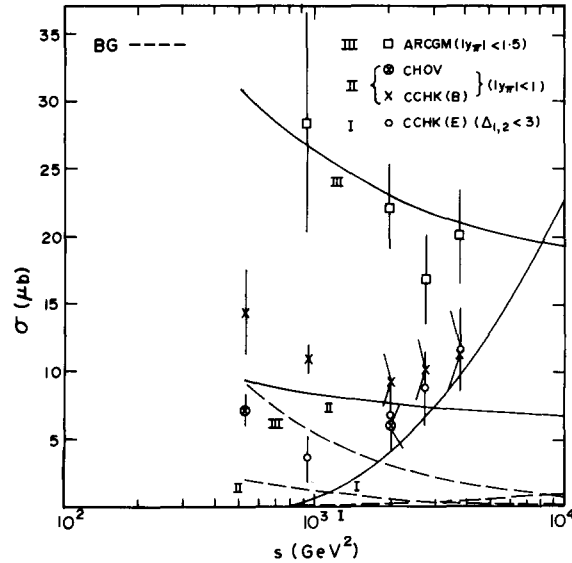
Fig. 6.4. Comparison of the predicted cross-sections for pp→ppπ⁺π⁻ with the experimental data (CCHK, CHOV and ARCGM) for the three kinematic cuts described in the text.

cut III at this energy. There is evidently good agreement with the experimental M distribution. However, one should again note that a sharp fall with increasing M is largely a kinematic effect – the range of y_c integration goes down linearly with increasing Δ_M (eq. (24b)). Thus the dynamical M^{-1} fall off due to DPE is accentuated into $M^{-2.5}$. Similarly the BG cont. falls off like $M^{-1.5}$ instead of rising like $M^{0.6}$ as per eq. (9).

One may finally note that there is no ρ signal in the ππ mass spectrum of CCHK (fig. 5b) and CHOV experiments in agreement with DPE. This is confirmed by the ππ angular distribution, which suggests a S-wave dominance.

It should be pointed out here that a fourth DPE probe experiment from ISR, by the CHM collaboration [235], does show a significant ρ signal. However, this experiment has a severe t cut $(t_1 < -0.35)$. This region contains only the tail end of the DPE signal and besides has poorer DPE/BG
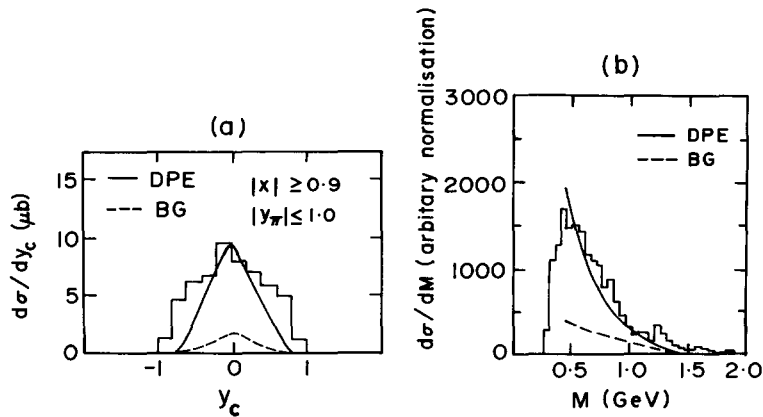
Fig. 6.5. (a) Comparison of the predicted y_c (cluster rapidity) distribution with the CCHK data (cut II). (b) Comparison of the predicted M (cluster mass) distribution with the CCHK data (cut III). Both the comparisons are made at $s = 940\,\text{GeV}^2$.

ratio compared to the CCHK cut ($t_{1,2} < -0.05$), since diffractive exchanges are sharply peaked in t. Indeed eqs. (8) and (9) suggest that the DPE signal contained in the CHM cut is only about 10% of that covered by CCHK, and the corresponding DPE/BG (i.e. PP/PR) ratio is smaller by a factor of 2. Thus whereas the PP/PR ratio for the CCHK cut is ~ 3 near ρ mass and ~ 1 near f (fig. 5b), the corresponding ratios for CHM are expected to be $\sim\frac{3}{2}$ and $\frac{1}{2}$ respectively. This enhancement of PR may still not be adequate to explain the ρ signal in the CHM data. It should be stressed, none-the-less, that the two cuts have very little overlap and to that extent there is no real contradiction between the two results.

We should add here that the CHM experiment has the advantage of being a genuine inclusive measurement ($pp \rightarrow ppX$) unlike the others. Therefore it will be very useful for DPE phenomenology if this measurement is extended to the low t region. Even with their present data they can do a meaningful test for the DPE signal by studying the energy dependence over the ISR range, for a fixed bite of low M (0.5 to 1) and y_c (-0.5 to 0.5), roughly corresponding to the cut II described above. Unfortunately the data analysed in ref. [235] correspond to a large mass region ($M^2 \simeq 10$–30) at fixed energy ($s \simeq 1000$) or a rather low energy region ($s \simeq 50$–1000) at fixed mass ($M = m_f$); and in either case and DPE signal is a priori expected to be negligible compared to the PR (and RR) background. This simply follows from the expected ratio PP/PR $\simeq 1/2$ at $M = m_f$ and $s \simeq 1000$, as noted above, and the extrapolation formula

$$\text{PP/PR} \propto (M^2/s)^{\alpha_R - \alpha_P}.$$

6.3. One pion exchange model

As an alternative to the duality hypothesis for the central vertex, several authors have worked with the OPE model [236, 237] shown below.
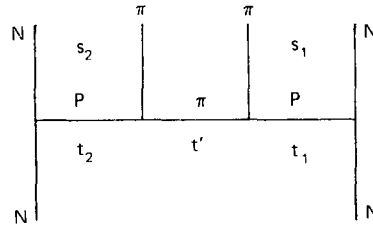
This essentially corresponds to a double Deck effect. The resulting cross-section is

$$\sigma^{\text{DPE}} = \frac{1}{16\pi^3 s^2} \int dt' \frac{e^{2at'}}{(\mu^2 - t')^2} \int ds_1 \cdot s_1 \sigma_{\text{el}}^{\pi N} \int ds_2 \cdot s_2 \sigma_{\text{el}}^{\pi N} \qquad (6.27)$$

where the pion pole is assumed to be $\sim e^{at'}/(\mu^2 - t')$. Unfortunately the cross-section is very sensitive to the slope parameter a. With $a \simeq 2$, as obtained from np charge exchange or Deck processes, the σ^{DPE} turns out to be too large by a factor of 3. A reasonable magnitude has been obtained, however, by changing a to $\simeq 4$ [233] or alternatively through some absorption mechanism [238].

6.4. Summary

(1) The three ISR experiments on $pp \rightarrow pp\pi\pi$ are in general agreement with each other. They provide rather strong evidence for DPE.

Table 6.1

The predicted DPE and BG contributions corresponding to the 3 experimental cuts are compared with the ISR data of CCHK (I and II), CHOV (II, shown in brackets) and ARCGM (III)

$\sqrt{s}$(GeV) \ σ(μb) Δ_M^{min}	I ($\Delta_{1,2} > 3$)					II ($|y_\pi| < 1$)					III ($|y_\pi| < 1.5$)				
	σ_{ch}^{DPE}		σ_{ch}^{BG}		σ_{ch}^{Expt}	σ_{ch}^{DPE}		σ_{ch}^{BG}		σ_{ch}^{Expt}	σ_{ch}^{DPE}		σ_{ch}^{BG}		σ_{ch}^{Expt}
	0.5	0	0.5	0		0.5	0	0.5	0		0.5	0	0.5	0	
23						7.5	13.2	2.0	3.0	14.4±3.1 (7.1±1.0)	21.0	29.8	9.5	11.9	
31	0.4	2.0	0.03	0.2	3.6±1.7	7.4	12.9	1.3	1.9	11.0±1.2	20.7	29.3	6.1	7.5	28.4±8.1
45	3.9	8.0	0.3	0.5	6.8±2.7	7.1	12.4	0.7	0.9	9.4±1.9 (6.0±1.5)	20.0	28.4	3.2	3.7	22.2±3.1
53	6.4	11.5	0.4	0.6	8.8±2.8	7.0	12.2	0.5	0.7	10.2±2.1	19.7	28.0	2.2	2.8	16.8±3.3
62	9.5	15.4	0.6	0.8	11.7±3.0	6.9	12.1	0.35	0.53	11.5±3.0	19.4	27.6	1.7	2.1	20.2±3.3
100	21.9	30.3	1.0	1.2		6.6	11.5	0.15	0.23		18.6	26.4	0.7	0.9	

(2) The support for DPE comes from the lack of correlation between the 2 outgoing protons and also from the energy dependence of the cross-section.

(3) In addition, the magnitude of the cross-section and its dependence on the momentum transfers $(t_{1,2})$ and the cluster mass M all agree with the prediction of DPE plus a semilocal duality hypothesis for the Pomeron–Pomeron cross-section. One may regard this as experimental support for both the hypotheses.

(4) The DPE cross-section rises exponentially down to $-t_{1,2} \simeq 0.05$, i.e. it shows no sign of vanishing near $t_{1,2} \simeq 0$.

(5) The features 2 and 3 support a factorising pole nature of Pomeron. The feature 4 then shows that the asymptotic constraint has no visible effect on DPE at ISR energies. The same were true about single diffraction and the PPP coupling discussed in the last section. It seems one can describe all diffractive processes up to the highest ISR energy, in terms of a factorising pole Pomeron, with an intercept ≥ 1, and normal residues – i.e. the asymptotic constraints seem to have little impact on finite energy phenomenology.

(6) DPE has been suggested as a "laboratory" for producing rare objects – f', η_c, glue balls etc. However, at ISR energy a reasonably clean DPE signal $(\Delta_{1,2} > 2.5)$ is restricted to the range $M < 1.5$. The corresponding range would go up to 4 GeV at the $\bar{p}$ collider energy. Even at ISR energy one can increase the cluster mass range by relaxing the $\Delta_{1,2}$ cuts, provided one uses specific final states as filters – e.g. K^+K^- for f' or 4π for glue ball.

7. Central region

According to the Feynman scaling hypothesis the inclusive cross-section in the central region (C.M. rapidity $y \simeq 0$) approaches a constant value at high energy. Furthermore, it is supposed to be independent of the rapidity y as well, thus giving an energy independent central plateau. This is the so-called pionisation plateau. Of course, the same thing is supposed to hold for the production of heavier particles too, but at relatively higher energies.

In the Mueller–Regge picture this corresponds to the double Regge diagram
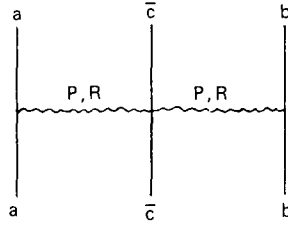
The leading term, corresponding to 2 Pomeron exchange, has these scaling features, i.e.

$$\frac{d\sigma}{\pi \, dy \, dp_T^2} = \gamma_{PP}(\kappa) \, u^{\alpha_P(0)-1} \cdot t^{\alpha_P(0)-1} = \gamma_{PP}(\kappa) \tag{7.1}$$

independent of s and y, for $\alpha_P(0) = 1$. The nonleading terms, corresponding to Pomeron–Reggeon and Reggeon–Reggeon exchanges give

$$\frac{d\sigma}{\pi \, dy \, dp_T^2} = \gamma_{PR}(\kappa) \cdot u^{\alpha_P(0)-1} t^{\alpha_R(0)-1} + (t \leftrightarrow u)$$

$$= \kappa^{-1/2} s^{-1/4} [\gamma_{PR}(\kappa) e^{-y/2} + \gamma_{RP}(\kappa) e^{y/2}]$$

$$= 2\gamma_{PR}(\kappa) \cdot \kappa^{-1/2} s^{-1/4} \cosh(y/2), \quad \text{for identical incident particles} \tag{7.1a}$$

and

$$\frac{d\sigma}{\pi \, dy \, dp_T^2} = \gamma_{RR}(\kappa) \, t^{\alpha_R(0)-1} u^{\alpha_R(0)-1} = \gamma_{RR}(\kappa) \cdot \kappa^{-1} s^{-1/2} \tag{7.1b}$$

where the summation over the leading vector and tensor meson trajectories is implied in γ_{PR} and γ_{RR}. Now, the simplest generalisation of the Harari–Freund 2-component duality to the 7-component scheme described earlier (subsection 1.3.3), implies the γ_{PR} term (corresponding to the components 5 and 6) to be zero if $a\bar{c}$ and $b\bar{c}$ are exotic and positive otherwise. Similarly the γ_{RR} term (corresponding to the component 3) is predicted to be zero if $ab\bar{c}$ is exotic (which will be true for almost all the processes of interest) and positive otherwise. According to these generalised EXD scheme, the central cross-sections should show precocious scaling for exotic $a\bar{c}$ and $b\bar{c}$ and approach the scaling limit from above if they are nonexotic.

Experimentally, however, all the central cross-sections rise with energy† in contrast to the dual Regge prediction. This has been known from the very beginning of the inclusive game, but initially the rise was believed to be restricted to the sub-ISR energies, at least for pionisation. In fact, the early ISR data was consistent with a constant pionisation cross-section within 10–15 per cent. However, the second generation of ISR experiments have shown as much as a 40 per cent rise for the π^- cross-section. Thus not only is the approach to scaling predicted by duality and the Mueller–Regge model invalid, but even the Feynman scaling phenomenon itself is in serious doubt.

---

† Only the pp → px central cross-section shows an initial fall which can be attributed to a spill over from the fragmentation region.

7.1. Models

There have been a plethora of models, attempting to explain this anomaly, and many of them are in the Regge framework. The present section would be devoted largely to reviewing models of this latter category. We should mention here that although the main attempt of these models have been to explain the energy dependence of the pionisation cross-section, there are two other features of the pionisation data which would provide important checks on the validity of these models. These are (1) the shape of the pionisation cross-section in y, which shows a significant curvature; and (2) the shrinkage of its p_T distribution with increasing energy.

7.1.1. Exchange degeneracy breaking

This was the first model proposed for the central cross-section rise [35]. As discussed earlier in subsection 1.3, it does away with the Harari–Freund hypothesis that the vacuum exchange (topological Pomeron) is simply represented by a singularity at $\alpha = 1$. Instead it assumes that the topological Pomeron (i.e. component 2 in the 2-component model or the components 5, 6 and 7 in the 7-component model), has an important nonleading singularity at the Reggeon level ($\alpha = \frac{1}{2}$) with a negative residue.

To see the motivation let us recall that duality predicts exchange degeneracy only for the planar amplitudes. That is, the planar component 1 is predicted to be zero (positive) for an exotic (nonexotic) 2-body system ab; and the planar components 1–4 are predicted to be zero (positive) for an exotic (nonexotic) 3-body system abc̄. It is possible, however, that the nonplanar components, generated through unitarity, have a singularity at the Reggeon level ($\alpha = \frac{1}{2}$). Then the physical amplitudes would have non-zero Reggeon contribution even for exotic channels, i.e. exchange degeneracy would be broken. In fact, Tye and Veneziano have given a plausibility argument based on unitarity, that the nonplanar components 5, 6 and 7 have a negative nonleading singularity at the Reggeon level. Moreover, specific Dual Unitarisation Models for the 2-body case give a negative nonleading singularity for the non-planar amplitude (component 2) at the Reggeon level [32]. At the same time one has to bear in mind the phenomenological successes of exchange degeneracy for the total and the inclusive cross-sections (fragmentation region). These would suggest against a large nonleading term in the component 2 for the 2 body case, and in the components 5 and 6 for the inclusive case. However, it is possible for the component 7 to have a large negative nonleading ($\alpha = \frac{1}{2}$) contribution, which could account for the central cross-section rise.

Up to the 1st nonleading term, the model gives, at $y = 0$,

$$\frac{\mathrm{d}\sigma}{\pi\,\mathrm{d}y\,\mathrm{d}p_T^2} = A(p_T^2) - B(p_T^2)s^{-1/4}. \tag{7.2}$$

Of course, the model has no prediction about the size of the central cross-section rise, i.e. the relative magnitude of B to A. None-the-less, it would have considerable predictive value if the pionisation data from the PS energy onwards could be fitted by the above 2 parameter formula. For, in addition to predicting the shape of the pionisation cross-section rise to be linear on a $s^{-1/4}$ plot, it would relate the slopes of these straight lines for different incident particles. This was believed to be the case before or even during the early ISR data on $pp \to \pi^\pm X$ which were consistent with a 10–15 per cent rise, as expected from a linear extrapolation from the PS and NAL energies. In particular there were attempts to fit the PS and NAL pionisation data for different incident particles, by straight lines and relate their slopes through factorisation [239–244], sometimes with conflicting results. However, with the improved

ISR data showing a 40 per cent rise for the $pp \to \pi^{\pm}X$ cross-sections, it is clear that the linear formula (2) cannot describe these cross-sections even for $s \geq 50\,\text{GeV}^2$ (fig. 1). Consequently there has been a loss of interest in this model for the central cross-section rise.

We should mention for completeness, that adding the 2nd nonleading term we get

$$\frac{d\sigma}{\pi\, dy\, dp_T^2} = A(p_T^2) - B(p_T^2)s^{-1/4} + C(p_T^2)s^{-1/2} \tag{7.3}$$

where C could have either sign. This formula can describe the $pp \to \pi^{\pm}X$ data of fig. 1 as we shall see later. Of course, the coefficient B now is very different from that obtained from the Ferbel's plot [239-243]. Unfortunately one cannot estimate the corresponding coefficient for other incident particles, since these data are limited to sub-ISR energies. Thus one cannot test the factorisation constraint. In summary, the exchange degeneracy breaking model, in its more general form (eq. (3)), is not ruled out by the ISR data. However, it can predict neither the gross size nor the shape of the central cross-section rise; nor can it relate the available data on these cross-section rise for different incident particles. Hence it seems to be of limited phenomenological interest.

7.1.2. Threshold effect in multiperipheral model

This is by far the most popular model for the central cross-section rise, within the Regge framework [245-250]. The source of the rise in this model is very different from that in the Mueller–Regge approach above. The rise, according to this model, is similar to the threshold rise of the total cross-section before it shows a constant (or const. $+s^{-1/2}$) behaviour. (See the diagram below.)
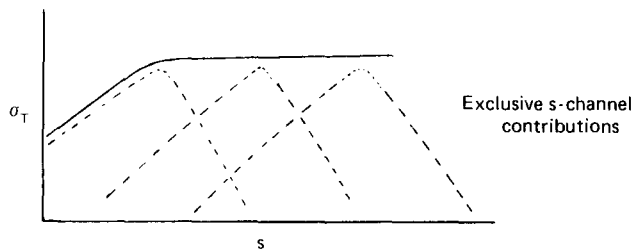
The latter part is simpler to interpret in terms of the t-channel Regge singularities and optical theorem but hard in terms of the exclusive s-channel contributions. In contrast the threshold rise is easier to understand in terms of the phase space factors of the exclusive s-channel contributions, but hard in terms of the t-channel Regge singularity. For the central cross-section rise, therefore, the model dispenses with the Mueller–Regge description in terms of the t-channel Regge exchanges. Instead it describes the central inclusive cross-section as a sum of the exclusive production cross-sections, which are described in turn by a multiperipheral model. Then the sharp t-dependence of the production vertex, characteristic of the multiperipheral model (or alternatively of the p_T cut-off of multiparticle data) together with the dependence of $t^{\min}$ on the total energy, results in a rapid rise of the central cross-section over the ISR energy range. Thus the rise is not of purely kinematic origin but comes from the interplay of a dynamical effect (the sharp t-dependence of the production vertex) with the kinematic one (the energy dependence of $t^{\min}$). We shall see later that with most reasonable choice of parameters, the predicted rise over the ISR range is in fact larger than the observed rise.

It should be emphasised, of course, that the multiperipheral model provides a consistent description of the total (or the inclusive) cross-section as a sum of exclusive s-channel contributions, which displays not only the threshold rise but the asymptotic Regge behaviour as well [47, 65]. Thus it is not a complimentary approach to the Mueller–Regge prescription but rather a specific dynamical realisation of this; and naturally it has more predictive power (see subsection 1.5).

For a detailed analysis we shall take the model of Caneschi [249, 250], as its connection with the standard multiperipheral model is most explicit. In this model, the cross-section for $pp \to cX$ is given by the square of the diagram below.
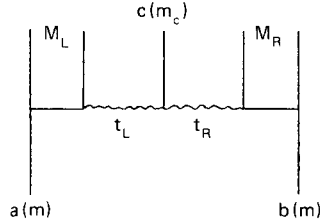
The c stands for a pion in the old version of the multiperipheral model and for a cluster of mass $\simeq 1$ GeV in the new version. The s dependence of the $pp \to cX$ cross-section is given by

$$\frac{d\sigma}{\pi \, dy \, dp_T^2} = \frac{C}{s} \int_{s_{LO}}^{s_{ac}} \frac{dM_L^2}{s_{ac}} (M_L^2 - s_{LO})^{\alpha_P} \int_{s_{RO}}^{s_{bc}} \frac{dM_R^2}{s_{bc}} (M_R^2 - s_{RO})^{\alpha_P} \int_{-\infty}^{t_M^{min}} \int_{-\infty}^{t_R^{min}} \exp\{A(t_L + t_R)\} \, dt_L \, dt_R$$

$$= \frac{C}{A^2 s} \int_{s_{LO}}^{s_{ac}} \frac{dM_L^2}{s_{ac}} (M_L^2 - s_{LO})^{\alpha_P} \int_{s_{RO}}^{s_{bc}} \frac{dM_R^2}{s_{bc}} (M_R^2 - s_{RO})^{\alpha_P} \cdot \exp\{A(t_L^{min} + t_R^{min})\}. \tag{7.4}$$

For the thresholds one may put

$$s_{LO} = s_{RO} = (m + m_c)^2 \tag{7.5}$$

and for $y = 0$, we have

$$s_{ac} \equiv (P_a + P_c)^2 = m^2 + m_c^2 + \kappa\sqrt{s}$$
$$s_{bc} \equiv (P_b + P_c)^2 = m^2 + m_c^2 + \kappa\sqrt{s}$$
$$\kappa = \sqrt{m_c^2 + p_T^2}. \tag{7.6}$$

The $t_{L,R}^{min}$ are given by

$$t_{L,R}^{min} = m^2 + M_{L,R}^2 + 2qq_{L,R} - \sqrt{s(q_{L,R}^2 + M_{L,R}^2)} \tag{7.7}$$

where

$$q = \tfrac{1}{2}\sqrt{s - 4m^2} \tag{7.8}$$

and

$$q_{L,R} = \frac{1}{2(\sqrt{s}-\kappa)}\{[(\sqrt{s}-\kappa)^2 - (M_{L,R} - \sqrt{M_{R,L}^2+p_T^2})^2][(\sqrt{s}-\kappa)^2 - (M_{L,R}+\sqrt{M_{R,L}^2+p_T^2})^2]\}^{1/2}.$$

(7.9)

Strictly speaking, eq. (7) above for $t_{L,R}^{\min}$ is exact only for $p_T = 0$. One can check, however, that it is an extremely good approximation for moderate $p_T (<1 \text{ GeV})$.

We see from the eq. (4) that the leading term in the $M_L^2(M_R^2)$ integration goes like $s_{ac}^{\alpha_P}(s_{bc}^{\alpha_P})$, corresponding to a s-independent cross-section. However, there are negative nonleading terms $s_{ac}^{\alpha_P-1}(s_{bc}^{\alpha_P-1})$ coming firstly from the $s_{LO}(s_{RO})$, but more importantly from the $s_{ac}^{-1}(s_{bc}^{-1})$ term present in $t_L^{\min}(t_R^{\min})$. As a result the cross-section has a negative nonleading term $\propto s^{-1/2}$. Although these nonleading terms in s_{ac} and s_{bc} were obtained without reference to the Mueller's optical theorem, they can be interpreted in terms of the Mueller–Regge singularities. For the square of the above diagram simply corresponds to:
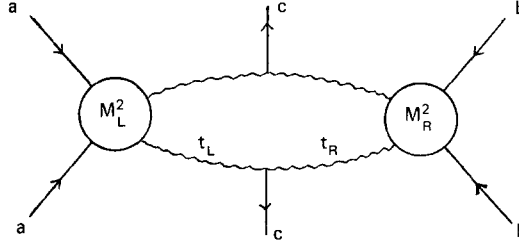
and taking the Pomeron singularity in the Reggeon-particle channels (M_L^2 and M_R^2) and doing the loop integration generates the leading Pomeron singularity along with a series of daughters in the channels $a\bar{c}$ and $b\bar{c}$.

Before evaluating the integral (4) above, one may get a qualitative estimate of the nonleading term. This involves evaluating the integral via mean value theorem, i.e.

$$\frac{d\sigma}{\pi\,dy\,dp_T^2} = \frac{C}{A^2 s} \cdot \frac{(s_{ac}-s_{LO})(s_{bc}-s_{RO})}{s_{ac}\cdot s_{bc}} \cdot (\bar{M}_L^2 - s_{LO})^{\alpha_P} \cdot (\bar{M}_R^2 - s_{RO})^{\alpha_P}$$
$$\cdot \exp\{A(t_L^{\min}(\bar{M}_{L,R}^2)+t_R^{\min}(\bar{M}_{L,R}^2))\}$$

(7.4a)

where the mean values $\bar{M}_{L,R}$ are estimated assuming the last factor to be a constant [249]. With $\alpha_P = 1$,

$$\bar{M}_{L,R}^2 = \tfrac{1}{2}[\kappa\sqrt{s}+m_c^2+m^2+(m+m_c)^2]$$

which gives after a lengthy but straightforward algebra

$$t_{L,R}^{\min}(\bar{M}_{L,R}^2) = -\tfrac{3}{4}\kappa^2 - [2\kappa(m_c^2+mm_c+\tfrac{1}{4}p_T^2)+\tfrac{3}{2}\kappa^3]/\sqrt{s} + O(1/s).$$

(7.10)

Substituting these in (4a) one gets

$$\frac{d\sigma}{\pi\,dy\,dp_T^2} = \frac{C\kappa^2}{A^2}\left[1 - \frac{\{3(m+m_c)^2-(m-m_c)^2\}}{\kappa\sqrt{s}} - \frac{A\{4\kappa(m_c^2+mm_c+\tfrac{1}{4}p_T^2)+3\kappa^3\}}{\sqrt{s}}\right] + O(1/s).$$

(7.4b)

In the older version of the multiperipheral model, where the pions are produced directly on the multiperipheral chain, we have $m_c = 0.14$, $\langle p_T^2 \rangle \simeq 0.1$ and the corresponding $A \simeq 5$. Then eq. (4b) reduces to $\propto 1 - 7/\sqrt{s}$. The s-dependence, coming from an exact evaluation of the eq. (4) is shown in table 1 (1st column). The 2nd column shows the prediction with both Reggeon and Pomeron exchange present in channels $(M_{L,R}^2)$ with equal strength, i.e.

$$\frac{d\sigma}{\pi \, dy \, dp_T^2} = \frac{C}{A^2 s} \int_{s_{LO}}^{s_{ac}} \frac{dM_L^2}{S_{ac}} ((M_L^2 - s_{LO})^{\alpha_P} + (M_L^2 - s_{LO})^{\alpha_R}) \int_{s_{RO}}^{s_{bc}} \frac{dM_R^2}{S_{bc}} ((M_R^2 - s_{RO})^{\alpha_P}$$

$$+ (M_R^2 - s_{RO})^{\alpha_R}) \cdot \exp\{A(t_L^{min} + t_R^{min})\}. \tag{7.11}$$

Since the two exchanges seem to occur with roughly equal strength in the total cross-section data, this should be a more realistic prediction of the model. Although the predicted rise of a factor of 2 between the PS and ISR energies is in rough agreement with data, the rise cannot be sustained through the ISR energy range. The 3rd column shows the rise at $x = 0.1$. There is a significant slowing down of the rise with increasing x (or y) in rough agreement with data. The shape in x (or y) is also in rough agreement. The last column shows the rise at $x = 0$, but for a higher p_T (=0.3). We note a small increase in the rise with increasing p_T, which is in disagreement with the observed shrinkage, however. The last 2 features (the slowing down of the rise away from the central region and the antishrinkage) are expected to hold also for the multiperipheral cluster model, discussed below.

Over the past 5 years, there have been overwhelming experimental evidences suggesting that the pions are not produced directly on the multiperipheral chain but through clusters of mass $m_c \simeq 1$ GeV and $\langle p_T^2 \rangle \simeq \frac{1}{2}$ GeV^2 (corresponding to $A \simeq 2$ GeV^{-2}). They come from the correlation analyses (next section) and also from the inclusive ρ, ω, η, f production data which seem to account for the bulk of the pion production [251]. With these values, eq. (4b) gives a s-dependence $\propto 1 - 40/\sqrt{s}$. Such a big nonleading term would mean firstly that $d\sigma/dy$ rises violently even for the ISR energy range and secondly that the higher order terms cannot be neglected*.

The $d\sigma/dy$ rise coming from the exact evaluation of eq. (11) is shown in table 2, for 3 values of the cluster mass $m_c = 1.25$, 1 and 0.75 GeV. It is also possible that $\sqrt{s_{LO}}$ and $\sqrt{s_{RO}}$, corresponding to the baryonic cluster mass, are not as large as $m + m_c$. Therefore, we have also shown the $d\sigma/dy$ rise for $\sqrt{s_{LO}}$ and $\sqrt{s_{RO}} = m + \frac{1}{2}m_c$. In general the predicted rise seems to be stronger than the data, even for the ISR range. If one sticks, however, to the lower end of the admissible range of mesonic and baryonic

Table 7.1
Pionisation cross-section rise for a multiperipheral pion model

s (GeV^2) / $d\sigma/dy$ (arbitrary units)	$P_T^2 = 0.1$ $x = 0$ P	$P_T^2 = 0.1$ $x = 0$ P + R	$P_T^2 = 0.1$ $x = 0.1$ P + R	$P_T^2 = 0.3$ $x = 0$ P + R
40	0.58	2.52	1.56	0.82
126.5	1.36	4.31	2.19	1.95
400	2.09	5.17	2.28	2.55
1265	2.64	5.35	2.21	2.73
4000	3.00	5.20	2.13	2.69

* This analysis was first done by Caneschi [250]. Unfortunately the numerical results of this work are incorrect.

Table 7.2

Pionisation cross-section rise for a multiperipheral cluster model (P + R; $x = 0$; $p_T^2 = \langle P_T^2 \rangle = 0.55$ GeV^2; $A \simeq \langle P_T^2 \rangle^{-1} = 1.9$ GeV^{-2}). Compare the 2nd column of table 1

s (GeV^2)	$d\sigma/dy$ (arbitrary units) $s_{LO}, s_{RO} = (m + m_c)^2$ m_c (GeV)			$s_{LO}, s_{RO} = (m + \frac{1}{2} m_c)^2$ m_c (GeV)		
	1.25	1	0.75	1.25	1	0.75
40	0	0	0.1	0	0.2	1.4
126.5	0.05	0.5	4	0.9	3.4	10.6
400	0.93	3.7	12	3.5	8.8	20.2
1265	3.01	8.2	20	5.9	12.8	25.7
4000	5.13	11.7	24	7.3	14.8	27.9
12650	6.57	13.6	26	8.0	15.5	28.3
40000	7.35	14.5	27	8.2	15.6	27.9

cluster masses (i.e. $m_c = 1$ GeV and $\sqrt{s_{LO}}$, $\sqrt{s_{RO}} = m + \frac{1}{2} m_c$), then the predicted rise of 60 per cent over the ISR range is not too far from the experimental rise of 40 per cent. But the two cannot be reconciled over the sub-ISR energies. The discrepancy may be due to the fact that with a cluster mass of $\simeq 1$ GeV and a mean cluster multiplicity of $\simeq 3$ pions, the average number of clusters produced is less than 4 at PS energies and is only 6–8 even at ISR. Thus the multiperipheral model in the simple form above is expected to work only at much higher energies than originally supposed – perhaps only ISR energies and above. Significant subasymptotic modifications are expected at lower energies. It should be noted in this connection that a recent multiperipheral cluster model calculation by Arneodo and Meunier [252], with a cluster mass $\simeq 1.3$ GeV, in fact gets a central cross-section decreasing from the FNAL to the ISR energies. The main difference of their model from the above is that they take the $M_{L,R}^2$ dependence of the Reggeon-particle amplitudes from an exclusive multi-Regge model via a Monte Carlo calculation, instead of their asymptotic approx. in terms of the leading Regge (P + R) exchanges. The latter has a strong phenomenological support, however, from the triple Regge analyses (sections 3, 5), where these Reggeon–particle amplitudes were seen to be well approximated by the leading Regge (P + R) exchanges down to rather low M^2. All the same, the above mentioned work helps to illustrate the degree of uncertainty in the model predictions at sub-ISR energies. Keeping this in mind, we have shown the predicted rise up to $s = 40000$, a typical energy for the Isabelle machine. One should note that the predicted rise flattens out rapidly after the ISR range, reflecting the $s^{-1/2}$ behaviour of the nonleading term. For instance the minimal choice of cluster masses, giving a 60 per cent rise in the range $400 < s < 4000$ gives only a 5 per cent rise in the range $4000 < s < 40000$, and the maximal choice, giving a 500 per cent rise over the former range gives only a 40 per cent rise over the latter.

Another characteristic prediction of the model is, of course, that the π and ρ production data should show a similar rise. This seems to be consistent with whatever ρ production data is available so far (fig. 4). Similarly a faster rise for $\bar{K}$ and $\bar{p}$ production is a natural feature of this model; as they would be associated with heavier clusters. Of course, a quantitative prediction for these processes is even more difficult, as it would involve the properties of these new clusters in addition to the mesonic and baryonic clusters mentioned above. Finally, the model seems to have one serious problem in common with its earlier version, i.e. in accounting for the observed shrinkage. We can think of no natural modification which can account for this.

In summary, the multiperipheral cluster model provides by far the most plausible explanation for the pionisation cross-section rise. On a quantitative level, however, its use is limited at best to the ISR

energies and above. It seems to have a problem also in the qualitative level, i.e. to account for the observed shrinkage in p_T.

In the models discussed above, the rise in the pionisation cross-section is completely unrelated to the total cross-section rise observed in the ISR range. There have been models, however, where these two rises are closely related. These are discussed below.

7.1.3. Gribov calculus and eikonal models

Although the asymptotic form of the Gribov calculus is completely different from the eikonal model, it is very similar to the latter in its perturbative form, which seems to be justified for any realistic range of energy. They involve summing over multiple Pomeron exchanges in the s-channel, as shown below:
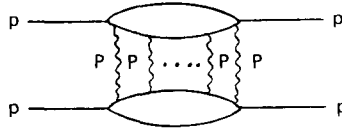
The only difference is that the s-channel intermediate states (the blobs) are restricted to the elastic channel in the eikonal model, whereas the Gribov calculus includes the diffractive inelastic channels as well. We shall describe below the Gribov calculus results for the total and the pionisation cross-section rise; but the essential conclusions would be valid also for the Cheng–Wu type eikonal models [253].

There are also two versions of the Gribov calculus model – (a) without and (b) with the energy conservation constraint. Essentially the version (a) is the pure Gribov calculus model whereas in version (b) some finite energy modifications are imposed on it. The formalism is almost identical for the 2 cases, but the phenomenological contents are very different.

The first point in the formalism is that the ν-Pomeron exchange diagram above gives a contribution to the pp total cross-section

$$\sigma^\nu = S_\nu X_\nu^2 \tag{7.12}$$

where

$$S_\nu = \sigma_B(-\tfrac{1}{2}Z)^{\nu-1}\frac{1}{\nu(\nu!)}$$

$$Z = \frac{\sigma_B}{4\pi(R^2 + \alpha_P' \ln s)}$$

$$\sigma_B = g^2 s^{\alpha_P(0)-1} \tag{7.13}$$

$$g_{PP}^P(t) = g\,\exp(\tfrac{1}{2}R^2 t).$$

Note that σ_B is the 1 Pomeron exchange Born term; and the above formulae are the familiar eikonal model results except for the factor X_ν which takes care of inelastic diffraction via an enhancement factor λ [254], i.e.

$$X_\nu = \tfrac{1}{2}[(1+\lambda)^\nu + (1+\lambda)^\nu]. \tag{7.14}$$

More precisely the low mass part (PPR) of inelastic diffraction is taken care of by this λ factor, whereas the scaling part (PPP) is added separately, as we shall see later.

The second and the most important point is that the s-channel unitarity content of the ν-Pomeron exchange diagram is given by the AGK cutting rule [255]. According to this, the diagram contributes to diffractive, multiperipheral and polyperipheral states, arising out of cutting it through zero, one and more than one Pomeron lines (diagram below) with given weight factors.
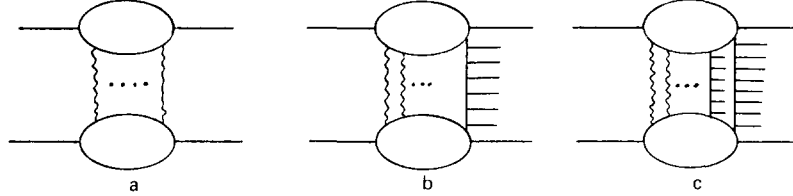
The weight factors are*

$$B^{\nu}_{n \geq 1} = (-)^{n-1} \frac{\nu!}{n!(\nu-n)!} 2^{\nu-1}; \qquad B_0 = 1 - 2^{\nu-1} \tag{7.15}$$

with

$$\sum_{n=0}^{\nu} B^{\nu}_n = 1.$$

Thus the 2-Pomeron exchange contributes to the diffractive $(n = 0)$, multiperipheral $(n = 1)$ and polyperipheral $(n = 2)$ states with weights -1, 4 and -2.

Version (a): If one does not impose any energy conservation constraint, then the production cross-section for the n-polyperipheral state relative to the multiperipheral state is simply given by the relative weight factors (15). Moreover, the average pion multiplicity (or pion density on the rapidity plot) for the former is simply n times that of the latter. Hence they contribute to $d\sigma/dy$ with weight factors nB^{ν}_n, i.e.

$$\frac{d\sigma}{dy} = \sum_{\nu=1}^{\infty} \sigma^{\nu} \sum_{n=1}^{\nu} nB^{\nu}_n \tag{7.16}$$

apart from a constant factor. Now one can easily check from eq. (15) that

$$\sum_{n=1}^{\nu} nB^{\nu}_n = 0 \qquad \text{for any } \nu \neq 1 \tag{7.17}$$

which is a generalisation of the cancellation between the 4×1 and -2×2 factors for 2-Pomeron exchange case mentioned above. This is the famous AGK cancellation, which means that $d\sigma/dy$ is simply given by the one Pomeron exchange Born term,

$$d\sigma/dy \propto \sigma_B \propto s^{\alpha_P(0)-1}. \tag{7.18}$$

---

* This applies to the eikonal model as well.

Thus if the Pomeron intercept $\alpha_P(0)$ is larger than 1 by Δ, then the pionisation cross-section is simply predicted to rise like s^Δ.

Capella et al. [221] have obtained a bare Pomeron intercept of 1.13, i.e.

$$\Delta = 0.13$$

from a detailed fit to the pp total cross-section rise using this model. However the precise value of Δ is sensitive to the detailed model assumptions, as we see from the simple considerations below. Restricting to 1 and 2 Pomeron exchange, one gets

$$\sigma_B = \sigma_T + \sigma_{el} + \sigma_D$$

i.e. the 1 Pomeron exchange Born term equals the sum of total, elastic and the inelastic diffraction cross-sections. With the inelastic diffraction rising by $\simeq 3$ mb over the ISR (as we saw in the section 5) and the corresponding rises of 4 and 1 mb for the total and the elastic cross-sections, one has a Born term going up from 55 to 63 mb. This corresponds to a $\Delta \simeq 0.07$.

The $\Delta = 0.07$ corresponds to a 15 per cent rise for the central cross-section over the ISR range, whereas the $\Delta = 0.13$ value corresponds to a 30 per cent rise. Of course, the rise continues indefinitely in this model. The other features of this model are a flat y-distribution and a rise which is independent of p_T (no shrinkage or antishrinkage) and also of the particle type (same rise for π, $\bar{K}$ and $\bar{p}$). All the three features are, of course, characteristic of a single pole exchange in the above Mueller amplitude, and all are at variance with the data.

Quite apart from the question of the central cross-section rise, however, the model has 2 serious problems, which may be inter-related.

(1) It violates energy-momentum conservation, at least asymptotically. The simplest way to see this [256] is to consider the sum rule

$$\frac{1}{\sigma_T} \int\limits_{-Y}^{Y} dy \int dp_T^2 \frac{d\sigma}{dy\, dp_T^2} (E + p_L)_c = \sqrt{s}$$

i.e.

$$\frac{1}{\sqrt{s}} \int\limits_{-Y}^{Y} dy \frac{d\sigma}{dy} e^y = \text{const.} \times \sigma_T \qquad (7.19)$$

with $Y = \frac{1}{2}\ln s$ and $y = \ln\{(E + P_L)/\kappa\}$. This follows from energy-momentum conservation and unitarity. Although a summation over the detected particle c is implied in this sum rule, we can restrict to pion for obtaining the following lower bound. Since the AGK cancellation gives $d\sigma/dy \propto s^\Delta$ over a region $-(1-\varepsilon)Y < y < (1-\varepsilon)Y$ for arbitrarily small ε, the left hand side has a lower bound $s^{\Delta-\varepsilon/2}$. This is inconsistent with the Froissart bound for σ_T for $\Delta > \frac{1}{2}\varepsilon$. And since the model satisfies s-channel unitarity, the inconsistency evidently implies violation of energy-momentum conservation. (2) The second problem which is phenomenologically more serious, is that the nondiffractive cross-section ($n \geq 1$) seems to satisy a Poissonian multiplicity distribution up to an incident momentum of 400 GeV/c

at least, whereas the model predicts a significant broadening at the high multiplicity end [257]. This is due to the polyperipheral terms $(n > 1)$ which have average multiplicities n times the multiperipheral term. The relative magnitudes of these terms

$$\sigma_n = \sum_{\nu=n}^{\infty} \sigma_n^{\nu} = \sum_{\nu=n}^{\infty} \sigma^{\nu} B_n^{\nu} \tag{7.20}$$

are fixed by eqs. (12–15). Thus the size of the high multiplicity tail is fairly unambiguous, and its discrepancy with the exponential multiplicity distribution seems to be quite serious.

Version (b): The energy-momentum conservation problem can be overcome by directly incorporating this constraint into the model, as first shown by Chang and Yan [256]. They postulated that for the polyperipheral term with n cut Pomerons, the total energy $\sqrt{s}$ is shared equally between the n chains. Thus each chain has an effective s

$$s_n = s/n^2. \tag{7.21}$$

The average multiplicity for this term is then

$$n(\ln s - 2 \ln n) \tag{7.22}$$

as compared to $\ln s$ for the multiperipheral term. This means that the pion density of the nth polyperipheral term is still n times that of the multiperipheral term at $y = 0$, but the width of rapidity distribution goes down with increasing n. Thus the AGK cancellation no longer holds for the entire rapidity range $\pm\frac{1}{2}\ln s$; and as a result the inconsistency associated with eq. (19) above is averted*. Moreover, the same modification also helps to remove the discrepancy with the observed multiplicity distribution as shown by Snider and Wyld [257]. The reason simply is that the eq. (22) gives an appreciable reduction of the polyperipheral multiplicity from the original value $n \ln s$. For instance, at $\ln s \simeq 6$, corresponding to the top of the fitted energy range, the average multiplicity for $n = 2$ relative to $n = 1$ goes down from 2 to 1.5. Thus the departure from a Poissonian distribution is significantly reduced at the available energies.

These energy conservation effects are expected, of course, to reduce not only the multiplicity of the polyperipheral terms but also their magnitude σ_n at finite energies. As a result one can reproduce the 10 per cent rise of σ_T over the ISR range even with a Pomeron intercept of 1, as shown by Capella and Kaidalov [254]. The corresponding rise of the pionisation cross-section is $\simeq 25$ per cent. They postulate a suppression factor

$$K_n(s) = \exp\left\{-\sum_{j=1}^{n} \frac{1}{s_j}\right\}, \qquad (n \geq 1)$$

$$K_0(s) = 1. \tag{7.23}$$

Moreover, instead of the energy equi-partition formula (21), they postulate a sequential partition

---

* One can in fact see that the average n goes up in this model like s^{Δ}; and since the AGK cancellation is expected to hold between $\pm(\frac{1}{2}\ln s - \ln\langle n\rangle)$, corresponding to a $\varepsilon \simeq 2\Delta$, the inconsistency is precisely averted [254].

formula for the jth chain

$$s_j = [(1-\alpha)^2]^{j-1} \alpha^2 s \qquad (7.21a)$$

where α is fraction of energy going into pion production. But, for comparison, we shall also show some of the results for the equipartition formula (21). The nondiffractive cross-section $\bar{\sigma}$ and the pionisation cross-section $d\sigma/dy|_{y=0}$ are given by

$$\bar{\sigma} = \sum_{n=1}^{\infty} \sigma_n K_n \qquad (7.24)$$

$$d\sigma/dy = \sum_{n=1}^{\infty} n\sigma_n K_n. \qquad (7.25)$$

The σ_n is given by eq. (20) and eqs. (12–15). In fact, the summation over ν can be done analytically, giving

$$\sigma_n = \frac{\sigma_B}{3n} [(1+\lambda)^2 F_n(Z_1) + (1-\lambda)^2 F_n(Z_2) + (1-\lambda^2) F_n(Z_3)] \qquad (7.26)$$

where

$$Z_1 = (1+\lambda)^2 Z, \qquad Z_2 = (1-\lambda)^2 Z, \qquad Z_3 = (1-\lambda^2)Z,$$

and

$$F_1(Z) = \frac{1-e^{-Z}}{Z}$$

$$F_n(Z) = \frac{1-e^{-Z}}{Z} - \frac{e^{-Z}}{Z} \left(Z + \frac{Z^2}{2!} \cdots \cdots + \frac{Z^{n-1}}{(n-1)!} \right), \qquad n>1.$$

The parameters used were

$$g^2 = 61.885 \text{ mb}, \qquad R^2 = 3.3 \text{ GeV}^{-2}, \qquad \alpha'_P = 0.25 \text{ GeV}^{-2}, \qquad \lambda = 0.4$$

which were taken from a fit to the pp elastic scattering. The Pomeron intercept was taken at the so-called critical value* $\alpha_P(0) = 1.0042$. Of course, the slight excess over 1 is of little phenomenological consequence. Finally α is set $= \frac{1}{3}$.

The resulting nondiffractive total cross-section and pionisation cross-section are shown in table 3. The individual contributions σ_n and $\sigma_n K_n$ are also shown for $n = 1$ to 5. It is interesting to note that the bulk of the pionisation cross-section rise comes not from the $n = 2$ term, but from those with $n \geq 3$.

This does not include, of course, the contribution from the triple Pomeron term. However, this term may not affect the energy dependence significantly, as the rising σ_{PPP} is partly compensated by the

---

* This corresponds to a renormalised intercept of 1 – the renormalisation being done by the triple Pomeron coupling.

Table 7.3

The nondiffractive cross-section $\Sigma_{n \geq 1} \sigma_n K_n$ and the pionisation cross-section $\Sigma \, n\sigma_n K_n$ from Gribov calculus model with finite energy modification. All the cross-sections are in mb

	ln s = 4		6		8		10	
n	σ_n	$\sigma_n K_n$	σ_n	$\sigma_n K_n$	σ_n	$\sigma_n K_n$	σ_n	$\sigma_n K_n$
1	18.4	15.6	20.1	19.6	21.6	21.6	23.1	23.1
2	7.1	4.1	7.5	6.9	7.8	7.7	8.1	8.1
3	3.5	0.9	3.6	3.0	3.7	3.6	3.7	3.7
4	1.9	0.08	1.9	1.2	1.9	1.8	1.8	1.8
5	1.1	0.0006	1.1	0.4	1.0	0.9	0.9	0.9
	$\sum_{n=1}^{10} \sigma_n K_n$	$\sum_{n=1}^{10} n\sigma_n K_n$	$\sum_{n=1}^{10} \sigma_n K_n$	$\sum_{n=1}^{10} n\sigma_n K_n$	$\sum_{n=1}^{10} \sigma_n K_n$	$\sum_{n=1}^{10} n\sigma_n K_n$	$\sum_{n=1}^{10} \sigma_n K_n$	$\sum_{n=1}^{10} n\sigma_n K_n$
	20.7	26.9	31.2 (33.6)	49.7 (58.6)	36.1 (36.7)	62.6 (66.1)	38.4	67.1

falling kinematic factor. One can get a qualitative estimate of this contribution by restricting to the lowest order in ν (=2). Then the contributions to σ_{in} and $d\sigma/dy$ are

$$-\sigma_{PPP}(4K_1' - 2K_2' - K_0')$$ (7.24a)

$$-\sigma_{PPP}(4K_1' - 4K_2')$$ (7.25a)

where the kinematic factors are assumed, as in ref. [254], to be

$$K_n'(s) = e^{-1/M^2} \cdot K_n(s/M^2), \qquad n \geq 1$$ (7.23a)

$$K_0'(s) = 1$$

with an effective $M^2 \simeq 5$. Using the phenomenological estimate of σ_{PPP} from section 5* one gets the following contributions at the two ends of the ISR energy range:

$(\sigma_{in})_{PPP}$	$(d\sigma/dy)_{PPP}$	ln s
−4 mb	−3.25 mb	6
−5.6 mb	−0.9 mb	8

of course these estimates are only qualitative, since one is restricting to the lowest order in ν and besides the kinematic factors (23a) are even more speculative than (23). It is also possible that a part of the PPP contribution have already been accounted for through the choice of the λ factor.

We see from table 3, that the model predicts a 15 per cent rise for $\bar{\sigma}$. Adding to this the above estimate for $(\sigma_{in})_{PPP}$ would give a 10 per cent rise for the sum. This essentially corresponds to a 10 per cent in the total inelastic cross-section σ_{in}, since this sum = $\sigma_{in} - \sigma_{PPR}$; and σ_{PPR} is small and practically energy independent.

---

* Unfortunately the σ_{PPP} values used in ref. [254] are roughly smaller by a factor of 2.

The corresponding rise in the pionisation cross-section is 25 per cent with possibly another 5 per cent coming from the triple Pomeron contribution. However, both the σ_{in} and the pionisation cross-section rises are sensitive to the choice of the kinematic factors $K_n(s)$. To illustrate this, the results for the energy equipartition formula (21) are shown in the brackets, for the ISR energy range. One sees that both the rise go down by a factor of 2.

The other phenomenological features of the model are the following: (1) The rise slows down appreciably beyond the ISR range. For instance, the 25 per cent rise over the ISR range $\ln s = 6$ to 8 corresponds to only a 7 per cent rise over $\ln s = 8$ to 10. (2) Since the width of the rapidity distribution goes down with increasing n, one expects the pionisation cross-section to be convex in y. For the same reason the rate of rise should go down with increasing y. (3) K^- and $\bar{p}$ cross-sections are expected to show a faster rise than π, since the kinematic suppression for a chain containing K^- or $\bar{p}$ should be more severe. For the same reason one expects some antishrinkage in p_T. It is practically impossible of course, to quantify these effects. It is interesting to note, however, that all these features are very much unlike the pure Gribov calculus model with $\alpha_P(0) > 1$ (i.e. the version (a) above) but very similar to the multiperipheral model.

In summary, the pure Gribov calculus or eikonal model seems to have serious conflict with the observed Poissonian multiplicity distribution in addition to violating asymptotic energy-momentum conservation. The version, incorporating the energy-momentum conservation constraint, can reproduce the multiplicity distribution in the available range (going up to 400 GeV/c incident momentum), but the departure from the Poissonian shape would show up at higher energies. A significant departure at the highest ISR energy has been claimed in ref. [257], although it seems to us that the size is sensitive to the choice of the energy distribution function etc. In any case, the multiplicity distribution data at the highest ISR energy will be very helpful. If it shows a distinct broadening over the Poissonian shape at the high multiplicity end, it would provide the first experimental evidence for this model. On the other hand a roughly Poissonian distribution at this energy can still be reconciled with this model, but it will make the model phenomenologically less attractive. As regards the pionisation cross-section rise, the model prediction is sensitive to the choice of parameters, but is in general a little over twice the rise in the total inelastic cross-section. Thus if one assumes the model to account for the 10 per cent rise in the total inelastic cross-section over the ISR range, then the corresponding pionisation cross-section rise is fairly unambiguous (≈ 25 per cent). The other feature of the predicted pionisation cross-section are similar to the model II above.

7.1.4. Dipole Pomeron model

The dipole Pomeron has been invoked before as a model for the total cross-section rise. It gives a logarithmic rise for the total cross-section and can also reproduces the observed geometrical scaling property of the elastic amplitude [258]. Its application to the central inclusive corss-section has been worked out by Roberts [259]. Substituting a dipole Pomeron in the double Regge exhcange diagram gives an invariant cross-section

$$\frac{d\sigma}{\pi \, dy \, dp_T^2} = \beta(\kappa^2)\left(\ln\frac{t}{s_0}\right)\left(\ln\frac{u}{s_0}\right) = \tfrac{1}{4}\beta(\kappa^2)\left[\left(\ln\frac{\kappa^2 s}{s_0^2}\right)^2 - 4y^2\right].$$ (7.27)

Note that the rise depends on the scale-parameter s_0, which is expected to be different from one process to another. Thus there is no quantitative correlation in this model between the pionisation and the total cross-section rises. However, the size of the observed pionisation cross-section rise would require an

extremely small scale parameter ($s_0 \simeq m_\pi^2$), for which one sees no prior justification. Moreover, although eq. (27) has some convexity in y, the magnitude is far smaller than the observed y-dependence (figs. 5, 6). All these make the model rather unattractive. There is one attractive feature of this model, however – this is about the only model which can naturally account for the shrinkage in p_T. This is evident from eq. (27), assuming of course that the scale parameter is insensitive to κ. The size of the shrinkage also seems to be in agreement with data (fig. 7).

7.1.5. Other models

Finally let us discuss some models of the total cross-section rise, which have negligible impact on the pionisation cross-section rise. The purpose is simply to demonstrate that a rise in the total cross-section does not necessarily lead to a rise in the pionisation cross-section.

Firstly consider the s-channel unitarity model, i.e., the so-called 2-component model [207]. Here the total nondiffractive cross-section (i.e. the multiperipheral component) is simply described by a pole Pomeron with intercept $\simeq 1$. The rise of the diffractive component σ_{PPP} over the ISR range ($\simeq 3$ mb) completely accounts for the 10 per cent rise of the total inelastic cross-section. This corresponds to only a 5 per cent rise of the pionisation cross-section, since the average multiplicity associated with a PPP term is only half that of the nondiffractive term, as discussed in section 5. Although the model is known to conflict with t-channel unitarity, it has been quite popular in view of its phenomenological successes. The modern version of this model, where the multiperipheral component is treated via cluster emission has been phenomenologically the most popular model both for pionisation cross-section rise (i.e. model II above) and for the correlation phenomena (to be discussed in the next section).

Secondly there have been attempts to attribute the total cross-section rise to the opening up of the antiproton–proton pair production [260–265]. Let us look at its prediction for the pionisation cross-section. From the ISR antiproton spectrum one gets a total antinucleon production cross-section

$$\sigma_{\bar{N}} = \int \frac{d\sigma_{\bar{N}}}{dy_{\bar{N}}} dy_{\bar{N}} = 2 \int \frac{d\sigma_{\bar{P}}}{dy_{\bar{P}}} dy_{\bar{P}}$$

which goes up by 6 mb over the ISR range ($\sigma_{\bar{N}} = 4 \rightarrow 10$ mb). This means that the remaining nondiffractive cross-section

$$\sigma_0 = \sigma_{in} - \sigma_D - \sigma_{\bar{N}} \tag{7.28}$$

should go down by 6 mb (from 22 to 16 mb), which is attributed in this model to a bare Pomeron intercept $\alpha_P(0) < 1$. Now, the pionisation cross-section associated with the $N\bar{N}$ term is expected to show a kinematic suppression relative to σ_0. This has been parametrised by Chiu and Tow [266]:

$$\rho_{\bar{N}}(y_\pi) = \int dy_{\bar{N}} \frac{d\sigma_{\bar{N}}}{dy_{\bar{N}}} \left[1 - \exp\left\{ -\frac{(y_\pi - y_{\bar{N}})^2}{\Delta^2} \right\} \right] \frac{\rho_0(y_\pi)}{\sigma_0} \tag{7.29}$$

where Δ has been estimated to be $\simeq 1$. Such a suppression factor implies the rise in $\rho_{\bar{N}}(0)$ is in fact less than the fall in $\rho_0(0)$. Putting in the ISR antiproton spectrum one sees that the sum $\rho_{\bar{N}}(0) + \rho_0(0)$ goes down by 7 per cent, which is enough to neutralise the 5 per cent rise expected from the PPP contribution.

Lastly one can consider combinations of different models, as for instance, the $N\bar{N}$ production model

above with a pure eikonal or Gribov calculus model for the remainder. Such models would account for the 6 mb fall for σ_0 quite naturally, that is with $\alpha_P(0) = 1$. This simply comes from the $-2\sigma_D$ term occurring in the nondiffractive cross-section. With a constant ρ_0, resulting from the AGK cancellation, the sum $\rho_{\bar{N}}(0) + \rho_0(0)$ would rise by 25–30 per cent. One should note, however, that there are versions of eikonal and Gribov calculus model without the AGK cutting rule – i.e. where one has the $-2\sigma_D$ term at the single chain level without any polyperipheral term. For this version, of course, the pionisation predictions are identical to the earlier case – i.e. a $\rho_{\bar{N}} + \rho_0$ falling by 7 per cent over ISR.

7.2. Fits to the central cross-section data

We shall describe in this section some quantitative fits to the central cross-section data.

7.2.1. s-dependence

Consider first the s-dependence of the invariant cross-section $d\sigma/\pi \, dy \, dp_T^2$ at fixed y (=0) and P_T (=0.2 GeV). We shall take the simplest formulae characteristic of the models (I–IV) above (see eqs. (3), (4b), (18) and (27)), i.e.

$$
\begin{align}
&\text{(I)} \quad A - Bs^{-1/4} + Cs^{-1/2} \\
&\text{(II)} \quad A - Bs^{-1/2} + Cs^{-1} \\
&\text{(III)} \quad As^B \\
&\text{(IV)} \quad [A + B \ln s]^2
\end{align}
\tag{7.30}
$$

and leave the parameters free, to be determined by the fits. We are treating them of course, as empirical formulae inspired by the above models, rather than as realistic parametrisation of these model predictions. Thus, for instance, the B-parameter in II will not be constrained by the values obtaining from the multiperipheral cluster model (II); and that in III will not be constrained to be the same for π and $\bar{p}$ production, as required by the pure Gribov calculus (or eikonal) model (IIIa). Unfortunately we do not have a simple parametric form for the Gribov calculus model with the energy conservation threshold (IIIb). However, its phenomenological features are very similar to the model II, as discussed earlier.

The experimental $\pi^{\pm}$, (p, $\bar{p}$) and $K^{\pm}$ cross-sections are shown in figs. 1, 2 and 3 respectively, for the ISR, FNAL, Serpukov and the top PS energies. The ISR data points are from the British–Scandinavian–MIT collaboration [267], which are consistent with the earlier British–Scandinavian data [268] (not shown), but considerably more accurate. It gives roughly a 40 per cent rise for $\pi^{\pm}$, 50 per cent for K^+, 70 per cent for K^- and 80 per cent for $\bar{p}$, whereas p is essentially flat. Quantitative fits to the K cross-sections have not been attempted since it has large uncertainties, particularly at the low energy end. For the same reason quantitative fits to the ρ cross-section shown in fig. 4 have not been attempted.

The fits to the π^- and $\bar{p}$ cross-sections with formulae (30) are shown in figs. 1 and 2. (The corresponding particle–antiparticle differences are fitted separately below.) The corresponding parameter values and χ^2/ν are shown in table 4. All the data points down to the top PS energy ($s = 46$) are included in the fit, except for the fit II for π^- which is restricted to the ISR and FNAL points. One sees that essentially all the 4 formulae give acceptable fits over this energy, despite some discrepancies at the lowest energy point ($s = 46$). The predictions diverge significantly, however, beyond the ISR
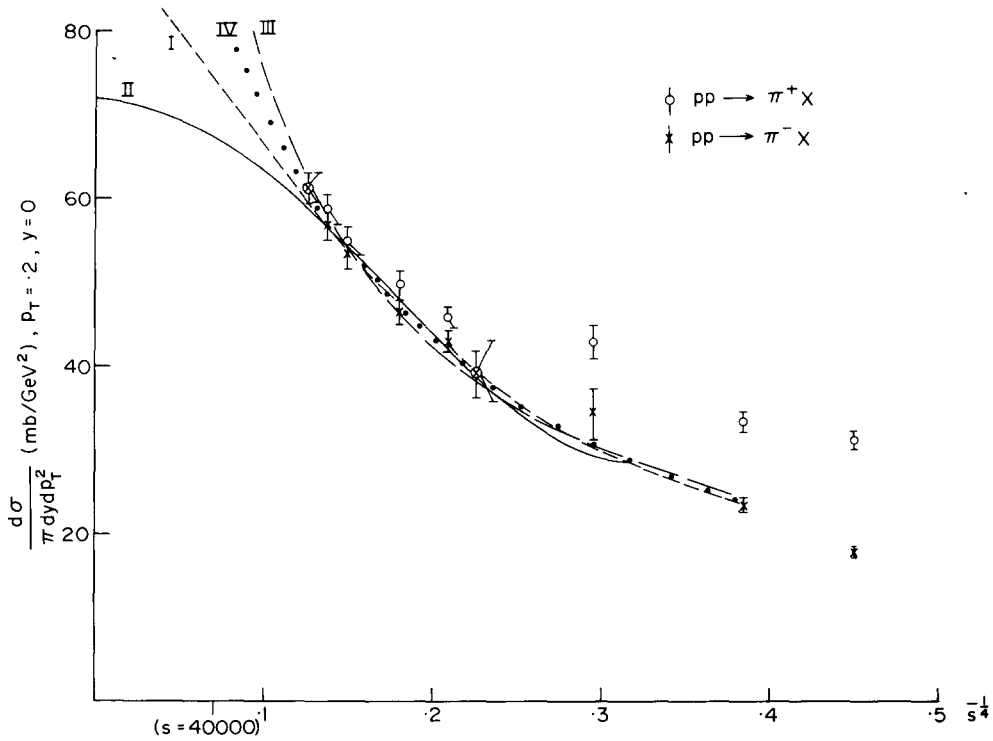
Fig. 7.1. Central cross-sections for pp→π±X. In addition to the ISR data points [267], those from FNAL [269], Serpukov [270], and the PS energy [212] are also shown. The fits to the π⁻ cross-section are with the formulae of eq. (30).
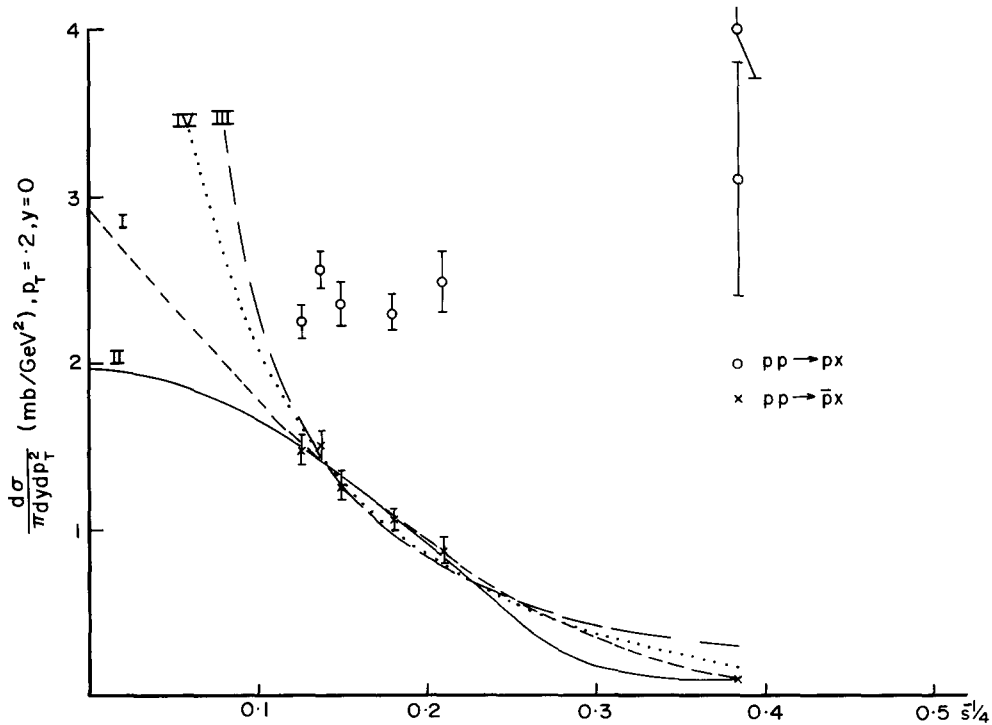
Fig. 7.2. Central cross-sections for pp→(p, p̄)X. In addition the ISR data [267], the 24 GeV/c data points of refs. [212, 271] are shown. The fits to the p̄ cross-sections are with the formulae of eq. (30).

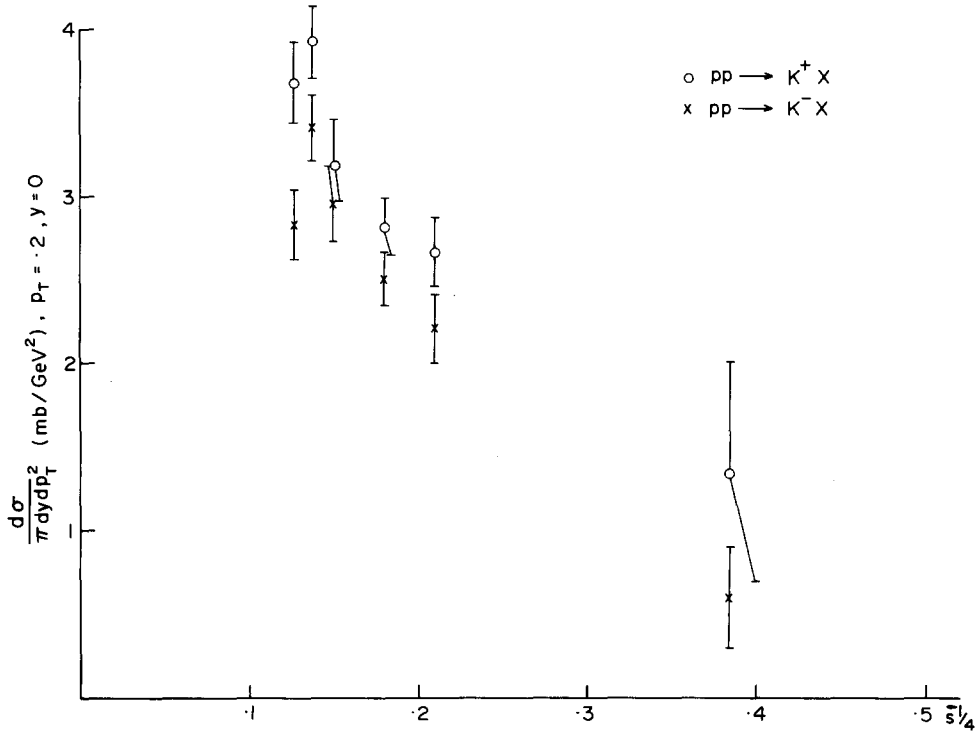Fig. 7.3. Central cross-sections for pp→K±X. In addition to the ISR data [267] the 24 GeV/c points [212] are shown.
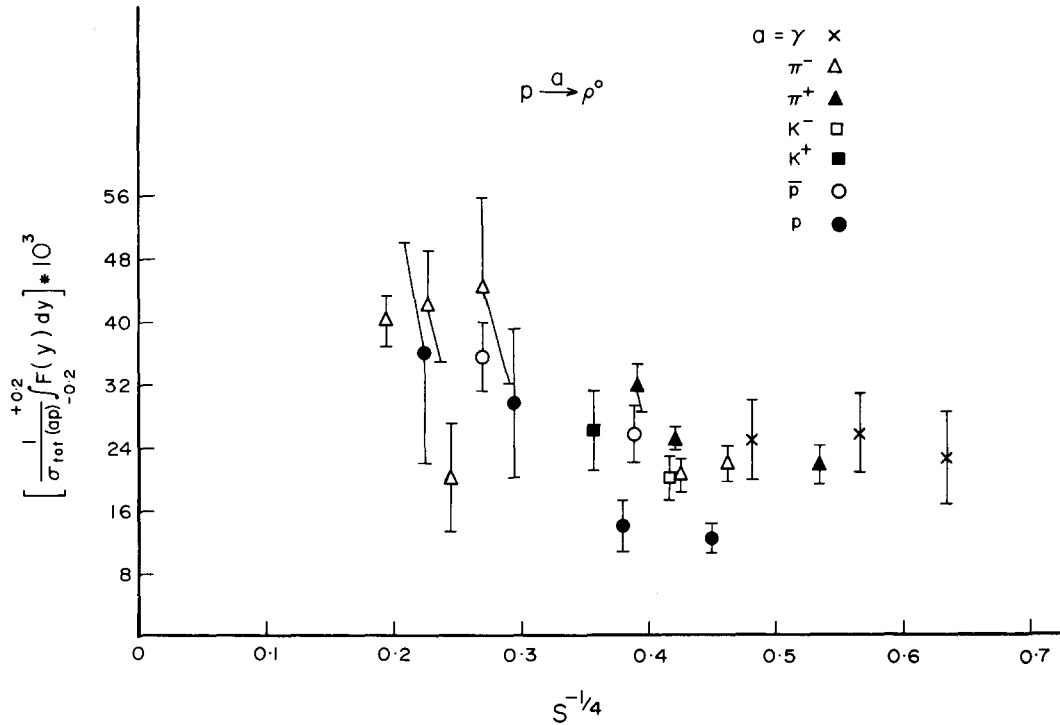
Fig. 7.4. Central ρ-production cross-section for various incident particle normalised by their respective total cross-sections [95–101].

Table 7.4

Fits to the invariant cross-section $d\sigma/\pi$ dy dp_T^2 ($y = 0, p_T = 0.2$) for π^- and $\bar{p}$ with formulae (30)

Model	π^-				$\bar{p}$			
	A	B	C	χ^2/ν	A	B	C	χ^2/ν
I	$95\dfrac{mb}{GeV^2}$	$333\dfrac{mb}{GeV^{3/2}}$	$381\dfrac{mb}{GeV}$	$\dfrac{4.5}{5}$	2.93	12.9	14.4	$\dfrac{2.1}{3}$
II	$71.9\dfrac{mb}{GeV^2}$	$888\dfrac{mb}{GeV}$	4617 mb	$\dfrac{4.2}{3}$	1.97	31.8	130	$\dfrac{2.6}{3}$
III	$11\dfrac{mb}{GeV^2}$	0.21	$-$	$\dfrac{6.6}{6}$	0.065	0.39	$-$	$\dfrac{21.5}{4}$
IV	$2.39\left(\dfrac{mb}{GeV^2}\right)^{1/2}$	$0.65\left(\dfrac{mb}{GeV^2}\right)^{1/2}$	$-$	$\dfrac{2.7}{6}$	-0.31	0.19	$-$	$\dfrac{7.6}{4}$

energy range. For instance, between the top ISR energy and $s = 40000$ (typical of the Isabelle machine) model II predicts only a 10 per cent rise for π^-, in contrast to a 25 per cent rise for I and rise of 50 per cent and more for IV and III. The corresponding rises for $\bar{p}$ are 20 per cent, 50 per cent, 100 per cent and more. Thus data in the Isabelle energy range should provide a crucial test for these models.

7.2.2. y-dependence

Consider next the y-dependence. The formulae (30) extended to non-zero y give

(I) $A - Bs^{-1/4}\cosh(y/2) + Cs^{-1/2}$

(II) $A - Bs^{-1/2}\cosh(y) + Cs^{-1}$

(III) As^B (7.31)

(IV) $[A + B \ln s]^2 - 4B^2y^2$.

The ISR cross-sections at $s = 2025$ ($\sqrt{s} = 45$) are plotted against y in figs. 5 and 6 for π and $\bar{p}$. These data points are from the British–Scandinavian collaboration, the British–Scandinavia–MIT data being restricted essentially to $y = 0$. Because of this and also because some p_T values other than 0.2 are included, the normalisation prediction has been left free. However, the shape in y is completely specified by the above formulae using the parameters* of table 4. These are also shown in figs. 5 and 6. The flat y-distribution of model III and the marginal convexity of model IV are clearly in disagreement with data. The model II prediction provides the maximum convexity and the best agreement with data. Only the $\bar{p}$ data at $p_T = 0.1$, shows a convexity even sharper than this prediction, but with rather large error bars.

7.2.3. Shrinkage in p_T

Fig. 7 shows the π cross-section rise at ISR as a function of p_T. The British–Scandinavian data and the British–Scandinavian–MIT data – the latter covering a smaller p_T region but with considerably better accuracy – are shown separately. The shrinkage phenomenon seems to be clearly discernible, particularly from the latter data. As discussed earlier the only model which can naturally account for

---

* Although these parameters show some p_T-dependence, the effect is negligible over the p_T range shown.
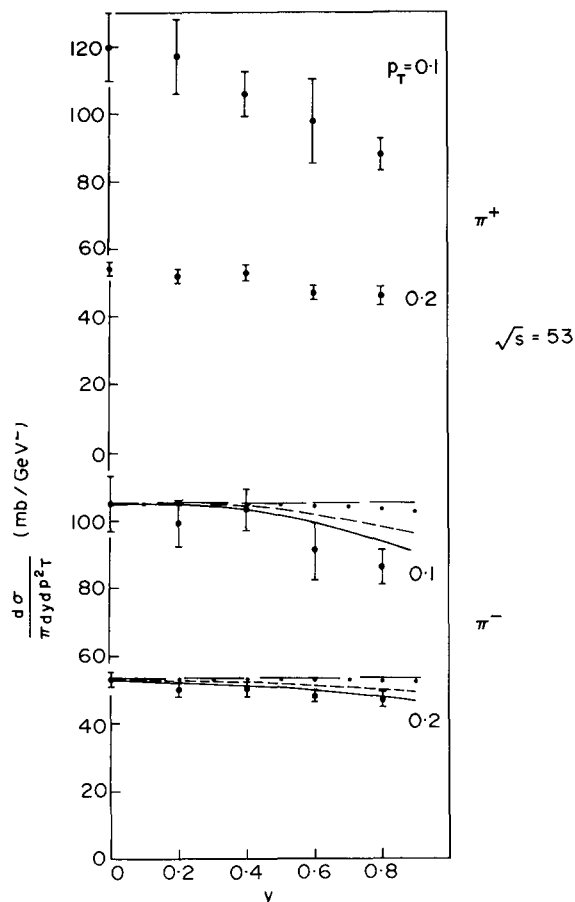
Fig. 7.5. The CM rapidity distribution of the British–Scandinavian $pp \to \pi^{\pm} X$ data [268]. The π^{-} distribution is compared with the predictions of eq. (31).
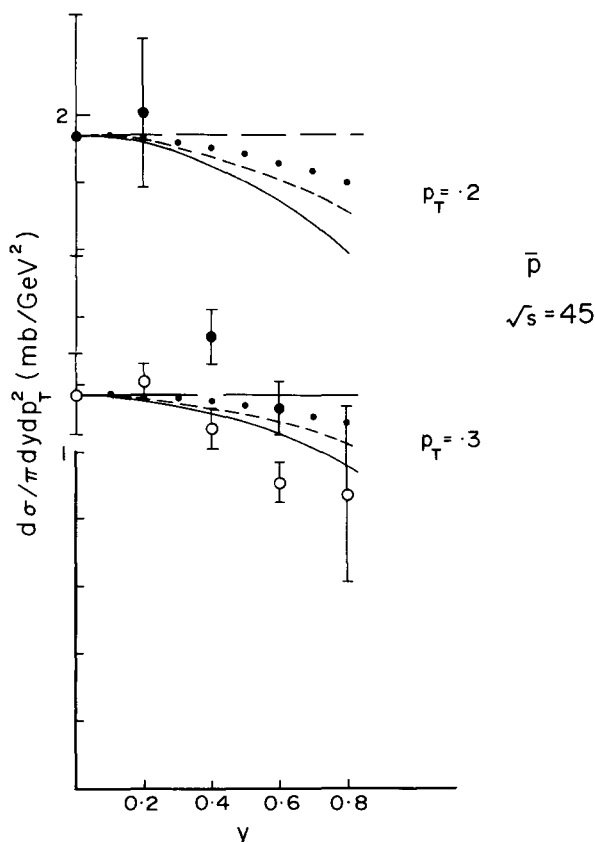
Fig. 7.6. The CM rapidity distribution of the British–Scandinavian $pp \to \bar{p} X$ data [268] compared with the predictions of eq. (31).

shrinkage is model IV. The prediction of the model (see eq. (27)) corresponding to the parameters of table 4 are shown in this figure. As discussed earlier the model III predicts a p_T independent rise and model II predicts a small antishrinkage, whereas model I has essentially no prediction.

7.2.4. p_T-dependence

Although the Regge models have essentially no prediction for the p_T-dependence, let us briefly summarise the experimental situation for completeness. The British–Scandinavian data covering a wide range of p_T and y have been parametrised as

$$\frac{d\sigma}{\pi \, dy \, dp_T^2} = A \exp(-BP_T + CP_T^2) \cdot \exp(-Dy^2) \tag{7.32}$$

where the parameters have been listed for the six detected particles at five ISR energies in ref. [268]. On the other hand, the British–Scandinavian–MIT data, restricted to a smaller range of p_T and to $y = 0$, can
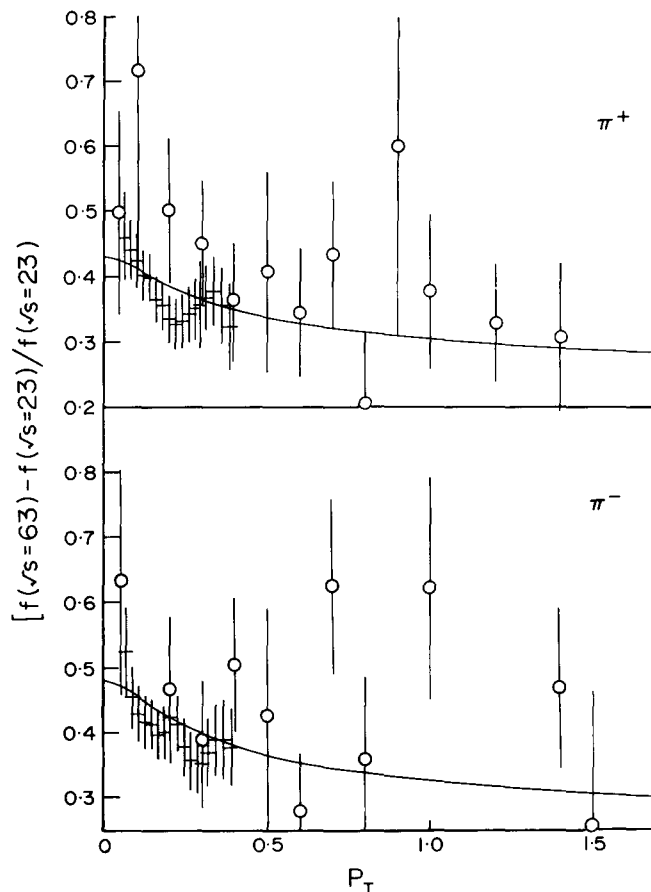
Fig. 7.7 The p_T-dependence of the central $\pi^\pm$ cross-sections ($+$ – British–Scandinavian–MIT [267], ϕ – British–Scandinavian [268]). The line is the prediction model IV.

be parametrised by 3 alternative forms,

$$\frac{d\sigma}{\pi \, dy \, dp_T^2} = As^\alpha \, e^{BP_T}$$
$$As^\alpha \, e^{BP^2}$$
$$As^\alpha \, e^{B\kappa} \qquad\qquad (7.33)$$

and the parameters have been listed in ref. [267]. However, the best fit is provided by the last parametrisation (in terms of the transverse mass κ). It is interesting to note that in the last parametrisation the slopes turn out to be roughly the same for all the six particle – more exactly for π and K. Moreover the magnitudes of the π and K cross-sections at the same transverse mass κ are roughly in the ratio 2/1. Both these features were predicted by Yazaki [272] from Mueller–Regge model and broken SU(3). The transverse mass parametrisation is supposed to take care of the SU(3) breaking in π and K masses, whereas the ratio of the central couplings is given by the f-dominated Pomeron model to be $(1 - \alpha_f(0))^{-1}/(1 - \alpha_{f'}(0))^{-1} \simeq 2/1$.

7.3. Particle–antiparticle cross-section difference

Let us finally look at the particle–antiparticle cross-section difference Δ in the central region. Quite early in the game, it was suggested by Chan et al. [273] that these differences may not be affected by the nonleading vacuum singularities (e.g. the Pomeron daughters of model II), responsible for the central cross-section rise. In this case, one gets at fixed $y(=0)$ and p_T,

$$\Delta_{ab}(c) \equiv \frac{d\sigma}{\pi \, dy \, dp_T^2}(ab \to cX) - \frac{d\sigma}{\pi \, dy \, dp_T^2}(ab \to \bar{c}X) = Bs^{-1/4} \qquad (7.34)$$

coming from the Pomeron–Reggeon exchanges of eq. (1a). Moreover the difference $\Delta_{ab}(\pi)$ for various incident particles are related by factorisation, assuming exchange degeneracy relation for the central Pomeron–Reggeon couplings. Thus one gets the ratio

$$\Delta_{PP}(\pi^+): \Delta_{\pi^+P}(\pi^+): \Delta_{K^+P}(\pi^+): \Delta_{\pi^-P}(\pi^+): \Delta_{K^-P}(\pi^+) = 2:3:7/4:-2:-3/4. \qquad (7.35)$$

The energy dependence of eq. (34) may be expected to hold over a wider energy range for the difference of $pp \to \pi^{\pm}X$ cross-sections, where the Reggeon–Reggeon exchanges $(\alpha s^{-1/2})$ are suppressed by exchange degeneracy. This cross-section difference data is plotted against $s^{-1/4}$ (fig. 8) from PS to the highest ISR energies. It seems to show a clear departure from linearity. The 2 solid lines are fits with

$$\Delta_{ab}(c) = Bs^{-1/4} + Cs^{-1/2} \qquad (7.34a)$$

but with very different parameter values as shown in table 5. Thus the data seems to be strongly suggestive of a nonleading term*, although still inadequate to fix its relative size. The corresponding fit to the $\Delta_{PP}(p)$ data is shown in fig. 9 and the parameter values given in table 5.

In the difference of $pp \to \pi^{\pm}X$ cross-sections, the above nonleading term can arise from exchange
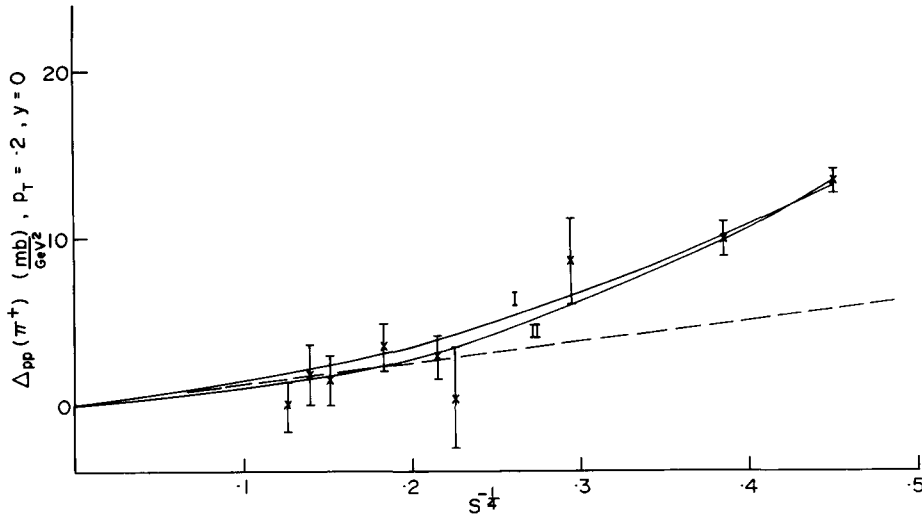
Fig. 7.8. The difference $pp \to \pi^{\pm}$ central cross-sections, from the data set of fig. 1. The solid lines are fits to eq. (34a).

* This was first noticed by Inami [244]. He had also observed systematic decrease of the nonleading part with increasing p_T from the old British–Scandinavian data. If true, this phenomenon could be naturally tied up with the decrease of the nonleading term with increasing p_T for the individual cross-sections, as evidenced by the Shrinkage phenomenon. However, the new British–Scandinavian data does not seem to show a systematic decrease of any statistical significance.
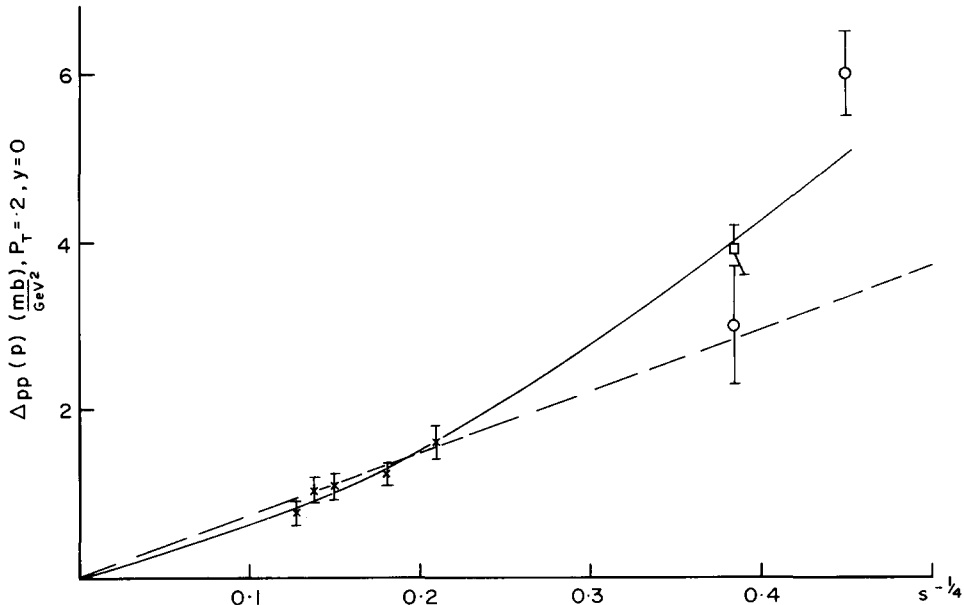
Fig. 7.9. The difference of pp → (p, p̄)X central cross-sections. The 12 GeV/c data [212] has been added to the data points of fig. 2. The solid line is a fit to eq. (34a).

degeneracy breaking as in model I. Alternatively it can arise from the Pomeron daughter contributions as in model II. In general such contributions are expected to show up in the cross-section differences too*, as pointed out in ref. [249]. In any case, if one optimistically assumes the nonleading contribution to be relatively small at the FNAL energies (as in fit II, say) then one can compare the factorisation predictions (eq. (35)) with the FNAL data. The data at $y = 0$ and integrated over p_T, give

$$\Delta_{PP}(\pi^+) = 6.9 \pm 2.3, \qquad \Delta_{\pi^+ p}(\pi^+) = 6.1 \pm 1.4, \qquad \Delta_{K^+ p}(\pi^+) = 3 \pm 1.5$$

at 100 GeV/c [274], and $\Delta_{\pi^- p}(\pi^+) = -2.7 \pm 0.3$ at 205 GeV/c [275], all in mb units. These seem to be roughly consistent with the factorisation prediction.

Finally one may note an interesting combination of cross-sections

$$(ab \to cX) - (\bar{a}b \to cX) + (ab \to \bar{c}X) - (\bar{a}b \to \bar{c}X)$$

from which both the Pomeron–Pomeron and the Pomeron–Reggeon exchanges drop out as shown by

Table 7.5
Fits to the difference of invariant cross-section pp → π^±X and also pp → (p, p̄)X, with eq. (34a) ($y = 0$, $p_T = 0.2$)

Fit	B (mb/GeV$^{3/2}$)	C(mb/GeV)	χ^2/ν
π(I)	2.5	60	3.4/7
π(II)	10	42	5.0/8
p	4.4	16	6.4/6

* The models III(a) and IV, on the other hand, would predict a slower than $s^{-1/4}$ fall for the cross-section difference, in disagreement with data.

Rushbrooke and Webber [92]. Thus the leading term here is the Reggeon–Reggeon term $as^{-1/2}$. These authors have shown that the relative magnitudes of these terms in $\pi^{\pm}p \to \pi^{\pm}X$ and $(p, \bar{p})p \to \pi^{\pm}X$ cross-section data conflicts with the exchange degeneracy prediction. One should bear in mind, however, that there are other mechanisms giving $s^{-1/2}$ terms, as mentioned above.

7.4. Summary

Let us summarise the essential conclusions of this section.

1. The most attractive explanations for the central cross-section rise are provided by the threshold effects in the multiperipheral cluster model (II) and the Gribov calculus model incorporating energy conservation (IIIb). These, at least, predict the rough scale of the rise unlike the other models.

2. An essential signal for the Gribov calculus model (III), however, is a 'broader than Poissonian' nondiffractive multiplicity distribution, which has not yet been observed. The approximately Poissonian distribution, observed up to $400\,GeV/c$ rules out the Pure Gribov Calculus model (IIIa), but is still consistent with IIIb, which has a delayed threshold in broadening. In this respect an accurate multiplicity distribution data at the highest ISR energy will be very useful. A distinct broadening at the high multiplicity end, would provide the first experimental confirmation of the model (in particular the underlying AGK cutting rule). On the other hand a nearly Poisson distribution can still be reconciled with the model but will make it phenomenologically unattractive.

3. The difficulty with the multiperipheral cluster model (II) is that, in its simplest form, it gives too rapid a rise, particularly in the sub-ISR energy range. It may be attributed to the average number of cluster (4 to 6) being too small for this simple form to be valid. None-the-less, the necessary 'low energy' modifications are called for if the model is to be of any phenomenological use, particularly at sub-ISR energies.

4. A second problem, shared by both these models, is that they predict a small antishrinkage in p_T whereas the data seem to show a shrinkage. We can think of no natural way to incorporate this feature into these models. The only model, which can naturally account for the shrinkage is the dipole Pomeron model (IV) which conflicts with the observed rapidity distribution, however, apart from being rather ad hoc. More accurate data on this shrinkage phenomenon is, of course, called for in view of its theoretical significance.

5. Both the models II and IIIb suggest a significant slow down of the rise beyond the ISR range. For instance, in contrast to a 40% rise in the ISR range $(6 < \ln s < 8)$ they predict a less than 10 per cent rise for the range $8 < \ln s < 10$. All the other models predict significantly faster rise over the latter range. The measurements at the Isabelle energies would, therefore, provide a critical test.

6. The canonical Mueller–Regge-Duality model seems to be untenable not only for the central cross-sections, but for the central particle–antiparticle cross-section differences too, at least if one includes the PS energy range.

Note added in proof:

(I) Multiplicity distribution at the highest ISR energy has been measured by the Aachen–CERN–Heidelberg–Munich collaboration; and the data seems to show a broader than Poisson distribution at the high multiplicity end [314, 315], in qualitative agreement with the Gribov calculus prediction. However, the fluctuation in the data points are too large to do a quantitative analysis.

(II) In the energy range of $s \sim 10^5 \, \text{GeV}^2$ (ln $s = 11$–12) there is cosmic ray data by the Brazil–Japan collaboration, with several unexpected features [316]. The most relevant ones for the pionisation cross-section are a larger $\langle p_T \rangle$ and more importantly a plateau height 50–100 per cent larger than at ISR. Such a large rise would evidently conflict with the two most popular models – the multiperipheral cluster model (II) and the Gribov calculus (IIIb). Several unconventional interpretations for this data have been suggested – ranging from the presence of an exotic component (quarks) in the primary cosmic rays to the excitation of a second class of clusters (mass $\sim 20 \, \text{GeV}$) above the incident energy of a few TeV [317]. However, the cosmic ray data has several experimental uncertainties [318, 319]. Therefore, it seems to us that any reliable conclusions can only be drawn after the SPS collider or Isabelle data are available.

(III) It has been noted recently that the average pion multiplicity (or equivalently the pionisation plateau height) in pp is very similar to that in e^+e^- collision. As a function of the pionisation energy $W' = W - W_{\text{leading nucleons}}$, the $\langle n_{\text{ch}} \rangle_{\text{pp}}$ seems in fact to be identical to $\langle n_{\text{ch}} \rangle_{e^+e^-}$ up to the highest available energy [320] – in this scale $(\langle W' \rangle \simeq \tfrac{1}{2}W)$ the ISR energies for pp correspond to the PETRA energies for e^+e^-. The limited amount of $\langle n_{\text{ch}} \rangle$ data available in other processes (e.g. pp, νp) are also very similar. It should be pointed out that over this range, the rise is equally consistent with the multiperipheral cluster model formula [314, 315] $\langle n_{\text{ch}} \rangle_{\text{pp}} = a + b \ln s + cs^{-1/2}$, $(b \simeq 2)$ and the perturbative QCD formula [321] $\langle n_{\text{ch}} \rangle_{e^+e^-} = a + b \exp[c(\ln s/\Lambda^2)^{1/2}]$. When data at LEP and Isabelle energies are available, it would be very interesting to check if the two multiplicities rise differently, as suggested by the two formulae above; or continue to follow a common path, underscoring a basic universality in the multiparticle production phenomena.

8. Two-particle correlations

The subject of two-particle inclusive cross-sections and correlations is, of course, vast enough to cover a complete review by itself. Naturally our discussion of this subject will not be anywhere near as thorough as that of the single particle inclusive processes. We shall instead concentrate on those aspects of the two-particle inclusive data which are most relevant for the Regge models. In particular we shall concentrate on the two-particle correlations in the central region for which the Regge models described in the last section (i.e. the Mueller–Regge Model, the multiperipheral cluster model and the Gribov calculus) make fairly precise predictions. In addition to the inclusive rapidity correlation we shall also discuss some aspects of the azimuthal correlation and the semi-inclusive rapidity correlation, which are particularly relevant for the cluster model.

In terms of the one and two-particle inclusive cross-sections

$$F_{ab}^c(y_c, P_{cT}) = E_c \frac{d\sigma_{ab}^c}{dp_c^3} = \frac{1}{\pi} \frac{d\sigma_{ab}^c}{dy_c \, dp_{cT}^2} \tag{8.1}$$

and

$$F_{ab}^{cd}(y_c, P_{cT}; y_d, P_{dT}) = E_c E_d \frac{d\sigma_{ab}^{cd}}{dp_c^3 \, dp_d^3} = \frac{1}{\pi^2} \frac{d\sigma_{ab}^{cd}}{dy_c \, dp_{cT}^2 \, dy_d \, dp_{dT}^2} \tag{8.2}$$

the correlation function is defined as

$$C_{ab}^{cd}(y_c, P_{cT}; y_d, P_{dT}) = \frac{1}{\sigma_{ab}} F_{ab}^{cd}(y_c, P_{cT}; y_d, P_{dT}) - \frac{1}{\sigma_{ab}} F_{ab}^{c}(y_c, P_{cT}) \cdot \frac{1}{\sigma_{ab}} F_{ab}^{d}(y_d, P_{dT}) \tag{8.3}$$

where the cross-section σ_{ab} in the denominator is usually taken to be the total inelastic cross-section

$$\sigma_{ab} = \sigma_{ab}^{\text{inelastic}}. \tag{8.4}$$

Very often the correlation function is presented in the normalised form

$$R_{ab}^{cd} = C_{ab}^{cd} \Big/ \left(\frac{1}{\sigma_{ab}} F_{ab}^{c} \frac{1}{\sigma_{ab}} F_{ab}^{d} \right). \tag{8.5}$$

We shall, of course, be mostly interested in $\pi\pi$ correlations in the pp collision i.e.

$$R_{pp}^{\pi^{\pm}\pi^{\pm}}.$$

However, the ISR correlation data available so far lacks particle or even the charge identification. What are available are the charge–charge correlation R_{pp}^{cc} and the charge–γ correlation $R_{pp}^{c-\gamma}$. Assuming the charged particles in the central regions to be mostly pions and the central $\pi^{\pm}$ inclusive cross-sections to be roughly equal, we have the approximate relation

$$R_{pp}^{cc} = \left(\frac{1}{\sigma_{pp}} F_{pp}^{cc} \Big/ \frac{1}{\sigma_{pp}} F_{pp}^{c} \frac{1}{\sigma_{pp}} F_{pp}^{c} \right) - 1 \simeq \frac{1}{4} (R_{pp}^{\pi^{+}\pi^{+}} + R_{pp}^{\pi^{-}\pi^{-}} + R_{pp}^{\pi^{+}\pi^{-}} + R_{pp}^{\pi^{-}\pi^{+}}) \tag{8.5a}$$

$$R_{pp}^{c-\gamma} \simeq R_{pp}^{\pi^{\pm}\pi^{0}} \simeq \frac{1}{2}(R_{pp}^{\pi^{+}\pi^{0}} + R_{pp}^{\pi^{-}\pi^{0}}). \tag{8.5b}$$

These should be reasonable approximations over the ISR energy range.

8.1. Mueller–Regge model

Asymptotically, the two particle inclusive cross-section in the central region is given by
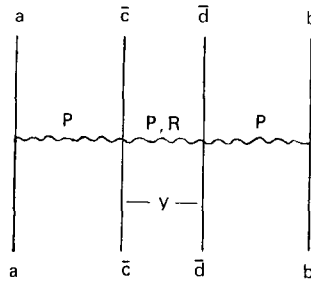
$$F_{ab}^{cd} = \beta_P^a \beta_P^b \gamma_{PP}^c(p_{cT}) \gamma_{PP}^d(p_{dT}) + \beta_P^a \beta_P^b \gamma_{PR}^c(p_{cT}) \gamma_{PR}^d(p_{dT}) \, [2 \cosh y]^{-1/2}$$ (8.6)

where R stands for the leading vector-tensor trajectories with

$$\alpha_R(0) \simeq \tfrac{1}{2}.$$

The asymptotic single particle inclusive cross-sections in the central region are

$$F_{ab}^{c,d} = \beta_P^a \beta_P^b \gamma_{PP}^{c,d}(p_{cT}, p_{dT})$$ (8.7)

and total cross-section

$$\sigma_{ab}^T = \beta_P^a \beta_P^b.$$ (8.8)

Hence, assuming a factorising pole Pomeron, the asymptotic correlation function, defined in terms of the total cross-section, is given by

$$C_{ab}^{cd} = \frac{1}{\sigma_{ab}^T} F_{ab}^{cd} - \frac{1}{\sigma_{ab}^T} F_{ab}^c \frac{1}{\sigma_{ab}^T} F_{ab}^d$$

$$= \gamma_{PR}^c(p_{cT}) \cdot \gamma_{PR}^d(p_{dT}) \cdot [2 \cosh y]^{-1/2}$$ (8.9)

and

$$R_{ab}^{cd} = \frac{\gamma_{PR}^c(p_{cT}) \, \gamma_{PR}^d(p_{dT})}{\gamma_{PP}^c(p_{cT}) \, \gamma_{PP}^d(p_{dT})} \cdot [2 \cosh y]^{-1/2}.$$ (8.10)

Thus the model predicts an asymptotic correlation function that is firstly independent of the energy and the type of the incident particles and secondly independent of the individual rapidities y_c, y_d for a given rapidity difference $y(=y_c - y_d)$. Thirdly it predicts an exponential fall off with increasing rapidity difference $(\sim e^{-y/2})$ – i.e. a short range correlation with a range of ~ 2 units in rapidity. Finally it also predicts the magnitude of this correlation, since the Pomeron–Reggeon vertex $\gamma_{PR}^{c,d}$ can be estimated from the energy dependence of the single particle central cross-section – i.e. the slope on a $s^{-1/4}$ plot as discussed in the last section (fig. 7.1).

In the past there has been several exploratory studies of the inclusive correlations $R_{pp}^{\pi\pi}$ in the Mueller–Regge picture [104, 242–244, 276]. However, in most of these analyses the central Pomeron–Reggeon vertex was estimated from the slope of the $s^{-1/4}$ plot of the pionisation cross-section, over the PS energies. As we saw in the last section, this slope is about $\tfrac{1}{3}-\tfrac{1}{4}$ of the asymptotic slope, as measured by the FNAL and ISR data; and the error gets squared in the estimate of the correlation function. The one exception is the work of Inami [244] who estimated the central Pomeron-ρ vertex from the central $\pi^\pm$ cross-section difference at ISR and computed the resulting difference of $\pi^+\pi^-$ and $\pi^-\pi^-$ correlations.

In the following, the central P–ρ and P–f vertices will be estimated from the asymptotic slopes of the central $\pi^\pm$ cross-sections, as measured over the top FNAL and ISR energies; and the resulting $\pi^+\pi^-$ and $\pi^-\pi^-$ correlations compared with the data over this energy range. Still the comparison is expected

to be of only qualitative significance, however, because of the following uncertainties:

(1) The Mueller–Regge model can predict the correlation, only if one assumes the net Pomeron contribution as appearing in the total (and the inclusive) cross-section, to be a factorising pole singularity. On the other hand, it seems quite plausible, as discussed in the last section, that the net Pomeron contribution may have in addition to the pole, a cut component arising from the elastic and diffractive contributions. In that case, normalising with respect to the total cross-section would have no particular significance; and the correlation function would in general contain a long range component, whose magnitude cannot be predicted by the model. In any case the correlation data is usually normalised with respect to the inelastic cross-section (eqs. (3–5)) whereas the predicted correlation function (eqs. (9, 10)) corresponds to normalisation by the total cross-section.

(2) The model prediction applies to the truly asymptotic correlation, whereas the correlation data is expected to have substantial sub-asymptotic effects even over the top FNAL and ISR energy range. One expects this from the significant energy dependence of the single particle inclusive cross-section observed over this range and the significant difference between the two particle cross-sections ($\pi^+\pi^+$ and $\pi^-\pi^-$) observed at FNAL*.

In view of the above uncertainties a quantitative agreement or disagreement between the prediction and data will not be of great theoretical significance. It will be significant, however, if there is an order of magnitude difference between the two. We shall, indeed see that whereas the difference of $\pi^+\pi^-$ and $\pi^+\pi^+$ correlations predicted from the p–p vertex is in rough agreement with data, the individual correlation functions, predicted from the p–f vertex, are too large by roughly two orders of magnitude.

8.2. Comparison with inclusive correlation data

8.2.1. Short range correlation
The eqs. (6–9) above, give

$$C_{pp}^{\pi^+\pi^-} = (\gamma_{pf}^{\pi^2} \pm \gamma_{pp}^{\pi^2})[2\cosh y]^{-1/2} \tag{8.11}$$

i.e.

$$C_{pp}^{\pi^+\pi^-} - C_{pp}^{\pi^-\pi^-} = 2\gamma_{pp}^{\pi^2}[2\cosh y]^{-1/2} \tag{8.12}$$

where the transverse momenta of the pions have been integrated over. The energy dependence of the central $pp \to \pi^\pm X$ cross-sections are given by

$$F_{pp}^{\pi^\pm} = \beta_P^{p^2}\gamma_{PP}^{\pi} + 2\beta_P^p(\beta_f^p\gamma_{Pf}^{\pi} \pm \beta_\rho^p\gamma_{P\rho}^{\pi})s^{-1/4} \tag{8.13}$$

i.e.

$$\Delta_{pp}^{\pi} = 4\beta_P^p\beta_\rho^p\gamma_{P\rho}^{\pi} \cdot s^{-1/4}. \tag{8.14}$$

---

* However, there seems to be an effective cancellation of these subasymptotic effects in the combination R, so that R appears to be roughly energy independent and symmetric between the $++$ and $--$ channels, down to 100 GeV/c.

The slope of the p_T integrated ISR data on Δ_{pp}^π [267] gives

$$4\beta_P^p\beta_p^p\gamma_{Pp}^\pi = 2 \pm 1 \text{ mb}. \tag{8.15}$$

The central value corresponds to the slope 10 mb/GeV^2, obtained for $p_T = 0.2$ in the last section, and the error bar includes both the uncertainty in the ISR data and the possible contributions from $s^{-1/2}$ terms as described in the last section. With

$$\beta_P^p \simeq 6.3 \text{ mb}^{1/2}, \qquad \beta_\rho^p \simeq \tfrac{1}{5}\beta_P^p \simeq 1.2 \text{ mb}^{1/2} \tag{8.16}$$

as obtained from the total cross-section data [28] one gets

$$\gamma_{Pp}^\pi = 0.07 \pm 0.035. \tag{8.17}$$

The resulting correlation difference is

$$C_{pp}^{\pi^+\pi^-} - C_{pp}^{\pi^-\pi^-} \sim 0.007 \, (\cosh y)^{-1/2} \tag{8.18}$$

with an uncertainty of a factor of 2 on either side. Normalising with

$$F_{pp}^{\pi^\pm} \simeq 7 \text{ mb}, \qquad \sigma_{pp} \simeq 40 \text{ mb} \tag{8.19}$$

appropriate for the top FNAL energy, gives

$$R_{pp}^{\pi^+\pi^-} - R_{pp}^{\pi^-\pi^-} = 2\gamma_{Pp}^{\pi^2} [2 \cosh y]^{-1/2} / (F_{pp}^{\pi^\pm}/\sigma_{pp})^2 \simeq 0.23 \, [\cosh y]^{-1/2} \tag{8.20}$$

again with a normalisation uncertainty of a factor of 2.

The highest energy correlation data available with charge identification is the FNAL data at $400 \text{ GeV}/c$ [277], shown in fig. 1. A priori the Mueller–Regge prediction is expected to work only for a large rapidity difference $-y > 1$ say. None-the-less, one sees from fig. 1, that the correlation difference

$$R_{pp}^{\pi^+\pi^-} - R_{pp}^{\pi^-\pi^-}$$

is in reasonable agreement with the above prediction both in shape and normalisation.

In contrast the individual correlations $R_{pp}^{\pi^\pm\pi^-}$ are predicted to be larger than the difference (eq. (20)) by 2 orders of magnitude, in violent disagreement with data. One can see this simply by comparing the asymptotic slopes of the cross-section F_{pp}^π and the difference Δ_{pp}^π on a $s^{-1/4}$ plot. We see from the analysis of the last section (figs. 1, 8 and tables 4, 5) that the former slope ($= -333$) is larger than the latter ($= 10$) by a factor of ~ -30. Although the analysis of the last section was carried out specifically at $p_T = 0.2$, essentially the same magnitudes of slopes hold for the p_T integrated cross-sections, as well. It then follows from eqs. (13, 14 and 16) that

$$\gamma_{Pf}^\pi \simeq -12\gamma_{Pp}^\pi \tag{8.21}$$
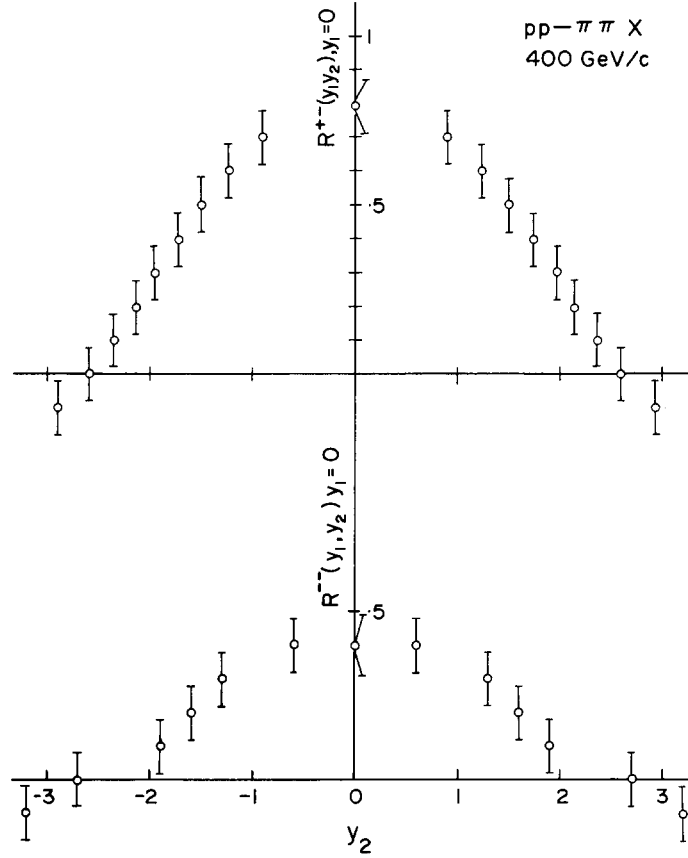
Fig. 8.1. The $\pi^+\pi^-$ and $\pi^-\pi^-$ correlation data for 400 GeV/c pp collision from the Michigan-Rochester Coll. [277].

which means that the individual correlations $R_{pp}^{\pi^\pm\pi^-}$ should be larger than the corresponding correlation difference of eq. (20) by roughly 2 orders of magnitude. This is evidently in violent contradiction with the $R_{pp}^{\pi^\pm\pi^-}$ data of fig. 1*. In fact the rough size of the $\pi^+\pi^-$ correlation seems to be of similar magnitude as the correlation difference, which implies

$$\gamma_{Pf}^\pi \simeq \pm\gamma_{Pp}^\pi \qquad\qquad\qquad\qquad (8.21a)$$

– the positive sign corresponding to the exchange degeneracy prediction. It may be pointed out that in the past, there has been an attempt to reconcile this feature of the correlation data with the exchange degeneracy breaking evidently required by the pionisation cross-section rise by postulating the antiexchange degeneracy solution – i.e. the negative sign in eq. (21a) above [242]. Such a solution, was indeed

---

* Indeed the same contradiction exists with the ISR data on charge–charge correlation (fig. 3a) and charge–γ correlation (fig. 3b) as one can easily check from eqs. (5a, b); i.e. $R^{cc} = R^{c-\gamma} = \gamma_{Pf}^{\pi 2}[2\cosh y]^{-1/2}/(F_{pp}^\pi/\sigma_{pp})^2 \sim 20(\cosh y)^{-1/2}$.

roughly consistent with the slopes of $F_{pp}^{\pi^-}$ and Δ_{pp}^{π} as measured from the PS data (see figs. 7.1 and 7.8). As we saw in the last section however, the asymptotic slopes, as measured by the ISR data, are a factor of 3–4 higher for $F_{pp}^{\pi^-}$ and ~2 lower for Δ_{pp}^{π}. This results in the γ_{Pf}^{π} vertex being an order of magnitude larger than γ_{Pp}^{π} and the corresponding $\pi^+\pi^-$ correlations being two orders of magnitude larger than their difference.

In summary, the Mueller–Regge description of the ISR pionisation cross-section rise requires a large γ_{Pf}^{π} vertex, which results in a $\pi\pi$ correlation 2 orders of magnitude larger than the data. Thus the data on pionisation cross-section rise and $\pi\pi$ correlation are in gross disagreement with the Mueller–Regge model irrespective of any exchange degeneracy constraints. However the less ambitious scheme where the central $\pi^\pm$ cross-section rises are attributed to some kind of a threshold effect and only the difference is interpreted in terms of the Mueller–Regge model, gives a γ_{Pp}^{π} vertex in rough agreement with the difference of $\pi^+\pi^-$ correlations. Moreover the short-range parts of the individual correlations $\pi^+\pi^-$ are in rough agreement with the exchange degeneracy prediction $\gamma_{Pf}^{\pi} = \gamma_{Pp}^{\pi}$. There is a priori no reason of course, why the above threshold effects should not affect the central cross-section difference and the correlations substantially; and to that extent some or all of these agreements may be fortuitous.

8.2.2. Long range correlation

The correlation data $R_{pp}^{\pi^+\pi^-}$ shown in fig. 1 and R_{pp}^{cc} shown in fig. 3a seem all consistent with a purely short range correlation (of range ~2); although within the error bars a long range component of ~0.1 to · 0.2 units may also be accommodated. One should note however, that normalising the correlation function by the total instead of the inelastic cross-section would add a long range component of ≃0.2 units (see eqs. (3–5) above). Thus the correlation function, as normalised by the total cross-section, would seem to have a positive long range component. In terms of the Mueller–Regge model this would imply that the net Pomeron contribution to the total and the inclusive cross-section cannot be described by a factorising pole singularity. Of course, the size of the long range component is quite small and the subasymptotic effects, as discussed earlier, are significant even in the ISR energy range.

8.2.3. Energy and rapidity (in)dependence

Finally let us check if the central correlation data are, indeed, independent of the incident energy and particle type and also of the individual rapidities $y_{c,d}$, for a fixed rapidity difference y. Fig. 2 shows the dependence on the energy and the type of the incident particle. It is an updated version of the compilation of Ko [278], which shows the Serpukov and FNAL data on $R^{\pm\mp}$ (0,0) for pp and $\pi^\pm p$ collision. Evidently both the correlations are roughly independent of the incident energy and particle type. (The R^{++} data are very similar to the R^{--}.) Fig. 3a shows the energy independence of the central charge-charge correlation data $R^{cc}(0,0)$ from ISR*. One can also check with eq. (5a) above, that its magnitude is consistent with those of $R^{\pm\mp}$ (0,0) shown in fig. 2. Fig. 4 shows that this correlation is independent of the individual rapidities, for a fixed rapidity difference ($y = 0$). This last feature is, of course, clearly visible only at the top ISR energy, because of the larger rapidity range available there.

---

* One may note that the corresponding $C(0,0)$ would show significant rise (by a factor of ≃2 over the ISR range).
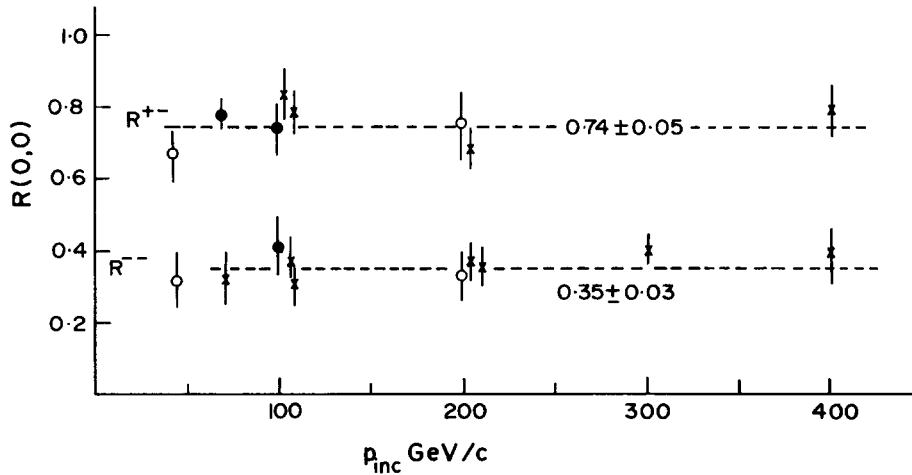
Fig. 8.2. Compilation of $R^{+-}(0,0)$ and $R^{--}(0,0)$ in pp, $\pi^- p$ and $\pi^+ p$ collision. The 400 GeV pp data has been added to the compilation of Ko [278].
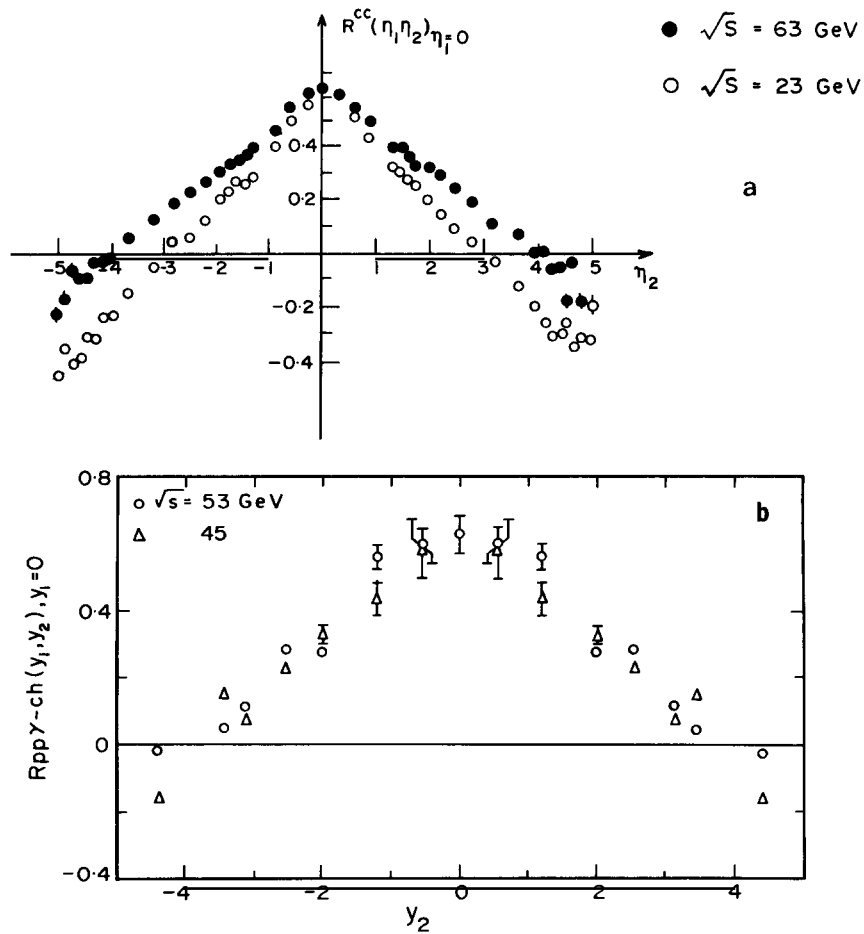

Fig. 8.3. Correlation data from ISR: (a) Charge–charge correlation data of the Pisa–Stonybrook Coll. [279]. (b) Charge–γ correlation data of the CENR–Hamburg–Vienna Coll. [280].
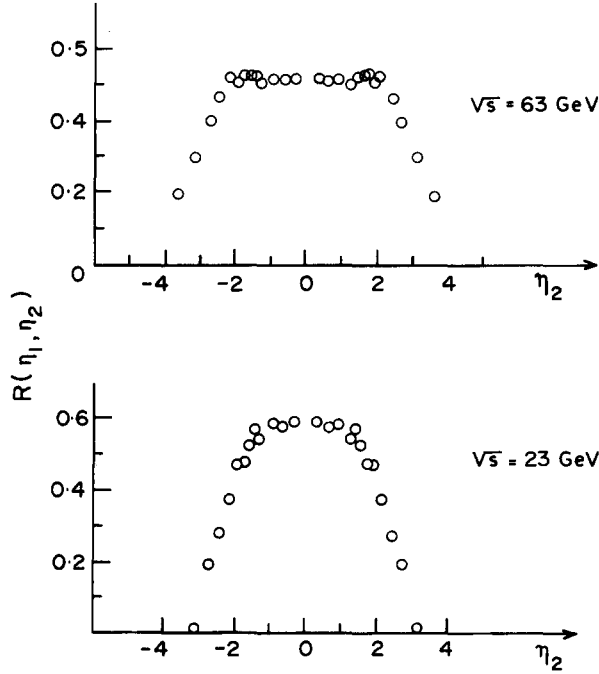
Fig. 8.4. Rapidity dependence of the ISR charge–charge correlation data (Pisa–Stonybrook Coll. [279]) at fixed rapidity difference $\eta_1 - \eta_2 = 0$.

Before closing this subsection it may be appropriate to comment on the choice of variable. For the Mueller–Regge analysis, the cd invariant mass

$$M^2 = m_c^2 + m_d^2 + 2m_{cT}m_{dT}\cosh y - 2p_{cT} \cdot p_{dT}$$ (8.22)

is evidently a more appropriate variable than the rapidity difference y. Whereas most correlation data are given only in the rapidity variables there is one piece of correlation data, which is available in the M^2 variable as well – i.e. the ANL–FNAL 200 GeV/c data. This correlation data (in M^2) has been analysed in terms of the Mueller–Regge model by Berger et al. [281]. It is reassuring that this analysis agrees with the conclusions listed above. In particular the $\pi^+\pi^-$ data (fig. 5a) shows a short range correlation of range consistent with $\alpha_R(0) \approx 0.5$ and magnitude roughly consistent with eq. (20) above, i.e.

$$R_{pp}^{\pi^+\pi^-} \sim 0.23(\sqrt{2}\langle m_{\pi T}\rangle)M^{-1} \sim 0.15M^{-1}.$$ (8.23)

On the other hand the $\pi^+\pi^+$ correlation is of much smaller magnitude and shorter range (fig. 5b), which may be interpreted in terms of a low lying effective trajectory ($\alpha(0) \approx -0.5$), coming from exchange degeneracy breaking contributions (e.g. non-leading trajectories, Regge–Regge cuts, etc.). One may note that the corresponding ($\pi^-\pi^-$) correlation data of fig. 1 seems to show a somewhat larger magnitude and range but the difference is compatible with the size of the error bars.

Fig. 8.5. Invariant mass dependence of the 200 GeV/c correlation data of the ANL–FNAL Coll., taken from ref. [281]. (a) R^{+-}, (b) R^{--}/R^{+-}.
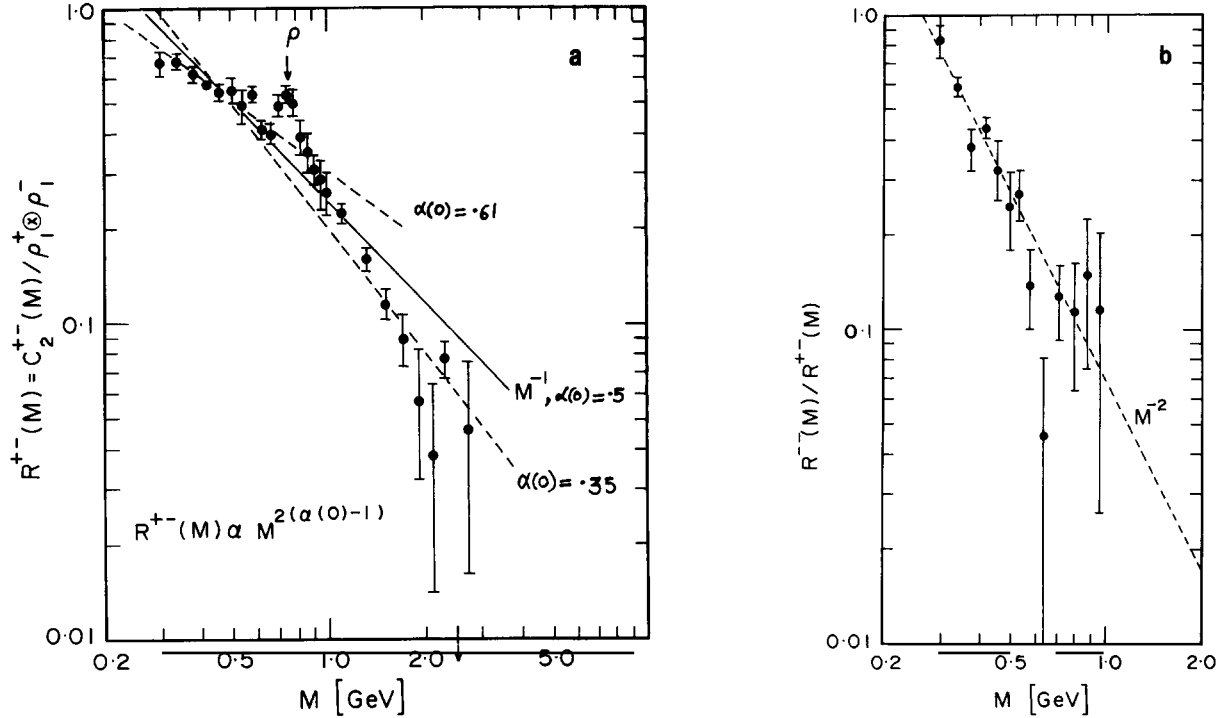
8.3. Multiperipheral cluster model

This model has been by far the most successful Regge model in describing the correlation data. It was discussed in the last section, in the context of the pionisation cross-section rise. The correlation data, of course, has a much wider scope in testing the model predictions and in determining the model parameters. There is, indeed an extensive literature devoted to the analyses of inclusive and semi-inclusive correlation data in the multiperipheral cluster model. We shall, therefore, discuss it in some detail.

This is an extension of the standard multiperipheral model, where the objects produced along the multiperipheral chain are not pions, but the multipion resonances like η, ρ, ω, f, A_2 (see diagram below). The phenomenological motivation for this are the following: (a) Inclusive resonance production data indicate that these resonances already account for the bulk (60–90%) of the pion production [251]. (b) In the simplest multiperipheral model the average number of objects produced (eq. (28) below) is roughly a third of the average number of pions ($\langle n_\pi \rangle \simeq 3 \ln s$) experimentally observed. This would suggest the objects to be clusters of $\simeq 3$ pions (i.e. $\simeq 2$ charged pions) on the average. (c) This pion multiplicity corresponds to an average subenergy for neighbouring pions

$$M_{\pi\pi} \simeq \langle m_{\pi T}\rangle (2 \cosh (0.3))^{1/2} \simeq 0.5 \text{ GeV}$$

where significant resonance enhancements are expected any way. Since, the simplest multiperipheral model has no correlation between the neighbouring pions, such effects must be put in by hand. (d)

Finally to reproduce the pionisation cross-section rise over the ISR range in the multiperipheral model one seems to require the mass of the produced objects to be ~ 1 GeV as we saw in the last section.

A realistic treatment of the multiple resonance production would, of course, involve a multitude of resonance parameters. It would also involve the inter-cluster correlation effects coming, for instance, from charge and energy momentum conservation. In the simplest and most popular version of the model, however, one assumes uncorrelated production of identical and neutral clusters, representing some sort of an average over the produced resonances. This production amplitude is described by the familiar multiperipheral diagram,
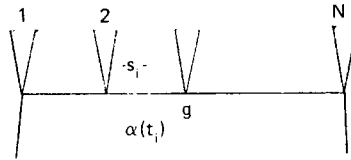
i.e.

$$A_N = g^N \prod_{i=1}^{N-1} s_i^{\alpha(t_i)} f(t_i).$$ (8.24)

The model is widely covered in the literature [2, 6, 47, 65, 282]. Integrating over the subenergies and the momenta transfer one gets the following asymptotic results. The N cluster production cross-section

$$\sigma^N = s^{2\alpha_R-2} g^{2N} (\ln s)^N/N!$$ (8.25)

$$\sigma \equiv \sum_N \sigma^N = s^{2\alpha_R-2+g^2} = \text{const.}$$ (8.26)

i.e.

$$g^2 = 2 - 2\alpha_R \simeq 1 \qquad \text{for } \alpha_R \simeq 0.5.$$ (8.27)

The average cluster multiplicity

$$\langle N \rangle = g^2 \ln s \simeq \ln s.$$ (8.28)

The multiplicity distribution can be written in the familiar Poisson form

$$\sigma^N = \sigma \, e^{-\langle N \rangle} \cdot \langle N \rangle^N/N!.$$ (8.25a)

The inclusive cluster distribution is

$$\frac{1}{\sigma} \frac{d\sigma^c}{dy} \equiv \rho(y) = \frac{\langle N \rangle}{\ln s} \tag{8.29}$$

which is both s and y independent.

8.3.1. Short range correlation

One expects a short range correlation between pions coming from the decay of the same cluster. Its magnitude and range would depend on the cluster parameters – mass, spin and decay multiplicity. For simplicity it has been customary to assume an isotropic decay, corresponding to a spin zero cluster. It would evidently be more appropriate to consider spin 1 or 2, characteristic of the above mentioned resonances; but one hopes the results would not change appreciably. In any case, given this isotropic decay assumption, one sees that the correlation function can be approximated by a Gaussian

$$\exp\{-(y_1 - y_2)^2 / 4\delta^2\}$$

with $\delta \simeq 0.7\text{--}0.9$. We sketch the derivation following Berger [6].

Defining (w, q, θ, ϕ) as the energy momentum and angles of the decay pion in the cluster rest frame and y as the corresponding rapidity we have

$$\omega = m_{\pi T} \cosh y, \qquad q \cos \theta = m_{\pi T} \sinh y$$

i.e.

$$\frac{q}{\omega} d \cos \theta = d \tanh y = \frac{dy}{\cosh^2 y}. \tag{8.30}$$

Thus the invariant decay pion distribution can be written as

$$D(q) \equiv \omega \frac{d^3 D}{dq^3} = \omega \frac{d^3 D}{q^2 \, dq \, d \cos \theta \, d\phi} = 2 \cosh^2 y \frac{d^3 D}{dq^2 \, d\phi \, dy}$$

i.e.

$$\frac{dD}{dy} = \frac{2}{\cosh^2 y} \int D(q) \, dq^2 \, d\phi. \tag{8.31}$$

For isotropic decay distribution $(D(q) = D(q))$ we have

$$\frac{dD}{dy} = \frac{4\pi}{\cosh^2 y} \int_{(m_\pi \sinh y)^2}^{\infty} D(q) \, dq^2 = \frac{4\pi \langle q \rangle^2}{\cosh^2 y} \int_{L}^{\infty} D(r) \, dr^2$$

with

$$r = q/\langle q \rangle \quad \text{and} \quad L = (m_\pi \sinh y/\langle q \rangle)^2. \tag{8.32}$$

Empirically $\langle q \rangle$ is large compared to m_π and hence for small y, $L \simeq 0$ and

$$\mathrm{d}D/\mathrm{d}y \propto (\cosh y)^{-2}$$

which can be numerically approximated by the Gaussian

$$\mathrm{d}D/\mathrm{d}y \propto \exp(-y^2/2\delta^2), \qquad \delta \simeq 0.9. \tag{8.33}$$

Correction due to $L \neq 0$, in general, reduce δ by a small amount ($\delta \simeq 0.7$–0.9); but to a first approximation it is independent of both cluster mass and multiplicity. Normalising the integrated distribution D to the average cluster decay multiplicity $\langle K \rangle$ gives

$$g(y) \equiv \frac{\mathrm{d}D}{\mathrm{d}y} \simeq \frac{\langle K \rangle}{\delta\sqrt{2\pi}} \exp(-y^2/2\delta^2), \qquad \delta \simeq 0.7\text{–}0.9. \tag{8.34}$$

From eqs. (29) and (34) we get the single pion inclusive cross-section

$$\frac{1}{\sigma}\frac{\mathrm{d}\sigma^\pi}{\mathrm{d}y} = \int \rho(y_c)\, g(y - y_c)\, \mathrm{d}y_c$$

$$= \frac{\langle N \rangle}{\ln s} \cdot \langle K \rangle = \frac{\langle n_\pi \rangle}{\ln s} \tag{8.35}$$

which is both energy (s) and rapidity (y) independent. The corresponding 2 pion inclusive cross-section is

$$\frac{1}{\sigma}\frac{\mathrm{d}^2\sigma^\pi}{\mathrm{d}y_1\,\mathrm{d}y_2} = \int \mathrm{d}y_c\, \rho(y_c)\, g(y_1 - y_c, y_2 - y_c) + \int \mathrm{d}y_{c1}\, \mathrm{d}y_{c2}\, \rho(y_{c1})\rho(y_{c2})\, g(y_1 - y_{c1})\, g(y_2 - y_{c2}) \tag{8.36}$$

where the 1st term corresponds to both the pions coming from the same cluster and the 2nd to those coming from different clusters. The factorisation of the two cluster densities in the 2nd term, simply reflects the uncorrelated cluster production assumption as discussed above. As a result this term drops out from the correlation function

$$C^{\pi\pi}(y_1, y_2) \equiv \frac{\mathrm{d}^2\sigma^\pi}{\sigma\,\mathrm{d}y_1\,\mathrm{d}y_2} - \frac{\mathrm{d}\sigma^\pi}{\sigma\,\mathrm{d}y_1} \cdot \frac{\mathrm{d}\sigma^\pi}{\sigma\,\mathrm{d}y_2}$$

$$= \int \mathrm{d}y_c\, \rho(y_c)\, g(y_1 - y_c, y_2 - y_c). \tag{8.37}$$

Assuming for simplicity, that the two decay pion distributions from the same cluster are independent, gives

$$g(y_1 - y_c, y_2 - y_c) = \frac{\langle K(K-1) \rangle}{2\pi\delta^2} \exp\left\{ -\frac{(y_1 - y_c)^2 + (y_2 - y_c)^2}{2\delta^2} \right\}. \tag{8.38}$$

Substituting eqs. (38) and (29) in (37) and using the identity

$$\int_{-\infty}^{\infty} \exp\left\{-\frac{(y_1-y)^2+(y_2-y)^2}{2\delta^2}\right\} \cdot dy = \delta\sqrt{\pi} \cdot \exp\left\{-\frac{(y_1-y_2)^2}{4\delta^2}\right\} \tag{8.39}$$

one gets

$$C^{\pi\pi}(y_1, y_2) = \frac{\langle K(K-1)\rangle}{2\delta\sqrt{\pi}\langle K\rangle} \left(\frac{\langle n_\pi\rangle}{\ln s}\right) \exp\{-(y_1-y_2)^2/4\delta^2\}$$

$$= \frac{\langle K(K-1)\rangle}{2\delta\sqrt{\pi}\langle K\rangle} \left(\frac{d\sigma^\pi}{\sigma\, dy}\right) \exp\{-(y_1-y_2)^2/4\delta^2\}. \tag{8.40}$$

The corresponding normalised correlation function is

$$R^{\pi\pi}(y_1, y_2) = \frac{\langle K(K-1)\rangle}{2\delta\sqrt{\pi}\langle K\rangle} \left(\frac{d\sigma^\pi}{\sigma\, dy}\right)^{-1} \exp\{-(y_1-y_2)^2/4\delta^2\}. \tag{8.41}$$

Thus the correlation function is independent of the incident energy and the individual rapidities $y_{1,2}$ for a fixed rapidity difference. One may also note that the correlation function and the other physical quantities described above are all independent of the type of incident particles. The correlation range is $2\delta \simeq 2$, i.e. similar to that predicted by the Mueller–Regge model. The detailed shapes differ (i.e. Gaussian versus exponential); but the accuracy of the correlation data is inadequate to distinguish between the two. Besides, the cluster model prediction (eq. (40)) is expected to work better at small rapidity difference (i.e. $L \simeq 0$), whereas the Mueller–Regge prediction (eq. (11)) is more reliable at larger rapidity difference. The most distinctive feature of the cluster model, however, is the size of the predicted short range correlation. As we see from eqs. (40 and 41), this size is governed by the cluster decay multiplicity, which has essentially no connection with the pionisation cross-section rise. Before proceeding to compare this with the correlation data, however, we must estimate the long range correlation predicted by the model, since the 2 components cannot be clearly disentangled from the data.

8.3.2. Long range correlation

As we have seen in the last sections, the total inelastic cross-section σ contains a small diffractive component $\sigma_D(\simeq\frac{1}{5}\sigma)$ in addition to the above multiperipheral component, which may be denoted as σ_M. It is common practice to neglect the interference between the two since they have small overlap in the phase space. One can then show by straightforward algebra that the net correlation

$$C^{\pi\pi}(y_1, y_2) = \frac{\sigma_M}{\sigma} C_M^{\pi\pi}(y_1, y_2) + \frac{\sigma_D}{\sigma} C_D^{\pi\pi}(y_1, y_2) + \frac{\sigma_D}{\sigma_M} C_{MD}^{\pi\pi}(y_1, y_2) \tag{8.42}$$

where $C_M^{\pi\pi}$ is the short range correlation coming from the multiperipheral component (i.e. eq. (40)) and $C_D^{\pi\pi}$ is the corresponding correlation from the diffractive component shown below.
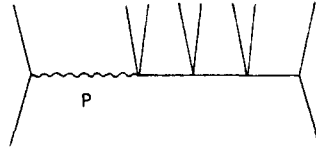
The quantity

$$C_{\mathrm{MD}}^{\pi\pi}(y_1, y_2) = \left(\frac{1}{\sigma}\frac{\mathrm{d}\sigma^\pi}{\mathrm{d}y_1} - \frac{1}{\sigma_\mathrm{D}}\frac{\mathrm{d}\sigma_\mathrm{D}^\pi}{\mathrm{d}y_1}\right)\left(\frac{1}{\sigma}\frac{\mathrm{d}\sigma^\pi}{\mathrm{d}y_2} - \frac{1}{\sigma_\mathrm{D}}\frac{\mathrm{d}\sigma_\mathrm{D}^\pi}{\mathrm{d}y_2}\right) \tag{8.43}$$

gives a long range correlation. It has no dynamical content, but simply arises from the way the correlation function is defined above. In general whenever there are several noncoherent components in the cross-section, the correlation function, will contain long range components. We see from eqs. (42, 43) that the contribution of the product term to $R^{\pi\pi}(y_1, y_2)$ is

$$\frac{\sigma_\mathrm{D}}{\sigma_\mathrm{M}}\left(1 - \frac{1}{\sigma_\mathrm{D}}\frac{\mathrm{d}\sigma_\mathrm{D}^\pi}{\mathrm{d}y_1}\bigg/\frac{1}{\sigma}\frac{\mathrm{d}\sigma^\pi}{\mathrm{d}y_1}\right)\left(1 - \frac{1}{\sigma_\mathrm{D}}\frac{\mathrm{d}\sigma_\mathrm{D}^\pi}{\mathrm{d}y_2}\bigg/\frac{1}{\sigma}\frac{\mathrm{d}\sigma^\pi}{\mathrm{d}y_2}\right). \tag{8.44}$$

8.4. Comparison with inclusive correlation data

There have been a number of fits to the ISR correlation data in this model [283–287]. We shall just enumerate the essential features.

We have seen in section 5 that depending on whether diffraction is dominated by (a) PPR or (b) PPP the ratio

$$\frac{\mathrm{d}\sigma_\mathrm{D}^\pi}{\sigma_\mathrm{D}\,\mathrm{d}y}\bigg/\frac{\mathrm{d}\sigma^\pi}{\sigma\,\mathrm{d}y}$$

in the central region is 0 or $\frac{1}{2}$ respectively. These are the choices, for instance of Pirila and Pokorski [283] and of Berger and Fox [285] respectively, whereas Le Bellac, Miettinen and Roberts [287] obtain a ratio $\simeq\frac{1}{3}$; (c) by taking a mixture of the PPP and PPR terms. With a $\sigma_\mathrm{D}/\sigma_\mathrm{M} \simeq \frac{1}{4}$, the corresponding magnitudes of the long range component in R are roughly

(a) 0.25,   (b) 0.06,   (c) 0.12. $\tag{8.45}$

Thus in the charge–charge correlation $R^{cc}(0, 0)$ the major part (0.4–0.6) is attributed to the short range components. Now the component $C_\mathrm{D}^{\pi\pi}$ coming from the diffractively excited cluster, can be calculated in the same way as the component $C_\mathrm{M}^{\pi\pi}$. One then sees from eq. (40) that the ratio

$$C_\mathrm{D}^{\pi\pi}/C_\mathrm{M}^{\pi\pi} = \frac{\mathrm{d}\sigma_\mathrm{D}^\pi}{\sigma_\mathrm{D}\,\mathrm{d}y}\bigg/\frac{\mathrm{d}\sigma_\mathrm{M}^\pi}{\sigma_\mathrm{M}\,\mathrm{d}y}.$$

Hence the diffractive cluster contribution to $R^{cc}(0, 0)$ is a tiny fraction i.e. roughly

(a) 0,   (b) 0.06,   (c) 0.04. $\tag{8.46}$

Any way subtracting (45) and (46) from the net $R^{cc}(0,0)$ ($\simeq 0.65$) one gets the multiperipheral cluster contribution. This gives using eqs. (40, 41) and a charged pion central cross-section

$$\frac{1}{\sigma}\frac{d\sigma^{\pi\,ch}}{dy} \simeq 1.8,$$

$$\frac{\langle K(K-1)\rangle}{\langle K\rangle} \simeq \text{(a) } 2, \quad \text{(b) } 2.7, \quad \text{(c) } 2.4. \tag{8.47}$$

Fig. 6 shows the predicted charge–charge correlation, with the choice (c) (and $\delta = 0.9$) along with the highest ISR energy data. The part coming from pure diffraction plus the long range product term is shown separately. The change of sign near the ends of the rapidity plot, simply comes from the change of sign of the long range term (eq. (44)).

Finally let us see what does the size of the charge–charge correlation imply for the cluster decay multiplicity. Since the diffraction is dominated by the PPP term, the phenomenologically acceptable solutions are only (b) and (c) i.e. for the cluster charge multiplicity K,

$$\frac{\langle K(K-1)\rangle}{\langle K\rangle} \simeq 2.4\text{–}2.7. \tag{8.47a}$$

This would still not give the average charge multiplicity $\langle K\rangle$ without knowing the dispersion. For instance, the above quantity corresponds to $\langle K-1\rangle$ for a narrow multiplicity distribution and to $\langle K\rangle$ for a Poisson distribution. The two quantities, average multiplicity and dispersion, can be separately determined only from the semi-inclusive correlation, which has the further advantage of eliminating the diffractive contributions. Before going into the semi-inclusive correlation analysis, however, let us simply state the results. It suggests a very narrow decay multiplicity distribution, and a significantly smaller value of $\langle K(K-1)\rangle/\langle K\rangle \simeq 1$. Thus the average cluster decay multiplicity from the inclusive and the semi-inclusive correlation analyses seem to be $\simeq 3.5$–4 charged pions (5–6 pions) and $\simeq 2$ charged pions (3 pions) respectively. The latter estimate agrees with what one expects from the pionic multiplicity of the prominent resonances and also with the result ($\langle N\rangle \simeq \ln s \simeq \frac{1}{3}\langle n_\pi\rangle$) of the simplest multiperipheral model; but the former estimate is evidently too large. Part of this discrepancy may be
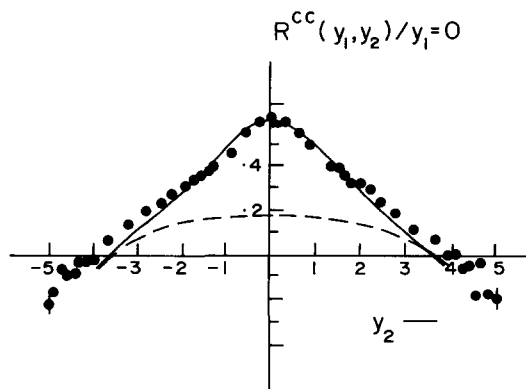

Fig. 8.6. Comparison of the ISR charge–charge correlation data [279] with the multiperipheral cluster model prediction. The dashed line shows the contribution from the diffractive cluster plus the long range product term.

attributed to the uncertainty in the diffractive contributions. Besides restricting oneself to the region $|y_1 - y_2| < 2$, one could get a reasonable fit with somewhat smaller δ and $\langle K(K-1)\rangle/\langle K\rangle$ (by around 20%). But we do not see enough room in these to account for the whole or even the major part of the discrepancy. In fact this discrepancy (in particular the internal inconsistency of a factor of 2 between the inclusive and the semi-inclusive estimates of $\langle K(K-1)\rangle/\langle K\rangle$) seems to be the single major failing of the cluster model.

8.5. Semi-inclusive rapidity correlation (cluster decay multiplicity)

The semi-inclusive correlation measures the correlation function, for a fixed number of particles in the final state – charged pions or separately π^+ and π^-. Thus it gives the correlation as a function of the particle number n, from which one can estimate the cluster decay multiplicity and dispersion separately. It also has the advantage of filtering out the diffractive contribution by taking large $n(\geq \langle n \rangle)$. It is therefore considered the most reliable basis for determining the cluster decay properties; and a large number of experimental [288–296] and phenomenological [297–304] papers have been devoted to this purpose. The semi-inclusive rapidity correlation is defined as

$$C_n(y_1, y_2) = \rho_n^2(y_1, y_2) - \rho_n^1(y_1)\rho_n^1(y_2)$$

$$= \frac{1}{\sigma_n} \cdot \frac{d^2\sigma_n}{dy_1\,dy_2} - \frac{1}{\sigma_n} \cdot \frac{d\sigma_n}{dy_1} \cdot \frac{1}{\sigma_n} \cdot \frac{d\sigma_n}{dy_2} \tag{8.48}$$

which obey, of course, the normalisation constraints

$$\int \rho_n^1(y_1)\,dy_1 = n$$

$$\int \rho_n^2(y_1, y_2)\,dy_1\,dy_2 = (n-1)\int \rho_n^1(y_1)\,dy_1 = n(n-1) \tag{8.49}$$

$$\int C_n(y_1, y_2)\,dy_1\,dy_2 = -\int \rho_n^1(y_1)\,dy_1 = -n.$$

The cluster model expressions for these quantities were first derived by Berger [297]. We shall sketch this derivation, which is less elegant but far more transparent than the alternative derivation via generating functions [304].

Dealing with final states of fixed multiplicity n involves convolution of cluster decay multiplicity dist. $p(K)$ with the multiplicity dist. P_N $(\equiv \sigma_N/\sigma)$ of cluster production. Let us define the probability of a cluster i, in a N cluster and n particle state, decaying into K_i particles as

$$\bar{P}_i(K_i, N, n) = \sum_{K_N} \cdots \sum_{K_1} \prod_{j=1}^{N} p_j(K_j) \tag{8.50}$$

where the summation is over $N-1$ quantities K_j $(j \neq i)$ for a fixed K_i, and subject to the constraint

$$\sum_{j=1}^{N} K_j = n$$

i.e. effectively over $N - 2$ quantities. The probability of a N cluster state decaying into n particles is then

$$q_N(n) = \sum_{K_i} \bar{p}_i(K_i, N, n).$$
(8.51)

It is easy to check that

$$\sum_n q_N(n) = 1$$

$$\langle n \rangle_N \equiv \sum_N n q_N(n) = N \langle K \rangle.$$
(8.52)

The net probability of producing n particles is then

$$Q_n \equiv \sigma_n/\sigma = \sum_N P_N q_N(n)$$
(8.53)

with

$$\langle n \rangle \equiv \sum_n n Q_n = \langle N \rangle \langle K \rangle.$$
(8.54)

Similar to eq. (50) above, one can define the joint probability of clusters i and j $(i \neq j)$, in a N cluster and n particle state, decaying to K_i and K_j particles as

$$J_{ij}(K_i, K_j, N, n) = \sum_{K_N} \cdots \sum_{K_1} \prod_{l=1}^{N} p_l(K_l)$$
(8.55)

with K_i and K_j held fixed and

$$\sum_T K_l = n.$$

Of course

$$\bar{p}_i(K_i, N, n) = \sum_{K_j} J_{ij}(K_i, K_j, N, n)$$
(8.56)

and from the standard definition of averaged quantities

$$\langle K \rangle_n = \frac{1}{Q_n} \sum_N P_N \sum_{K_i} K_i \bar{p}_i(K_i, N, n)$$

$$\langle K(K-1) \rangle_n = \frac{1}{Q_n} \sum_N P_N \sum_{K_i} K_i(K_i - 1) \bar{p}_i(K_i, N, n).$$
(8.57)

All the above relations hold for arbitrary production and decay distributions, as long as the two processes are independent.

Now in the multiperipheral or in any independent cluster production model one has

$$\rho_N^1(y_c) = \frac{1}{\sigma_N}\frac{d\sigma_N}{dy} = \frac{N}{Y} \tag{8.58}$$

and

$$\rho_N^2(y_{c1}, y_{c2}) = \frac{1}{\sigma_N}\frac{d^2\sigma_N}{dy_{c1}\,dy_{c2}} = \frac{N-1}{N}\rho_N^1(y_{c1})\rho_N^2(y_{c2}). \tag{8.59}$$

Then following the same procedure as subsection 8.3 (see eqs. (34–36)) one gets

$$\rho_n^1(y_1) = \frac{1}{\sigma_n}\frac{d\sigma_n}{dy_1} = Q_n^{-1}\sum_N P_N \int dy_c\,\rho_N^1(y_c)\frac{\exp\{-(y_1 - y_c)^2/2\delta^2\}}{\delta\sqrt{2\pi}} \cdot \sum_K K\bar{p}(K, N, n)$$

$$= (YQ_n)^{-1}\sum_N P_N q_N^{(n)} \cdot n = n/Y. \tag{8.60}$$

And

$$\rho_n^2(y_1, y_2) = \frac{1}{\sigma_n}\frac{d^2\sigma_n}{dy_1\,dy_2} = \frac{\exp\{-(y_1 - y_2)^2/4\delta^2\}}{2\pi\delta^2} \cdot Q_n^{-1}\sum_N P_N \int dy_c\,\rho_N^1(y_c)\exp\left\{-\left(y_c - \frac{y_1 + y_2}{2}\right)^2\Big/\delta^2\right\}$$

$$\cdot \sum_K K(K-1)\bar{p}(K, N, n) + Q_n^{-1}\sum_N P_N \int\int dy_{c1}\,dy_{c2}\,\rho_N^2(y_{c1}, y_{c2})\frac{\exp\{-(y_1 - y_{c1})^2/2\delta^2\}}{\delta\sqrt{2\pi}}$$

$$\cdot \frac{\exp\{-(y_2 - y_{c2})^2/2\delta^2\}}{\delta\sqrt{2\pi}} \cdot \sum_{K_1, K_2} K_1 K_2\, J(K_1, K_2, N, n)$$

$$= \frac{\exp\{-(y_1 - y_2)^2/4\delta^2\}}{2\delta\sqrt{\pi} \cdot Y \cdot Q_n}\sum_N P_N \cdot N \sum_K K(K-1)\bar{p}(K, N, n)$$

$$+ \frac{1}{Y^2 Q_n}\sum_N P_N \cdot N(N-1)\sum_{K_1, K_2} K_1 K_2\, J(K_1, K_2, N, n). \tag{8.61}$$

Now because of the factors N and $N(N-1)$ inside the summation, this equation cannot be expressed in terms of the average quantities at fixed n like

$$\langle K\rangle_n, \quad \langle K(K-1)\rangle_n \quad \text{etc.}$$

This can be done only for specific cluster decay distributions. We shall consider two distributions (I) δ-function and (II) Poissonian, as typical of a narrow and a broad cluster decay distribution respectively.

8.5.1. δ-function decay
Here

$$p(K) = \delta(K - K_0)$$

$$\bar{p}_i(K_i, N, n) = \delta(n - NK_0)\,\delta(K_i - K_0)$$

$$q_N(n) = \delta(n - NK_0) = \frac{1}{K_0}\,\delta\left(N - \frac{n}{K_0}\right)$$

$$Q_n = \frac{1}{K_0}\,P_N\bigg|_{N = n/K_0}$$

$$J_{ij}(K_i, K_j, N, n) = \delta(n - NK_0) \cdot \delta(K_i - K_0) \cdot \delta(K_j - K_0).$$

(8.62)

Hence

$$\langle K \rangle_n = K_0 = \langle K \rangle$$

$$\langle K(K - 1) \rangle_n = K_0(K_0 - 1) = \langle K(K - 1) \rangle.$$

(8.63)

From eqs. (61) and (62) one gets

$$\frac{1}{\sigma_n}\frac{d^2\sigma_n}{dy_1\,dy_2} = \frac{\exp\{-(y_1 - y_2)^2/4\delta^2\}}{2\delta\sqrt{\pi}} \cdot \frac{n(K_0 - 1)}{Y} + \frac{n(n - K_0)}{Y^2}$$

i.e.

$$C_n(y_1, y_2) = \frac{\overline{\exp\{-(y_1 - y_2)^2/4\delta^2\}}}{2\delta\sqrt{\pi}} \cdot \frac{n(K_0 - 1)}{Y} - \frac{nK_0}{Y^2}$$

which can be re-expressed using eq. (63) as

$$C_n(y_1, y_2) = \frac{\exp\{-(y_1 - y_2)^2/4\delta^2\}}{2\delta\sqrt{\pi}} \cdot \frac{n}{Y} \cdot \frac{\langle K(K - 1) \rangle_n}{\langle K \rangle_n} - \frac{n}{Y^2}\left(1 + \frac{\langle K(K - 1) \rangle_n}{\langle K \rangle_n}\right).$$

(8.64)

One usually substitutes back the density function ρ_n^1 for n/Y and writes

$$C_n(y_1, y_2) = \frac{\exp\{-(y_1 - y_2)^2/4\delta^2\}}{2\delta\sqrt{\pi}}\,\rho_n^1(y_1)\,\gamma(n) - \frac{1}{n}\rho_n^1(y_1)\,\rho_n^1(y_2) \cdot (1 + \gamma(n)),$$

(8.65)

$$\gamma(n) \equiv \langle K(K - 1) \rangle_n / \langle K \rangle_n.$$

Although eq. (65) is no more exact than (64), one hopes by this to partially take account of the observed deviation from the plateau.

8.5.2. Poisson decay

Here

$$p(K) = e^{-Z} \cdot Z^K/K!, \qquad Z = \langle K \rangle.$$

And since the product of N Poisson is again a Poisson, i.e.

$$\sum_{K_N} \cdots \sum_{K_1} \prod_{i=1}^{N} p(K_i) \, \delta\left(\sum K_i - n\right) = e^{-NZ}(NZ)^n/n!.$$

One has

$$\bar{p}_i(K_i, N, n) = e^{-Z} \cdot \frac{Z^{K_i}}{K_i!} \cdot e^{-(N-1)Z} \cdot \frac{((N-1)Z)^{n-K_i}}{(n-K_i)!} = e^{-NZ} \cdot Z^n \cdot \frac{(N-1)^{n-K_i}}{K_i! \, (n-K_i)!}$$

$$q_N(n) = e^{-NZ} \cdot Z^n \sum_{K_i} \frac{(N-1)^{n-K_i}}{K_i! \, (n-K_i)!} = \frac{e^{-NZ} \cdot Z^n \cdot N^n}{n!} \qquad\qquad (8.66)$$

$$J_{ij}(K_i, K_j, N, n) = e^{-NZ} \cdot \frac{Z^n (N-2)^{n-K_i-K_j}}{K_i! \, K_j! \, (n-K_i-K_j)!}.$$

From eqs. (57) and (66) one gets, following some simple algebra

$$\langle K \rangle_n = \langle K \rangle \, \sigma_{n-1}/\sigma_n$$
$$\langle K(K-1) \rangle_n = \langle K \rangle^2 \, \sigma_{n-2}/\sigma_n \qquad\qquad (8.67)$$
$$\langle K(K-1) \rangle / \langle K \rangle = \langle K \rangle.$$

From eqs. (61), (66) and (67) one gets, again following some simple algebra,

$$\frac{1}{\sigma_n} \frac{d^2\sigma_n}{dy_1 \, dy_2} = \frac{\exp\{-(y_1-y_2)^2/4\delta^2\}}{2\sigma\sqrt{\pi}} \cdot \frac{(n-1)\langle K \rangle_n}{Y} + \frac{n(n-1)}{Y^2} - \frac{(n-1)\langle K \rangle_n}{Y^2}$$

i.e.

$$C_n(y_1, y_2) = \frac{\exp\{-(y_1-y_2)^2/4\delta^2\}}{2\delta\sqrt{\pi}} \cdot \rho_n^1(y_1) \cdot \frac{n-1}{n} \langle K \rangle_n - \frac{1}{n} \rho_n^1(y_1) \rho_n^1(y_2) \left(1 + \frac{n-1}{n} \langle K \rangle_n\right). \qquad (8.68)$$

Now

$$\langle K \rangle_n \cdot \frac{n-1}{n} = \frac{\langle K(K-1) \rangle_n}{\langle K \rangle_n} \left[\frac{\sigma_{n-1}/\sigma_n}{\sigma_{n-2}/\sigma_{n-1}} \cdot \frac{n-1}{n}\right] \simeq \frac{\langle K(K-1) \rangle_n}{\langle K \rangle_n} \qquad\qquad (8.69)$$

since the last factor is $\simeq 1$ for almost any reasonable distribution (it is exactly 1 for a Poisson distribution in n). Thus to a good accuracy one again gets eq. (65), for the correlation function. Moreover, the cluster parameter

$$\gamma(n) \equiv \frac{\langle K(K-1) \rangle_n}{\langle K \rangle_n} = \frac{\langle K(K-1) \rangle}{\langle K \rangle} \cdot \frac{\sigma_{n-2}}{\sigma_{n-1}} \xrightarrow{n \simeq \langle n \rangle} \frac{\langle K(K-1) \rangle}{\langle K \rangle}. \qquad\qquad (8.70)$$

As mentioned earlier the (1) δ-function and (2) Poisson cases are prototypes of a narrow and a broad decay multiplicity distribution. Thus in either case the semi-inclusive correlation function is expected to

obey eq. (65), and the resulting cluster parameter $\gamma(n)$ at $n \simeq \langle n \rangle$ should correspond to the quantity

$$\langle K(K-1) \rangle / \langle K \rangle$$

evaluated earlier from the inclusive correlation. There are two significant differences however. (a) The above quantity corresponds to $\langle K \rangle - 1$ for case I and to $\langle K \rangle$ for case II. Thus from the same inclusive correlation (or the semi-inclusive correlation at $n \simeq \langle n \rangle$) one would get a bigger or smaller cluster decay multiplicity depending on whether the multiplicity distribution is narrow or broad. (b) Whereas for case I the parameter γ is n-independent, for case II it increases significantly with n for $n > \langle n \rangle$ as one sees from eq. (70) (e.g. for a Poisson distribution in n it will be proportional to n). Thus from the n-dependence of the semi-inclusive correlation data, one can distinguish between narrow and broad decay multiplicity distributions.

8.5.3. Comparison with data

Let us now compare the above predictions with the semi-inclusive rapidity correlation data. The data come primarily from 4 experiments – Pisa–Stony Brook [288] and Aachen–CERN–Munich [289] collaborations at ISR and ANL–FNAL–Stony Brook [290] and Rochester–Michigan [292] bubble chamber collaborations at FNAL. We shall concentrate on the PSB data, which alone has sufficient statistics for a quantitative study of the rapidity and the n dependence. It, of course, has two problems. Firstly it gives only the pseudo rapidity η as it lacks momentum measurement. Secondly it has rather serious counting problem – the measured cross-section $d\sigma_n/dy$ and $d\sigma_n/dy_1 dy_2$ actually correspond to several prong cross-sections around the observed value of n. The counting losses (and gains) have, however, been estimated by this group, on the basis of which they obtain an effective n and the corresponding C_n function (see ref. [288] for details). These C_n functions are then seen to satisfy the proper normalisation constraints (eq. (49)) and also to agree with the other measurements mentioned above. There is only one nagging discrepancy – at very large n ($\simeq 2\langle n \rangle$) the 200 GeV/$c$ bubble chamber data [290] seems to give a significantly lower correlation ($C_{14}(0, 0) = -1.2 \pm 0.6$) than the corresponding ($\sqrt{s} = 23$) PSB data ($C_{14}(0, 0) = 0.236 \pm 0.052$). Following the practice in the literature we shall ignore the bubble chamber result in this region in view of its poor statistics.

The semi-inclusive charge–charge correlation data from the 200 GeV/c FNAL experiment and the PSB experiment at $\sqrt{s} = 23$ are shown in figs. 7 and 8 for $n = 8$ and an effective $n = 9.1$ respectively (i.e. $n \simeq \langle n \rangle$). The uncertainty in the FNAL data is evidently too large for a quantitative analysis, but within this large uncertainty it is consistent with the PSB data. The PSB data is compared with the prediction of eq. (65) for several cluster parameters. The data is evidently incompatible with a large cluster parameter $\gamma \simeq 2$, as suggested by the inclusive data. The latter gives either too large a height ($\delta = 0.7$) or too large a width ($\delta = 1$) for the short range peak. A reasonable agreement is obtained however, with a small cluster parameter $\gamma = 0.8$ and $\delta = 0.62$. For a more detailed analysis, the PSB group have extracted the short range peak from their data, by fitting it to

$$C_n(0, y) = A_n \exp(-y^2/4\delta^2) - B_n \rho_n^1(y) \tag{8.71}$$

(compare eq. (65)*). The short range parts corresponding to the first term, have been reproduced from

---

* It should be mentioned, however, that the relative magnitudes of the coefficients B_n and A_n so obtained are in agreement with eq. (65) for $n \simeq \langle n \rangle$, but show significant departure at larger n values.
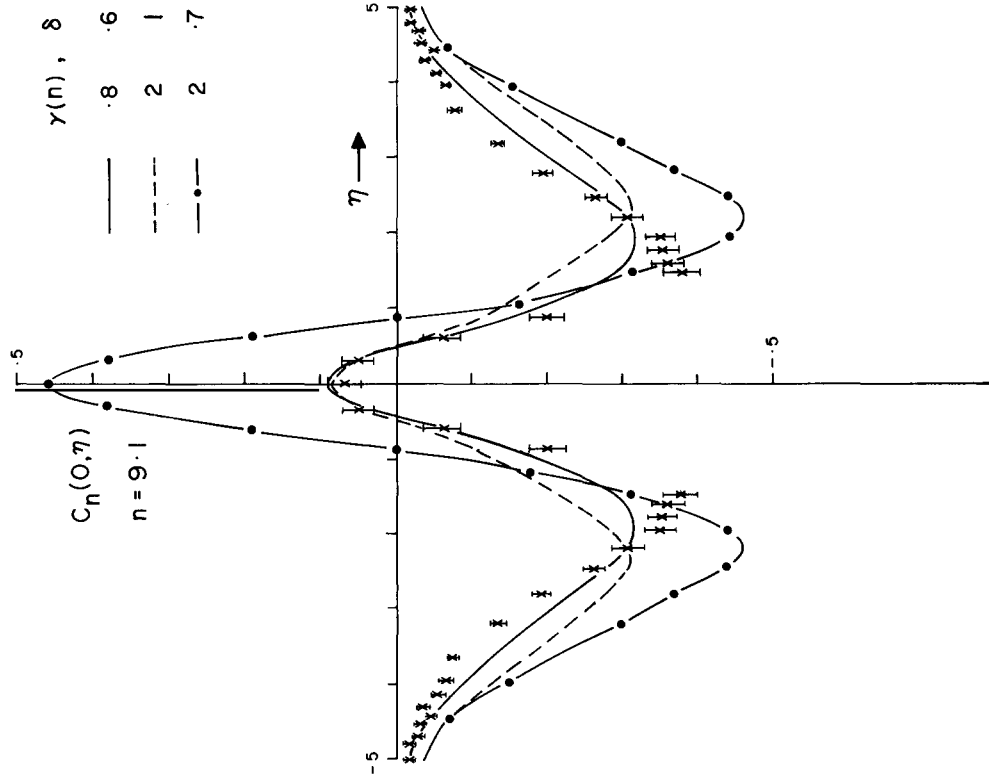
Fig. 8.8. Comparison of cluster model prediction (eq. (6.5)) with the charge–charge semi-inclusive correlation data $C_n(0, \eta)$ from $\sqrt{s} = 23$ PSB experiment [288]. The observed $n = 10, 11$ corresponding to an effective $n = 9.1$.
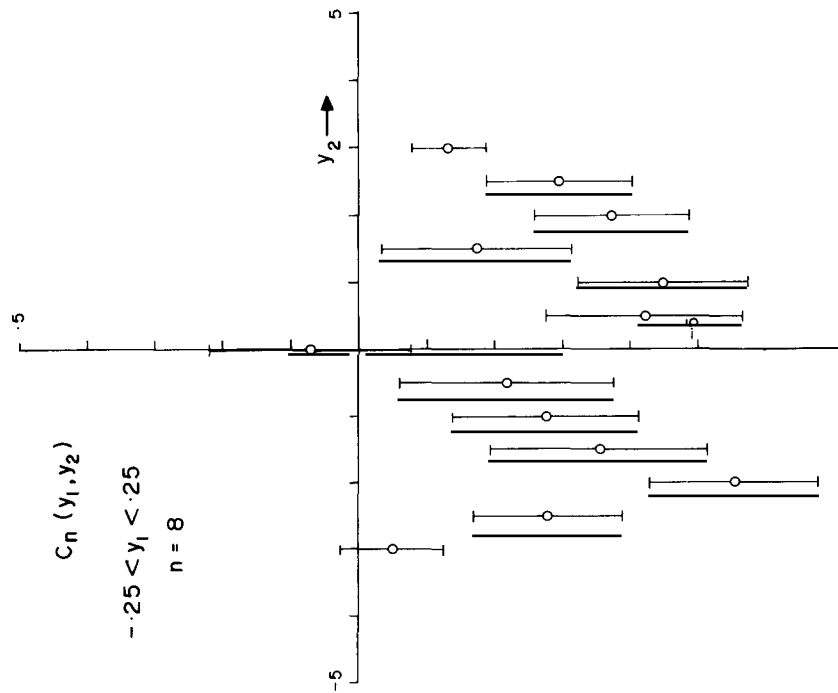

Fig. 8.7. The charge–charge semi-inclusive correlation data $C_n(y_1, y_2)$ from the 200 GeV FNAL experiment [290].

ref. [288] along with their fits (fig. 9). The fits yield a $\delta \simeq 0.6$ and the corresponding $\gamma(n)$ are shown in fig. 10. One notes that at the highest ISR energy $\sqrt{s} = 62$, the cluster parameter γ is practically n-independent. There is an appreciable n-dependence, however, at $\sqrt{s} = 23$. This would be an embarrassment for the cluster model, since the cluster parameters are energy independent quantities. It has however, been demonstrated by Arneodo and Plaut [300] that things like energy conservation and leading particle effect, when incorporated into the above formalism, can account for such a spurious energy dependence. More precisely they start with a $\gamma \simeq 1.2$, independent of energy and practically independent of n and generate the correlation functions C_n through a Monte Carlo calculation, which incorporates the above effects. When these correlation functions are fitted to the simple formula (65), one gets an effective $\gamma(n)$ (fig. 11), showing the same energy and n-dependence as the PSB result (fig. 10).

Thus it is reasonable to conclude that the semi-inclusive longitudinal correlation data is in agreement with the cluster model with $\delta \simeq 0.7$ and a practically n-independent cluster parameter $\gamma \simeq 1$. This suggests a narrow multiplicity distribution for cluster decay and an average decay multiplicity of $\simeq 2$ charged pions ($\simeq 3$ pions) per cluster; which is perfectly consistent with its identification with the prominent resonances (η, ρ, ω, f, A_2). Note finally that the corresponding multiplicity of $\simeq 1$ positive (or negative) pion per cluster implies a negligible short range component in C_n^{++} (or C_n^{--}). This is consistent with the meagre FNAL data available on these quantities.
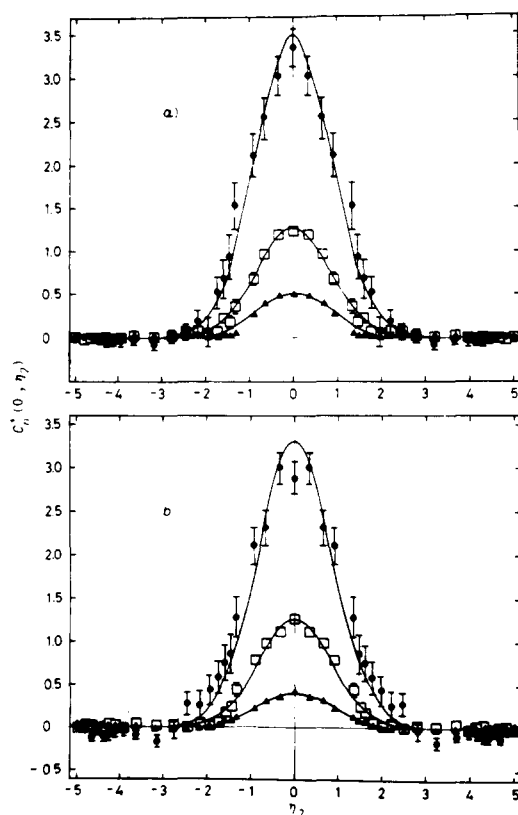

Fig. 8.9. The short range part of the PSB data [288] on $C_n(0, \eta)$ compared with the cluster model prediction with $\delta = 0.6$. (a) $\sqrt{s} = 23$ GeV: $n_{obs} = 10, 11(\blacktriangle)$; $14, 15(\square)$; $20, 21(\bullet)$. (b) $\sqrt{s} = 62$ GeV: $n_{obs} = 10, 11(\blacktriangle)$; $20, 21(\square)$; $30, 31(\bullet)$.
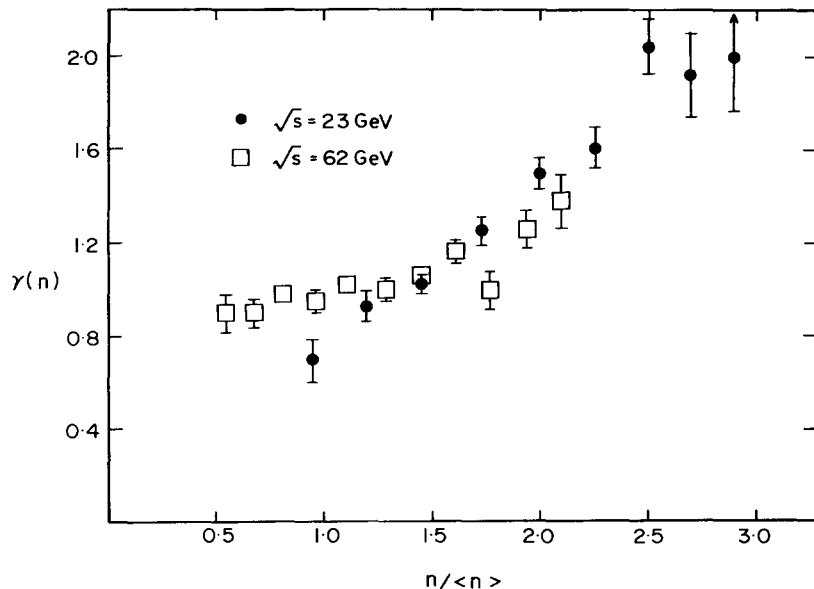
Fig. 8.10. The cluster parameter $\gamma(n)$ obtained by the PSB fit to their data on $C_n(0, \eta)$; as shown in fig. 9.
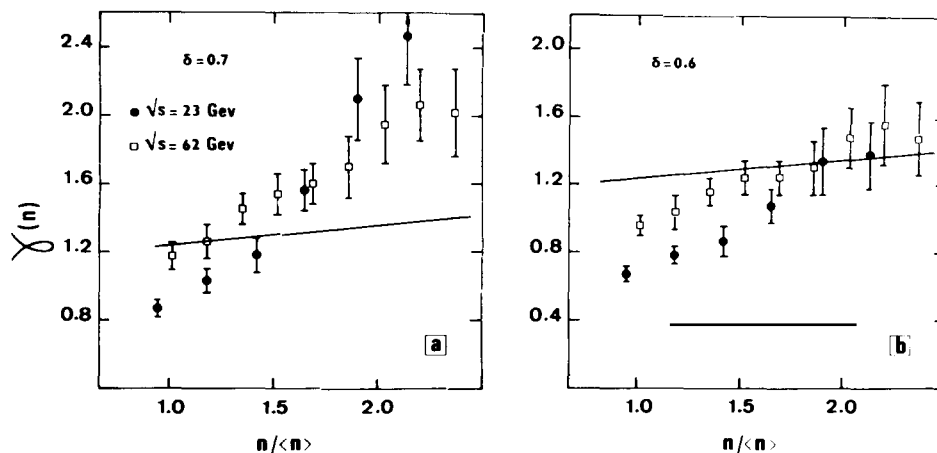
Fig. 8.11. Incorporating energy conservation and leading particle effects into a cluster model with a practically n-independent cluster parameter γ (solid line) leads to an effective $\gamma(n)$ very similar to the PSB fit (fig. 9). This is taken from a Monte Carlo calculation by Arneodo and Plaut [300].

8.6. Azimuthal correlation (cluster mass)

The rapidity correlations, described above, provided a fairly precise estimate of the cluster decay multiplicity ($\langle K \rangle \simeq 3$) but not of the cluster mass M. This is because the width δ is insensitive to the cluster mass or the q (decay pion momentum in the cluster rest frame) as long as the latter is large compared to the pion mass*. To estimate this one must consider the azimuthal correlation between the decay pions.

---

* None-the-less a value of $M = 1.3$ GeV has been obtained by Arneodo and Meunier [252], corresponding to $\delta = 0.7$ and $K = 3$ (see eqs. (32–34) above). It is reassuring that this is roughly consistent with the estimate from azimuthal correlation (eq. (91)).

Before going to the azimuthal correlation however, let us note that the sharp transverse momentum cut-off of the decay pions ($\langle p_T^2 \rangle \simeq 0.15$) already provide an upper-bound on the cluster mass (or q-value). This is because the p_T distribution is obtained by convoluting the cluster transverse momentum k_T with q_T; and a small $\langle p_T \rangle$ implies that $\langle q_T \rangle$ cannot be too large irrespective of $\langle k_T \rangle$. Let us briefly describe a semiquantitative estimate of this bound following Hayot et al. [305].

Let z be the longitudinal direction and x the direction of the cluster transverse momentum k_T. Since we are not interested in the cluster longitudinal momentum, we can work in a frame where this quantity is zero. Then in terms of the cluster transverse rapidity η

$$M_T = M \cosh \eta, \qquad k_T = M \sinh \eta \tag{8.72}$$

and

$$p_x = q_x \cosh \eta + E \sinh \eta, \qquad p_y = q_y \tag{8.73}$$

where E, q are the pion energy, momentum in the cluster rest frame. Assuming isotropic cluster decay as before,

$$\langle q_x \rangle = \langle q_y \rangle = 0$$
$$\langle q_x^2 \rangle = \langle q_y^2 \rangle = \tfrac{1}{2} \langle q_T^2 \rangle \tag{8.74}$$

and neglecting pion mass terms, one gets the approximate equality*,

$$\langle E \rangle^2 \simeq \langle q_T^2 \rangle. \tag{8.75}$$

Since the cluster production and decay are independent one can average over the two separately. Thus eqs. (72–75) give

$$\langle p_T^2 \rangle = \langle q_x^2 \rangle \langle \cosh^2 \eta \rangle + \langle E^2 \rangle \langle \sinh^2 \eta \rangle + \langle q_y^2 \rangle$$
$$= \langle q_T^2 \rangle \cdot (1 + 2\langle k_T^2/M^2 \rangle)$$
$$\simeq \langle E \rangle^2 \cdot (1 + 2\langle k_T^2/M^2 \rangle). \tag{8.76}$$

Finally

$$\langle E \rangle \simeq M/\langle K \rangle \simeq M/3$$

i.e.

$$\langle p_T^2 \rangle \simeq 0.15 \simeq \frac{M^2}{9} \left(1 + 2\left\langle \frac{k_T^2}{M^2} \right\rangle\right) \tag{8.77}$$

which gives an upper bound on the average cluster mass

$$M \lesssim 1.2 \text{ GeV}.$$

---

* The exact relation would depend, of course, on the shape of q-distribution. For a Boltzmann distribution one can easily check that $\langle E \rangle^2 = (4/\pi)\langle q_T^2 \rangle$.

If the quantity

$$X = \langle k_{\mathrm{T}}^2/M^2 \rangle \tag{8.78}$$

is $\ll 1$ (i.e. for small cluster transverse momentum) the cluster mass will be close to the upper bound. But for large cluster transverse momentum it could be significantly smaller. Thus for an estimate of the cluster mass one needs some knowledge of its average transverse momentum $\langle k_{\mathrm{T}} \rangle$. This can be obtained from the inclusive azimuthal correlation data as we see below.

We shall again restrict to the aspects of azimuthal correlation most relevant for the present analysis. A more detailed account can be found in refs. [304, 306, 307]. The quantity most readily calculable in the cluster model is

$$\langle p_{\mathrm{T}1} \cdot p_{\mathrm{T}2} \rangle / \langle p_{\mathrm{T}}^2 \rangle$$

whereas that more easily measurable is $\langle \cos \phi \rangle - \phi$ being the azimuthal angle between the two detected pions. The two are not exactly the same, of course, since the former is a weighted average of $\cos \phi$ which emphasises the large p_{T} contribution. Assuming this quantity to be not too severely p_{T} dependent however, one expects

$$\langle p_{\mathrm{T}1} \cdot p_{\mathrm{T}2} \rangle / \langle p_{\mathrm{T}}^2 \rangle \simeq \cos \phi. \tag{8.79}$$

The azimuthal correlation data seems to show a short range component of this quantity in $\Delta y = y_1 - y_2$ (see fig. 13). Let us concentrate on this short range component, for which one can give a fairly unambiguous estimate. This component corresponds evidently to both the charged pions coming from the same cluster. For this configuration one gets from eqs. (73, 74)

$$\langle p_{\mathrm{T}1} \cdot p_{\mathrm{T}2} \rangle^{\mathrm{S}} = \langle p_{x1} p_{x2} \rangle + \langle p_{y1} p_{y2} \rangle$$
$$= \langle q_{x1} q_{x2} \rangle \langle \cosh^2 \eta \rangle + \langle E_1 E_2 \rangle \langle \sinh^2 \eta \rangle + \langle q_{y1} q_{y2} \rangle. \tag{8.80}$$

Now it simply follows from energy momentum conservation $(\Sigma_i E_i = M, \Sigma_i q_i = 0)$ that

$$\left\langle \left(\sum_i E_i \right)^2 \right\rangle = K \langle E^2 \rangle + K(K - 1) \langle E_1 E_2 \rangle = M^2$$

$$\left\langle \left(\sum_i q_{xi} \right)^2 \right\rangle = K \langle q_x^2 \rangle + K(K - 1) \langle q_{x1} q_{x2} \rangle = 0 \tag{8.81}$$

and similarly for the y-component. Plugging these in eq. (80) gives via eqs. (74–78)

$$\frac{\langle p_{\mathrm{T}1} \cdot p_{\mathrm{T}2} \rangle}{\langle p_{\mathrm{T}}^2 \rangle} = -\frac{(1 + X)}{(1 + 2X)(K - 1)} + \frac{X}{1 + 2X} \cdot \tag{8.82}$$

One has to finally multiply this quantity by the probability of both the charged pions coming from the same cluster to get the net short range component, i.e.

$$\frac{\langle p_{\mathrm{T}1} \cdot p_{\mathrm{T}2} \rangle^{\mathrm{SR}}}{\langle p_{\mathrm{T}}^2 \rangle} = \left[-\frac{(1 + X)}{(1 + 2X)(K - 1)} + \frac{X}{1 + 2X} \right] \cdot \left[\frac{N^{\mathrm{S}}}{N^{\mathrm{S}} + N^{\mathrm{D}}} \right] \tag{8.83}$$

where (see eq. (36))

$$N^S = \int dy_c\, \rho(y_c)\, g(y_1 - y_c, y_2 - y_c) \simeq \langle K(K-1)\rangle_{ch} \cdot \frac{\exp\{-(y_1 - y_2)^2/4\delta^2\}}{2\delta\sqrt{\pi}}$$

$$N^D = \int dy_{c1}\, dy_{c2}\, \rho(y_{c1})\, \rho(y_{c2})\, g(y_1 - y_{c1})\, g(y_2 - y_{c2}) \simeq \langle K\rangle_{ch}^2. \tag{8.84}$$

Here we have approximated the cluster density $\rho(y_c) \simeq 1$ following eqs. (28, 29). Substituting for the cluster charge multiplicity $\langle K\rangle_{ch} \simeq 2$ gives

$$N^S/(N^S + N^D) \simeq \tfrac{1}{5}\exp\{-(y_1 - y_2)^2/4\delta^2\} \tag{8.85}$$

i.e.

$$\langle\cos\phi\rangle^{SR} \simeq \left[-\frac{(1+X)}{(1+2X)(K-1)} + \frac{X}{(1+2X)}\right]\tfrac{1}{5}\exp\left\{-\frac{(y_1 - y_2)^2}{4\delta^2}\right\}. \tag{8.86}$$

Note that a negative (positive) short range component is $\langle\cos\phi\rangle$ would correspond to the average cluster transverse momentum being small, $X \ll 1$ (large, $X \simeq 1$). The data seems to suggest a negative component as we see below.

The fig. 12 shows the distribution at ISR from the CERN–Bologna experiment [308]. The data sample has been so chosen as to minimise the effects from diffraction and Bose statistics (see ref. [308] for details). One could, of course, calculate the $\langle\cos\phi\rangle$ from this. We are interested however in the Δy distribution, which is available only for the asymmetry parameter (fig. 13)
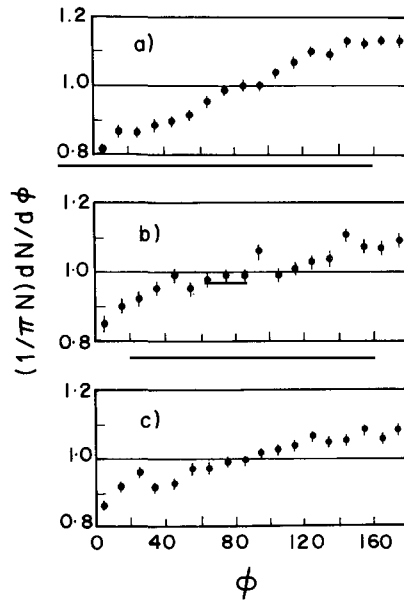
Fig. 8.12. Azimuthal-correlation–angle distribution of the 2 pion inclusive cross-section [308]; (a) $\pm\mp$ pairs, (b) $--$ pairs, (c) $=++$ pairs ($\Delta y < 1.5$).
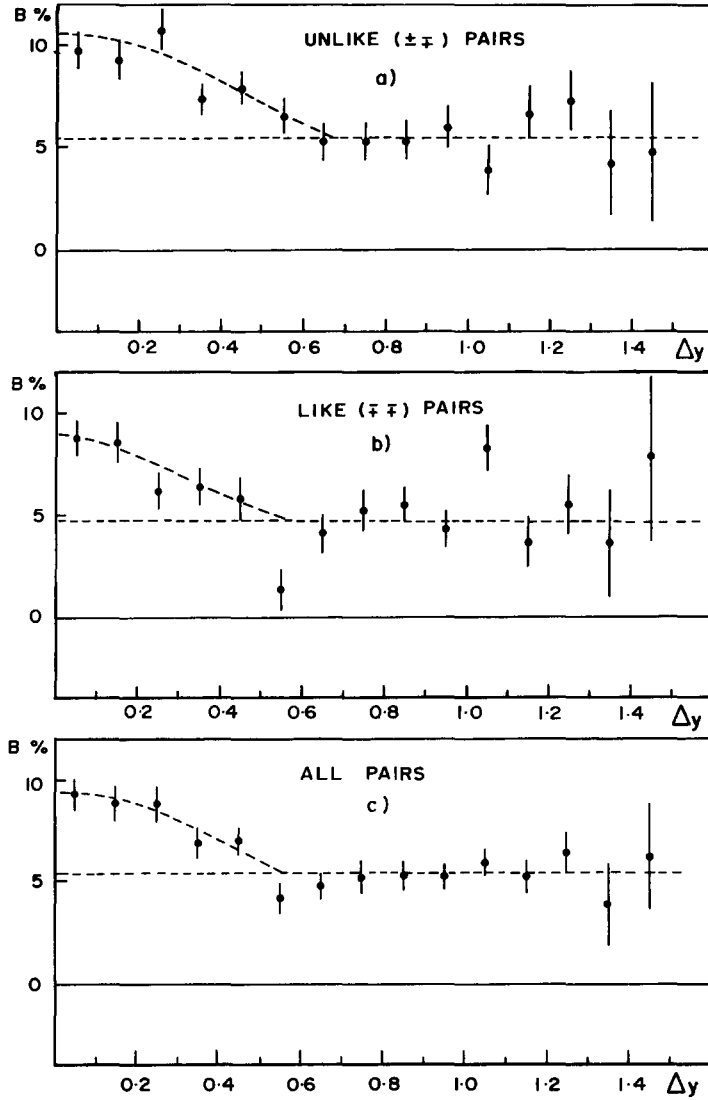
Fig. 8.13. Asymmetry parameter as a function of Δy; (a) unlike, (b) like, (c) all charge pairs. The dashed line indicate the procedure followed in separating the short range component [308].

$$B = \left(\int_{\pi/2}^{\pi} \frac{dN}{d\phi} d\phi - \int_{0}^{\pi/2} \frac{dN}{d\phi} d\phi \right) \bigg/ \int_{0}^{\pi} \frac{dN}{d\phi} d\phi. \tag{8.87}$$

One sees none-the-less from fig. 12 that the numerator is peaked near $\cos \phi \simeq \pm 1$. Thus to a crude approximation

$$B \simeq \int_{0}^{\pi} \frac{dN}{d\phi} (-\cos \phi) \, d\phi \bigg/ \int_{0}^{\pi} \frac{dN}{d\phi} d\phi \simeq -\langle \cos \phi \rangle. \tag{8.88}$$

Of course, a comparison of the shape of y distribution would require estimating the long range component and also a more realistic treatment of the quantities $\rho(y_c)$ etc. than done above*. We shall therefore, restrict to the $\Delta y = 0$ region where the prediction should be most reliable and isolate the short range component from the data, following the rather simplistic procedure, as indicated in fig. 13. The data seems to suggest a short range component (all charge pairs)

$$B_{\Delta y=0}^{SR} \simeq 0.04. \tag{8.89}$$

This implies through eq. (86)

$$X \simeq 0.3 \tag{8.90}$$

with $K = 3$. Putting this in eqs. (77, 78) gives finally

$$M \simeq 1\,\mathrm{GeV}, \qquad \langle k_T^2 \rangle \simeq 0.3\,\mathrm{GeV}^2 \tag{8.91}$$

where both the estimates should be taken with an uncertainty of 50% on either side. One should note finally that both the estimates are roughly consistent with those obtained in the last section, from the pionisation cross-section rise in the multiperipheral cluster model. They are also consistent with the average mass and transverse momentum of the resonances (η, ρ, ω, f, A_2) which seem to dominate pion production – the 16 GeV data suggests roughly a common $\langle k_T^2 \rangle \simeq 0.3$, for the production of these resonances [251]. Finally such an average transverse momentum is also very roughly consistent with the multiperipheral cluster model calculation of the elastic overlap function, which gives [304]

$$\alpha_P' \simeq 0.14/\langle k_T^2 \rangle. \tag{8.92}$$

8.7. Other types of correlation (cluster charge)

There are a number of more modern and fancy correlation functions on which one has data from FNAL. These are (a) gap distributions (inclusive), (b) left–right fluctuation parameter (semi-inclusive), (c) zone characteristics (inclusive and semi-inclusive) and (d) charge transfer correlation (inclusive). A clear and comprehensive account of these correlation data vis a vis the cluster model predictions is contained in the two papers of Arneodo and Plaut [300], referred to earlier. We shall simply state their main conclusions. Firstly the gap distribution can accommodate any cluster size in the range $\langle K \rangle_{ch} = 2$ to 4, when finite energy effects are taken into account. Secondly the semi-inclusive fluctuation parameter is sensitive to the cluster rapidity width δ and the width of decay multiplicity distribution and also to the energy conservation and leading particle effects. Thus any information on the cluster size $\langle K \rangle_{ch}$ derived from this quantity is highly model dependent. Finally the same is also true for the two other quantities. Thus these new correlation quantities cannot provide an unambiguous estimate of the cluster parameters unlike the good old semi-inclusive rapidity correlation data. Furthermore, the cluster parameters estimated from the latter (i.e. $\delta \simeq 0.7$, $\langle K \rangle_{ch} \simeq 2$ and dispersion much narrower than Poisson)

---

* A more detailed calculation by Arneodo and Meunier [309], where the long range component is estimated in a multiperipheral model (via the neighbouring cluster term), seems to be in very rough agreement with the shape of this data over $\Delta y = 0$–3, for $X \simeq 0.3$.

are seen to be consistent with all the new correlation functions when the energy conservation and the leading particle effects are taken into account*.

There is one aspect, however, where these new correlation functions provide additional information on the cluster characteristics – i.e. the cluster charge distribution. The analysis of the longitudinal and azimuthal correlations, as given above, involved only the average cluster charge; and therefore cannot distinguish between different charge distributions of the cluster as long as the average charge is zero. The simplest model, of course, is to assume neutral cluster, which also has the advantage of being strictly consistent with the independent cluster emission hypothesis. However, the neutral cluster model would conflict with the identification of the cluster with the prominent resonances, a good fraction of which came in charged $(Q = \pm1)$ states. It is therefore significant to study the correlations, which can probe the cluster charge distribution. These are the gap distribution, zone characteristics and charge-transfer correlations. Let us just look at the simplest of these quantities – the gap distribution. For independent cluster emission, the probability of occurrence of large rapidity gaps r (i.e. $r \gg \delta$) between final pions, which is the same as that between neighbouring clusters, is given by

$$G(r) \simeq e^{-\rho r}, \qquad r \gg \delta \tag{8.93}$$

where ρ is the cluster rapidity density $(\simeq 1)$ as discussed earlier. Moreover one can measure the charge transfer across a gap

$$\Delta Q(y) = \sum_{i=1}^{n} Q_i \, \theta(y - y_i) - Q_{\text{beam}} \, \theta(y - y_{\text{beam}}) - Q_{\text{target}} \, \theta(y - y_{\text{target}}) \tag{8.94}$$

where y is the rapidity of any point on the gap. Now in the neutral cluster model there is no charge to be transferred between the clusters and hence the probability of large gaps $(r \gg \delta)$ with $\Delta Q = \pm1$ are expected to be small relative to those with $\Delta Q = 0$. On the other hand, a significant percentage of charged $(Q = \pm1)$ clusters, would imply charge transfers of ±1 units between clusters; and hence the large gaps with $\Delta Q = \pm1$ are as probable as those with $\Delta Q = 0$. Fig. 14 shows the FNAL data on $|\Delta Q| = 0$, 1 and 2 distributions along with the fits of Arneodo and Plaut. Whereas the large gaps with $|\Delta Q| = 2$ are indeed suppressed, those with $|\Delta Q| = 1$ remain twice as frequent as those with $\Delta Q = 0$, thus implying a significant fraction of charged $(Q = \pm1)$ cluster. The fits correspond to a fraction of charged clusters $R_c \simeq 0.55$ with the other cluster parameters fixed at the values obtained from the semi-inclusive rapidity correlation. Similar fits have been obtained by these authors to the FNAL data on the zone characteristics and charge transfer correlation. They have also demonstrated that in each case there is a perceptible discrepancy with the neutral cluster model, even with the leading charge flow taken into account [312, 313]. For an acceptable fit they need a significant fraction of the cluster to be charged $(R_c \simeq 0.45$ to $0.70)$. Let us note finally that a charged cluster fraction in this range is also consistent with its identification with the prominent meson resonances.

In closing this subsection it should be noted that the estimate of the cluster properties from the correlation data did not explicitly invoke the multiperipheral dynamics for cluster production. It only used the hypothesis of independent cluster emission leading to such general properties as the energy

---

* It may be recalled that the gap distribution data was first used by Pirila, Thomas and Quigg [310], who obtained a $\langle K \rangle_{\text{ch}} \simeq 2$ in the asymptotic approximation (eq. (93)). Ludlam and Slansky [311] pointed out that the gap distribution was insensitive to the cluster size in the presence of finite energy effects, and suggested a significantly larger cluster size ($\langle K \rangle_{\text{ch}} \simeq 4$) on the basis of the semi-inclusive fluctuation parameter. They had assumed, however, too broad rapidity width ($\delta \simeq 0.85$) and decay multiplicity distribution (Poissonian) for the cluster and ignored the leading particle effect.
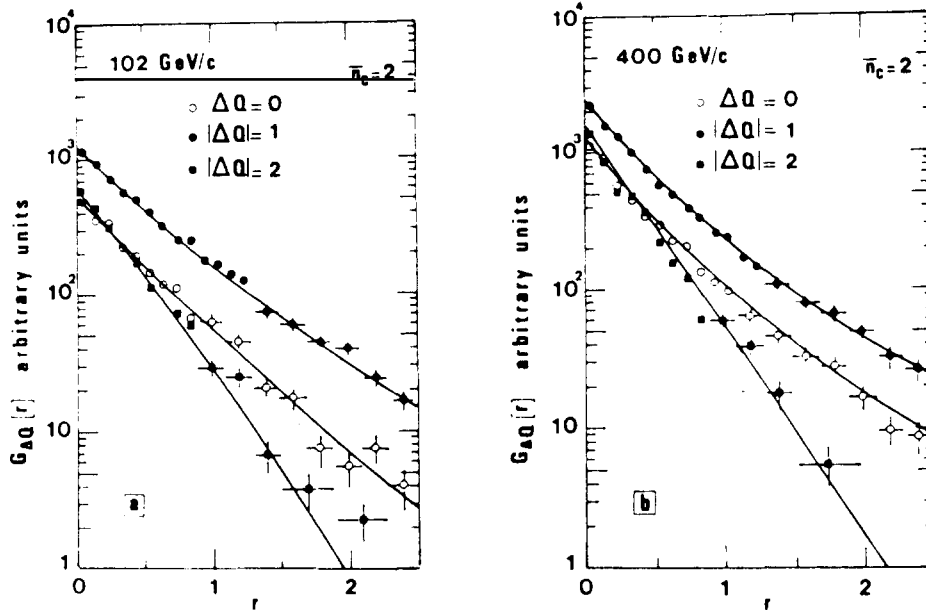
Fig. 8.14. The FNAL data on gap distribution compared with the cluster model calculation of Arneodo and Plaut. The model corresponds to a $\delta = 0.7$, $\langle K \rangle_{ch} = 2$, dispersion narrower the Poisson and $R_c = 0.55$. Figure taken from ref. [300].

and rapidity independent cluster density and exponential gap distribution. Of course, the multi-peripheral model is the simplest and theoretically the most attractive realisation of the independent cluster emission hypothesis. The results are expected to be valid, none-the-less, in a wider class of cluster production models. It is only in the comparison with the cluster characteristics obtained from the pionisation cross-section rise or with the elastic overlap function (eq. (92)) that the multiperipheral dynamics of cluster production is explicitly tested.

8.8. Gribov calculus and Eikonal models

Finally let us look at the implications of Gribov calculus or Eikonal models along with the AGK cutting rule, on correlation. This model has been described at length in the last section. A priori it seems reasonable to expect that incorporation of the polyperipheral terms, corresponding to the number of cut Pomeron lines:

$$n \geq 2$$

will significantly affect the results of the last sections, which were based on the 2-component model ($n = 0, 1$). Unfortunately, however, these effects have remained almost entirely unexplored.

One of the very few places where this effect has been explored is forward–backward multiplicity correlation [307]. The ISR data by the ACHM collaboration seem to show a positive correlation – the average multiplicity in the forward hemisphere $\langle n_F \rangle$ goes up with increasing multiplicity in the backward hemisphere n_B. In the independent cluster emission model one expects no correlation between the two hemispheres, particularly at large multiplicity*. In the Gribov calculus model, on the other hand,

---

* At small multiplicity n_B, a positive correlation is expected from energy-momentum conservation as also from the diffractive component ($n = 0$).

increasing n_B provides an increasing bias in favour of the polyperipheral $(n \geq 2)$ events and hence predicts an increasing $\langle n_F \rangle$. The trend of the data is compared with the standard 2-component cluster model and the Gribov calculus model in fig. 15 (taken from ref. [307]). The data seems to favour the Gribov calculus model. One may note, however, that the model prediction shown here is restricted to the lowest polyperipheral contribution $(n \leq 2)$ and hence only qualitative.

We have tried to see if the Gribov calculus model could help to resolve the anomalously large cluster size $\langle K(K-1) \rangle / \langle K \rangle \approx 2.5$ charged particles (eq. (47a)), as estimated from the inclusive rapidity correlation data in subsection 8.4. The answer seems to be in the affirmative. We have to make, of course, some simplistic assumptions. The terms with different number of cut Pomeron chains (n) would populate different multiplicity domains and hence add incoherently in the cross-section. They would thus give rise to long range interference terms in the correlation analogous to the 3rd term in eq. (42). In contrast the terms with the same n but different number of uncut Pomerons (ν) would add coherently and hence give no such interference term. We shall therefore assume that they are jointly described by an independent cluster emission model. This seems to us a reasonable assumption, in so far as one is not explicitly using a multiperipheral production dynamics. Any way, granting this assumption it is straightforward to obtain the following formulae, where σ_n refers to the cross-section with n cut Pomerons and all the uncut Pomerons (ν) summed over.

$$C(y_1, y_2) = \frac{1}{\sigma} \sum_n \frac{d^2 \sigma_n}{dy_1 \, dy_2} - \frac{1}{\sigma} \cdot \sum_n \frac{d\sigma_n}{dy_1} \cdot \frac{1}{\sigma} \cdot \sum_{n'} \frac{d\sigma_{n'}}{dy_2}$$

$$= \sum_n \frac{\sigma_n}{\sigma} C_n(y_1, y_2) + \frac{1}{2} \sum_{n,n'} \frac{\sigma_n \sigma_{n'}}{2} (\rho_n(y_1) - \rho_{n'}(y_1))(\rho_n(y_2) - \rho_{n'}(y_2)) \tag{8.95}$$
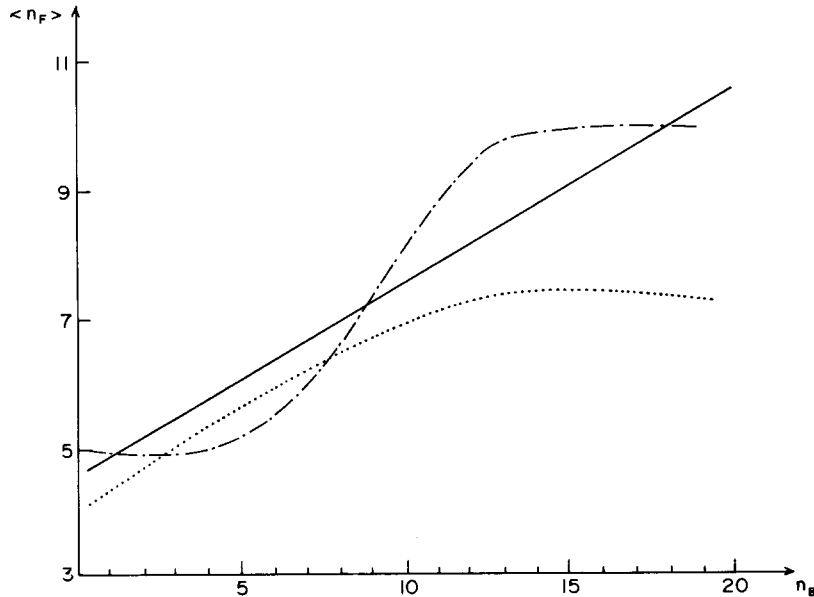

Fig. 8.15. The average forward multiplicity $\langle n_F \rangle$ as a function of the backward multiplicity n_B. Full line – trend of ISR data at $\sqrt{s} = 63$; dotted line – results of the 2-component cluster model of Arneodo and Plaut; dotted-dashed line – results of the Gribov calculus model with 1 and 2 Pomeron chains $(n = 1, 2)$. Figure taken from ref. [307].

where*

$$C_n(y_1, y_2) = \frac{1}{\sigma_n} \frac{d^2\sigma_n}{dy_1 \, dy_2} - \rho_n(y_1)\rho_n(y_2)$$

$$\rho_n(y) = \frac{1}{\sigma_n} d\sigma_n/dy$$

$$\sigma = \sum \sigma_n. \tag{8.96}$$

Now each short-range component is given by the independent cluster model result of eq. (40), i.e.

$$C_n(y_1, y_2) = \frac{\langle K(K-1)\rangle}{2\delta\sqrt{\pi}\langle K\rangle} \left(\frac{d\sigma_n}{\sigma_n \, dy}\right) \cdot \exp\left\{-\frac{(y_1-y_2)^2}{4\delta^2}\right\}. \tag{8.97}$$

Thus

$$C(y_1, y_2) = \frac{\langle K(K-1)\rangle}{2\delta\sqrt{\pi}\langle K\rangle} \cdot \rho(y) \cdot \exp\left\{-\frac{(y_1-y_2)^2}{4\delta^2}\right\} + \tfrac{1}{2}\sum_{n,n'} \frac{\sigma_n\sigma_{n'}}{\sigma^2}(\rho_n(y_1)-\rho_{n'}(y_1)) \cdot (\rho_n(y_2)-\rho_{n'}(y_2))$$

or

$$R(y_1, y_2) = \frac{\langle K(K-1)\rangle}{2\delta\sqrt{\pi}\langle K\rangle} \cdot \rho^{-1}(y) \cdot \exp\left\{-\frac{(y_1-y_2)^2}{4\delta^2}\right\}$$

$$+ \rho^{-2}(y) \cdot \tfrac{1}{2}\sum_{n,n'} \frac{\sigma_n\sigma_{n'}}{\sigma^2} \cdot (\rho_n(y_1)-\rho_{n'}(y_1)) \cdot (\rho_n(y_2)-\rho_{n'}(y_2)). \tag{8.98}$$

Thus the short range part of the correlation is identical to that of the 2-component model, while the long range part is substantially bigger at $y_1 = y_2 = 0$, since it has a multitude of interference terms, all of which are positive at this point. We have evaluated the long range part by taking the σ_n and $\rho_n(0)$ from the model of Capella and Kaidalov [254] (i.e. table 7.3). For the highest ISR energy (ln $s = 8$), we get

$$R^{LR}(0, 0) \simeq 0.48 \tag{8.99}$$

in contrast to a value of $\simeq 0.06$ only for the 2-component case†. We may add that the result converges rather slowly in n. Restricting to $n \le 2$ (i.e. the 1st polyperipheral term) gives a value of $\simeq 0.20$.

Of course, with such a large long range component as in eq. (99), the remainder would give a small cluster size

$$\langle K(K-1)\rangle/\langle K\rangle \simeq 1 \tag{8.100}$$

in agreement with the semi-inclusive correlation result. One may also note that the long range component is not so long range after all, in the presence of the energy-conservation effects, discussed in

---

* The eqs. (42, 43) earlier are, of course, a special case of eqs. (95, 96) here with $n = 0, 1$; although expressed in a slightly different form.

† This corresponds to the case b of subsection 8.4, i.e. $\rho_0(0)/\rho_1(0) = \tfrac{1}{2}$. The corresponding value, for the case a $(\rho_0(0)/\rho_1(0) = 0)$, is 0.64 as against 0.25 in the 2-component model.

the last section. With increasing y_2 the $\rho_n(y_2)$ is expected to go down rapidly for high n, so that the interference terms change sign one by one. Thus the shape of the correlation data can also be reproduced, qualitatively at least.

Let us finally note that in contrast to the inclusive correlation, the semi-inclusive correlation analysis of the last subsections may not be significantly affected for n (referring here to the multiplicity) $\simeq \langle n \rangle$. The reason simply is that for these multiplicities, both the diffractive and the polyperipheral components are expected to be effectively suppressed. Of course, more detailed conclusions like the constancy of the cluster size with increasing n may get modified. The systematic investigation of such questions are evidently called for. However, they are beyond the scope of this project.

8.9. Summary

Let us summarise the essential conclusions of this section.

(1) The Mueller–Regge description of the ISR pionisation cross-section rise, implies an inclusive rapidity correlation, almost 2 orders of magnitude larger than the data. Thus the Mueller-Regge model is grossly inconsistent with the ISR data on inclusive correlation plus the pionisation cross-section rise irrespective of any exchange degeneracy constraints.

(2) The inclusive rapidity correlation data can be described in terms of a multiperipheral cluster model plus diffraction with a cluster size parameter

$$\langle K(K-1) \rangle / \langle K \rangle \simeq 2.5 \text{ charged particles}$$

and a rapidity width $\delta \simeq 0.9$. However, this size parameter is twice as large as the corresponding estimate from the semi-inclusive rapidity correlation. The former can be brought down by around 25% within the uncertainty of the estimate of the diffractive contribution and δ; but not by a factor of 2.

(3) Any way, the estimates from the semi-inclusive rapidity correlation data have been considered the cleaner ones, since the diffractive contribution gets filtered out by choosing $n \gtrsim \langle n \rangle$. One gets a cluster size parameter

$$(\langle K(K-1) \rangle / \langle K \rangle)_{n=\langle n \rangle} \simeq 1 \text{ charged particle}$$

and a rapidity width $\delta \simeq 0.7$. Moreover the cluster size parameter seems to be roughly independent of n, which implies a narrow width for its decay multiplicity distribution. Thus one gets an average multiplicity $\langle K \rangle \simeq 2$ charged particles (or 3 pions) per cluster.

(4) The azimuthal correlation data, combined with the pion average transverse momentum square $(\langle p_T^2 \rangle \simeq 0.15)$ provide estimates of cluster mass M and average transverse momentum square $\langle k_T^2 \rangle$ but with considerably larger uncertainty. One gets

$$M \sim 1 \text{ GeV}, \qquad \langle k_T^2 \rangle \sim 0.3 \text{ GeV}^2$$

where both the estimates should be taken with an uncertainty of $\pm 50\%$.

(5) Other correlation quantities like gap distribution, fluctuation parameter, zone characteristics and charge transfer correlation seem to provide no more information on the cluster parameters like δ, $\langle K \rangle$ and multiplicity dispersion, than those obtained earlier from the rapidity correlation data. However, they provide an estimate of the cluster charge distribution – i.e. roughly half the clusters come in charged ($Q = \pm 1$) states.

(6) The cluster properties estimated in (3–5) above, are strongly suggestive of their identification with the prominent meson resonances – i.e. η, ρ, ω, f, A_2. It may be added that these resonances seem to largely saturate, the inclusive pion production (60–90%) and have roughly a common $\langle k_T^2 \rangle \simeq 0.3$.

(7) The above analyses (2–5) of correlation data assume independent cluster production, but not specifically the multiperipheral production dynamics. They are expected to be valid for a wider class of cluster models. To test specifically the multiperipheral model for cluster production one may compare the cluster mass and $\langle k_T^2 \rangle$ estimated above with those obtained from the pionisation cross-section rise ($M \simeq 1$ GeV) and the elastic overlap function calculation

$$k_T^2 \simeq 0.14/\alpha_P' \simeq 0.5\,\text{GeV}^2$$

both using the multiperipheral dynamics explicity. Noting the 50% uncertainty in the former estimates and equally large ones in the latter, one may conclude that there is a very rough agreement (to within a factor of 2) with the multiperipheral model prediction.

(8) The Gribov calculus model predictions for correlation remain almost totally unexplored. It seems to offer a possibility to describe both the inclusive and semi-inclusive ($n \simeq \langle n \rangle$) rapidity correlations with a small cluster size parameter, $\langle K(K-1) \rangle/\langle K \rangle \simeq 1$. However, the calculation is admittedly crude, and besides it remains to be seen whether or not it will change some of the more attractive results of the standard cluster model.

(9) It is important to note that within the correlation data, what are most sensitive to the cluster production models are the long range parts whereas the short range parts mostly probe the intra-cluster characteristics. A more detailed study of the long range behavior of the correlation quantities (correlation function, azimuthal asymmetry parameter etc.) is called for.

(10) Lastly we should draw attention to the absence of practically any correlation data involving heavier particles (kaons, nucleons). This would provide valuable information on mechanisms of new quantum number excitation.

In concluding this section it must be stressed that compared to the single particle inclusive case, the study of correlation, is still very much an open subject. The rough agreement amongst the cluster parameters estimated from different types of correlations and from the multiperipheral model calculations of the pionisation cross-section rise and the elastic overlap function do not mean that the issue is settled. They only mean that one has a sufficiently interesting case for a rigorous quantitative investigation. The models and the quality of data are both very crude. It is not clear whether with more refined models and data the agreement will improve or get worse. There are evidences, in fact, that some of the more sophisticated model predictions are in poorer agreement with data [252]. Indeed, the subject is in its infancy, unlike those discussed in the previous sections. And it will be a great pity to leave it off at this stage.

Acknowledgements

Jacob for entrusting the project to us and for his kind letters of encouragement, which helped us during the long haul.

References

[1] For a review see e.g. W. Kittel, Proc. X Intl. Symp. on Multiparticle Dynamics, Goa, India (1979).
[2] W.R. Frazer et al., Revs. Modern Phys. 44 (1972) 284.
[3] D. Horn, Phys. Rep. 4C (1972) 1.
[4] Chan Hong-Mo, Proc. IV Intl. Conf. on High Energy Collisions (Oxford) 1972.
[5] M. Jacob, Proc. Intl. School of Subnuclear Physics, Erice, Sicily, 1971.
[6] E. Berger, Proc. Intl. School of Subnuclear Physics, Erice, Sicily, 1973.
[7] R.G. Roberts and D.P. Roy, Lectures given at the XIII Cracow School of Theoretical Physics (1973); Acta Physica Polonica B5 (1974) 23.
[8] R.G. Roberts, Proc. 14th Scottish Universities Summer School, Edinburgh, 1973.
[9] R.C. Brower, C.E. De Tar and J.H. Weis, Phys. Rep. 14C (1974) 258.
[10] R.P. Feynman, Phys. Rev. Lett. 23 (1969) 1414.
[11] J. Benecke, T.T. Chou, C.N. Yang and E. Yen, Phys. Rev. 188 (1969) 2159.
[12] A.H. Mueller, Phys. Rev. D2 (1970) 2963.
[13] H.P. Stapp, Phys. Rev. D3 (1971) 3177.
[14] J.C. Polkinghorne, Nuovo Cim. 7A (1972) 555.
[15] C.I. Tan, Phys. Rev. D4 (1971) 2412.
[16] C.E. Detar, C.E. Jones, F.E. Low, J. Weis, J.E. Young and C.I. Tan, Phys. Rev. Lett. 26 (1971) 675.
[17] P.V. Landshoff, Nucl. Phys. B15 (1970) 284.
[18] C.E. De Tar and J.H. Weis, Phys. Rev. D4 (1971) 3141.
[19] J. Kwiecinski, Nuovo Cim. Lett. 3 (1972) 619.
[20] M.B. Einhorn, J. Ellis and J. Finkelstein, Phys. Rev. D5 (1972) 2063.
[21] P. Olesen, Preprint CERN-TH-1376 (1971).
[22] A.I. Sanda, Phys. Rev. D6 (1972) 280.
[23] For a review see e.g. R.J.N. Phillips and D.P. Roy, Reports on Progress in Physics 37 (1974) 1035.
[24] R. Dolen, D. Horn and C. Schmid, Phys. Rev. Lett. 19 (1967) 402; Phys. Rev. 166 (1968) 1768.
[25] P. Hoyer, R.G. Roberts and D.P. Roy, Nucl. Phys. B56 (1973) 173.
[26] P.G.O. Freund, Phys. Rev. Lett. 20 (1968) 235.
[27] H. Harari, Phys. Rev. Lett. 20 (1968) 1395.
[28] V. Barger and R.J.N. Phillips, Nucl. Phys. B32 (1971) 93.
[29] S.N. Ganguli, Nucl. Phys. B91 (1975) 69.
[30] C. Quigg and E. Rabinovici, Phys. Rev. D13 (1976) 2525.
[31] R.G. Roberts, R.V. Gavai and D.P. Roy, Nucl. Phys. B133 (1978) 285.
[32] G.F. Chew and C. Rosenzweig, Phys. Rev. D12 (1975) 3907.
[33] J.W. Dash, S.T. Jones and E.K. Manesis, Phys. Rev. D18 (1978) 303.
[34] D. Gordon and G. Veneziano, Phys. Rev. D3 (1971) 2116;
     G. Veneziano, Nuovo Cim. Lett. 1 (1971) 681.
[35] S.-H.H. Tye and G. Veneziano, Phys. Lett. 38B (1972) 30; Nuovo Cim. 14A (1973) 711.
[36] M.B. Einhorn, M.B. Green and M.A. Virasoro, Phys. Lett. 37B (1971) 292; Phys. Rev. D6 (1972) 1675; D7 (1973) 102.
[36a] J. Ellis, J. Finkelstein, P. Frampton and M. Jacob, Phys. Lett. 35B (1971) 227.
[37] Chan Hong-Mo, C.S. Hsue, C. Quigg and J.M. Wang, Phys. Rev. Lett. 26 (1971) 672.
[38] Chan Hong-Mo and P. Hoyer, Phys. Lett. 36B (1971) 79.
[39] J.L. Rosner, Phys. Rev. Lett. 21 (1968) 950.
[40] D.P. Roy and M. Suzuki, Phys. Lett. 28B (1969) 558.
[41] J.L. Rosner, Phys. Rev. Lett. 22 (1969) 689.
[42] R.V. Gavai and D.P. Roy, Nucl. Phys. B137 (1978) 301.
[43] T. Inami and H.I. Miettinen, Phys. Lett. 49B (1974) 67.
[44] Y. Eylon and H. Harari, Nucl. Phys. B80 (1974) 349.
[45] G.C. Rossi and G. Veneziano, Nucl. Phys. B123 (1977) 507.
[46] M. Imachi, S. Otsuki and T. Toyoda, Prog. Theo. Phys. 57 (1977) 517;
     Y. Igarashi et al., Suppl. Prog. Theo. Phys. 63 (1978) 122.
[47] S. Fubini, in: Strong Interaction and High Energy Physics, ed. R.G. Moorhouse (Oliver and Boyd, Edinburgh, 1964).
[48] J. Pumplin and G.L. Kane, Phys. Rev. Lett. 32 (1974) 963.

[49] D. Leith, Proc. 16th Intl. Conf. on High Energy Physics, Chicago, 1972.

[50] R. Carlitz, M.B. Green and A. Zee, Phys. Rev. D4 (1971) 3439.

[51] V. Barger and R.J.N. Phillips, Nucl. Phys. B32 (1971) 93.

[52] T. Inami and R.G. Roberts, Nucl. Phys. B93 (1975) 497.

[53] L.A.P. Balazs, Phys. Lett. 40B (1972) 269; 48B (1974) 232.

[54] I.A. Verdiev, O.V. Kancheli, S.G. Matinyan, A.M. Popova and K.A. Termartirosyan, JETP 19 (1964) 148.

[55] J. Finkelstein and K. Kajantie, Phys. Lett. 26B (1968) 305; Nuovo Cim. 56A (1968) 659.

[56] V.N. Gribov and A.A. Migdal, Soviet J. Nucl. Phys. 8 (1968) 583.

[57] H.D.I. Abarbanel, G.F. Chew, M.L. Goldberger and L.M. Saunders, Phys. Rev. Lett. 26 (1971) 937.

[58] C.E. Jones, F.E. Low, S.H.H. Tye, G. Veneziano and J.E. Young, Phys. Rev. D6 (1972) 1033.

[59] C.E. De Tar, D.Z. Freedman and G. Veneziano, Phys. Rev. D4 (1971) 906;
G. Veneziano, Phys. Lett. 36B (1971) 397.

[60] R.C. Brower and J.H. Weis, Phys. Lett. 41B (1972) 631.

[61] J. Cardy and A. White, Phys. Lett. 47B (1973) 445.

[62] I.G. Halliday and C.T. Sachradjda, Phys. Rev. D8 (1973) 3598.

[63] V.N. Gribov, Proc. 16th Intl. Conf. on High Energy Physics, Chicago, 1972.

[64] H.D.I. Abarbanel, J. Bronzan, R. Sugar and A. White, Phys. Rep. 21 (1975) 119.

[65] For a review see e.g. J. Paton, Proc. VI Intl. Coll. on Multiparticle Reactions, Oxford, 1975.

[66] K. Paler et al., Phys. Lett. 43B (1973) 437.

[67] CERN/HERA Compilation, 1979.

[68] E. Beier et al., Phys. Rev. D17 (1978) 2864 and 2875.

[69] P. Bosetti et al., Nucl. Phys. B60 (1973) 307.

[70] A.C. Borg et al., Nucl. Phys. B106 (1976) 430.

[71] P.A. Baker et al., Nucl. Phys. B89 (1975) 189.

[72] W.P. Swanson et al., Phys. Rev. D6 (1972) 170.

[73] See e.g. B.M. Udgaonkar, Phys. Rev. Lett. 8 (1962) 142.

[74] See e.g. D.P. Roy, Proc. VI Intl. Coll. on Multiparticle Reactions, Oxford, 1975.

[75] P. Hoyer, R.G. Roberts and D.P. Roy, Phys. Lett. 44B (1973) 258.

[76] B. Nicolescu, Nucl. Phys. B134 (1978) 495.

[77] R.V. Gavai and D.P. Roy, Phys. Lett. 82B (1979) 139.

[78] A.S. Carroll et al., Phys. Lett. 61B (1976) 303.

[79] P. Bosetti et al., Nucl. Phys. B54 (1973) 141. The M^2/s, t double distribution of this data was obtained through R.G. Roberts.

[80] Chan Hong-Mo, H.I. Miettinen and W.S. Lam, Phys. Lett. 40B (1972) 112.

[81] K.C. Moffiet et al., Phys. Rev. D5 (1972) 1603.

[82] J. Whitmore et al., Phys. Lett. 60B (1976) 211.

[83] H.I. Miettinen, Phys. Lett. 38B (1972) 431.

[84] J. Whitmore, Phys. Rep. 27C (1976) 187.

[85] $p \xrightarrow{p} \pi^{\pm}$ data:
(0.0365, 0.0719) Bromberg et al., Nucl. Phys. B107 (1976) 82;
(0.0727) Morse et al., Phys. Rev. D15 (1977) 66;
(0.087) Ammosov et al., Saclay Preprint (1976);
(0.147, 0.203) Blobel et al., Nucl. Phys. B69 (1974) 454;
(0.134) Sims et al., Nucl. Phys. B41 (1972) 317;
(0.163) Boggild et al., Nucl. Phys. B57 (1973) 77;
(0.051) Cho et al., Phys. Rev. Lett. 31 (1973) 413;
(0.087) Bumazchnov et al., Phys. Lett. 50B (1974) 283.

[86] $p \xrightarrow{\bar{p}} \pi^{\pm}$ data:
(0.073) Whitmore et al., Phys. Rev. Lett. 38 (1977) 996;
(0.151) Boos et al., Nucl. Phys. B121 (1977) 381;
(0.203) Gall et al., Proc. Intl. Symp. $\bar{p}p$ Int., Loma-Koli, Finland (1975) 414;
(0.230, 0.307) Gregory et al., Nucl. Phys. B78 (1974) 222; B122 (1977) 435.

[87] $p \xrightarrow{\pi^+} \pi^{\pm}$ data:
(0.0727) Morse et al., Phys. Rev. D15 (1977) 66;
(0.167) Go et al., Phys. Rev. D11 (1975) 3092;
Powers et al., Phys. Rev. D8 (1973) 1947;
(0.180, 0.251) Bosetti et al., Nucl. Phys. B54 (1973) 141;
(0.154, 0.287) Crennell et al., Phys. Rev. Lett. 28 (1972) 643;
(0.167, 0.267) Alston et al., Phys. Lett. 39B (1971) 402.

[88] $p \xrightarrow{\pi^-} \pi^\pm$ data:
   (0.073) Morris et al., Phys. Lett. 56B (1975) 395;
   (0.117) Abdrakhmanov et al., Nucl. Phys. B72 (1974) 189;
   (0.145) Shephard et al., Phys. Rev. Lett. 27 (1971) 1164;
   (0.167, 0.250) Go et al., Phys. Rev. D11 (1975) 3092;
                  Powers et al., Phys. Rev. D8 (1973) 1947;
   (0.180) Bosetti et al., Nucl. Phys. B54 (1973) 141;
   (0.213) Borzatta et al., Nuovo Cimento 15A (1973) 45;
   (0.167, 0.250) Alston et al., Phys. Lett. 39B (1971) 402.

[89] $p \xrightarrow{K^+} \pi^\pm$ data:
   (0.0727) Morse et al., Phys. Rev. D15 (1977) 66;
   (0.200) Stone et al., Phys. Rev. D5 (1972) 1621;
   (0.179) Chliapnikov et al., Nucl. Phys. B112 (1976) 1.

[90] $p \xrightarrow{K^-} \pi^\pm$ data:
   (0.128) Faccini et al., Nucl. Phys. B127 (1977) 109;
   (0.191) Borg et al., Nucl. Phys. B106 (1976) 430;
   (0.179, 0.224) Bosetti et al., Nucl. Phys. B60 (1973) 307;
   (0.200) Barletta et al., Phys. Rev. D7 (1973) 3233.

[91] $p \xrightarrow{\gamma} \pi^\pm$ data:
   (0.234) Moffiet et al., Phys. Rev. D5 (1972) 1603;
   (0.258) Grandsman et al., Nucl. Phys. B61 (1973) 32.

[92] J.G. Rushbrooke and B.R. Weber, Phys. Rep. 44C (1978) 1.

[93] J. Bartke et al., Nucl. Phys. B107 (1976) 93.

[94] J.R. Fry et al., Nucl. Phys. B58 (1973) 420.

[95] Data on K_S^0, ρ^0, Λ and $\Sigma_{1385}^\pm$ in pp interactions were obtained from:
   V. Blobel et al., Nucl. Phys. B69 (1974) 454; B92 (1975) 221;
   K. Jaeger et al., Phys. Rev. D11 (1975) 1756, 2405;
   H. Boggild et al., Nucl. Phys. B57 (1973) 77;
   Ammosov et al., Nucl. Phys. B115 (1976) 269;
   J.W. Chapman et al., Phys. Lett. 47B (1973) 465;
   A. Sheng et al., Phys. Rev. D11 (1975) 1733;
   K. Bockmann et al., preprint BONN-HE-77-21;
   H. Kichimi et al., Phys. Lett. 72B (1978) 411.

[96] Data on K_S^0, ρ^0, Λ and $\Sigma_{1385}^\pm$ in $\bar{p}p$ interactions were obtained from:
   S. Banerjee et al., Nucl. Phys. B150 (1979) 119;
   M.T. Regan et al., Nucl. Phys. B141 (1978) 65;
   S.N. Ganguli and B. Sadoulet, Nucl. Phys. B53 (1973) 458;
   D.R. Bertrand et al., Nucl. Phys. B128 (1977) 365;
   E.G. Boos et al., Dubna preprint El-11666 (1978);
   Jabiol et al., Nucl. Phys. B127 (1977) 365;
   R. Raja et al., Phys. Rev. D15 (1977) 627;
   A.M. Cooper et al., Nucl. Phys. B136 (1978) 365;
   R. Hamatsu et al., Nucl. Phys. B123 (1977) 189;
   J.F. Baland et al., Nucl. Phys. B140 (1978) 220;
   J. Canter et al., Phys. Rev. D20 (1979) 1029;
   D.I. Ermilova et al., Nucl. Phys. B137 (1978) 29.

[97] Data on K_S^0, ρ^0 and Λ in K^+p interactions were obtained from:
   P.V. Chliapnikov et al., Nucl. Phys. B112 (1976) 1; B131 (1977) 93; B97 (1975) 1; B133 (1978) 93;
   P. Granet et al., Nucl. Phys. B140 (1978) 389.

[98] Data on K_S^0, ρ^0, Λ and Σ_{1385} in K^-p interactions were obtained from:
   S.N. Ganguli et al., Nuov. Cim. 44A (1978) 345;
   H. Muirhead et al., Nucl. Phys. B99 (1975) 376;
   P. Bosetti et al., Nucl. Phys. B60 (1973) 307;
   A. Borg et al., Nuov. Cim. 22A (1974) 559;
   U. Gensch et al., France-Soviet Union and CERN-Soviet Union collaboration, paper submitted to Tokyo Conf. (1978);
   P. Beilliere et al., Nucl. Phys. B90 (1975) 20;
   P. Schmitz et al., Nucl. Phys. B137 (1978) 13;
   F. Barreiro et al., Nucl. Phys. B126 (1977) 319;

M. Baubillier et al., Nucl. Phys. B148 (1979) 18;
H. Grassler et al., Nucl. Phys. B118 (1977) 189;
M. Bardadin-Otwinowska et al., Nucl. Phys. B98 (1975) 418;
U. Kriegel et al., France-Soviet Union and CERN-Soviet Union collaboration, paper submitted to Tokyo Conf. (1978).
[99] Data on K_s^0, ρ^0, Λ and Σ_{1385} in π^+p interactions were obtained from:
P. Bosetti et al., Nucl. Phys. B94 (1975) 21;
P.H. Stuntebeck et al., Phys. Rev. D9 (1974) 608;
Crennell et al., Phys. Rev. Lett. 28 (1972) 643;
Gordon et al., Phys. Rev. Lett. 34 (1975) 284;
H. Saariko, Preprint HU-P-156 (1978) Helsinki;
M. Deutschmann et al., Nucl. Phys. B103 (1976) 426;
J. Lowsky, Ph.D. Thesis of Bonn University (1976).
[100] Data on K_s^0, ρ^0 and Λ in π^-p interactions were obtained from:
F. Barreiro et al., Phys. Rev. D17 (1978) 669;
Stuntebeck et al., Phys. Rev. D9 (1974) 608;
D. Ljung et al., Phys. Rev. D15 (1977) 3163;
Bogert et al., Phys. Rev. D16 (1977) 2098;
A. Forino et al., Bologna-Florence-Genoa-Milano-Oxford-Pavia collaboration, preprint (1978);
M. Deutschmann et al., Nucl. Phys. B103 (1976) 426;
D. Fong et al., Phys. Lett. 60B (1975) 124;
V.P. Kenney et al., paper submitted to Tokyo Conf. (1978).
[101] Data on ρ^0 in γp interactions were obtained from:
Kogan et al., Nucl. Phys. B122 (1977) 383.
[102] P. Bosetti et al., Nucl. Phys. B81 (1974) 61.
[103] K. Alpgard et al., Nucl. Phys. B109 (1976) 207.
[104] R.C. Brower, R.N. Cahn and J. Ellis, Phys. Rev. D7 (1973) 2080.
[105] J.G. Rushbrooke et al., Phys. Rev. Lett. 39 (1977) 117.
[106] R.D. Field, 'BNL workshop on physics with polarized targets', June 3–8 (1974).
[107] F.E. Paige and D.P. Sidhu, Phys. Rev. D14 (1976) 2307.
[108] F. Barreiro et al., Phys. Rev. Lett. 40 (1978) 595.
[109] J.V. Beaupre et al., Nucl. Phys. B67 (1973) 413.
[110] A.C. Borg et al., Nuov. Cim. 34A (1976) 21.
[111] F. Barreiro et al., Phys. Rev. D17 (1978) 681.
[112] P.V. Chliapnikov et al., Nucl. Phys. B105 (1976) 510.
[113] P.D. Higgins et al., Phys. Rev. D19 (1979) 73.
[114] D. Brick et al., preprint August (1979), Phys. Rev. D21 (1980) 632.
[115] H. De Kerret et al., Phys. Lett. 69B (1977) 372.
[116] G. Goggi et al., Nucl. Phys. B143 (1978) 365.
[117] A.V. Barnes et al., Nucl. Phys. B145 (1978) 45.
[118] A.V. Barnes et al., Phys. Rev. Lett. 37 (1976) 76.
[119] W.D. Apel et al., Nucl. Phys. B154 (1979) 189.
[120] W.D. Apel et al., Nucl. Phys. B152 (1979) 1.
[121] O.I. Dahl et al., Phys. Rev. Lett. 37 (1976) 80.
[122] S.N. Ganguli and B. Sadoulet, Nucl. Phys. B53 (1973) 458.
[123] F. Barreiro et al., Phys. Rev. D17 (1978) 669.
[124] F. Barreiro et ' Nucl. Phys. B126 (1977) 319.
[125] V. Blobel et al., Nucl. Phys. B135 (1978) 379.
[126] K. Alpgard et al., Nucl. Phys. B105 (1976) 349.
[127] H. Blumenfeld et al., Nucl. Phys. B125 (1977) 253.
[128] P.V. Chliapnikov et al., Nucl. Phys. B112 (1976) 1.
[129] S.N. Ganguli et al., Nuov. Cim. 44A (1978) 345.
[130] H. Muirhead et al., Nucl. Phys. B99 (1975) 376.
[131] P. Beilliere et al., Nucl. Phys. B90 (1975) 20.
[132] R. Blokzijl et al., Nucl. Phys. B98 (1975) 401.
[133] M. Baubillier et al., Nucl. Phys. B148 (1979) 18.
[134] S.N. Ganguli, Nuov. Cim. Lett. 20 (1977) 554.
[135] R.G. Kennett, Ph.D. thesis, CALT-68-742 (1979).
[136] R.L. Anderson et al., Phys. Rev. Lett. 37 (1976) 1111.
[137] R.D. Peccei and A. Pignotti, Phys. Rev. Lett. 26 (1971) 1076.

[138] M.S. Chen et al., Phys. Rev. D5 (1972) 1667.
[139] C. Risk, Phys. Rev. D5 (1972) 1685.
[140] J. Singh et al., Nucl. Phys. B 140 (1978) 189.
[141] H. Abramowicz et al., Nucl. Phys. B105 (1976) 222.
[142] S.N. Ganguli et al., Nucl. Phys. B128 (1977) 408.
[143] F.E. Paige and T.L. Trueman, Phys. Rev. D12 (1975) 2422.
[144] J. Pumplin, Phys. Rev. D13 (1976) 1249.
[145] A. Capella, J. Kaplan and J. Tran Thanh Van, Nucl. Phys. B105 (1976) 333.
[146] J. Bartels and G. Kramer, Nucl. Phys. B120 (1977) 96.
[147] J.F. Owens, Nucl. Phys. B131 (1977) 209.
[148] J. Pumplin, Phys. Rev. D13 (1976) 1261.
[149] F.E. Paige and D.P. Sidhu, Phys. Rev. D13 (1976) 3015.
[150] G.R. Goldstein and J.F. Owens, Nucl. Phys. B118 (1977) 29.
[151] S.J. Barish et al., Phys. Rev. D12 (1975) 1260.
[152] D.P. Roy and R.G. Roberts, Phys. Lett. 40B (1972) 555.
[153] J.M. Wang and L.L. Wang, Phys. Rev. Lett. 26 (1971) 1287.
[154] J. Finkelstein, Phys. Rev. D6 (1972) 931.
[155] J. Finkelstein, Phys. Rev. D18 (1978) 336.
[156] M. Bishari and H.J. Yesian, Phys. Lett. 38B (1972) 312.
[157] S.U. Chung et al., Phys. Lett. 57B (1975) 384.
[158] F. Wagner, Proc. 17th Intl. Conf. on High Energy Physics, London, 1974.
[159] M.J. Corden et al., Nucl. Phys. B138 (1978) 235.
[160] A.D. Martin, 4th Symp. on Multiparticle Dynamics, Pavia (1973).
[161] B. Hyams, Phys. Lett. 51B (1974) 272.
[162] A.D. Martin and C. Michael, Nucl. Phys. B84 (1975) 83.
[163] M.J. Emms et al., Phys. Lett. 58B (1975) 117.
[164] K. Paler et al., Nucl. Phys. B96 (1975) 1.
[165] C. Sorensen, Phys. Lett. 49B (1974) 86.
[166] H.D.I. Abarbanel and D.J. Gross, Phys. Rev. Lett. 26 (1971) 732.
[167] R.J.N. Phillips, G.A. Ringland and R.P. Worden, Phys. Lett. 40B (1972) 239.
[168] G.R. Goldstein and J.F. Owens, Nucl. Phys. B103 (1976) 145.
[169] R.D. Field and G.C. Fox, Nucl. Phys. B80 (1974) 367.
[170] A.C. Irving and R.P. Worden, Phys. Rep. 34 (1977) 117.
[171] J. Soffer and D. Wray, Nucl. Phys. B73 (1974) 231.
[172] A. Lesnik et al., Phys. Rev. Lett. 35 (1975) 770.
[173] P. Aahlin et al., Nuov. Cim. Lett. 21 (1978) 236.
[174] M.L. Faccini-Turluer et al., Z. Physik C1 (1979) 19.
[175] J.F. Owens, Phys. Lett. 63B (1976) 341.
[176] G.A. Ringland and D.P. Roy, Phys. Lett. 36B (1971) 110.
[177] S. Banerjee et al., Nucl. Phys. B150 (1979) 119.
[178] D.R. Bertrand et al., Nucl. Phys. B128 (1977) 365.
[179] F. Barreiro et al., Phys. Rev. D17 (1978) 669.
[180] S.N. Ganguli et al., Nuov. Cim. 44A (1978) 345.
[181] A. Borg et al., Nuov. Cim. 22A (1974) 559.
[182] S.U. Chung et al., Phys. Rev. D11 (1975) 1010.
[183] M. Baubillier et al., Nucl. Phys. B148 (1979) 18.
[184] H. Abramowicz et al., Nucl. Phys. B105 (1976) 222.
[185] H. Grassler et al., Nucl. Phys. B136 (1978) 386.
[186] W. Barletta et al., Nucl. Phys. B51 (1973) 499.
[187] V. Blobel et al., Nucl. Phys. B122 (1977) 429;
      S. Erhan et al., Phys. Lett. 82B (1979) 301.
[188] K. Heller et al., Phys. Lett. 68B (1977) 480.
[189] G. Bunce et al., Phys. Rev. Lett. 36 (1976) 1113.
[190] K. Heller et al., Phys. Rev. Lett. 41 (1978) 607.
[191] B. Andersson, G. Gustafson and G. Ingelman, Phys. Lett. 85B (1979) 417.
[192] A.B. Wicklund et al., as reported in ref. [106].
[193] L. Dick et al., Phys. Lett. 57B (1975) 93.
[194] R.D. Peccei and A. Pignotti, Phys. Rev. Lett. 26 (1971) 1076.
[195] J.M. Wang and L.L. Wang, Phys. Rev. Lett. 26 (1971) 1287.
[196] R. Rajaraman, Phys. Rev. Lett. 27 (1971) 693.

[197] Chan Hong-Mo, H.I. Miettinen and R.G. Roberts, Nucl. Phys. B54 (1973) 411.
[198] CHLM Coll., M.G. Abbrow et al., Nucl. Phys. B51 (1973) 388; B54 (1973) 6; B72 (1974) 376; B73 (1974) 40; B108 (1976) 1.
[199] IC-R Coll., F. Sannes et al., Phys. Rev. Lett. 30 (1973) 766;
     K. Abe et al., Phys. Rev. Lett. 31 (1973) 1527; Phys. Lett. 53B (1974) 114.
[200] UCLA-FNAL Coll., F.T. Dao et al., Phys. Lett. 45B (1973) 399.
[201] Mich.-Roch. Coll., J.P. DeBrion et al., Phys. Lett. 52B (1974) 477;
     J.W. Chapman et al., Phys. Rev. Lett. 32 (1974) 257.
[202] ANL-FNAL Coll., S.J. Barish et al., Phys. Rev. Lett. 31 (1973) 1080;
     J. Whitmore et al., Phys. Rev. D11 (1975) 3124.
[203] C.-S. Coll., S. Childres et al., Phys. Rev. Lett. 32 (1974) 389;
     R.D. Schamberger et al., Phys. Rev. Lett. 34 (1975) 1121.
[204] K. Abe et al., Phys. Rev. Lett. 31 (1973) 1530.
[205] A.B. Kaidalov et al., Phys. Lett. 45B (1973) 493.
[206] A. Capella, H. Hogaasen and V. Rittenberg, Phys. Rev. D8 (1973) 2040;
     A. Capella, Phys. Rev. D8 (1973) 2047.
[207] D. Amati, L. Caneschi and M. Ciafaloni, Nucl. Phys. B62 (1973) 173.
[208] R.G. Roberts and D.P. Roy, Nucl. Phys. B77 (1974) 240.
[209] C.-S. Coll., R.D. Schamberger et al., Phys. Rev. D17 (1978) 1268.
[210] DRRF Coll., Y. Akimov et al., Phys. Rev. Lett. 35 (1975) 763, 766; 39 (1977) 1432;
     V. Bartenev et al., Phys. Lett. 51B (1974) 299.
[211] FSASF Coll., D.S. Ayres et al., Phys. Rev. Lett. 37 (1977) 1724; 38 (1977) 880. The data points were obtained from G. Mikenberg through
     R.G. Roberts.
[212] BHM Coll., V. Blobel et al., Nucl. Phys. B69 (1974) 454.
[213] J.V. Allaby et al., Nucl. Phys. B52 (1973) 316.
[214] M. Bishari, Phys. Lett. 38B (1972) 510.
[215] B. Robinson et al., Phys. Rev. Lett. 34 (1975) 1475.
[216] J. Hanlon et al., Phys. Rev. Lett. 37 (1976) 967.
[217] R.G. Roberts (private communication).
[218] R.M. Edelstein et al., Phys. Rev. D5 (1972) 1073.
[219] C-S data, S. Childres et al., Phys. Lett. 65B (1976) 177.
[220] S.Y. Chu, B.R. Desai, B.C. Shen and R.D. Field, Phys. Rev. D13 (1976) 2967.
[221] A. Capella, J. Kaplan and J. Tran Thanh Van, Nucl. Phys. B105 (1976) 333.
[222] R.G. Roberts, Rutherford Preprint, RL-75-164, T. 138 (1975).
[223] K. Hidaka, Phys. Rev. D16 (1977) 690.
[224] P. Hoyer and H.B. Thacker, Nucl. Phys. B116 (1976) 261.
[225] W.R. Frazer and D.R. Snider, Phys. Lett. 45B (1973) 136.
[226] R.G. Roberts and D.P. Roy, Phys. Lett. 46B (1973) 201.
[227] K. Kajantie and P.V. Ruuskanen, Phys. Lett. 45B (1973) 149.
[228] F.C. Erne (private communication).
[229] J. Kwiecinski, R.G. Roberts and D.P. Roy, Nucl. Phys. B102 (1976) 353.
[230] CCHK Coll., D. Drijard et al., Nucl. Phys. B143 (1978) 61.
[231] CHOV Coll., H. de Kerret et al., Phys. Lett. 68B (1977) 385.
[232] ARCGM Coll., L. Baksay et al., Phys. Lett. 61B (1976) 89.
[233] B.R. Desai, B.C. Shen and M. Jacob, Nucl. Phys. B142 (1978) 258.
[234] M. Jacob (private communication).
[235] CHM Coll., J. Armitage et al., Phys. Lett. 82B (1979) 149.
[236] R. Shankar, Nucl. Phys. B63 (1974) 168.
[237] L.A. Ponomarev, Paper submitted to the 18th Intl. Conf. on High Energy Physics, Tbilisi, 1976.
[238] J. Pumplin and F. Henyey, Nucl. Phys. B117 (1976) 377.
[239] T. Ferbel, Phys. Rev. Lett. 29 (1972) 448.
[240] S. Raichoudhury, Nuovo Cim. Lett. 5 (1972) 7.
[241] R.F. Amann and M.L. Blackmon, Phys. Lett. 44B (1973) 266.
[242] J.R. Freeman and C. Quigg, Phys. Lett. 47B (1973) 39.
[243] S. Pinsky and G. Thomas, Phys. Rev. D9 (1974) 1350.
[244] T. Inami, Nucl. Phys. B77 (1974) 337.
[245] S. Humble, Phys. Lett. 40B (1972) 373.
[246] E.J. Squires and D.M. Weber, Nuovo Cim. Lett. 7 (1973) 193.
[247] B. Petersen, Proc. Recontre de Moriond (1973).
[248] R. Blutner, Nucl. Phys. B73 (1974) 125.
[249] L. Caneschi, Nucl. Phys. B68 (1974) 77.

[250] L. Caneschi, Nucl. Phys. B108 (1976) 417.
[251] P.K. Malhotra, Proc. 7th Intl. Colloquium on Multiparticle Reactions, Tutzig (1976).
[252] A. Arneodo and J.L. Meunier, Zeitschrift fur Physic C2 (1979) 77.
[253] H. Cheng and T.T. Wu, Phys. Rev. D1 (1970) 2775; Phys. Lett. 45B (1973) 367;
      H. Cheng, Proc. 4th Intl. Symp. of Multiparticle Hadrodynamics, Pavia (1973).
[254] A. Capella and A. Kaidalov, Nucl. Phys. B111 (1976) 477.
[255] V.A. Abramovski, V.N. Gribov and O.V. Kancheli, Proc. 16th Intl. Conf. on High Energy Physics, Chicago (1972).
[256] S.J. Chang and T.M. Yan, Phys. Rev. D10 (1974) 1531.
[257] D.R. Snider and H.W. Wyld, Phys. Rev. D11 (1975) 2538.
[258] R.J.N. Phillips, Rutherford Preprint, RL-74-034 (1974).
[259] R.G. Roberts (private communication).
[260] T.K. Gaiser and C.I. Tan, Phys. Rev. D8 (1973) 3881.
[261] M. Suzuki, Nucl. Phys. B64 (1973) 486.
[262] D. Sivers and F. von Hippel, Phys. Rev. D9 (1974) 830.
[263] J. Koplik, Nucl. Phys. B82 (1974) 93.
[264] T.K. Gaiser, H.I. Miettinen, C.I. Tan and D.M. Tow, Phys. Lett. 51B (1974) 83.
[265] C.B. Chiu and E. Ugaz, Nucl. Phys. B86 (1975) 153.
[266] C.B. Chiu and D.M. Tow, Univ. of Texas, Austin, Preprint (1976).
[267] BSM Coll., K. Guettler et al., Phys. Lett. 64B (1976) 111; Nucl. Phys. B116 (1976) 77.
[268] BS Coll., B. Alper et al., Nucl. Phys. B100 (1975) 237.
[269] Y. Cho et al., Phys. Rev. Lett. 31 (1973) 413.
[270] V.V. Ammosov et al., Saclay Preprint (June 1976).
[271] V. Amaldi et al., Nucl. Phys. B86 (1975) 403.
[272] S. Yazaki, Phys. Lett. 43B (1973) 225.
[273] Chan Hong-Mo, P. Hoyer, H.I. Miettinen and D.P. Roy, Phys. Lett. 40B (1972) 406.
[274] W.M. Morse et al., Phys. Rev. D15 (1977) 66.
[275] W.B. Fretter et al., Phys. Lett. 57B (1975) 197.
[276] R.F. Amann and K. Geer, Syracuse Preprint SU-4205-21 (1973).
[277] T. Ferbel, Proc. SLAC Summer Inst. of Particle Physics (1974).
[278] W. Ko, Proc. 17th Intl. Conf. on High Energy Physics, London (1974).
[279] Pisa-Stony Brook Coll., S.R. Amendolia et al., Phys. Lett. 48B (1974) 359.
[280] CERN-Hamburg-Vienna Coll., H. Dibon et al., Phys. Lett. 44B (1973) 313.
[281] E.L. Berger, R. Singer, G.H. Thomas and T. Kafka, Phys. Rev. D15 (1977) 206.
[282] G.F. Chew and A. Pignotti, Phys. Rev. 176 (1968) 2112;
      G.F. Chew, M.L. Goldberger and F.E. Low, Phys. Rev. Lett. 22 (1969) 208.
[283] P. Pirilla and S. Pokorski, Phys. Lett. B43 (1973) 502.
[284] W. Schmidt-Parzefall, Phys. Lett. 46B (1973) 399.
[285] E.L. Berger and G.C. Fox, Phys. Lett. 47B (1973) 162.
[286] F. Hayot and A. Morel, Nucl. Phys. B68 (1974) 323.
[287] M. LeBellac, H.I. Miettinen and R.G. Roberts, Phys. Lett. 48B (1974) 115.
[288] Pisa-Stony Brook Coll., S.R. Amendolia et al., Nuovo Cim. 31A (1976) 17.
[289] Aachen-CERN-Munich Coll., K. Eggert et al., Nucl. Phys. B86 (1975) 201.
[290] ANL-FNAL-Stony Brook Coll., R. Singer et al., Phys. Lett. 49B (1974) 481.
[291] ANL-FNAL-MSU-IOWA-Maryland Coll., B.Y. Oh et al., Phys. Lett. 56B (1975) 400.
[292] Rochester-Michigan Coll., C. Bromberg et al., Phys. Rev. D15 (1977) 1215.
[293] France-Soviet Coll., J. Derre et al., Nuovo Cim. 33A (1976) 721.
[294] J. Whitmore, Phys. Rep. 10C (1974) 273.
[295] P. Darriulat, Proc. 6th Intl. Colloquium on Multiparticle Reactions, Oxford (1975).
[296] L. Foa, Phys. Rep. 22C (1975) 1.
[297] E. Berger, Phys. Lett. 49B (1974) 369; Nucl. Phys. B85 (1975) 61.
[298] F. Hayot and M. LeBellac, Nucl. Phys. B86 (1975) 333.
[299] A. Morel and G. Plaut, Nucl. Phys. B78 (1974) 541.
[300] A. Arneodo and G. Plaut, Nucl. Phys. B107 (1976) 262; B113 (1976) 156.
[301] J. Ranft and G. Ranft, Phys. Lett. 49B (1974) 369; Nucl. Phys. B83 (1974) 285.
[302] R. Baier and F. Widder, Nuovo Cim. 30A (1975) 169.
[303] F.W. Bopp, Siegen Preprint, SI-77-4 (1977).
[304] M. LeBellac, CERN Lecture Notes, CERN 76-14 (1976).
[305] F. Hoyot, F.S. Henyey and M. LeBellac, Nucl. Phys. B80 (1974) 77.
[306] J.L. Meunier and G. Plaut, Nucl. Phys. B87 (1975) 74.

[307] M. LeBellac, Proc. European Conf. on particle Physics, Budapest (1977).
[308] CERN-Bologna Coll., M. Basile et al., Nuovo Cim. 39A (1977) 441.
[309] A. Arneodo and J.L. Meunier, Nucl. Phys. B143 (1978) 163.
[310] P. Pirila, G.H. Thomas and C. Quigg, Phys. Rev. D12 (1975) 92.
[311] T. Ludlam and R. Slansky, Phys. Rev. D12 (1975) 59, 65.
[312] A. Bialas, K. Fialkowski, M. Jesabek and M. Zielinski, Acta Phys. Polonica B6 (1975) 59.
[313] R. Baier and F.W. Bopp, Nucl. Phys. B79 (1974) 344; Acta Phys. Aust. 47 (1977) 251.
[314] W. Thome et al., Nucl. Phys. B129 (1977) 365.
[315] G. Giacomelli and M. Jacob, Phys. Rep. 55 (1979) 1.
[316] Brazil-Japan Collaboration: Y. Fujimoto, in: Proc. Multiparticle Dynamics, Kyoto, 1978.
[317] See J. Dias de Deus and W.A. Rodrigues, Nuovo Cimento 55A (1980) 34, and references therein.
[318] T.K. Gaiser and G.B. Yodh, Annual Review of Nuclear and Particle Science (in press).
[319] B.S. Acharya, M.V.S. Rao, K. Sivaprasad and S. Rao, TIFR preprint (to be published).
[320] M. Basile et al., Phys. Lett. 95B (1980) 311.
[321] Ch. Berger et al., Phys. Lett. 95B (1980) 313.